Focused Ion Beam (FIB) Fabrication of Novel 2D/3D Nanoscale Structures: Process Modeling and Applications

Thesis Report

Submitted in partial fulfillment of the requirements of the degree of

Doctor of Philosophy

of the

Indian Institute of Technology Bombay, India

and

Monash University, Australia

by

Vivek Garg

Supervisors:

Prof. Rakesh G. Mote (IIT Bombay)

Prof. Jing Fu (Monash University)

The course of study for this award was developed jointly by

Monash University, Australia and the Indian Institute of Technology Bombay, India

and was given academic recognition by each of them.

The programme was administrated by

The IITB-Monash Research Academy

(2020)

Copyright Notice

© Vivek Garg (2020)

Declaration

This thesis is an original work of my research and contains no material which has been accepted for the award of any other degree or diploma at any university or equivalent institution and that, to the best of my knowledge and belief, this thesis contains no material previously published or written by another person, except where due reference is made in the text of the thesis.

Print Name: Vivek Garg

Date: 07/04/2020

Table of Contents

List of Tables

List of Figures

List of Symbols and Abbreviations

D	Diameter
P	Period
h	Height
w	Base width (pillars)
λ	Wavelength
I_B	Current
A	Milling area
T_M	Milling time
Q	Charge
q	Electron charge
$D(x, y)$	Ion distribution in Cartesian coordinates
x_p, y_p	Beam starting position coordinates
$Y(\theta)$	Angle dependent sputter yield
M	Mass
ρ	Density
v	Velocity
F	Force
R	Displacement
σ	Standard deviation
N	Total number of pixels
n_x, n_y	Number of pixels in x and y directions respectively
D_x, D_y	Step-size in x and y directions respectively

t_D	Dwell Time
QE	Quantum Efficiency
$P_{in}\ (\lambda)$	Incident light power at a wavelength λ
$P_{abs}\ (\lambda)$	Absorbed light power at a wavelength λ
I_{SC}	Short Circuit Current
$g\ (\lambda)$	Absorption Anhancement
R	Reflection
T	Transmission
$\|E\|^2$	Electric Field Intensity
$x\ (\lambda),\ y\ (\lambda),\ z\ (\lambda)$	Color Matching Functions
n	Refractive index
k	Extinction Coefficient
E	Energy
$\Phi(x)$	Screening Function
$g(r)$	Radial Distribution Function
a_0	Bohr radius (0.539 Å)
ϵ_0	Vacuum Permittivity (8.85×10^{-12} F/m)
pA	Pico-Ampere
nA	Nano-Ampere
kV	Kilo-Volt
kHz	Kilo-Hertz
ms	Milli-second
µs	Micro-second
ns	Nano-second

ps	Pico-second
fs	Femto-second
UV	Ultra-violet
NA	Numerical Aperture
FWHM	Full Width at Half Maximum
HFW	Horizontal Field Width
DPI	Dots Per Inch
CMOS	Complementary Metal Oxide Semiconductor
CIS	CMOS Image Sensor
KOH	Potassium Hydroxide
DI	De-Ionized
FIB	Focused Ion Beam
LMIS	Liquid Metal Ion Source
GIS	Gas Injection System
GAE	Gas Assisted Etching
SEM	Scanning Electron Microscope/Microscopy
TEM	Transmission Electron Microscope/Microscopy
EDS	Energy Dispersive X-Ray Spectroscopy
EBL	Electron Beam Lithography
AFM	Atomic Force Microscope/Microscopy
MBE	Molecular Beam Epitaxy
CNT	Carbon Nanotube
CVD	Chemical Vapor Deposition
DRIE	Deep Reactive Ion Etching

NW	Nanowire
NH	Nanohole
NP	Nanoparticle
ND	Nanodisk
CIE	Commission Internationale de l'Eclairage
FDTD	Finite-Difference Time-Domain
PBC	Periodic Boundary Conditions
PML	Perfectly Matched Layer
MC	Monte Carlo
SRIM	Stopping and Range of Ions in Matter
TRIM	Transport of Ions in Matter
MD	Molecular dynamics
LAAMPS	Large scale atomic/molecular massively parallel simulator
Ovito	Open Visualization Tool
TDE	Threshold Displacement Energy
SW	Stillinger-Weber
ZBL	Ziegler–Biersack–Littmark
RDF	Radial Distribution Function
c-Si	Crystalline Silicon
a-Si	Amorphous Silicon
Mo	Molybdenum
W	Tungsten
Ga	Gallium
Si_3N_4	Silicon Nitride

As	Arsenide
GaAs	Gallium Arsenide

Abstract

This work aims at fabrication of novel 2D/3D nanoscale structures by focused ion beam (FIB). The nature of accelerated ions in a focused ion beam system is directly used and Gaussian pillar like subwavelength nanostructures are fabricated in a single-step on Si. The fabricated nanostructures are tunable via FIB parameters- current, dwell time, beam overlap, and can be adjusted for desired functionality. High index nanostructures lead to unique light-matter interactions and strong optical resonances for potential light trapping applications. Gaussian shaped subwavelength nanostructures are investigated for broadband light trapping and antireflection properties through Finite-Difference Time-Domain (FDTD) calculations, exhibiting 10-20% reflection for a broadband wavelength range against previously reported silicon (Si) structures (such as nano-cones, nano-wires, nano-pyramids etc.). The unique shape of Gaussian pillar structures enables reflection suppression from the smaller tip and efficient light trapping, which are confirmed through light reflection and absorption density calculations. Experimental results provide evidence for antireflection properties, exhibiting 10-20% reflection from fabricated nanostructures. Considering the tunable structure and rapid fabrication approach of Gaussian shaped nanostructures, the work provides realization of nanoscale light management structures for localized light trapping and antireflection applications.

A novel approach for color filtering in reflection mode via direct fabrication of subwavelength nanostructures on high-index, low-loss, and inexpensive Si substrate is further developed. Nanostructures having a unique geometry of tapered holes are fabricated exploiting the Gaussian nature of a gallium source FIB. The fabrication process is rapid and single-step, i.e., without any pre- or post-processing or mask preparation, in contrast to previously reported nanostructures for color filtering. These nanostructures are tunable via FIB parameters and a wide color palette is created. Color filtering via interaction of visible light with nanostructured surfaces offers high resolution printing of structural colors. FDTD calculations reveal that the unique tapered nanohole geometry facilitates enhanced color purity via selective absorption of a narrow band of incident light wavelengths and makes it possible to obtain a wide variety of colors suitable for realistic

color printing applications. The proposed approach is demonstrated for color printing applications via fabrication of butterflies and letters on Si.

Freestanding 3D Si nanostructures, combining ion beam implantation with bulk structuration via wet etching, are developed. The freestanding 3D Si nanostructures fabricated by wet etching of ion implanted Si are employed for *in-situ* ion induced bending for developing designed complex 3D nanostructures. The detailed experiments on Si NWs are carried out to characterize the bending behavior and mechanism. Monte Carlo simulations and TEM nanostructural characterizations are carried out to investigate the bending phenomenon. The bidirectional nature of ion induced bending at 30 kV provides an additional degree of freedom. The developed approach is demonstrated for 3D nanostructure fabrication, and the process capability is established through the fabrication of high aspect ratio, complex 3D structures, such as ultra-long NWs, folded nanomesh etc. A unique “bacterial box trap” is also demonstrated for bacteria trapping as an outlook for a versatile strategy for capturing bacterial cells via fabrication and controlled manipulation of Si mesh. Further, multi-scale modeling of the *in-situ* ion irradiation induced bending is presented incorporating molecular dynamics (MD) simulations together with finite element analysis (FEA). MD simulations reveal the ion solid interactions, defects formation due to ion irradiation of Si. The atomic scale simulations indicate the development and evolution of localized tensile-compressive stresses in the lattice with increased ion dose. Such reversal of localized stresses, provide the alternate bending directions, estimated through finite element analysis. These findings are in excellent agreement with the experiments, providing new insights for ion induced bending of nanostructures, and pave the way towards a versatile platform for facile fabrication of 3D nanostructures with anticipated functionalities.

Chapter 1. Introduction

1.1 Background

Advances in micro-nanofabrication tools and techniques are pushing the structure size into nano/pico regime. Such micro/nano/pico structures carry potential in various applications like energy harvesting, opto-electronics, sensing, biomedical engineering etc. Conventional lithography techniques are widely used to fabricate microstructures commercially. This is mainly because of promising high throughput due to their parallel processing nature with the use of a mask. However, structures at nano level pose tremendous challenges on mask preparation and 3D structures are nearly impossible with such techniques.

Focused ion beam is an important and advanced technology in the field of micro/nano fabrication. It has wide range of capabilities from milling and deposition to imaging at micro/nano scale. The distinct advantage of FIB lies in the fact that it enables mask-less direct fabrication on various materials, making it suitable for applications in the field of nanotechnology. Focused ion beam instrument, when combined with imaging technologies like scanning electron microscope (SEM), offers a wide range of applications for fabrication and characterization of micro/nano structures. This is because the FIB milling does not require any intermediate resist layer as in other photo or e-beam lithographic techniques, and thus enables direct writing of micro/nano structures. Focused ion beam has a short wavelength with high energy density, which helps focusing the beam to a smaller spot size of 5-10 nanometer (nm). It allows control of beam shape and size for fabrication of desired structures. The unique fabrication capabilities of FIB make it an excellent tool for rapid prototyping applications. A great detail of research exists in the literature for FIB principle, its applications, and limitations [1]–[6]. Focused ion beam processing has also been applied for processing and characterization of biological, organic materials etc. [7]–[9], allowing its use for multidisciplinary research.

1.2 Motivation

1.2.1 3D Micro-Nano Fabrication: Diverse Applications

3D micro-nanostructures find a wide range of multidisciplinary applications in science and technology. The surface texturing of surfaces develops novel electromagnetic properties and a myriad of applications in optics, such as color filtering, perfect absorbers, negative refractive index, spatial resolution beyond the diffraction limit, high sensitivity detectors etc. In addition, texturing of surfaces is not just limited to applications in optics or material science, but also finds novel application in other domains, such as biology. The textured surfaces have been widely adopted for microfluidics, bio-photonics, antibacterial applications. In this section, the importance of 3D micro-nanostructures with specific applications are presented and discussed as an outlook to the thesis objective.

A variety of 3D plasmonic silver (Ag) hollow nanostructures as building blocks for applications in plasmonics is shown through SEM images in Figure 1.1 (a). These nanostructures were realized through metal deposition over previously fabricated templates, based on secondary electron generation through ion beam exposure of a resist polymer coating over a Si_3N_4 membrane and subsequent dissolution of unexposed region in a solvent [10]. Such 3D hollow nanostructures can be designed for multifunctional applications such as broad band optical absorption, enhanced light trapping etc. Silicon (Si) is an important material in semiconductor and solar cell industry. However, due to a high refractive index of Si, a large portion of incident light is reflected from the surface, resulting in poor efficiency of Si solar cells. The texturing of Si can be used to reduce the reflection from the surface and improve the solar cell performance [11]. The amorphous silicon (a-Si) nanocones (Figure 1.1 (b)), realized through reactive ion etching (RIE) of self-assembled silica nanoparticles over a-Si coated indium tin oxide (ITO) glass substrate, can function as absorbers and antireflection layers to improve the solar cell efficiency over the visible spectrum (400-800 nm) [12]. The a-Si nanoscone arrays provide index matching with air, developing the improved absorption. Structured metal films, realized through gold (Au) coating of nanostructure templates fabricated by two photon polymerization of UV-curable photoresists, for enhanced optical absorption over mid-infrared range (800-2500 nm) are shown in Figure 1.1 (c) [13]. The Au coated 3D nanostructures exhibited a high absorption (~90%) over mid-infrared range [13] and can be used for potential device designs, optical surfaces for sensor applications. Fabrication of X-ray optics, for high

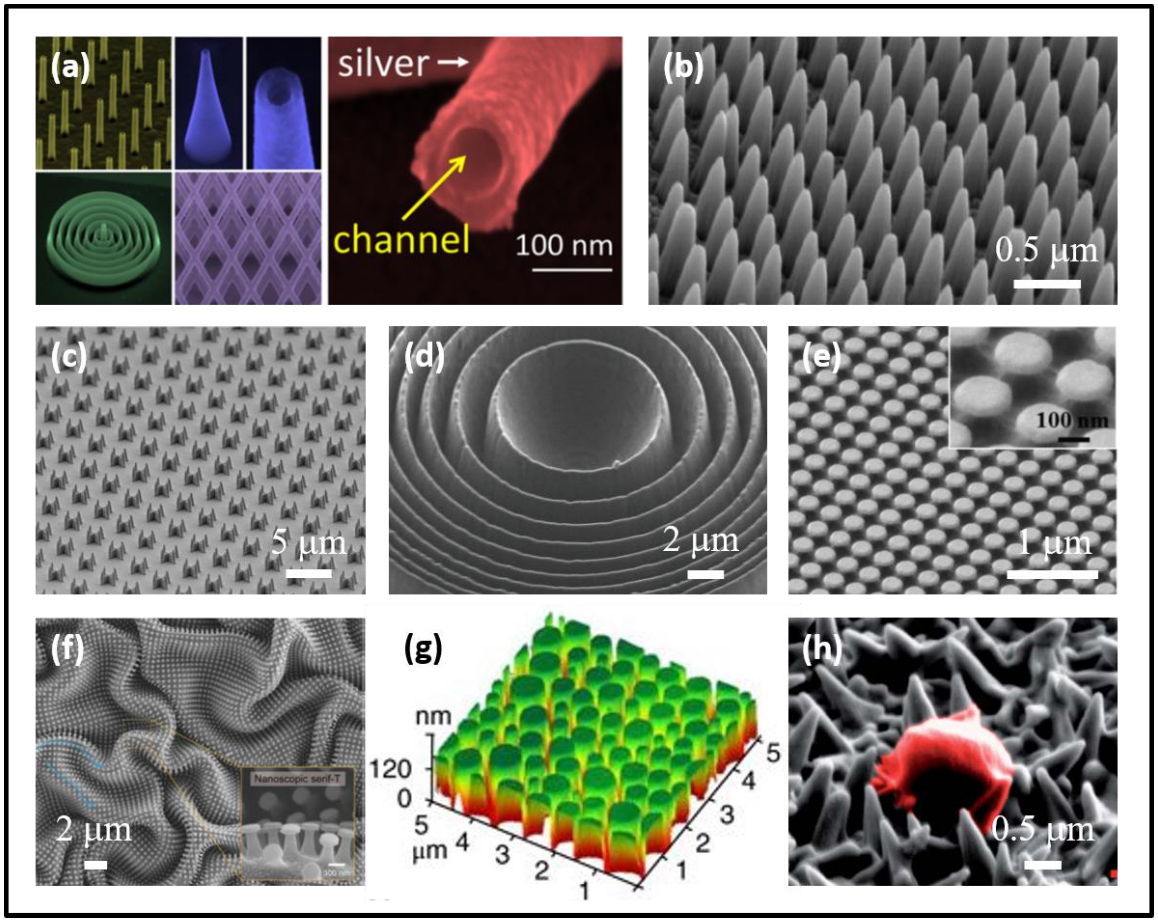

Figure 1.1: SEM image showing (a) 3D hollow Ag nanostructures as building blocks for plasmonics [10], (b) Si nanocone structures for optical absorption enhancement over visible range (400-800 nm) [12], (c) Au coated 3D microstructures for optical absorption enhancement over mid-infrared range (800-2500 nm) [13], (d) 3D plastic kinoform for X-ray optics [14], (e) Au coated SiO_2 nanopin plasmonic metasurfaces for color filtering and sensing [15], (f) 3D Au-polystyrene super-omniphobic surfaces with extreme pressure resistance [16], (g) AFM image showing Si_3N_4 nanostructure for bio-photonics [17], (h) Au nanospikes structures for antibacterial surface applications [18]

performance focusing, require 3D nanoscale features. Figure 1.1 (d) shows the profile of a zone plate, called kinoform, fabricated through two photon polymerization of photosensitive material [14]. A tightly focused, high-power infrared laser is used for absorption of photons and subsequent polymerization of the photoresist. The 3D printing of micro-nanostructures through laser induced polymerization can provide realization of optical elements with improved efficiencies. Subwavelength nanostructures, based on the careful design, can also be employed for color filtering and colorimetric sensing applications. Au coated SiO_2 nanopin cavity resonators on Si substrate for reflective color filtering and colorimetric sensing are shown in Figure 1.1 (e). The fabrication of nanopin structures was carried out using a combination of electron beam lithography (EBL) and Si etching [15], which requires a series of steps and careful design mask design. Such nanostructures exhibit color change with change in surrounding medium refractive index and can be used for sensing applications. Attempts have also been made for realization of multiscale structures for applications in fluidics with improved pressure resistance capabilities. For example, springtail inspired multiscale structures (Figure 1.1 (f)) were fabricated with nanoscale features, realized through a combination of nanoimprinting, secondary sputtering lithographic techniques, thin film deposition; while microscale features were realized through heat induced shrinking and wrinkling in a polymer substrate [16]. Such multiscale nanostructures exhibited superomniphobic behaviour with extreme pressure resistance. 3D micro-nanostructures also find applications in the applications domain beyond optics, such as biomedical applications. The engineered silicon nitride (Si_3N_4) photonic nanostructures shown in Figure 1.1 (g) exhibited hydrophilicity, anti-biofouling properties and can be used for development of optomechanical sensing element [17]. The progress and development of such biophotonic nanostructures inspires multifunctional applications in medical field and can be employed for practical implants. The incorporation of nanostructures on a substrate has also been reported to exhibit the antibacterial properties due to mechanical rupture of the bacteria. Figure 1.1 (h) shows multidirectional Au nanospikes structures realized through electrodeposition method [18]. The nanospike structures were found to exhibit antibacterial activity and provide a route towards Au-based dental implants.

The fabrication of micro-nanostructures, thus, is an important field for exploration of novel applications in science, technology and has gained a significant attention among the researchers. A wide variety of fabrication techniques have been developed over the past decade to fabricate and explore the exotic properties of micro-nanostructures [19]–[22]. The experimental realization of 3D structures for extended functionalities with fabrication simplicity and without involving multiple steps, however, is still a key challenge. Most of the processes used for surface texturing either involve complex multiple steps and require post processing for contamination or lead to uneven, uncontrolled geometry [11]. For example, two photon polymerization method is limited to photosensitive materials, and cannot be extended to other materials. Further, the inaccuracies and contamination during the fabrication process can cause poor performance for specific applications. Thus, a simpler methodology and designs are required for controlled 3D surface texturing, which will ensure the targeted performance in addition to the ease of fabrication.

1.2.2 Fabrication with Focused Ion Beam

Focused ion beam has evolved as a tool for rapid prototyping of microsystems owing to its one-step or mask-less fabrication capability and high resolution. Focused ion beam nanofabrication is a single-step, mask-less process offering advantages in terms of high current density, ability to fine focusing etc., making it suitable for direct writing of micro/nanostructures [23]–[25]. Depth control methods such as pixel dwell time [26], 2D slice-by-slice [27], continuous slicing [28], inverse mapping [29] etc. have been employed for controlled texturing via FIB direct milling through a variable dwell time or beam scanning. However, it involves complex calculations of dwell time, slicing layers etc. and pose challenges for fabrication accuracy. Lithographic approach, based on the ion implantation through FIB and selective chemical etching can also be utilized for surface texturing [30]. The lithographic approaches rely heavily on chemical etching methods, which are difficult to control while preserving the fabrication geometry. In addition, gas assisted FIB etching can be used for surface texturing in the presence of an etching gas (for example XeF_2 for Si) at an increased milling rate. However, it is difficult to control the process due to surface chemistry involved [31]. Further, the effect of FIB Gaussian beam profile, scanning, dwell time etc. have been investigated through simulations and experiments [31], [32]. The process, however, still requires better control and optimization for fabrication accuracy [23] and the issues such as FIB induced damage, ion contamination, redeposition, beam tail effect etc. [33] must be addressed. FIB based depth control methods involve complex calculations of dwell time, slicing layers etc. and pose challenges for control of accuracy. Lithography methods, on the other hand, are dependent on ion implantation and chemical etching, making it difficult to control the fabrication geometry. Gas assisted deposition methods are restricted to few materials (Pt, W, C etc.), based on availability of organometallic compounds, and fabricated geometries consist of impurities. The gas assisted etching methods become complex due to surface chemistry involved and it is difficult to control the process. Moreover, most of the fabrication process discussed have been used for micro-fabrication and pose tremendous challenges at nanoscale. Recent studies [6] have suggested promising methods for realization of complex micro-nanostructures, however, the issues associated with FIB based micro/nanofabrication must be addressed, and it becomes interesting to explore this exciting tool for future developments and novel applications.

1.3 Objective

Focused ion beam is a specialized process and involves several complexities in terms of beam control and fabrication accuracy. Accurate FIB fabrication of micro/nanostructures for specific applications require deep insight into the process. The accuracy of FIB fabricated profiles depends on number of parameters such as scanning strategy, beam current, acceleration voltage, beam dwell time, etc. A better understanding of the milling mechanisms and material removal at micro/nano level is required for accurate fabrication. This will allow accurate fabrication of optical elements or any other 3D structure for specific applications in optics, photonics etc. The proposed research is based on FIB process for nanofabrication and its application in creating novel nanostructures. The aim of this study is to investigate ion-material interactions, followed by rapid computation of ion beam-based material removal (milling or etching) to create 2D/3D structures at micro/nano scale. The methodology is employed to fabricate functional nanostructures for diverse applications like anti-reflection, color filters, nanostructure controlled manipulation etc. This work aims at achieving following objectives:

- Investigation of ion solid interactions in a focused ion beam
- Fabrication of novel 2D/3D nanoscale structures by focused ion beam
- Development of FIB fabricated 2D/3D Si nanoscale functional structures for diverse applications such as anti-reflection, color filters, strain engineering and controlled manipulation of nanostructures etc.

1.4 Research Approach and Outline

The report is organized in the following way. Chapter 2 presents a brief review of literature on focused ion beam nanofabrication. The research starts with rapid prototyping of highly ordered subwavelength nanostructures through FIB nanofabrication in Chapter 3 for nanoscale light trapping and antireflection applications. Chapter 4 presents FIB direct fabrication of subwavelength nanostructures for multicolor generation. Experiments and simulations are further presented for silicon color filters realized through the single-step fabrication to study the optical properties. Chapter 5 presents controlled manipulation or weaving of nanostructures *in situ* by kiloelectronvolt gallium (keV Ga) ion irradiation for developing designed complex 3D nanostructures by tuning the ion dose and energy. Chapter 6 provides investigation of ion solid interactions for ion induced bending. Molecular dynamics (MD) simulations together with finite element analysis (FEA) are presented to investigate the ion irradiation of nanostructures and substantiate the bending mechanism. Finally, Chapter 7 provides conclusions and outlook for future work.

Chapter 2. Literature Review

2.1 Focused Ion Beam

Focused ion beam technique utilizes a finely focused beam of ions for milling, imaging, deposition, implantation etc. A high energy ionized beam of ions in a FIB system is produced from a liquid metal ion source (LMIS) by the application of electric field. This beam is focused onto a target surface, which results in number of phenomena such as sputtering of constituent atoms, generation of collision cascade, surface modification etc. Heavy ions also produce secondary electrons from the target surface, which can be used for imaging applications. Focused ion beam can also be used for deposition, implantation, and lithography applications. In this section FIB instrument, basic principle, and important parameters for FIB fabrication are discussed.

2.1.1 The Instrument

A typical dual beam FIB-SEM instrument has a liquid metal ion source (LMIS), an ion column, an electron column, a stage, detectors, a gas injection system (GIS), a vacuum system, and a computer. An illustration of a Carl Zeiss Auriga dual beam FIB-SEM system (compact-4558) at IIT Bombay is shown in Figure 2.1 (a). Focused ion beam system is similar to a scanning electron microscope, where an electron beam is used. Both the systems employ charged particles, which can be used for imaging, etching, and deposition applications. Use of ions in FIB offers several advantages over the electrons, due to the reason that ions are comparatively massive and larger. Ions have much more direct effect on the sample as compared to electrons, whereas electrons penetrate deeper due to their smaller size. Energetic ions carry higher momentum than electrons, which is used for material removal and milling applications. Another difference between the two systems lies in the beam steering and focusing optics. In SEM, magnetic fields are used to focus the electron beam due to smaller mass of electrons. On the other hand, charged ion beam requires stronger field, hence electrostatic lenses are used. In a dual beam system, FIB and SEM columns are arranged at an angle to each other, which allows milling/deposition/etching by FIB and simultaneous observation through SEM. The angle between the electron and ion beam is slightly different in different manufacturers, for example: the angle is 54° in Zeiss, Hitachi, 52° in Thermofisher, and 55° in Tescan dual beam systems. The sample is made normal to FIB by tilting the sample stage according to the angle between FIB and SEM. A typical configuration of FIB-SEM columns and sample inside the vacuum chamber in a dual beam system is shown in Figure 2.1 (b).

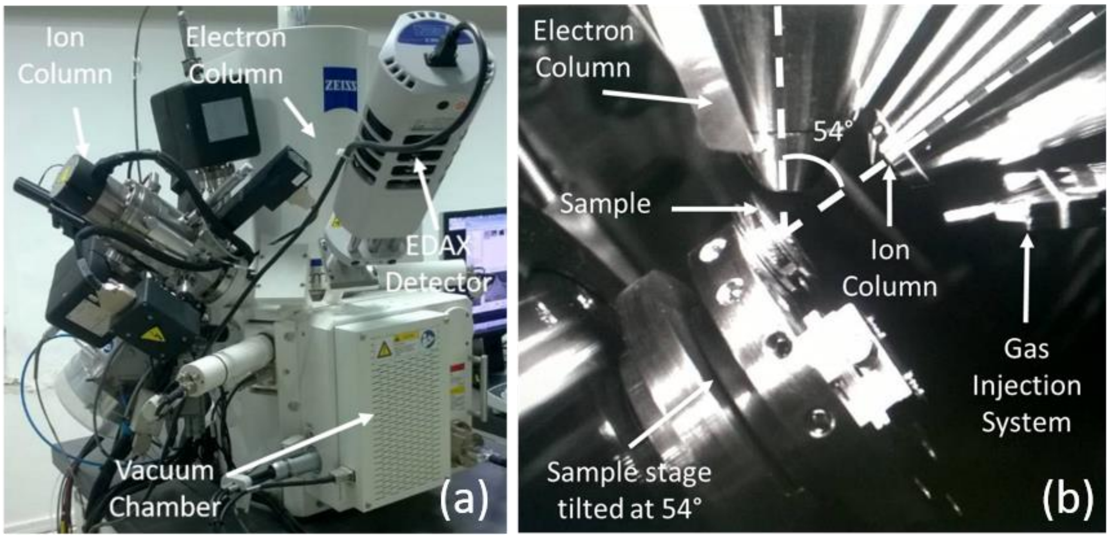

Figure 2.1: (a) Carl Zeiss Auriga compact-4558 FIB SEM system, (b) Dual beam sample configuration inside vacuum chamber

A highly focused ion beam is obtained from LMIS, which has a tungsten (W) needle. The tungsten needle is attached to a reservoir of source material. Gallium (Ga) is most commonly used FIB source because of the following reasons,

- Low melting point (29.8°C)- requires less heating and avoids any interaction of Ga with tungsten needle
- Low vapor pressure- it can be used in pure form and promotes long life, avoiding the Ga evaporation
- Gallium has suitable mechanical, electrical, and vacuum properties. Gallium emission provide high angular intensity with a small spread of energy
- Low volatility at melting point- long source life

The heated LMIS flows and wets the tungsten needle of tip radius of 2-5 μm. Gallium requires less reheating and remains liquid at ambient conditions for weeks due to its super cooling properties. If an electric field (10^8 V/cm) is applied at the end of wet tungsten needle, it will cause Ga to form a point source (2–5 nm) of conical shape (Taylor cone). This shape is formed because of balance between surface tension of liquid metal and electrostatic force set up by the applied electric field. Once the cone tip is formed and is small enough, extraction voltage pulls Ga from the tungsten tip by ionization. The Ga ions are passed through the ion column, where an acceleration voltage (1–50 kV) is applied. A set of apertures and lenses are used in the ion beam column to focus the ion beam of various diameters at target surface. The spot size (diameter) and shape of the beam govern its machining and imaging capabilities.

2.1.2 Ion Solid Interactions

The incident ion beam loses its energy to the target electrons and atoms, when scanned over the target surface. Most ions are deflected/backscattered from their path because of the collision with the target atoms while few ions penetrate over a certain distance inside the sample. Because of the collisions, sample constituent atoms are displaced from their lattice positions. The collision also results in recoil and sputtering of constituent atoms, formation of defects, electron emission and excitation, photon emission etc. [1]. Mixing of constituent atoms, phase transformation, crystallization, amorphization, and permanent damage might also occur because of thermal and radiation induced effects. Ion implantation on the target surface due to the FIB operation and sputtering results in change of surface morphology and craters are formed because of atoms being removed. A schematic of focused ion beam interaction with sample surface is shown in Figure 2.2. The collision of ions with target material nucleus and electrons can be considered separately due to large difference in their masses,

- Elastic or nuclear collision- between incident ions and nucleus. Kinetic energy and momentum are conserved. The incident ion recoils the target atom and scattering of ion takes place.

- Inelastic or electronic collision- between incident ions and electrons. It results in excitation and ionization of the constituent electrons.

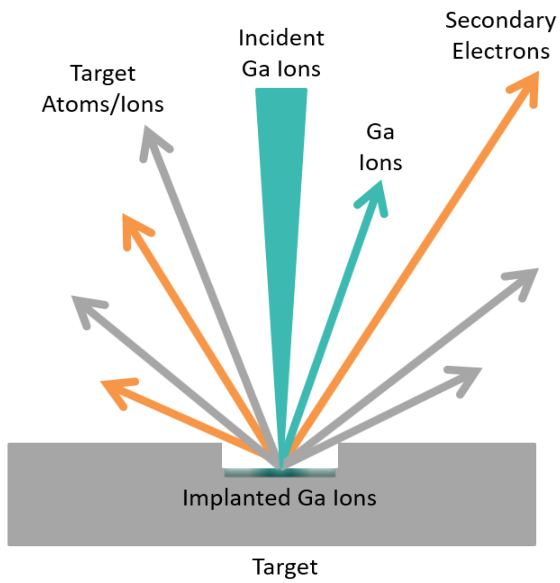

Figure 2.2: Schematic illustration of Ga ions interaction with target material: sputtering of the target atoms/ions, Ga ion implantation and generation of secondary electrons from the target surface

Following main effects take place due to ion solid interactions [1],

- Thermal heating- the sample surface gets heated due to ion beam interactions.
- Radiation damage- the sample is damaged due to displacement of atoms from their lattice positions. The depth of ion penetration depends on material properties and operating parameters such as the ion beam energy, incidence angle. The ions are implanted in the sample.
- Sputtering- the atoms are removed from sample surface due to the incident ions.
- Electron emission- the electrons are emitted from the target surface due to ion solid interactions. These electrons are used for imaging.
- Chemical effects- these are produced due to ion-electron interaction and ion-atom interaction. Examples are ion assisted etching, ion induced deposition etc.

The ion solid interactions for amorphous materials can be modeled using Monte Carlo (MC) simulations by SRIM/TRIM (Stopping and Range of Ions in Matter, Transport of Ions in Matter) codes developed by Ziegler and Biersack [35]. These simulations are helpful for calculation of sputter yield, interaction volume etc. However, MC simulations are based on binary collisions and effects of neighboring atoms are not considered.

2.1.3 Governing Parameters and Effects

Focused ion beam nanofabrication is a complex process and requires accurate control of processing parameters for desired fabrication. A brief introduction of important FIB governing parameters and effects are discussed here.

2.1.3.1 Acceleration Voltage

An extraction voltage is applied to pull the Ga ions from the wet tungsten needle tip. The energy and velocity of the ions depend on the applied acceleration voltage in the ion column. Ions will travel faster if a high acceleration voltage is applied and the energy imparted to the target sample will also be higher [36]. An increase in acceleration voltage does not influence the probe current. An acceleration voltage of 30 kV is generally used to get the highest possible resolution and sputtering yield [37]. This value of acceleration voltage makes the system suitable for most applications.

2.1.3.2 Beam Current

Ion beam current is an important parameter for fabrication of high aspect ratio structures. It defines the resolution capability of the FIB system. Beam spot size is controlled by the beam current. It is difficult to measure the spot size in actual practice, so the beam current is generally used as a process parameter. The sputtering yield is controlled by changing the beam current. At high values of beam current (i.e. larger spot size), the sputtering rate is higher. The higher material removal rate, however, is at the expense of the fabrication accuracy. If a high resolution and accurate profile is required, a low beam current must be used. During typical milling applications, a high beam current is used for bulk material removal applications, while low beam currents are used for fine polishing. Typical minimum spot size of Carl Zeiss Auriga system at MEMS department IIT Bombay is 8 nm at a beam current of 1 pA and acceleration voltage 30 of kV.

2.1.3.3 Dwell Time

Dwell time in a FIB system is the duration of time for which the beam is stationary at a particular position (pixel). Ion beam dwell time defines the duration of time for which a particular pixel is scanned by the ion beam [31]. The dwell time is generally of the order of micro-seconds (μs) to milli-seconds (ms). Final geometry of FIB fabrication depends on the dwell time, making it an important parameter. There are two challenges associated with the optimization of the dwell time. First, excessively large dwell time results in redeposition of sputtered atoms/ions and the surface accuracy becomes poor. The fabrication depth is also more than the intended value. These effects are applicable for fabrication, where depth removed per pixel is of the order of beam diameter [38]. Second, a low dwell time results in undesired material removal outside the targeted area. This occurs in the fabrication of non-rectilinear profiles such as circle, ellipse etc. A significant portion of target material is exposed to the unintended ion dose and results in an irregular profile and undesired milling [38]. Thus, a careful choice and optimization of FIB dwell time is required for the desired accuracy of fabrication. This aspect is even more challenging for 3D features nanofabrication by FIB.

2.1.3.4 Ion Dose

The ion dose is a function of beam current and exposure time. The ion dose is expressed as number of ions per unit area exposed (ions/cm^2), it is the number of ions bombarded onto the target material through a defined area. Ion dose can be calculated as:

$$\text{Ion Dose} = \frac{\text{Ion number (ions)}}{\text{Area } (cm^2)} = \frac{\text{Q/q}}{\text{A}} = \frac{I_B(\text{Amp}) \times T_M(sec)}{\text{q} \times \text{A } (cm^2)} \tag{2.1}$$

where, I_B is the ion beam current used for milling, T_M is the milling time, A is the milling area, and q is the electron charge, i.e. 1.6×10^{-19} Coulomb/ion.

2.1.3.5 Ion Range

Focused ion beam with high-energy ions impacts the target surface. High-energy ions impart their energy to the surface atoms and travel a certain path inside the target material. The trajectory followed by the energetic ions is known as “collision cascade” and the total length of the path travelled by the ion before coming to rest is termed as “range”. The projected values of ion range in amorphous targets can be calculated using the Monte Carlo simulation based SRIM code developed by Ziegler and Biersack [35]. The ion range depends on ion solid interactions and material properties. Ion range a Ga ions in a few different materials is presented in Table 2.1 [39].

Table 2.1: The ion range of Ga ions and sputtering yield of various materials at 30 kV [39]

Material	Si	Al	Cu	Ag
Ion Range (nm)	27	24	10	11
Sputter Yield (atoms/ion)	2.6	4.4	11	14

2.1.3.6 Sputter Yield

Sputter yield is defined as the number of target atoms ejected per incident ion at the target surface. It depends on following parameters [40],

- Incident ions- mass, energy, dose, incidence angle etc.
- Target material- mass, crystal orientation, crystallinity, surface binding energies, conductivity, surface curvature etc.

There exists a threshold value of the incident ion energy for each material, below which no sputtering takes place. Table 2.1 shows the sputter yield for four different materials with gallium as an ion source at 30 kV. The sputter yield can be calculated as,

$$\text{Sputter Yield} = \frac{\text{Number of atoms removed from the target surface}}{\text{Number of incident ions}} \quad (2.2)$$

2.1.3.7 Incidence Angle

The angle at which the ion beam is focused onto the target material. Many applications demand for normal ion beam incidence. As the incidence angle increases from normal incidence, the probability of the target atoms escaping from the surface during cascade increases. At glancing angles, the surface channeling plays an important role that causes the sputter yield to decrease, which is another reason for the smaller depth at large incidence angles.

2.1.3.8 Beam Overlap

The scanning in FIB process, as illustrated in previous section, takes place along a predefined path and ion beam is moved to subsequent pixel locations with a distance equal to step size. Focused ion beam is blanked while moving from one pixel to another. The ion beam diameter and step size, in addition to dwell time, are two important parameters that determine the profile of depth being milled. Beam overlap is defined with respect to step size [40],

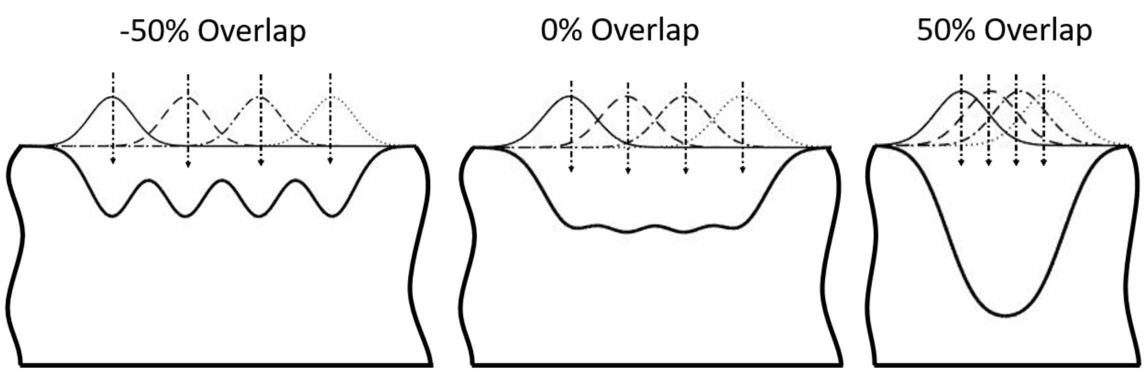

Figure 2.3: Concept of beam overlap in FIB and effect on fabrication profile: negative, zero, and positive overlap

$$\text{Beam Overlap} = \frac{\text{Beam Diameter} - \text{Step Size}}{\text{Beam Diameter}} \tag{2.3}$$

The concept of beam overlap is represented schematically in Figure 2.3. Beam overlap is 50 percent, if the step size is half of the beam diameter. It is a critical FIB parameter and must be optimized for different applications. Negative overlap for deposition, zero overlap for etching, and positive overlap are generally used for milling applications [40].

2.1.3.9 Scan Mode and Pixel Spacing

The ion beam can be scanned over a target surface in two different modes- raster scan and serpentine scan [40]. In raster mode, scanning is always in the same direction. The beam always moves to the initial point of next scanning line. Figure 2.4 (a) shows the schematic diagram of FIB raster scanning. In this mode of scanning, the sputtered atoms continuously redeposit on the milling area, which results in the loss of fabrication accuracy. Raster

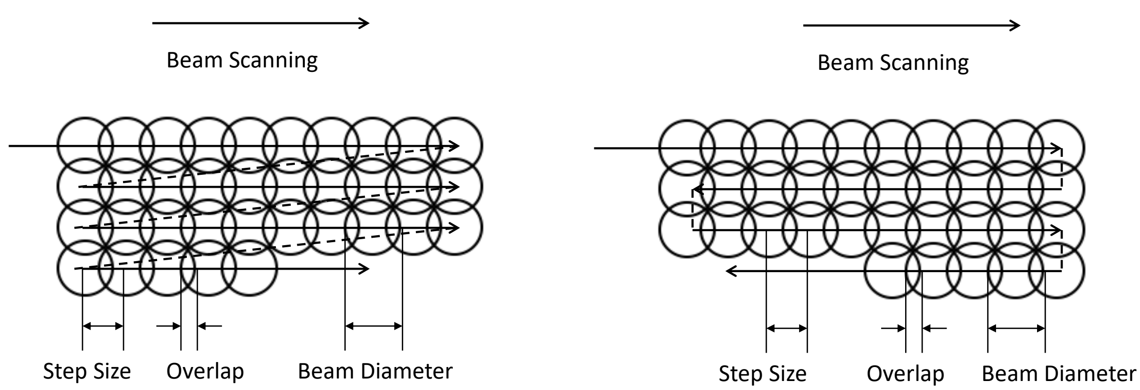

Figure 2.4: Schematic illustration of FIB scanning: (a) Raster scan, (b) Serpentine scan

scanning is suitable for fabrication of V shaped channels or inclined bottom surfaces. In serpentine scanning, the ion beam moves in reverse direction for next scan line. It results in faster operation and fabrication time is less as compared to the raster scan for a same area. The schematic diagram representing serpentine scanning mode is shown in Figure 2.4 (b). The redeposition of sputtered material is less in serpentine scanning mode, as the redeposited atoms from the previously scanned line are removed in the subsequent line scan. This mode of scanning is favorable for high aspect ratio structures with vertical sidewalls and flat bottom. Pixel spacing can be defined as the distance between the centers of two adjacent pixels. Milling by FIB will be uniform, if the spacing between adjacent pixels and scan lines is proper and small enough [23].

2.1.4 Capabilities

Focused ion beam technology finds applications in the major areas of material science due to its wide range of capabilities [23]. Ga ions in a FIB instrument can be used for imaging, milling, and deposition/etching applications. The secondary ions and electrons are generated due to the interaction between incident ions and surface atoms can be used for imaging applications. In FIB imaging, like a scanning electron microscope, the beam is scanned over the sample surface (Figure 2.5 (a)). These secondary ions or electrons are collected for imaging by means of the biased detectors. The detectors collect emitted ions or electrons based on the voltage applied to it. The resolution of FIB imaging depends upon the ion beam spot size [2].

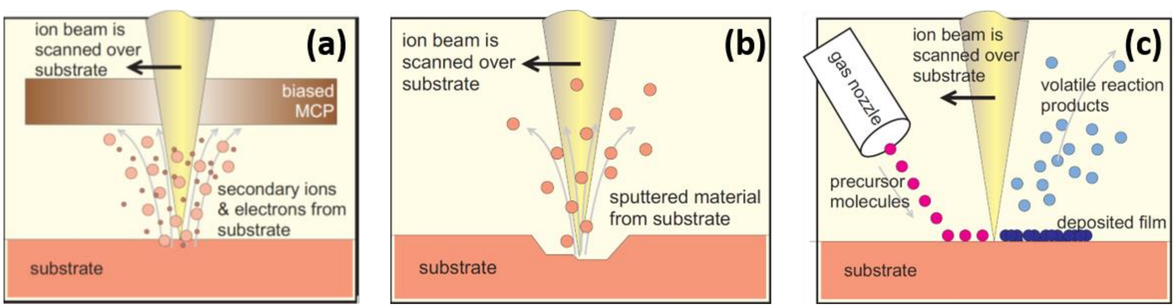

Figure 2.5: Focused ion beam capabilities (a) Imaging, (b) Milling, and (c) Deposition [2]

Focused ion beam has proven to be a powerful tool for material analysis and characterization. The channeling contrast produced by FIB is better than the contrast provided by the electrons in a SEM. This capability is utilized for observing grain boundary orientations and crystal defects such as dislocations. However, due to the ion beam interactions with the sample surface, some damage also occurs. It limits the use of FIB for imaging of soft materials. Some of the ions from the beam penetrate the sample and get implanted in the surface, resulting in change of surface properties. The depth of implantation depends upon the beam energy and material damage up to an extent takes place based on the beam parameters. These effects can be reduced by using a low energy and finely focused beam of ions.

Material from the sample surface can be removed very precisely using a high energy and focused beam of ions. If the high energy beam is scanned over the surface, as shown in Figure 2.5 (b), it results in sputtering of the atoms from the sample surface. The milling process can be observed simultaneously and sample surface can be analyzed by FIB imaging technique. The milling rate is generally small, as the material removal takes place atom by atom, and sputtered atoms from the surface are also redeposited sometimes. To enhance the milling rate, an etching gas can be used in the work chamber. This technique is called gas assisted etching [2]. There are various techniques by which ion beam can be scanned over the target surface. The milling depth by FIB depends upon several factors such as- ion beam dwell time, scanning technique, beam overlap, beam current etc.

Focused ion beam can also be used for deposition/etching applications in the presence of an organometallic compound [2]. The deposition process using FIB is shown in Figure 2.5 (c). An organometallic compound is sprayed over the sample surface in the form of a gas. The ion beam is subsequently scanned over the sample surface and compound is decomposed by the action of ion beam. The desired reaction products remain on the surface as a thin film, while the volatile products are removed with the help of vacuum inside the chamber. The deposited material is completely not pure, as some organic contaminants as well as gallium ions are also implanted. Tungsten, platinum, carbon etc. are some of the common materials that are deposited by FIB. The applications of FIB with these methods are discussed in detail in next section on micro/nanofabrication with FIB.

2.1.5 Limitations

Focused ion beam is a powerful tool for fabrication structures at micro/nano scale. However, like any other process, it also involves some limitations. Major issues/limitations in FIB milling for 3D micro/nanofabrication are as follows [3], [36],

- Overlap effect- To fabricate a smooth surface, the spacing between the pixels should be less than the beam size. However, this results in more milling than intended and consequently the milled depth is higher.
- Beam tail effect- it is due to the beam shape, which has a Gaussian distribution on ions. The tail of the beam results in extra milling, thus making it difficult to control the depth and maintain accuracy.
- Sputter yield- it depends on the angle of incidence. The incidence angle changes with the progress of machining as the surface geometry changes. Thus, the sputter yield changes with time, leading to the non-uniform material removal.
- Redeposition effect- few sputtered atoms redeposit on the sample surface itself, which results in fabrication inaccuracies.

In addition to the above-mentioned limitations, FIB also has scalability limitations. This makes FIB milling restricted to a smaller volume and suitable for rapid prototyping applications, however this issue can now be avoided to an extent employing plasma FIB with higher material removal rate [41].

2.2 Micro/Nanofabrication with Focused Ion Beam

The accuracy of fabrication during FIB processing depends primarily on the ion beam parameters, in addition to the target material. Fabrication of micro/nanostructures by FIB is a widely researched area due to its inherent characteristics, and several techniques have been developed. Fabrication techniques by FIB can be classified into the following categories based on the mechanism: direct milling methods- these makes use of either variable dwell time or scanning technique for controlling the depth [26]–[28]; lithography methods- these methods use ion implantation caused by FIB as a resist and subsequent selective chemical etching or deep reactive ion etching for material removal [30], [42]–[46]; gas assisted deposition/etching methods- makes use of FIB induced deposition or etching in the presence of an organometallic gas by deposition or removal of material [24], [31], [47]–[50]; ion irradiation induced self-organization methods [51]–[56]; ion irradiation induced bending methods [57]–[59]; and methods involving FIB induced nanostructure growth [60], [61]. Table 2.2 summarizes the techniques for fabrication of micro/nano-structures with FIB and each method is discussed in detail in the following sections.

Table 2.2: Fabrication of micro/nanostructures with FIB

Direct Milling	Pixel Dwell Time Method [26]
	2D Slice-by-Slice Method [27]
	Continuous Slicing Method [28]
Lithography	Ion Implantation and Deep Reactive Ion Etching/Chemical Etching [30], [42]–[44]
	Grayscale Lithography [45], [46]
Gas Assisted Deposition/Etching	FIB Induced Deposition [47]–[49]
	FIB Induced Etching [24], [31], [50]
Focused Ion Beam Induced Material Self-organization [51]–[56]	
Focused Ion Beam Induced Bending [57]–[59]	
Focused Ion Beam Induced Nanostructure Growth [60], [61]	

2.2.1 Direct Milling

Focused ion beam is used for fabrication of micro/nanostructures by removing successive layers of atoms from the surface. Material from the sample surface can be removed precisely using a high energy and finely focused beam of ions. If the high energy beam is scanned over the surface, it results in sputtering of atoms from the sample surface. The milling process can be observed *in-situ* and the sample surface can be analyzed by FIB/SEM imaging. The unique capability of precisely controlled machining by FIB can be used for fabrication of required geometry. By controlling the depth of machining, it will be possible to fabricate the 3D geometries using FIB. Complex structures using FIB can be developed, if the precise control over machining depth is possible. Various depth controlling methods using FIB to fabricate the 3D structures are discussed and each method is explored in detail for its advantages, limitations, and applications.

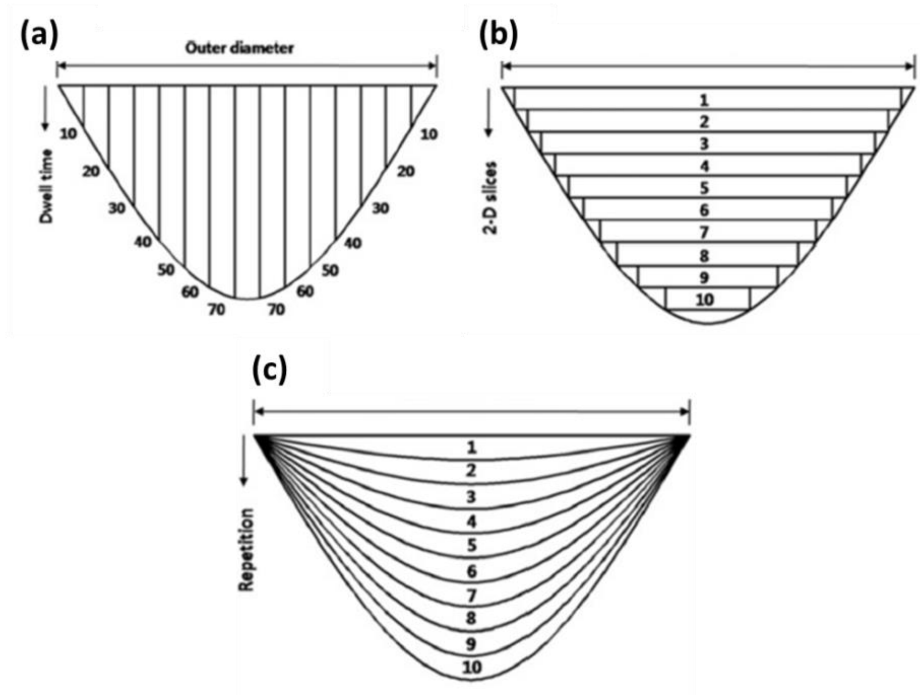

Figure 2.6: Focused ion beam depth control methods for micro/nanofabrication: (a) Pixel dwell time method [26], (b) 2D slice-by-slice method [27], (c) Continuous slicing method [28]

2.2.1.1 Pixel Dwell Time Method

A technique by controlling pixel dwell time for the fabrication of curved microstructures has been demonstrated [26]. A mathematical approach was developed for computation of dwell time at each pixel. The ion beam is deflected point by point, and the longer the beam dwells on a particular pixel, the more material is removed at the sample surface. Thus, by controlling the dwell time of the beam, the depth of the geometry produced can be controlled and 3D structures can be fabricated. The method is illustrated in Figure 2.6 (a).

Geometries like parabolic, circular, and sinusoidal have been used as initial shapes for experiments. Algorithms have also been used for generating the pixel dwell time from the geometry. The dwell time per pixel is calculated based on depth relationship, symmetry etc. The method has certain limitations in terms of computation and large computer memory, however, it formed the basis for fabrication of 3D curved surfaces by depth control. The angle dependence of sputter yield and stair case effects are prominent and lead to the deviation of experimental results from actual profile. The overlap effect also takes place due to smaller pixel size than the ion beam diameter, which subsequently alters the geometry. Number of techniques such as 2-D slice-by-slice [27], continuous slicing [28] etc. exist in the literature, which improve the depth control by pixel dwell time method in accurate and efficient manner.

2.2.1.2 2D Slice-by-Slice Method

In 2D slice-by-slice method, the constant dwell time and sputter yield are considered. The fabrication of 3D structures is done by the fabrication of many 2D slices with thin and constant thickness [27]. This is shown in Figure 2.6 (b). The depth to be milled is divided into N number of slices and each slice is milled in each step, so the total number of steps are N. Sputter yield and dwell time are fixed for each slice. The problems caused by angle dependence of sputter yield are removed by this approach. The same dwell time results in saving of computation time and computer memory. The milling depth for each slice is dependent on the slice thickness. This method is fast as compared to pixel dwell time method. A wide range of experiments were carried out, including the fabrication of spherical profiles using different materials and processing parameters. The complete process of fabrication is performed automatically and involves all the parameters for creation of 2D slices. The accuracy of the process largely depends on the number of slices. If the depth is divided by a greater number of slices, it results in better accuracy. However, it involves more computation and milling time is increased significantly. If the slices chosen are less, it will result in poor surface profile and staircase effects will also take place. Thus, number of slices used to divide the depth has to be optimized. One more important parameter, surface roughness, depends on local curvature in FIB milling process.

It results in loss of accuracy as the milling progresses and surface profile is not maintained due to sputter angular dependence. It limits the aspect ratio of structures to be fabricated. The redeposition and beam tail effects require consideration for fabrication accuracy.

2.2.1.3 Continuous Slicing Method

The continuous slicing method is modified version of 2D slice-by-slice method. It employs 2D slice-by-slice method along with spiral scan. The discrete 2D slices are scanned by ion beam over a thousand times to fabricate a circular conical shape [28]. The method is shown in Figure 2.6 (c). Stair case effects are less, and sputtering rate is comparatively high due to continuous scanning in this method. Spiral scan results in the same material redeposition in the radial direction, thus the staircase effects are avoided, and depth is controlled. This approach can reduce the redeposition, if the number of scans are used repetitively. This method provides high sputtering yield. Numbers of experiments were carried out using the method and silicon micro-mold for polymer replication and replicas of micro-lenses were fabricated. The method has limitations in the manner that the profile is controlled by the beam overlap, making it important to carefully select the spot size and pixel dwell time. Beam tail effect and angle dependence of sputter yield still exist and limit the process capability. Similar approach is used by Langridge et al. [62] for fabrication of aspherical micro-lenses using FIB. Recent examples, demonstrating FIB nanofabrication of various photonic/plasmonic nanostructures are shown in Figure 2.7. By tilting the substrate, slanted annular aperture arrays milled in gold films are shown in Figure 2.7 (a) with a SEM cross-sectional image showing the morphological details, which were demonstrated for plasmonic resonance tuning via obliqueness control for potential applications in sensing [63].

A SEM image of 3D chiral photonic Si nanostructures is shown in Figure 2.7 (b), which were fabricated through FIB milling followed by annealing with oxidation of damaged layer to produce complex shaped crystalline Si metasurfaces and demonstrated for strong optical chirality combined with high transparency on a sapphire substrate [64]. Figure 2.7 (c) shows SEM image of periodic silver nanoparticle arrays, located on top of quartz trapezoidal pillars on a quartz substrate fabricated by thermal evaporation and FIB milling.

These pillars were demonstrated for plasmonic lattice mode through coupling of localized surface plasmonic resonances. An example of nanofabrication of optical elements with Xe plasma FIB [65] is also shown in Figure 2.7 (d). The high material removal rate of Xe plasma FIB, enable fabrication of large optical elements. A SEM image showing the lithium niobate micro-axicon is shown in Figure 2.7 (d). These examples show the unique capability of FIB milling based nanofabrication which can be utilized for various nanoscale structures.

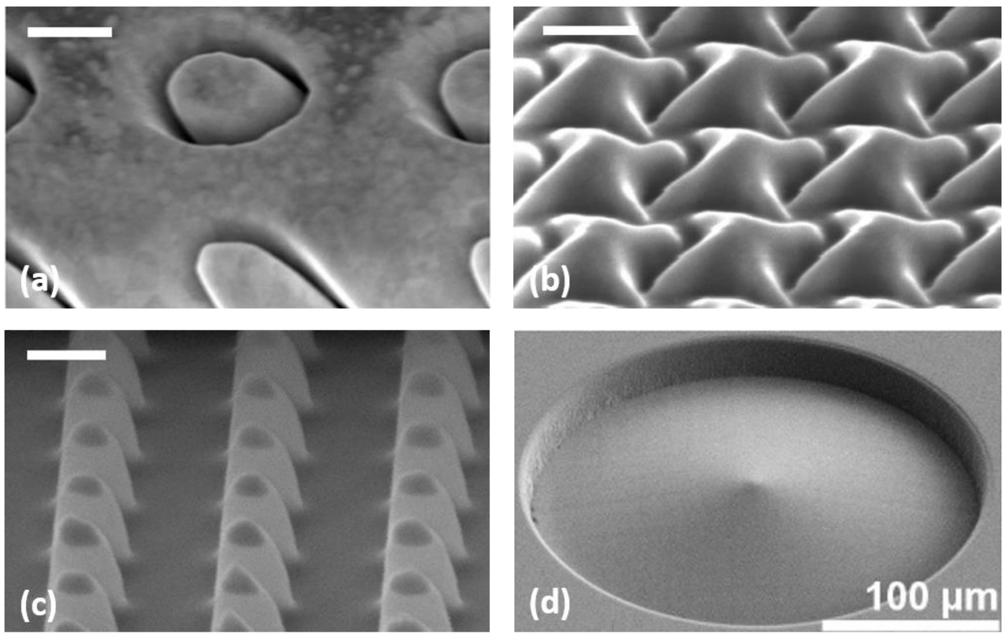

Figure 2.7: FIB 3D Nanofabrication of photonic/plasmonic structures: SEM image showing (a) Slanted annular aperture arrays in gold films [63], (b) 3D chiral photonic silicon nanostructures [64], (c) Periodic arrays with Ag nanoparticles on quartz trapezoidal pillars [66] (scale bar 250 nm), and (d) Lithium niobate micro-axicons milled with Xe beam using a plasma FIB [65]

To summarize, a brief review of FIB milling for micro/nanofabrication is presented and various techniques like pixel dwell time method, 2D slice-by-slice method, continuous slicing method etc. are discussed. Pixel dwell time method is dependent on the pixel size. However, when approximation for a curved surface is to be done using this method, it will result in poor resolution. The redeposition effect is prominent and accuracy is not maintained, which is further significant in high aspect ratio structures. The overlap effect needs to be considered to ensure desired shape and profile. On the other hand, 2D slice-by-slice method and continuous slicing method are more accurate, however, these too suffer from limitations like poor surface roughness. The profiles fabricated have limitations in terms of beam size. The pixel dwell time must be adjusted accordingly to incorporate overlap effects. This controls the versatile capability of process for fabrication and limits its applications. Thus, the effect of redeposition and overlap must be studied and incorporated in the strategies for depth control.

2.2.2 Lithography

Lithography is an important technique for transfer of a pattern from a mask with transparent or opaque areas to a sample surface [67] and is used by the researchers for more than three decades using focused ion beam [45], [68]. The sample is first irradiated using FIB and ions are implanted. The resistance of sample material to etching is increased selectively based on the exposed area. The surface itself acts as a mask and subsequent etching produces the patterns on the sample. Focused ion beam lithography offers certain advantages for nanofabrication when it is compared to other lithographic process such as UV lithography etc. The process is simple, single step, and can be used for nanofabrication and lithographic applications. The issues involved in the lithographic processes such as mask alignment, contamination etc. are omitted. The flexibility with ion beam lithography is more as it is a mask-less process and arbitrary shape/feature can be etched. In this section, techniques involving FIB lithography for fabrication of complex 3D micro/nanostructures are discussed in detail.

2.2.2.1 Ion Implantation and Deep Reactive Ion Etching

It has been shown in the literature that if gallium ions are implanted in silicon, it becomes resistant for reactive ion etching [44]. This property can be used for creating masks by implanting gallium ions in silicon using FIB, which can subsequently be used for etching. Researchers have used this property and successfully fabricated nanostructures [30], [42].

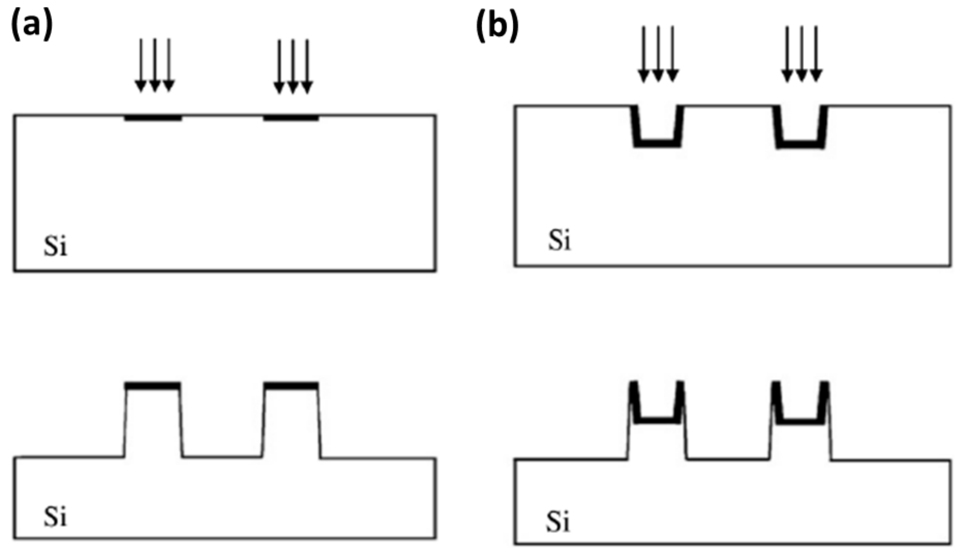

Figure 2.8: Focused ion beam lithography: Ion implantation and the corresponding Si structure after etching: (a) Low ion dose (b) High ion dose [30]

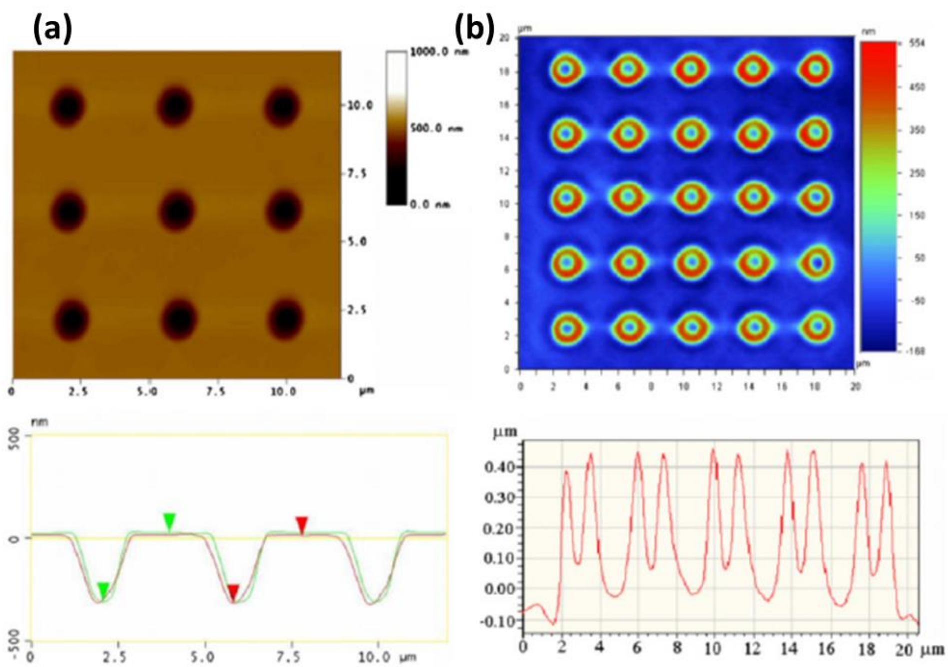

Figure 2.9: Nanohole fabrication by Gallium ion implantation and etching: (a) AFM image of the area implanted, (b) Interferometer image and profile showing topography after DRIE

Dose dependent mask resistance allows the fabrication of 3D structures in a single etch step. A schematic representation of the process is shown in Figure 2.8 [30]. Two different cases have been shown at low and high ion doses. The sample surface is first irradiated with focused ion beam, because of which gallium ion implantation takes place. The properties of the irradiated areas are changed due to the ion implantation and resistance to etching is increased. As a result, surface itself acts as a mask and structures can be produced. An example of nanohole fabrication by Qian et al. is shown in Figure 2.9 [30]. It shows the atomic force microscopic (AFM) image of the silicon after implantation (Figure 2.9 (a)), as well as the nanohole produced after deep reactive ion etching (DRIE) (Figure 2.9 (b)). Chekurov et al. [42] fabricated silicon nanostructures by local gallium implantation and cryogenic deep reactive ion etching. High aspect ratio 3D nanostructures with 40 nm as the smallest feature size were reported by the author using gallium implantation method.

2.2.2.2 Grayscale Lithography

FIB lithography technique has been explored for 3D capability and successfully achieved fabrication of 3D silicon based nanostructures [46]. An inorganic resist and direct patterning are used for the fabrication. An exposure dose gradient (grayscale structure), while can be used for 3D structures or dose of exposure can be fixed for development of binary structures. Further, it is possible to combine the linearly varying dose with gray levels to fabricate structures with linearly varying modulations. Patterns were written in inorganic layer using FIB, reducing the etching rate of sample during reactive ion etching (RIE). In this study, fabrication of nanostructures with the height of up to 200 nm was demonstrated. The surface quality, height, thickness of fabrication were controlled by the etching parameters. An example is shown in Figure 2.10 including the SEM image of the structure fabricated, sample tomography by atomic force microscopic (AFM) image, and the longitudinal structure profile using this technique. The pattern was written by a linearly varying dose in a binary grating. The advantage of this technique is that the number of gray levels is only limited by the exposure parameters and gray levels are not limited by the resist characteristics.

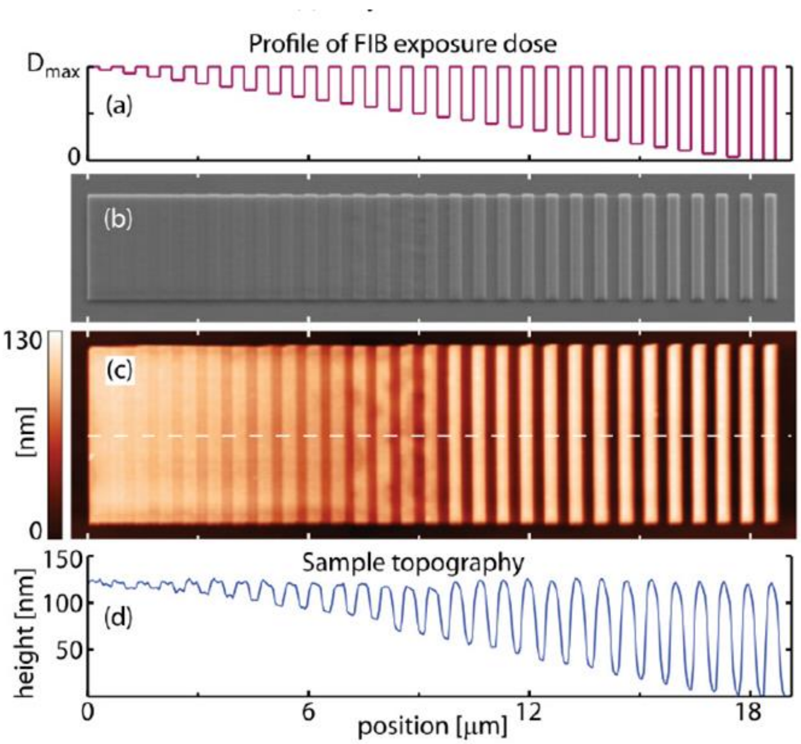

Figure 2.10: Focused ion beam grayscale lithography (a) Profile of applied FIB dose, (b) SEM image, (c) Topography, and (d) Height profile [69]

In summary, the lithography methods for the fabrication of 3D structures are discussed. FIB lithography-based approach offers excellent control, especially for inclined surfaces using grayscale method. The process is however slow and more suitable as a surface modification option rather than complete structure fabrication. The depth of the structures produced is completely controlled by etching, which is another limitation and restricts the process applications.

2.2.3 Gas Assisted Etching/Deposition

Focused ion beam is used for deposition/etching of metal and insulator materials in the presence of a gas. There are many similarities between FIB induced deposition and etching process. Deposition and etching gases both can adsorb/desorb without reacting with the sample surface. However, some etching gases (for example, chlorine on silicon) are also able to react with the sample surface. For etching, sputtering due to FIB will add to the material removal. While in the case of deposition, sputtering will complete the process. The basic requirements for precursor gas are same for both deposition and etching and the gas should stick to the surface for activation/dissociation for etching/deposition [40].

2.2.3.1 Etching

The milling rate by FIB is generally small, as the material removal takes place atom by atom, and usually the sputtering is accompanied by redeposition of the sputtered atoms from the surface. To enhance the milling rate, an etching gas can be used in work chamber. This technique is called "gas assisted etching (GAE)" [2]. Gas assisted FIB etching can be regarded as a local version of plasma etching or reactive ion etching with much higher ion energy [31]. Following steps take place in gas assisted FIB induced etching [40],

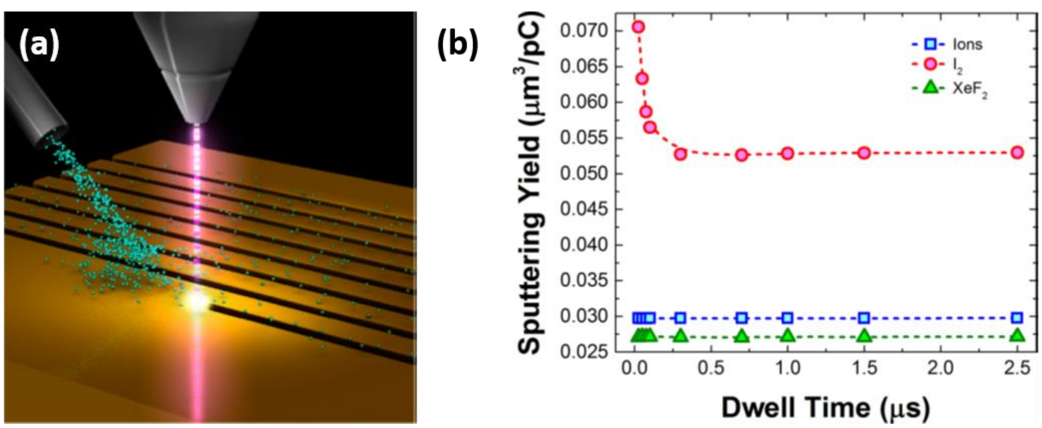

Figure 2.11: Focused ion beam induced etching of hybrid perovskites for photonic applications: (a) Schematic showing FIB etching in the presence of a precursor gas, (b) Enhanced sputtering yield of perovskite as a function of dwell time showing the effect of precursor gases (I_2, XeF_2) [70]

- A chemically neutral reactive gas through a nozzle is adsorbed on the sample surface
- The gas reacts with the sample either in the presence or absence of ion beam
- Volatile products are formed (desorption), which are removed from vacuum

Ion implantation, redeposition etc. can be reduced using gas assisted ion beam etching. However, care must be ensured to avoid spontaneous reaction of etching gas with the target surface. Figure 2.11 (a) shows the schematic diagram of gas assisted etching of hybrid perovskites with FIB [70]. Halide gaseous precursors (I_2, XeF_2) help formation of volatile etch products, helping the enhanced physical sputtering of the surface. It can be observed from the Figure 2.11 (b) that a high sputtering yield (>2 factor) was obtained for I_2 precursor within a short dwell time, indicating chemically assisted etching. The decline in sputtering yield with increasing dwell time indicate the material is now being removed by physical sputtering. Results indicate that FIB induced etching, with a careful selection of precursor gas, is a promising method for micro/nanostructures fabrication for materials with poor sputtering yield.

2.2.3.2 Deposition

Focused ion beam can be used for deposition of metal and insulator materials [2]. The operating principle is analogous to chemical vapor deposition (CVD). A previously formed thin film by the spray of a gas over the sample surface is decomposed by scanning the ion beam. In the process, volatile products are removed from the surface and desired products remain fixed over the sample. Generally, the deposition of platinum and tungsten is done on commercially available instruments. There are various phenomena that occur when an ion beam is scanned over target surface, where the precursor gas molecules are previously desorbed [31],

- Desorption of the molecules
- Dissociation of the molecules
- Reaction of molecules with target material

A deposition layer is sprayed over sample surface in the form of a gas. The ion beam is subsequently scanned over the sample surface and sprayed gas is decomposed by the action of ion beam. The desired reaction products remain on the surface as a thin film, while the volatile products are removed with the help of vacuum inside the chamber. The deposited material is not completely pure, as some organic contaminants as well as gallium ions are also implanted. Tungsten, platinum, carbon etc. are some of the common materials that are deposited by FIB.

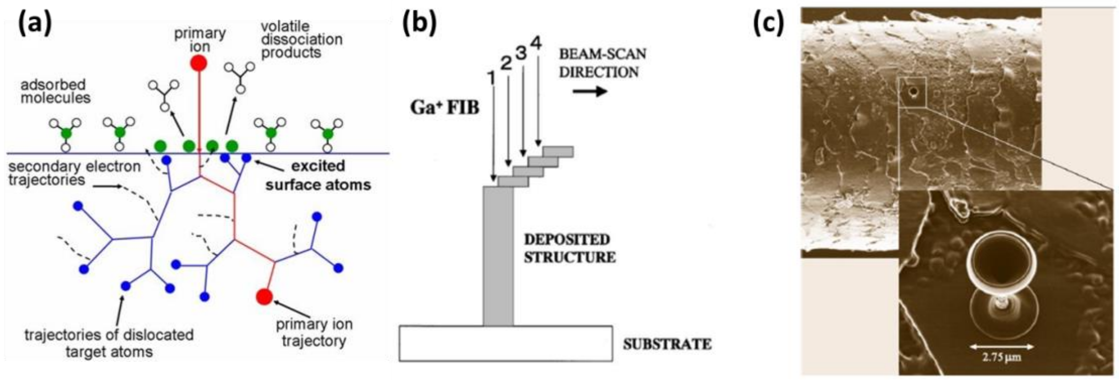

Figure 2.12: Focused ion beam induced deposition: (a) Surface interactions and generation of collision cascade for FIB induced deposition [31], (b) Fabrication process for 3D nanostructures, (c) An example showing micro wine glass on a human hair [71]

Focused ion beam induced deposition is a complex process and involves surface chemistry and ion interactions. The behavior of incident primary ion and adsorbed precursor molecules is shown in Figure 2.12 (a) [31]. Figure shows the impact of primary ion onto the target surface and interaction with adsorbed precursor gas molecule. Formation of volatile products takes place because of precursor molecules dissociation and these products escape the surface, leaving the non-volatile products behind. A thin layer is formed on the surface as a result. The ion beam interacts with the target atoms resulting in the formation of collision cascade; generation of secondary electrons. In FIB induced deposition methods, ion energy is used to initiate and localize chemical reaction in a specific location by direct writing technique. Due to the presence of a local gas near the sample surface, ion beam induces chemical reaction. This phenomenon can be utilized for fabrication of complex 3D structures, in which excited secondary electrons as well as the primary ions play an important role. The fabrication method of 3D structures by FIB chemical vapor deposition is shown in Figure 2.12 (b) [71]. The ion beam is scanned digitally over the sample surface. A pillar is first formed on the surface (position 1). The beam is then moved to another position (position 2) within the diameter of pillar. This process is repeated number of times to fabricate 3D structures. The deposition rate determines the growth in *z* direction. So, the height of structure fabricated is proportional to the irradiation time when the deposition rate is constant. This method is useful and complex shaped structures are developed in the literature. The process is however limited by long processing time and only small structures are feasible to fabricate using this method. By combining the growth in *z* direction with rotating beam scanning, it is possible to obtain 3D structures with rotational symmetry. An example is shown in Figure 2.12 (c), where a micro wine glass with an external diameter of 2.75 μm and a height of 12 μm is fabricated on a human hair [71], [72]. Results indicate that FIB-CVD is a promising method for 3D micro/nanostructures fabrication.

It is possible to fabricate the structure using FIB-CVD methods employing the use of computer software. The process is automated and processing parameters can be set up automatically depending upon the structure geometry. This makes the process faster and applicable to 3D profiles fabrication. A pattern generating system for the fabrication of 3D structures using FIB-CVD exists in the literature [73]. A computer aided design (CAD) model of the structure to be fabricated was made. The input to the system is taken as the structure CAD model. This CAD model is then sliced, the thickness of which is based on the resolution in z direction. The *x* and *y* coordinates of the slices are used to create the scan data. The sequence of ion beam scanning is determined based on the input CAD model and different parameters like dwell time etc. is calculated from the beam diameter, *xy* resolution and *z* resolution. The resolution in z direction is proportional to the dwell time. It is possible to fabricate the overhanging structures by this technique. However, to fabricate overhanging structures, it is important to control the beam position and sequence. A similar approach was adopted by Lalev et al. [74] for FIB deposition employing the data generated by CAD package to fabricate complex structure by this approach.

Recent examples from the literature have been shown in Figure 2.13 for demonstrating the process capabilities using FIB induced deposition. Figure 2.13 (a) shows schematic diagram of nano-spiral growth through FIB induced deposition in the presence of precursor gas molecules [75]. The ion beam interacts with the previously deposited precursor organometallic molecules, separating the organic component leaving metallic deposits. The coincident point between incident ion beam and precursor organometallic molecules

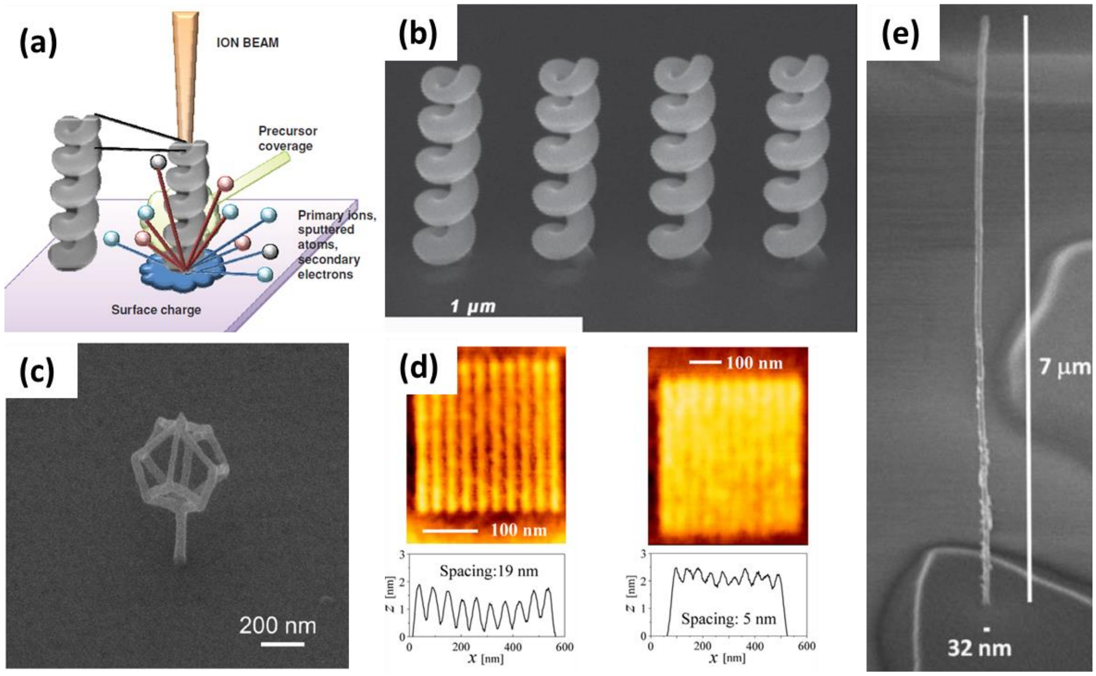

Figure 2.13: FIB assisted deposition growth and nanofabrication: (a) Schematic showing nano-spiral growth through ion beam induced deposition in the presence of precursor gas molecules, (b) SEM image of an array of 3D platinum chiral nano-spirals grown on Si substrate [75], (c) A deltahedron over a pillar grown on Si substrate through He-FIB induced deposition [76], (d) Atomic force microscopic (AFM) images of W-C lines and spaces fabricated using Ga-FIB-CVD showing sub 10nm nano-gaps [77], (e) A vertical 3D W-C hollow nanowire grown via He-FIB induced deposition [78]

over the substrate determines the growth location and can be controlled for nanostructure growth in 3D. Chiral nanostructure adopting this method is shown in Figure 2.13 (b) through a SEM image of an array of 3D platinum chiral nano-spirals grown on a Si substrate with total height of 1 μm. The interaction of light with such helical nanostructures can be manipulated as a function of light polarization, and these were demonstrated for circular dichroism. With the recent development of helium ion beam microscopy, the resolution achieved with FIB induced deposition is further improved. An example of a deltahedron over a pillar grown on Si substrate through He-FIB induced deposition is shown in Figure 2.13 (c), demonstrating the excellent process capability and sub 20 nm dimensions [76]. W-C lines and nano-gaps approaching the resolution limit of FIB induced deposition are shown in Figure 2.13 (d) through atomic force microscopic (AFM) images, where two gratings with ~19 nm and ~5 nm gaps are shown. Figure 2.13 (e) shows SEM image of a ~32 nm diameter, high aspect ratio (~200) superconducting hollow tungsten carbide nanowire grown with He-FIB induced deposition with the $W(CO)_6$ precursor. Such structures are important for optical applications and provide a great scope for further development from design and process point of view.

To summarize, a detailed review of FIB induced deposition/etching methods is presented and its capability and applications for micro/nanostructures fabrication are discussed. The FIB-CVD process shows extreme capability and extensive work has been done by the researchers. Automation of the process using programming methods makes it applicable for fabrication of complex structure. Few recent examples from the literature have been presented for process capability demonstration. Focused ion beam deposition methods are advantageous for fabrication of structures of smaller size, however, these methods become challenging for fabrication of large and complex structures due to processing times. FIB-CVD methods are suitable for small scale post processing or prototype fabrication.

2.2.4 Material Self-Organization

Focused ion beam induced self-organization is one of the most explored techniques to fabricate nanostructures by ion irradiation [51]. Submicron ripples and nano/micro-dots can be formed after ion beam irradiation of surface through self-organization and sputtering [55]. The orientation of nanostructures formed depends on the incidence angle and the ion beam parameters such as overlap, current, dwell time etc. Direct patterning approaches by FIB has limitations in terms of feature size due to beam diameter (least possible beam diameter 5-10 nm depending on ion source) [52]. Nanostructures fabricated by FIB induced self-organization on the other hand can overcome this limitation through ion irradiation induced surface erosion and strain on the substrate, developing surface energy disequilibrium and subsequently leading to relaxation and self-organization of surface atoms [52]–[56].

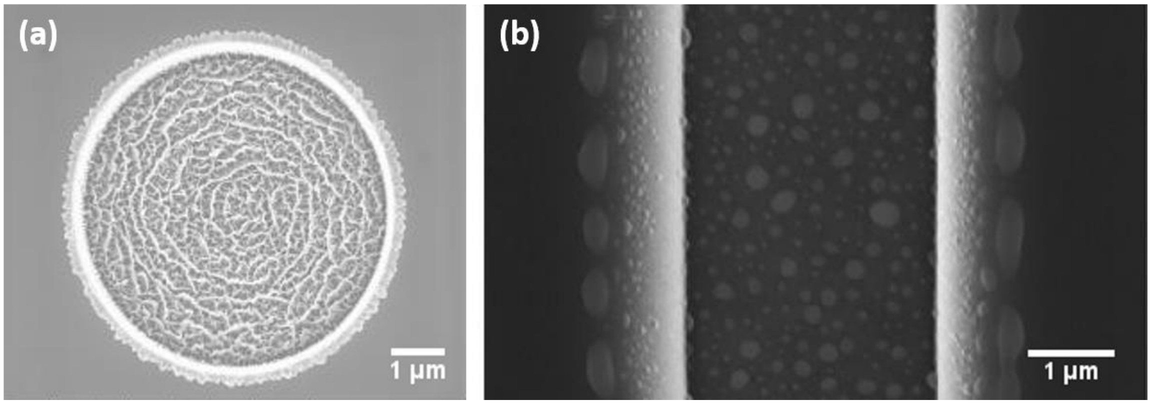

Figure 2.14: FIB induced self-organized nanostructures: (a) SEM image showing germanium nanostructures in the scan direction [79], (b) Ga droplets over GaAs surface [80]

Spontaneous nanoripple formation during ion irradiation on Germanium with 30 kV Ga FIB is shown in Figure 2.14 (a) [79]. The formation of such self-organized nanoripples was attributed to the linear propagation of FIB induced micro-explosions in the FIB scanning direction, which was further confirmed through observation of nanoripple orientation change with the raster scan direction. Self-organized nanostructures by FIB irradiation is not limited to the nanoripple structures, however nanodroplets/nanoparticles such as Ga nanodroplets can be created by FIB raster scanning over GaAs surface [80], [81]. The incident angle of the ion beam can control the droplet diameter, increasing the incident angle decreases the size of the resultant droplets as shown in Figure 2.14 (b). The higher sputtering rate for As atoms from the surface of GaAs, together with impinging Ga ions leads to Ga rich surface, which results in the formation of Ga droplets. Increase in the ion beam irradiation time increases the diameter of Ga droplets.

2.2.5 Controlled Bending

Ion irradiation and implantation are used extensively for inducing functionalities and engineering of nanostructures for diverse applications in the nanotechnology domain. Nanostructures, under ion irradiations, exhibit distinct transformations in contrast to their bulk counterparts, due to the nanostructure dimensions comparable to collision cascade. Tensile, compressive stresses can be developed in the lattice atoms under ion irradiations,

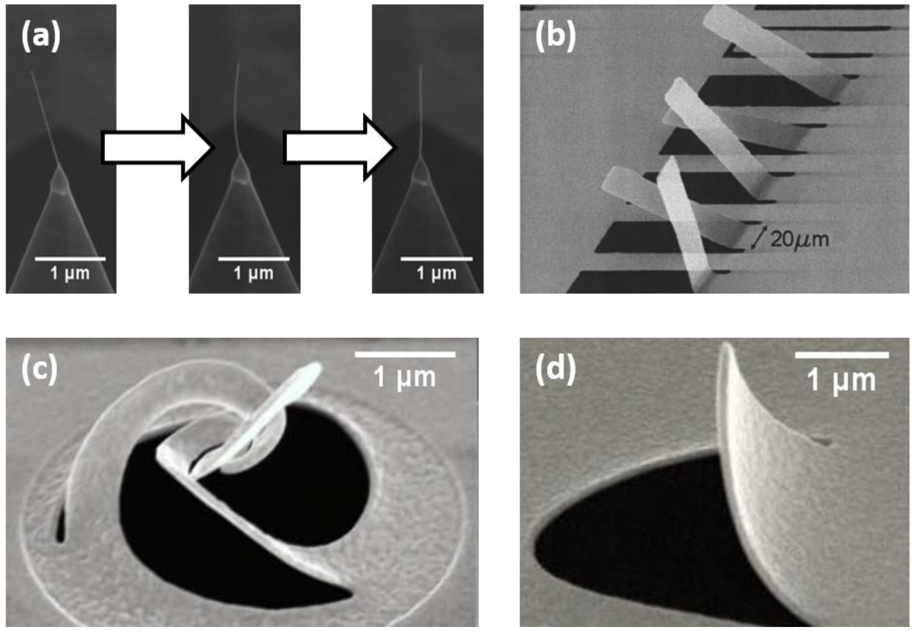

Figure 2.15: FIB induced bending through ion irradiations: (a) Alignment of a carbon nanotube (CNT) [57], (b) Silicon nitride (Si_3N_4) cantilevers [82], (c)-(d) Gold (Au) kirigami nanostructures [59]

inducing plastic deformation, which in turn can be used for controlled manipulation at nanoscale, thus providing opportunities for extended functionality and strain engineering of nanostructures. Si nanostructures, with a high index and large band gap, offer unique light-matter interactions for optical applications such as color filtering etc. Conventional lithography methods such as electron beam lithography (EBL) consist of multiple steps, requiring mask preparation, resist development, dry/wet etching etc. and the experimental realization of 3D, complex features for extended functionalities becomes especially challenging due to the design intricacy, with limitations on the feature size and aspect ratio.

In-situ kiloelectronvolt ion irradiation in a dual beam FIB-SEM microscope can be used for bending and controlled manipulation of freestanding nanostructures. The experimental studies on ion induced bending of nanostructures revealed that the bending effects are associated with the implanted-ions, generation of point defects, and dislocated lattice atoms, in addition to the sputtering effects at high ion doses, contributing to the generation of localized stresses developing ion irradiation induced plastic deformation.

Such controlled manipulation of nanostructures through ion induced strain-engineering can be utilized for new nanoscale configurations and applications. Figure 2.15 (a) shows successive SEM images of a carbon nanotube (CNT) on a SEM tip aligned through FIB irradiations. An array of bent silicon nitride (Si_3N_4) cantilever is shown through SEM image in Figure 2.15 (b), where control of bending angle is achieved through dose control. Figure 2.15 (c), (d) shows kirigami nanostructures realized through the ion irradiation induced stresses in gold (Au). Various nanostructure configurations can be realized through tuning of ion-dose and energy, providing an additional degree of freedom and extending ion beam application for realization of new functional 3D-nanostructures. In summary, controlled manipulation at nanoscale through *in-situ* ion irradiation with FIB provides a unique opportunity for 3D nanofabrication and realization of unique geometries having potential for development of future nanoscale devices and applications beyond material science in the diverse field of ion beams.

2.2.6 Nanostructure Growth

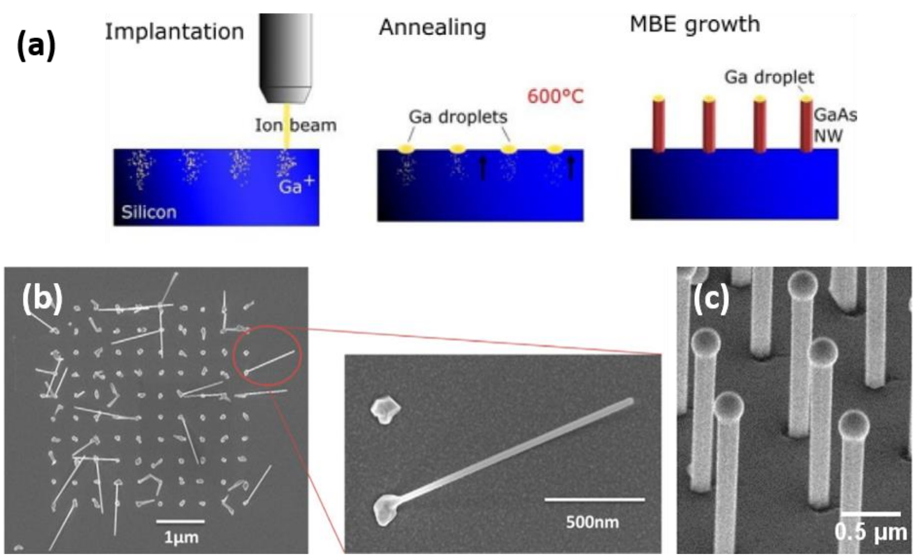

Figure 2.16: FIB induced nanostructure growth: (a) Schematic of Ga implantation, thermal annealing, molecular beam epitaxy (MBE) for self-catalyzed growth of gallium arsenide (GaAs) NWs on Si substrate shown through SEM image in (b)[60], (c) Gallium arsenide antimonide (GaAsSb) NWs on Si, with top showing the Ga droplets [61]

Ion implantation with FIB, in addition to inducing various functionalities, etch mask for chemical etching, controlled bending, etc. can also be used for site-selective growth of self-catalyzed nanostructures through molecular beam epitaxy (MBE) [60], [61]. Ion implantation in FIB with nanometer resolution allows growth of nanostructures such as nanowire, nanoparticle etc. Annealing of Ga implanted Si develop the formation of Ga droplets on the surface, which can act as nucleation points for self-catalysis of nanowires through MBE (Figure 2.16 (a)). The ion implantation followed by thermal annealing and MBE can be used for site-specific growth of nanostructures, making the approach suitable for numerous application areas. Figure 2.16 (b) shows the SEM image of gallium arsenide (GaAs) nanowires on Si substrate grown through this method [60]. This method can also be used for growth of vertical NWs via process optimization and careful selection of processing parameters. One such example, Gallium arsenide antimonide (GaAsSb) nanowires on Si, with NW top demonstrating the Ga droplets [61], is shown in Figure 2.16 (c). Single vertical NWs can be obtained with low ion dose implantation, while a high dose of ions give rise to multiple vertical NWs [61]. In addition to the ion beam parameters, the self-catalyzed growth of nanostructures is known to be dependent primarily by the growth temperature, element ratio etc., which can be controlled for a variety of nanostructures. The nanostructures grown through this method can offer huge potential for optical and optoelectronic applications such as photovoltaics, detectors etc.

2.3 Summary

A comprehensive literature review is presented on FIB and fabrication methods etc. have been discussed in detail for 3D and complex micro/nanofabrication. Basic principle of FIB is discussed along with its capabilities, limitations and applications. Focused ion beam is a promising technique due to its capability range and diverse applications. FIB can be used for milling, thus making it suitable for micro/nanomachining. It can be used for deposition, allowing it for applications in the field of thin films. It can also be used for imaging, which makes it powerful for microscopy analysis and materials applications. Focused ion beam is capable of fabrication of micro/nanostructures, nanopatterning, preparation of TEM samples, surface modification, surface analysis etc. in the diverse field of semiconductors, optoelectronics, geosciences, life sciences etc. However, like any other process, FIB also has certain limitations. The major issues in FIB micro/nanomachining are the control of accuracy as overlap, beam tail, redeposition effects etc. take place. Sputter yield also varies with time and incidence angle, making it even more difficult to control the accuracy in fabrication. These are main issues that makes the FIB nanofabrication a challenging area and great research interests exist among the researchers. Recent studies and developments have suggested promising methods for complex micro/nano-structures, however, a lot remains unexplored in terms of new materials and applications with FIB based micro/nano-fabrication.

Chapter 3. Rapid Prototyping of Highly Ordered Subwavelength Silicon Nanostructures with Enhanced Light Trapping

High index nanostructures lead to unique light-matter interactions and strong optical resonances for potential light trapping applications and improved optical performances. In this work, Gaussian shaped subwavelength 3D nanostructures are introduced, and rapid prototyping of these nanostructures is carried out on silicon (Si) in a single-step using focused ion beam (FIB) milling. The tapered geometry of Gaussian pillar structures provided reflection suppression from the smaller tip in contrast to its extended base, enabling trapping of light, confirmed through light reflection calculations and hot spots observed through absorption density distributions. The nature of accelerated ions in a FIB system is directly used and highly ordered Gaussian pillar like subwavelength nanostructures are fabricated in a single-step on Si. Simulations and experiments demonstrate nanostructure evolution from periodically spaced subwavelength nanoholes to Gaussian pillar structures with tuning of beam processing parameters, providing fabrication flexibility. The proposed light management structures, investigated through finite-difference time-domain (FDTD) calculations, exhibit 10-20% reflectance for a broadband visible wavelength range against planar Si and previously reported Si structures (such as nano-cones, nano-wires, nano-pyramids etc.). Experimental results support the theoretical predictions and provide evidence for antireflection properties from the fabricated nanostructures. Considering the rapid fabrication approach and tunable nature of Gaussian shaped nanostructures, exhibiting unique optical properties, this work provides realization of nanoscale light management 3D structures for localized light trapping and antireflection applications.

3.1 Introduction

Surface micro/nano texturing is a widely researched area for nanoscale light-matter interactions, manipulation, and light trapping for color filtering, antireflection, photovoltaic applications etc. [11], [83]–[85]. Silicon (Si), with a high index and large band gap, is widely investigated semiconductor for graded index, multiple light scattering, and

Mie resonances via fabrication of subwavelength structures for light trapping and unique antireflection properties [83], [84], [86]. Light management structures such as nano-cones, nano-wires, nano-lens, nano-holes, micro/nano-pyramids, hybrid nanostructures etc. have been developed over last decade and attracted immense interest for theoretical investigation along with experimental realization [87]–[93]. Significant efforts have been made to study the 3D geometries to realize improved light trapping performance compared to conventional and 2D geometries. Optical study on nanowire tips modified with nanocone structures enabled near 100% absorption through optimization of light harvesting based on scattering of light [94]. Funnel shaped nanowires, increasing the number of leaky mode resonances, in contrast to the uniform nanowires have been studied [95]. More recently, wedge shaped nanowall arrays have been studied for superior light management due to their gradient refractive index in contrast to 2D geometries [96]. Tapered Si nanowires realized using chemical vapor deposition technique in conjunction with gold nanodisk patterns fabricated by stepper lithography proved to be absorbing several light wavelengths based on variable diameter dependent light absorption [97]. Si nanopyramids fabricated by metal assisted chemical etch have been realized for Si surface texturing [98]. 2D array of thin Si pillars were fabricated for antireflective coating demonstrating light reflection under 5% via combination of electron beam lithography (EBL) and reactive ion etching (RIE) [99].

In this work, unique Gaussian-shaped Si pillar structures are proposed for efficient light trapping and exhibiting antireflection properties. The Gaussian profile of the incoming ions in FIB is directly tuned for fabrication of proposed nanostructures. This novel technique is demonstrated via single-step rapid fabrication of light trapping nanostructures on single crystalline Si. The optical behavior of the structures is studied through finite-difference time-domain (FDTD) calculations, and experiments. A significant enhancement in the light trapping allowing maximum reflectance of the order of 10-20% for a broad wavelength range of 400-1000 nm is noted.

3.2 Experiments and Simulations

Experiments were performed on <100> p-type single crystalline Si. A 4-inch Si wafer with 525 μm thickness was cut into 10 mm×10 mm sample size by a diamond cutter and cleaned using piranha solution (H_2SO_4:H_2O_2:3:1), deionized water (DI) for removal of any oxides, metallic, and organic contaminants. The nanofabrication was carried out using Carl Zeiss Auriga dual column FIB-SEM system with a gallium (Ga) ion source. The sample was placed at an eucentric height in the vacuum (pressure ~1×10^{-6} Pa) and milling was done at normal incidence by tilting the substrate normal to the ion beam. The reaction products/sputtered atoms during the FIB milling operation are exhausted into the vacuum system. All the milling experiments were carried out at ion beam acceleration voltage of 30 kV. To visualize the profile of fabricated geometry due to incident ion beam , cross-sectional SEM imaging was carried out through FIB milling of a trapezoidal trench near fabrication geometry. A protective thin layer of platinum (Pt) was deposited previously in order to avoid the Si redeposition. A MATLAB code was used to create text files to be used in FIB interface for milling and allowing full control of beam parameters including X and Y positions, dwell time and number of repetitions for 3D fabrication. The dual beam FIB-SEM system is also equipped with X-ray detector, which was used for energy dispersive X-ray spectroscopy (EDS) analysis of FIB irradiated area.

The fabricated nanostructures were analysed using scanning electron microscopy (SEM), atomic force microscopy (AFM), EDS analysis, and Raman spectroscopy. The AFM characterization was performed on Agilent 5500 system using a Si_3N_4 cantilever of tip radius 20 nm, spring constant of 48 N/m and resonant frequency of 190 kHz. The AFM artefacts due to the fabrication geometry and sharp features were minimized by using a finer tip cantilever in AFM measurements. X-ray detector inside the dual beam FIB-SEM system was used for EDS analysis of the structures after the fabrication. A confocal Raman imaging system (Witec alpha 300RAS) was used for performing Raman spectroscopy using 532 nm laser at 5 mW power for excitation. Reflection measurements were recorded on J&M Micro UV-Vis microscope spectrometer. A halogen lamp coupled with an optical fiber is used to illuminate the sample. The microscope has a beam splitter for recording measurements and simultaneous visualisation on a computer. Protected silver mirror (Thorlabs Inc., product PF07-03-P01) was used to normalize the reflectance from Si. A 50× objective lens with NA 0.65 is used to focus the sample and reflectance measurements. All the characterizations were done at room temperature in semi-clean environment conditions.

The optical performance of the fabricated Si nanostructures is studied numerically using finite-difference time-domain (FDTD) method (Lumerical Inc.) in order to get optimum feature size for antireflection properties. The periodic boundary conditions (PBC) is used to simulate the periodicity (i.e. along x and y-direction) and the perfectly matched layer (PML) along the illumination i.e. z-direction. The optical constants for Si were set from the literature [100]. A plane wave, broadband (λ=200-1500 nm) illumination was used to excite the structure.

3.3 Results and Discussion

3.3.1 Rapid Prototyping of Subwavelength Nanostructures

The Ga ions in FIB, when scanned over Si substrate, undergo electronic and nuclear stopping through collisions with electrons and Si nuclei before coming to rest. Si atoms are ejected from their lattice positions as primary knock out atoms, causing the sputtering action, if the energy transferred through Ga ions is more than displacement energy of Si. The Gaussian nature of the ion beam in FIB systems is known to produce tail effects while fabricating nanostructures via sputtering action. A nanostructure fabrication strategy is proposed, which overcomes the issue of Gaussian beam tail effect in the milling and utilizes it as an advantage. Si pillars with Gaussian geometry and less surface area based on the novel FIB nanofabrication approach have been demonstrated. Direct writing of 3D micro/nanostructures and surface texturing is possible in a single-step via beam positioning and control in a dual beam FIB-SEM system. The beam overlap during FIB milling results in un-milled/over-milled regions, which can be carefully tuned via adjusting the beam overlap during the scanning process. Figure 3.1 illustrates the FIB scanning schematic

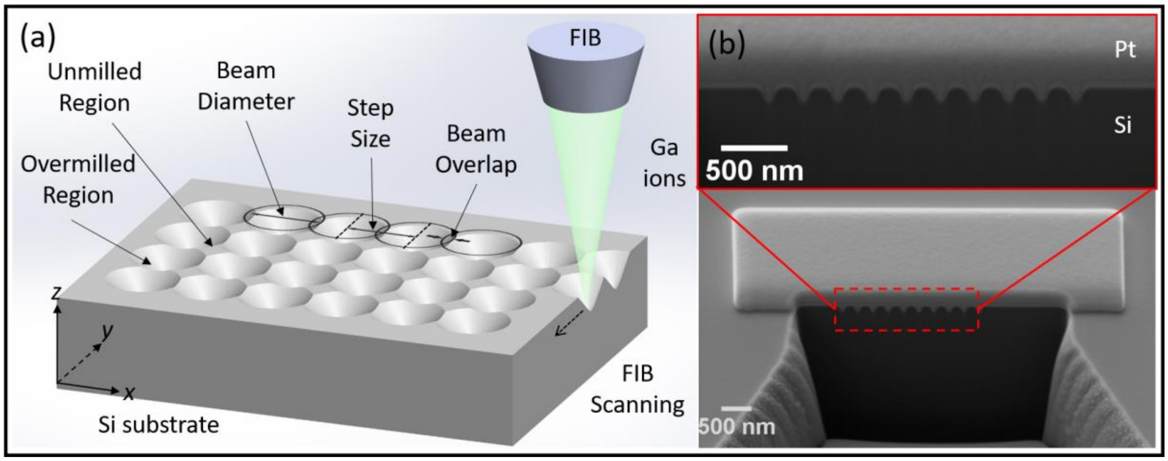

Figure 3.1: Illustration of FIB milling process showing: (a) Scanning step size, beam overlap, un-milled and over-milled regions due to the beam diameter, (b) Cross- sectional SEM image showing typical profile of curved surface milled due to Gaussian nature of incident ion beam

employing negative, zero, and positive beam overlap, including the evolution of fabricated nanostructures through simulations and experiments. To illustrate the effect of beam overlap on nanostructure evolution and fabricated geometry, the schematic of ion beam irradiations during FIB scanning is shown in Figure 3.1 (a). Figure 3.1 (b) illustrates typical profile of curved surfaces milled in Si due to Gaussian nature of incident ion beam through cross-sectional SEM imaging of a trapezoidal trench milled with FIB. The nature of incident ions in a FIB, as evident from magnified SEM image in Figure 3.1 (b), leads to the development of curved surfaces, which can be engineered through control of FIB processing parameters, such as beam overlap. Beam overlap during FIB scanning is defined with respect to the step size (overlap = 1−(step-size)/ (beam diameter)). Beam overlap, as shown in Figure 3.1 (a), can be adjusted via selection of step size or pixel size for a given beam diameter. This makes it possible to fine tune un-milled or over-milled regions and the subsequent fabrication of nanostructures by FIB. Thus, the Gaussian pillar-like features can be produced by setting beam overlap, under the same ion dose. To predict and investigate the nanostructures evolution as a function of beam overlap during FIB scanning, ion beam simulations were carried out. The incoming ions in a FIB can be represented through a Gaussian distribution with circular cross-section for estimation of the ion intensity of the beam [101]. Mathematically, the ion distribution $D(x,y)$ in Cartesian coordinates:

$$D(x,y) = \frac{D_0}{2\pi\sigma^2} e^{\left\{-\frac{x^2+y^2}{2\sigma^2}\right\}} \tag{3.1}$$

where σ is the standard deviation of Gaussian distribution of incident ion beam. The beam diameter at full width at half maximum (FWHM) is equal to 2.355σ [102]. The total number of ions incident at the target surface with the beam current I during a dwell time of t_d are, $D_0 = It_d/q$, where q is the electron charge. The ion beam moves pixel to pixel with a user defined step-size during the scanning in a FIB milling process [102]. If the total number of pixels are N, step-size D_x and D_y in x and y directions respectively, the total dose over the target surface during FIB scanning:

$$D(x,y) = \sum_{n_x=0}^{n_x=N} \sum_{n_y=0}^{n_y=N} \frac{D_0}{2\pi\sigma^2} e^{\left\{-\frac{(x-x_p-n_xD_x)^2+(y-y_p-n_yD_y)^2}{2\sigma^2}\right\}} \tag{3.2}$$

where x_p, y_p are ion beam starting position coordinates. The sputtered depth profile during FIB scanning, at a given ion beam energy and dwell time, is a function of incoming ion dose, ion incidence angle dependent target sputter yield $Y(\theta)$, and target atomic density ρ. In simplistic terms, the sputtered depth profile can be written as [103]:

$$Z(x,y) = \frac{Y(\theta)}{\rho} \sum_{n_x=0}^{n_x=N} \sum_{n_y=0}^{n_y=N} \frac{D_0}{2\pi\sigma^2} e^{\left\{-\frac{(x-x_p-n_xD_x)^2+(y-y_p-n_yD_y)^2}{2\sigma^2}\right\}} \tag{3.3}$$

The incidence angle dependent sputtering yield follows the cosine rule $Y(\theta) = Y(0)\cos\theta^{-f}$ [104], where $Y(0)$ is the sputtering yield at normal incidence angle. The exponent f (~1-2) depends upon mass of an ion and atom. The simulation results shown in Figure 3.2 (a)-(c), considering the FWHM of 100 nm and Si density of 2.58 g/cm^3 [105] show the effect of beam overlap over nanostructure evolution, which emerges as Gaussian shaped nanopillar from Gaussian shaped nanohole with increasing beam overlap. The

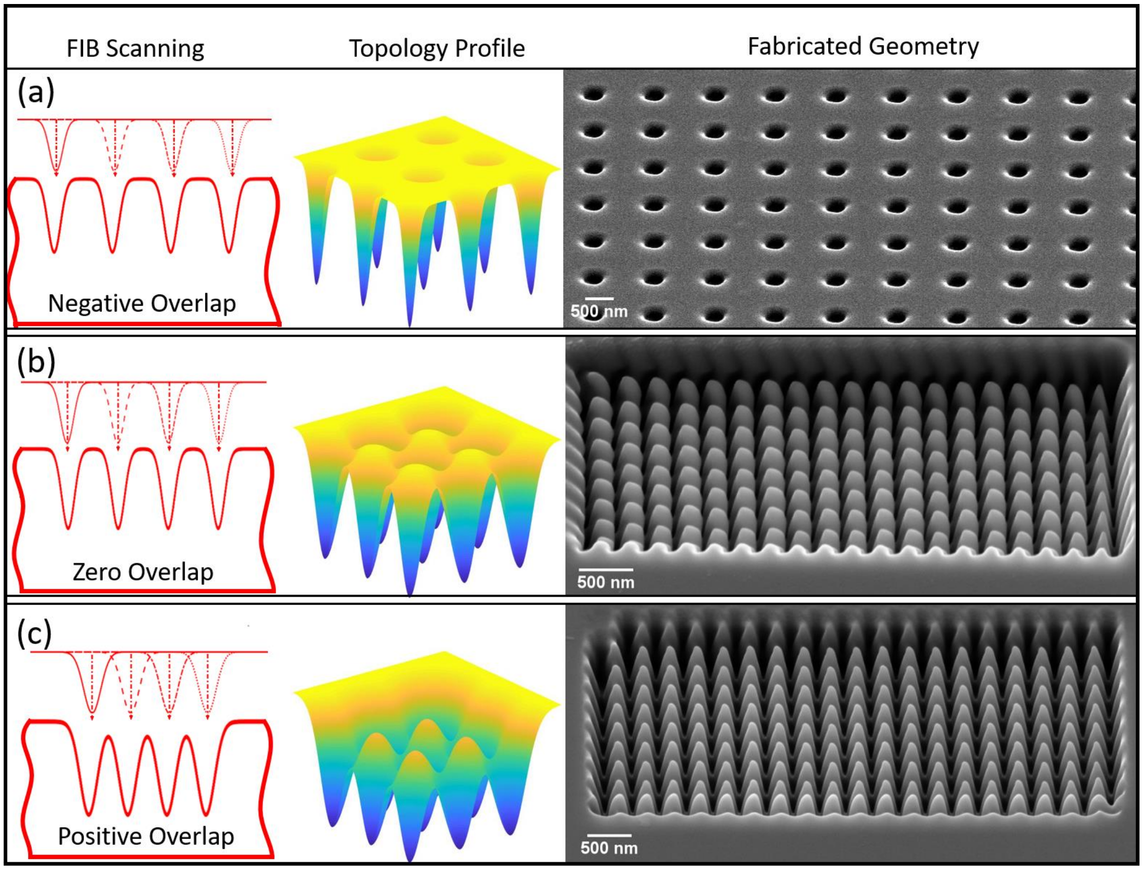

Figure 3.2: Scanning schematic of consecutive irradiations demonstrating the beam overlap tuning, predicted fabrication geometry, and fabricated geometry on Silicon with: (a) Negative, (b) Zero, and (c) Positive beam overlap. Representative SEM images of fabricated nanostructures are also shown in (a), (b), and (c) for comparison

evolution of nanostructure with beam overlap is also depicted through SEM image of fabricated nanostructures in Figure 3.2 (a)-(c). The dwell time of the ion beam was optimized via simulations and trial experiments to minimize the redeposition during ion milling and to ensure cleaner cuts into Si maintaining the fabrication accuracy. Figure 3.2 (a) shows FIB scanning with negative beam overlap between subsequent ion irradiations during milling. Negative overlap, as evident from the simulations and SEM image of fabricated nanostructures, results in the realization of an array of holes, which are periodically spaced based on the beam overlap value. Zero beam overlap, as shown in

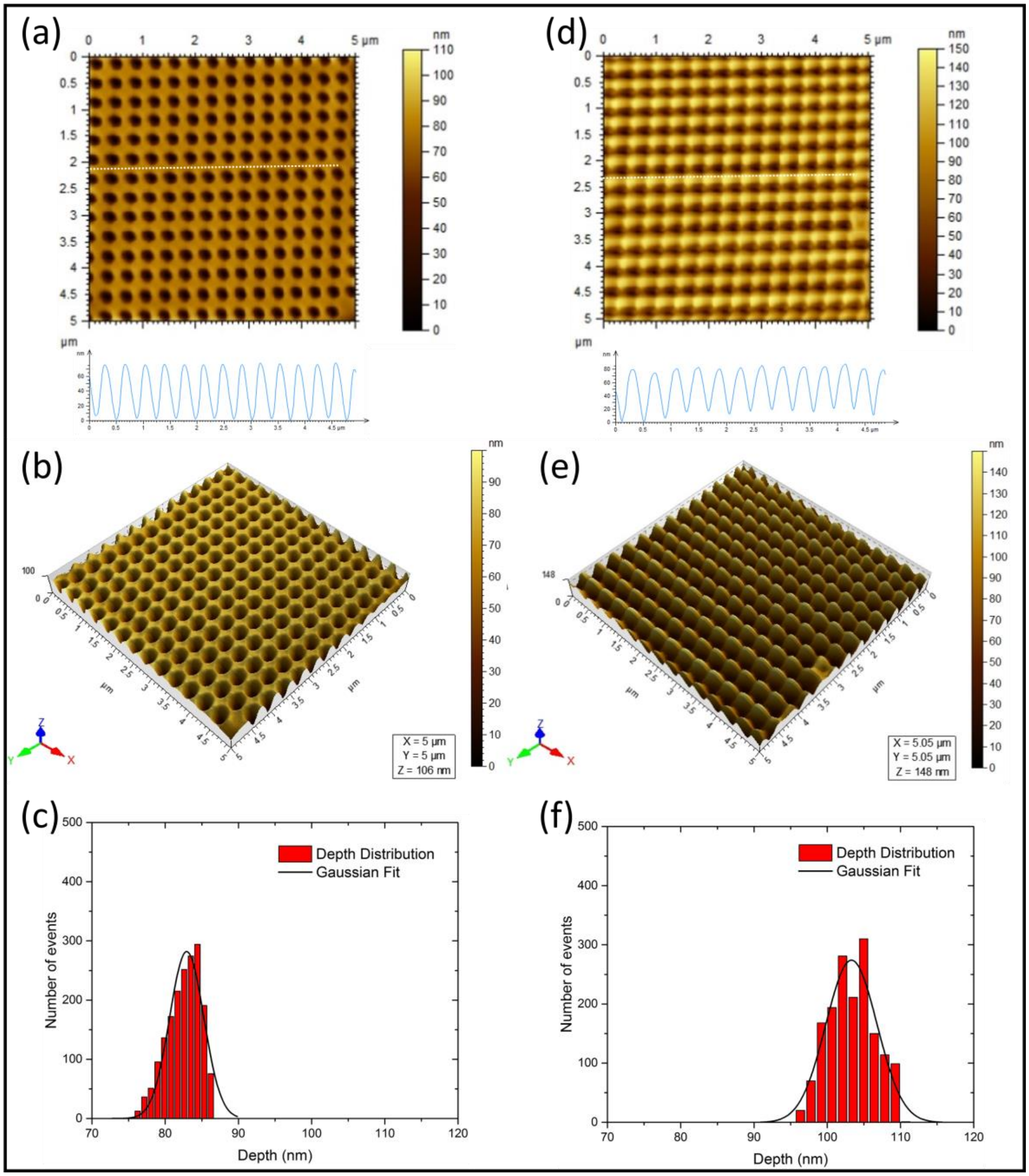

Figure 3.3: Representative Atomic Force Microscopic (AFM) image: (a)-(c) Nano-hole array (negative beam overlap), (d)-(f) Nano-pillar array (positive beam overlap). (a), (d) AFM 2D view with depth profile along white line indicated over corresponding AFM image; (b), (e) AFM 3D view; (c), (f) Depth distributions including Gaussian fit of distributions

Figure 3.2 (b), leads to the fabrication of pillar like structures. These pillars have a flat top profile due to the zero overlap between subsequent ion irradiations during the ion milling. The difference between the predicted and fabricated profiles, as evident from the SEM image showing slightly skewed pillars in contrast to simulated pillars, arises from the fast beam blanking/unblanking during FIB scanning from left to right. The topography of the pillars can be further improved, if a positive beam overlap is employed. Figure 3.2 (c) shows positive beam overlap (6%) during FIB scanning and fabricated pillars on Si. The fabricated pillar geometry, like zero beam overlap, is observed to be skewed slightly towards left, which may have been arising from the fast beam blanking/unblanking during beam scanning direction (left to right) employed here. These pillars have a sharp top profile due to over-milling arising from the overlap of consecutive ion beam irradiation steps. Thus, it is possible to fabricate highly ordered nanostructures via control of the beam overlap during FIB scanning process. The height of fabricated pillars is tunable via dwell time, while diameter and period (the spacing between consecutive pillars) are controlled through beam current and step-size respectively.

It is also observed that with increasing the current (i.e. beam size), the fabrication geometry changes from nano-hole (negative overlap) to nano-pillar geometry (zero to positive overlap). The AFM analysis of two geometries: nano-hole and nano-pillar array (at negative and positive overlap respectively) including the 2D, 3D, and topographic details are included in Figure 3.3. Figure 3.3 (a)-(c) show nano-hole array of maximum depth ~88 nm with a Gaussian profile in Z-direction and periodicity at 450 nm, fabricated due to negative overlap in the incoming Gaussian beam. Figure 3.3 (d)-(f) on the other hand, shows the nano-pillar feature array having Gaussian profile and maximum height ~110 nm with a periodicity of 300 nm. Figure 3.3 (a), (d) show representative AFM 2D images of nano-hole and nano-pillar array respectively including the depth profiles along the white line indicated over corresponding AFM images. 3D views of nano-hole and nano-pillar array are included in Figure 3.3 (b) and (e). The depth distributions of the nanostructures from AFM data have been plotted in Figure 3.3 (c), (f) and including a Gaussian fit of distributions to note the fabrication consistency. The AFM results of nano-structures revealed the uniformity and periodicity with which the fabrication can be carried out using

FIB. The developed Si pillars are highly ordered, which is important for improved optical performance.

3.3.2 Light Trapping and Antireflection Properties Calculations

The surface texturing of Si increases the probability of light absorption at the surface, enabling the carrier generation. The change in the surface geometry also leads to change in light propagation direction inside Si and optical path length is extended. These factors lead to enhanced light trapping in Si and improvement in optical absorption. The fabricated Gaussian pillar like structures promote multiple reflections of the incident light onto neighbouring pillars leading to overall reduction in reflection from the surface. Reflection reduction from the pillars depends on the feature size, coverage, uniformity, and the surface area. A design needs to be optimized for optical trapping supported through the structures for optical applications. A Schematic showing light trapping in Gaussian pillar structure with height ‘*h*’, base width ‘*w*’ and period ‘*P*’ is shown in Figure 3.4 (a). Figure 3.4 (b) show simulation set-up and boundary conditions for optical properties calculations. Figure 3.5 (a) and (b) show contour plots of reflectance for variation of pillar height and period respectively. The reflectance was found to be reducing (50%-10%) with the increased

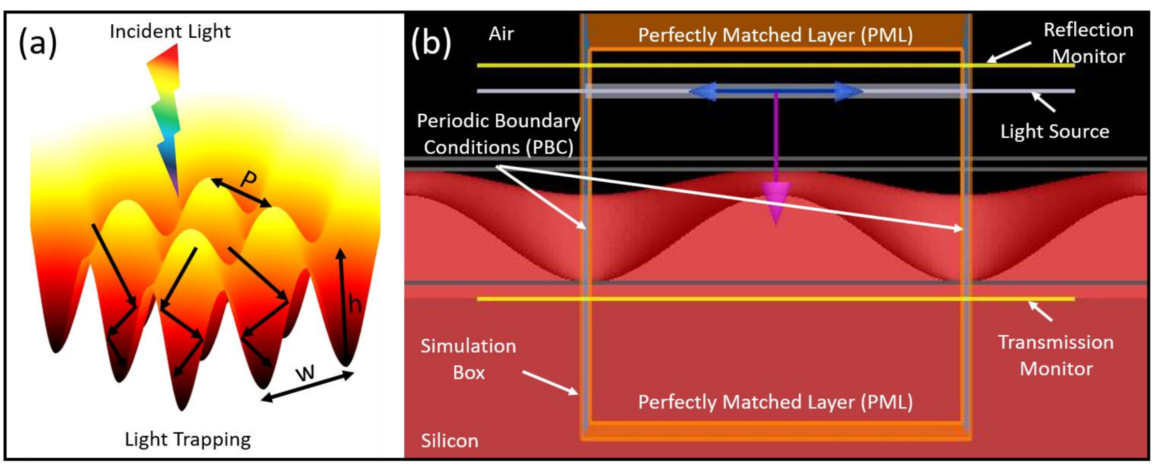

Figure 3.4: Gaussian pillar: (a) Schematic showing light trapping in Gaussian pillar structure with height ‘*h*’, base width ‘*w*’ and period ‘*P*’, (b) FDTD simulation set-up and boundary conditions for optical properties calculations

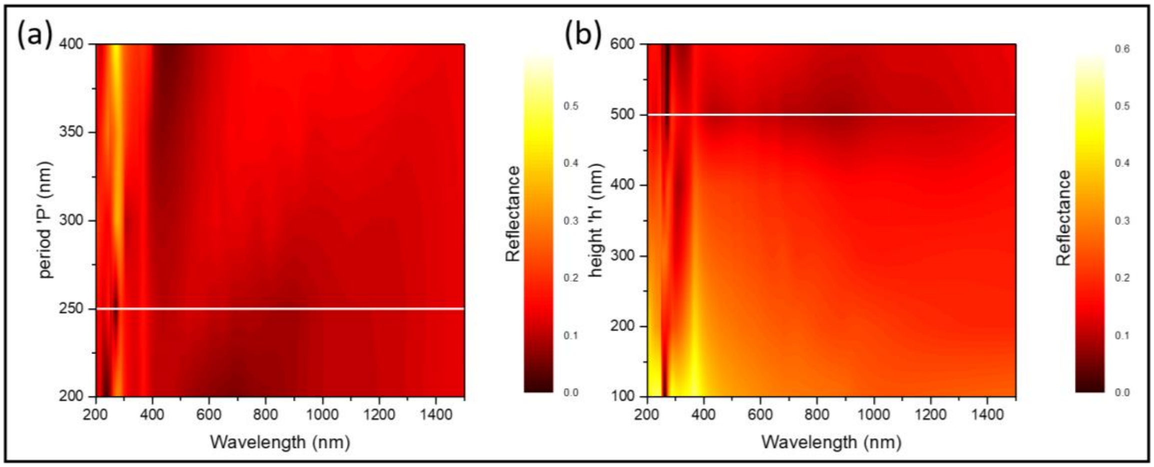

Figure 3.5: Contour plots of calculated reflectance for variation of pillar geometry: (a) Height '*h*', (b) period '*P*', optimized values (*h*=500 nm, *P*=250 nm) are indicated through white line on contour plot

height '*h*' due to availability of more space for light trapping via multiple reflections among consecutive Gaussian pillars and becomes minimum at 500 nm height. The reflectance was found to be increasing (10%-30%) with increased period '*P*'. This is attributed to the availability of more Si to reflect the incoming light. To suppress the reflectance and avoid planar Si, the pillar base was chosen equal to the period. This allows realization of pillars next to each other, leaving no planar surface in between. If a different base diameter '*b*' is used, it will result in reflectance increase from the textured Si surface. A Gaussian pillar with base diameter 250 nm, height 500 nm, and period 250 nm having a low aspect ratio of two and allowing 10-20% light reflectance for the fabrication and analysis is selected. The pillar base diameter is kept same as the period to absorb more incident light and explained in the following section. In Figure 3.6 (a) comparison of the reflectance spectra from optimized Gaussian pillar geometry with planar Si is shown, exhibiting significant reduction in reflectance. Gaussian pillar, in contrast to previously developed structures such as inverted periodic nano-pyramids [87], random nano-pyramids [98], random micro-pyramid [88], honeycomb structures [89] highly ordered periodic nano-wire array [90], nano wire [91] etc. for Si texturing, exhibit a significant reduction in reflectance having a value of 10-20% in a broadband visible wavelength range of 300-1000 nm. Gaussian pillars only show high reflectance value if compared to nanowire [90] in a narrow range of

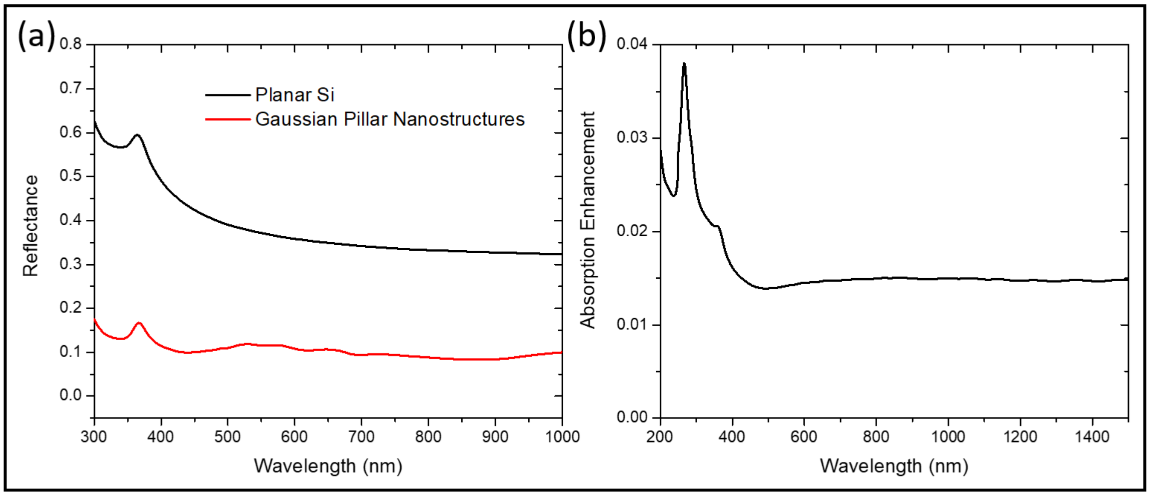

Figure 3.6: (a) Reflectance spectra of optimized Gaussian pillars and comparison against planar Si, (b) Absorption enhancement for light at normal incidence in Si substrate for designed Gaussian pillar

530-650 nm. The graded refractive index between air and Si due to geometrical variation of pillar nanostructures in contrast to planar Si suppresses the reflectance [83], [84]. Gaussian pillars have superior light trapping and antireflection properties as a result of reduced reflection from the smaller tip similar to theoretical prediction of nano-cone/wedge shaped structures [93], [96]. The smaller top diameter of Gaussian pillars results in reflection suppression, while the larger base contains more Si to absorb the light. The designed Gaussian pillars were also tested for varying light incidence angle, and their optical performance was found mostly insensitive to light incidence direction, polarizations yielding an average 10-15% reflectance. The unique shape of proposed Gaussian pillar also enables efficient light trapping in the area in-between the neighboring pillars and photon loss is minimized. It occurs due to the multiple light reflections from pillar surface in the area in-between neighboring pillars until the light incident angle is smaller than critical angle. The phenomenon of multiple light reflections corresponds to increased optical path length and light confinement.

The absorption enhancement, which is also a measure of photo electric conversion efficiency, is further calculated due to Gaussian pillars and compared against the planar Si substrate. The photo electric conversion efficiency of textured surfaces relies on photo generated current, which is proportional to the incident light intensity. The photo generated current is related to quantum efficiency [106]. The quantum efficiency is the ratio of absorbed light power to the incident light power at a wavelength. It indicates the amount of current that will be produced when illuminated by the light/photons of a wavelength, and can be written as $QE\ (\lambda)$:

$$QE(\lambda) = \frac{P_{abs}(\lambda)}{P_{in}(\lambda)} \tag{3.4}$$

where $P_{abs}\ (\lambda)$ and $P_{in}\ (\lambda)$ are absorbed and incident light power respectively at a wavelength λ. Quantum efficiency represents the spectral response and spectral distribution of short circuit current I_{SC}. Thus, quantum efficiency calculations are important, and it will determine the spectral response and short circuit current at different wavelengths. The quantum efficiencies of Si with and without Gaussian pillar is calculated, and following parameter, absorption enhancement $g\ (\lambda)$ is defined, to notice how the efficiency of a textured surface is improved,

$$g(\lambda) = \frac{QE_{Gaussian\ pillar}(\lambda)}{QE_{bare}(\lambda)} \tag{3.5}$$

The absorption in Si is calculated indirectly via measuring the reflectance (R) and transmission (T) through the textured surface. The absorption is then estimated as 1–(R+T). The absorption in Si with and without Gaussian pillar is calculated to determine the absorption enhancement. The calculations show that the increase in height and decrease in period leads to improvement in the absorption. Figure 3.6 (b) shows the absorption enhancement plot for the light at normal incidence on the Si substrate for designed Gaussian pillar with a base diameter of 250 nm, a height of 500 nm, and a period 250 nm. The results show absorption enhancement due to Gaussian pillars over the entire wavelength range. The absorption enhancement was high at shorter wavelengths i.e. below 400 nm. The enhancement in absorption provided a significant 50% increase over 400 nm and pillars were proven to be effective over a broad wavelength range. The variation in absorption enhancement values at longer wavelengths (over 400 nm) is due to the high absorption of shorter wavelengths in pillars and consideration of limited substrate thickness (2 µm) in the simulations. Thus, the results on absorption enhancement yielded an enhancement of 50% over a broadband wavelength range using the Gaussian pillars.

The pillar geometry can be considered as a combination of multiple cylinders with diameters gradually increasing towards its base. It enables number of leaky mode resonances and efficient coupling of short and long light wavelengths [95]. This phenomenon of light entrapment is confirmed in Figure 3.7 with electric field intensity distribution inside the Gaussian Si pillar and cavity between subsequent pillars. The distribution is shown for light wavelength λ=600 nm in Figure 3.7 (a) at *xz* (*y*=125nm), Figure 3.7 (b) *yz*-plane (*z*=125nm) through Gaussian pillars and compared against planar Si. The electric field distribution (real E_x) on the Gaussian pillars in *xy*, *yz* plane, including a magnified view is also shown in Figure 3.8 (a), (b). The contour plots for Gaussian pillar depict high electric field intensity distribution inside and, in the area, in-between the Gaussian pillar where bright intensity spots are observed. In case of planar Si, it can be noted that there is no light entrapment and light is reflected. This light trapping phenomenon support antireflection behavior exhibited through Gaussian pillars. The electric field intensity distribution demonstrated efficient light trapping into the substrate at longer wavelengths and it was found that electromagnetic field focusing shifts towards substrate with increasing wavelengths.

The phenomenon of light trapping through Gaussian pillars is further demonstrated via absorption density calculations. The optical absorption per unit volume of Si is calculated (watt/µm^3) with and without the use of Gaussian pillar, and comparisons are made to observe the effect of Gaussian pillars. The results are shown in Figure 3.9 at three different wavelengths- 400 nm, 600 nm, and 1000 nm to notice the absorption behavior of Si with and without Gaussian pillars. The contour plots for Gaussian pillar depict high absorption density inside and below Gaussian pillars where bright intensity spots are observed. In case of planar Si, it can be noted that there is no light absorption and light is reflected. Light with different wavelengths has different penetration depths corresponding to photon energy. The wavelengths shorter than 600 nm were mostly absorbed by Gaussian pillar

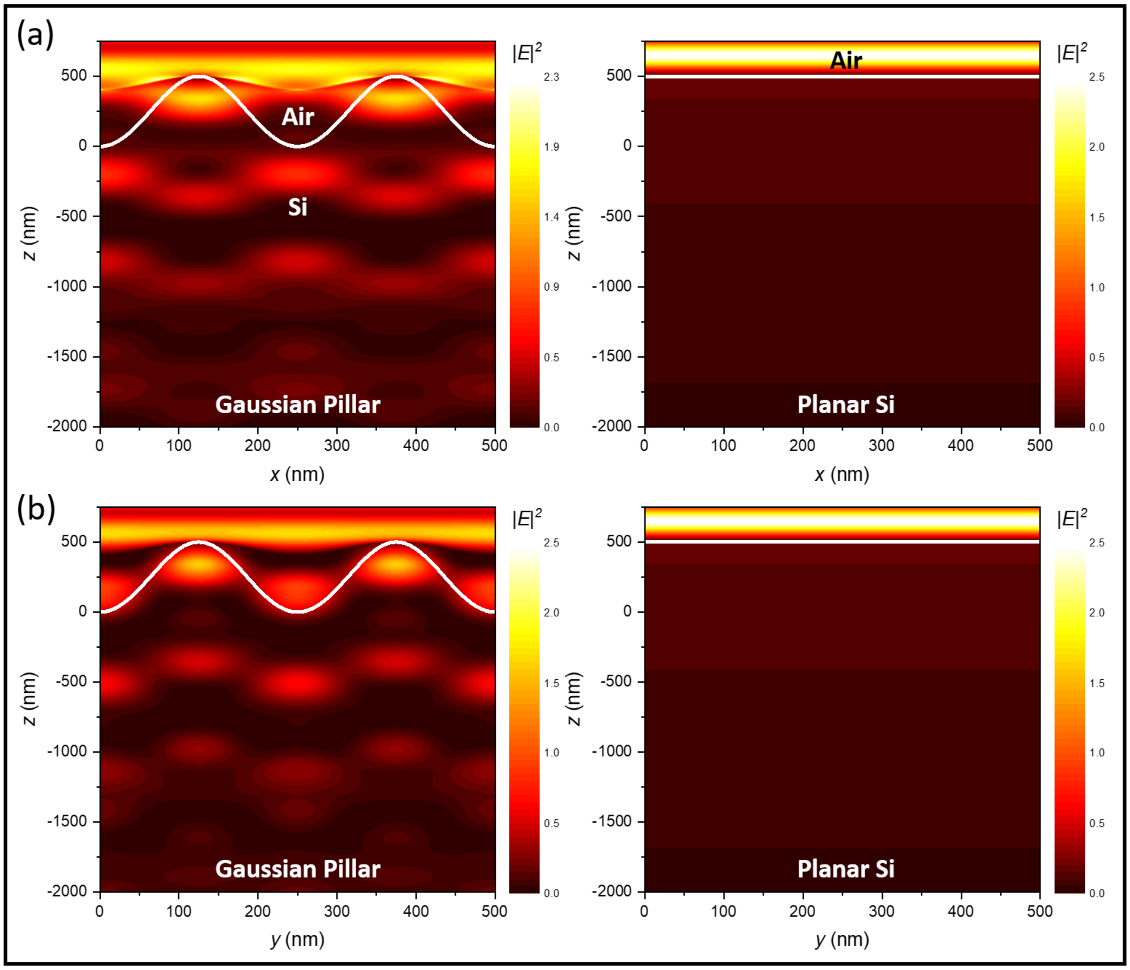

Figure 3.7: Electric field intensity distribution with incident light polarization in *x* direction representing light trapping in Gaussian Si pillars with *h*=500 nm, *P*=250 nm at (a) *xz* plane through pillar cross section at *y*=125 nm, (b) *yz* plane through pillar cross section at *x*=125 nm, against planar Si for incident wavelength of λ =600 nm

structure, while wavelengths greater than 600 nm were absorbed by the Si substrate. At 400 nm light is trapped in Gaussian pillars, giving rise to a high absorption density. At 600 nm pillar as well as substrate show absorption density enhancement as compared to bare Si substrate. The light is absorbed partly in Gaussian pillars as well as Si substrate, leading to improved light trapping. At 1000 nm, Gaussian pillars, however enable light trapping in the substrate, which corresponds to improved optical absorption density as compared to the bare substrate. The optical absorption density comparison at different light wavelengths

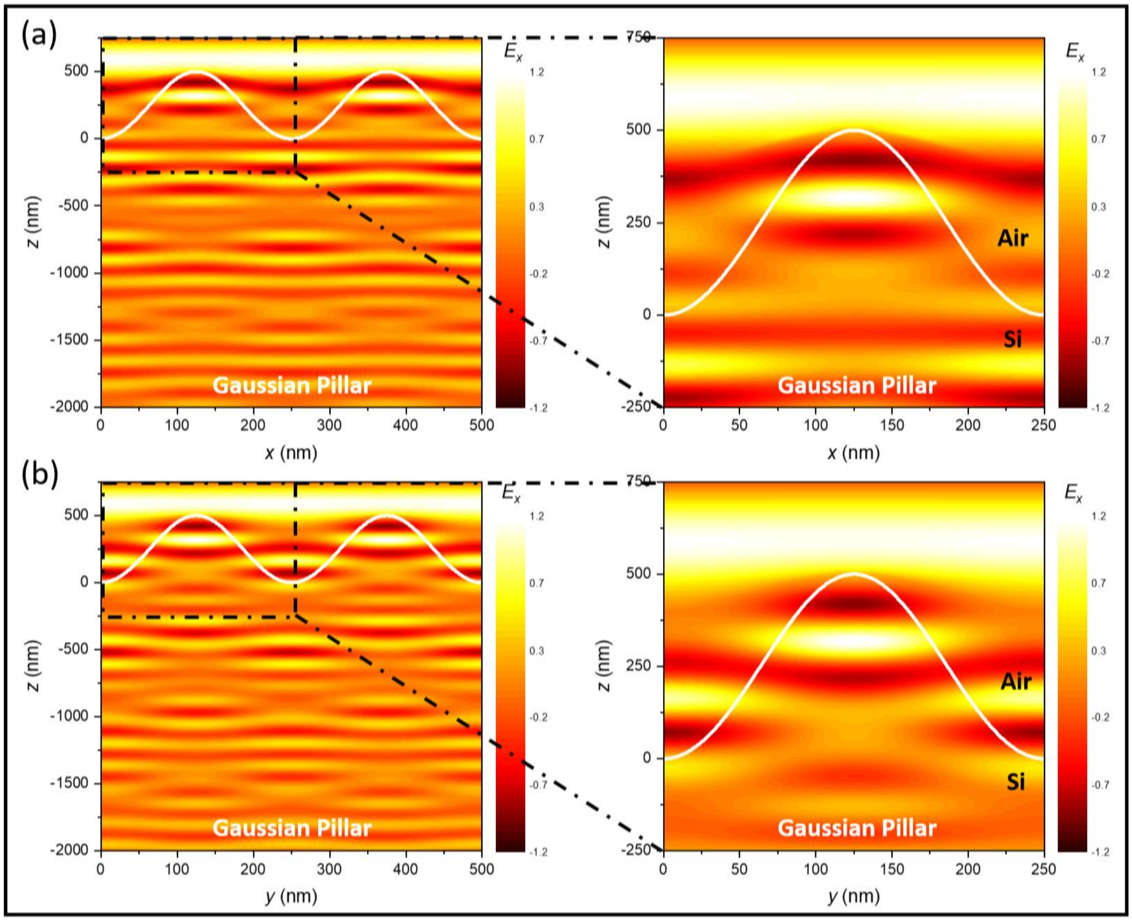

Figure 3.8: Electric field distribution (real E_x) on the Gaussian pillars in (c) *xy*, (d) *yz* plane, including a magnified view (white line indicates Air-Si interface)

also revealed electromagnetic field trapping shifting towards substrate at higher wavelengths. The absorption of shorter wavelengths of illuminated light by Gaussian pillar and light trapping in Si substrate at longer wavelengths due to Gaussian pillars lead to overall reduction in reflectance over entire wavelength range from Si. It is also possible to increase the absorption further via increasing the pillar height, if high absorption is required [94]. High density and periodicity of Gaussian pillars also ensures light coupling among the adjacent pillars. This coupling is attributed to the gradually increasing diameter of Gaussian pillars towards the base in contrast to cylindrical nanowires [90], [97]. The efficient light coupling of localized radial resonant modes inside the Gaussian pillar in addition to the cavity among the consecutive pillars provides a significant boost in the light

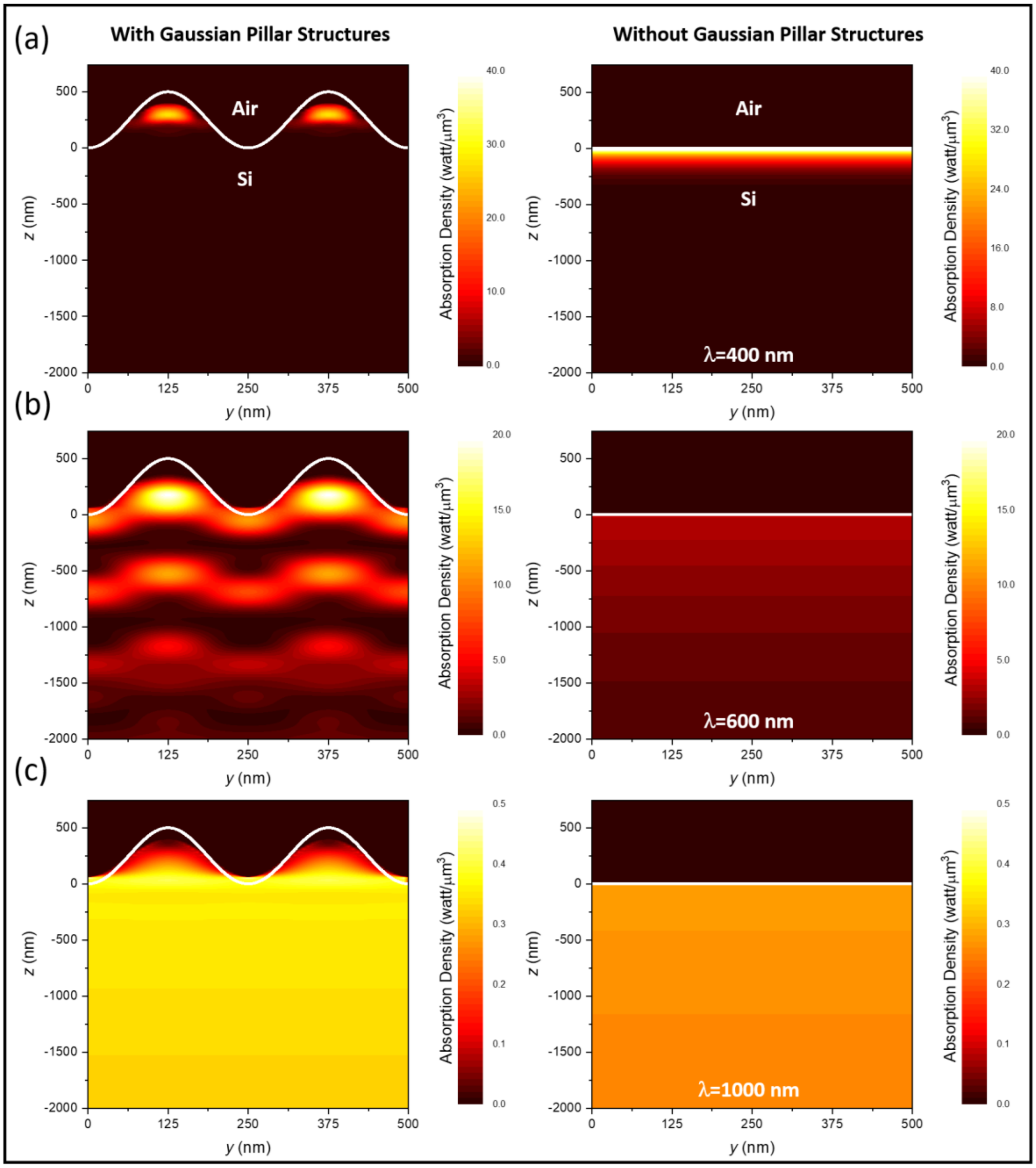

Figure 3.9: Optical absorption per unit volume (watt/μm^3) comparison for Si with and without Gaussian pillar structures in *yz* plane at a light wavelength of: (a) 400 nm, (b) 600 nm, and (c) 1000 nm (white line indicates the Si-air interface)

trapping and the suppression of reflectance. This work has focused on Si nanostructures for fabrication simplicity, it would however be interesting to extend this further and combine with plasmonic nanostructures for improved antireflection and waveguide coupling modes effects to study hybrid dielectric-plasmonic nanostructures [107].

3.3.3 Experimental Characterization of Subwavelength Nanostructures

The optimized Gaussian pillar nanostructures exhibiting antireflection properties have been fabricated on Si. In Figure 3.10 (a) SEM image of fabricated Gaussian pillars with designed parameters (period P=250 nm, height h=500 nm and diameter b=250 nm) is shown. The observed nanostructures demonstrated designed periodicity and fabrication uniformity. One challenge for FIB milling is the accurate control of beam and optimization of milling parameters. It is worth to mention that the proposed approach has reproducibility due to simple and single-step fabrication. It took only 130 seconds to pattern the Gaussian pillars on a 20 μm×10 μm area with a beam current of 200 pA. Horizontal field width (HFW) at a minimum magnification of 250× is 496 μm in the used dual beam instrument, so at the resolution of 1024×884 pixels in the FIB milling window, it is possible to fabricate such nanostructures on 496 μm×428 μm (approximately) area in a single operation, which can be further extended employing the automatic stage movement. The milling time can be further reduced using a larger beam current, but it will likely lead to heavy ion implantation in Si and compromise the fabrication accuracy. The EDS analysis was carried out in order to investigate the gallium contamination due to FIB processing [33], [108] in fabricated nanostructures, and data assessed by EDS analysis is shown in Figure 3.10 (b).

The table in the inset of Figure 3.10 (b) show element atomic and weight distribution. The results show very less distribution of Gallium (0.75 weight %). This is attributed to the strategy employed in the fabrication and suitability of developed method for optical and photonic applications. Additionally, a small percentage of oxygen (0.32 weight %) found from EDS analysis suggested negligible formation of silicon oxide layer, which is important for Si nanostructures. These artefacts can be eliminated further with thermal annealing of Si, which will lead to segregation of implanted Gallium at the surface [109]. The segregated gallium at the surface can be removed through distilled water and processing in ultrasonic cleaner over the melting point of gallium (29.8° C). FIB induced damage in Si was assessed by Raman spectroscopy. The Raman spectra results for

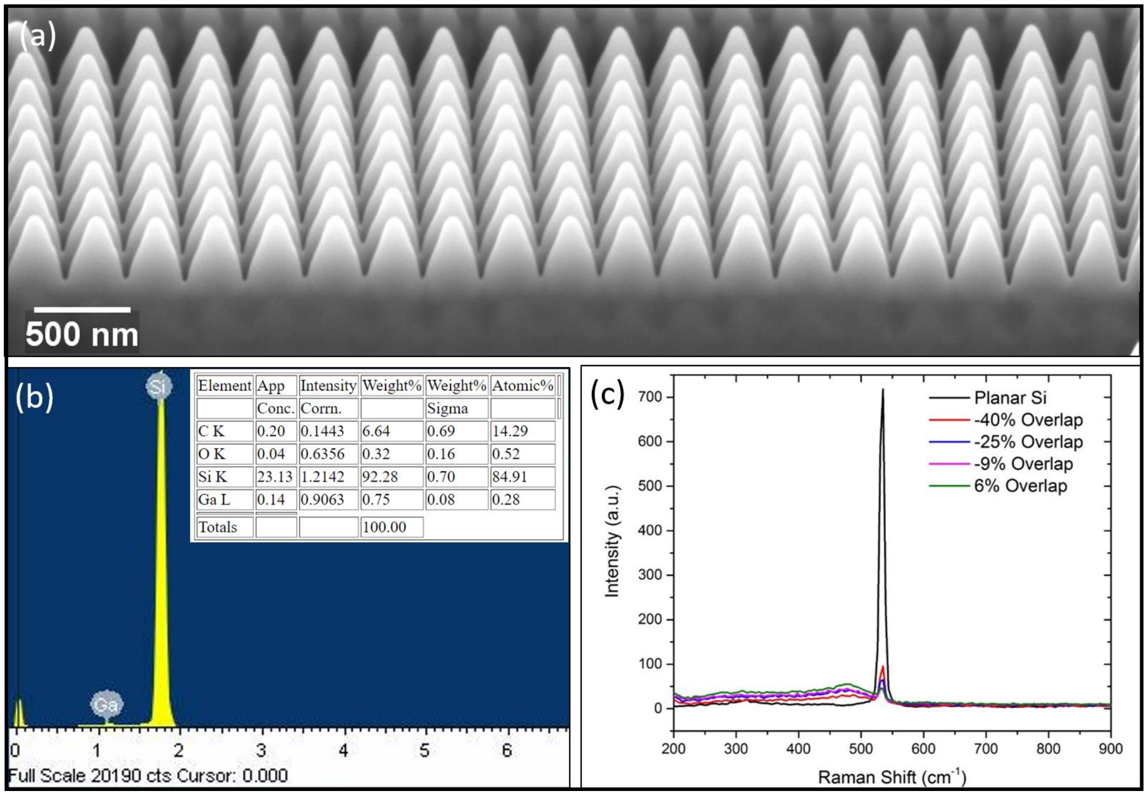

Element	App Conc.	Intensity Corrn.	Weight%	Weight% Sigma	Atomic%
C K	0.20	0.1443	6.64	0.69	14.29
O K	0.04	0.6356	0.32	0.16	0.52
Si K	23.13	1.2142	92.28	0.70	84.91
Ga L	0.14	0.9063	0.75	0.08	0.28
Totals			100.00		

Figure 3.10: (a) SEM image of fabricated designed Si Gaussian pillar nanostructures, (b) EDS analysis of FIB fabricated Si pillars, the table in the inset shows elemental composition and Ga atomic (0.28%) and weight (0.75%) distribution (c) Raman spectrum of FIB irradiated area with different overlap at a fixed dose of 2.2×10^{16} ions/cm^2 compared with planar Si substrate

fabricated nanostructures in Figure 3.10 (c) reveal the transformation of crystalline Si into amorphous Si due to ion beam processing. Recrystallization was found out to be increasing with the increase in beam overlap, as it leads to increased ion dose over a pixel even if the total dose is maintained as constant. The transition from crystalline to amorphous Si, as evident through the decrease in peak intensity at Raman shift of 521 cm^{-1}, by ion bombardments has been reported previously and is in accordance with results [5], [32]. This transition is recoverable using annealing methods [108] and crystalline Si nanostructures can be obtained. However, the amorphous layer of Si over crystalline Si is beneficial for improved light trapping and has potential for high efficiency solar cells [110]. The fabricated Gaussian pillar structures were further characterized experimentally for

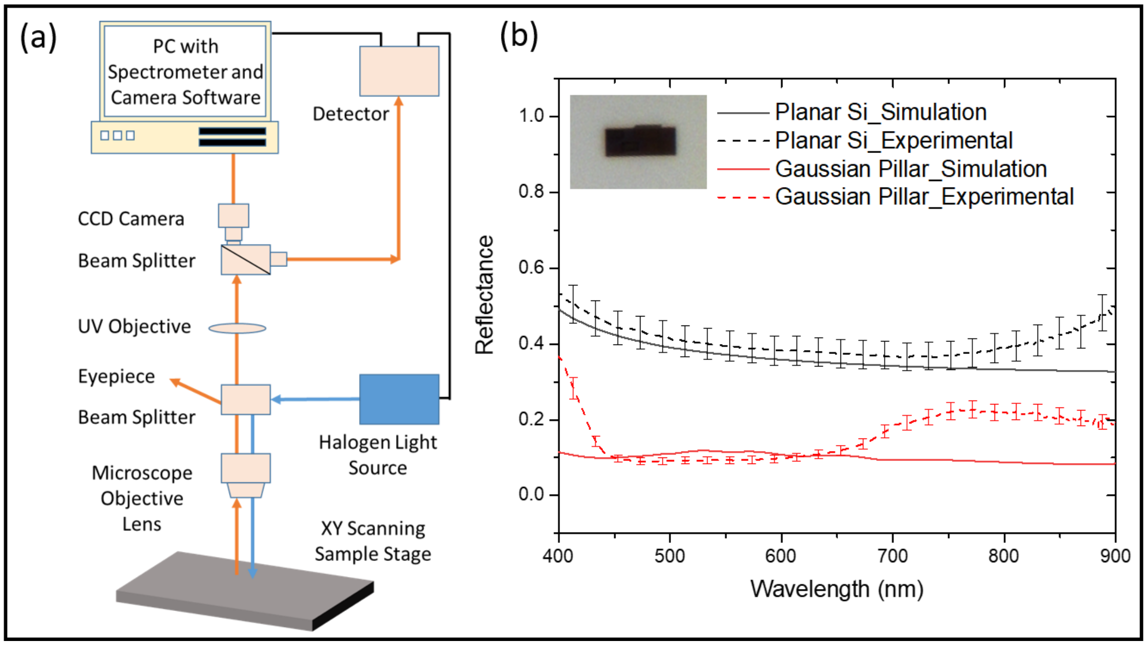

Figure 3.11: (a) Optical set-up for spectroscopic reflectance measurement for fabricated subwavelength nanostructures on Si, (b) Experimental reflectance measurements and comparison with simulation results, the inset includes optical microscopic image showing textured Si surface in black against planar Si substrate

antireflection properties and compared against calculated values from simulations. The optical set-up for reflectance measurements is shown in Figure 3.11 (a). Reflectance comparison for experimentally measured and simulated Gaussian pillars is shown in Figure 3.11 (b). The experimental results are in confirmation with the results observed with simulations in the wavelength range 450-650 nm. The variation between the experimentally measured and the simulated values can be attributed to the difference between the optical properties of Si used in the simulation and the actual optical characteristics of the ion beam fabricated materials. The reflectance normalization in experiments with respect to protected silver mirror can also introduce this variation to a large extent due to the reason that the mirror does not have a perfect unit reflectance. In addition, a slight variation in the fabricated geometry from the simulated geometry might also affect the reflectance values. Overall, the fabricated Gaussian pillars demonstrated good conformity with the predicted values from the simulations. The developed fabrication approach based on the inherent properties of ion beam is not limited to the light trapping and can be further extended to the different materials and potential applications where highly ordered nanostructures are required. The geometry and aspect ratio of fabricated features is tunable via ion beam parameters and a wide range of geometries is possible. Thus, the proposed technique can be used for rapid fabrication of a wide variety of 3D nanostructures geometries at nanoscale for potential applications beyond light trapping.

3.4 Summary

In this work, a novel, single-step, rapid nanofabrication approach was developed for realization of highly ordered Gaussian pillar shaped 3D nanostructure via FIB milling. Simulations and detailed experiments were presented for evolution of periodically spaced Gaussian shaped subwavelength holes to Gaussian pillars with increasing beam overlap during ion beam scanning. The fabricated pillars are tunable via FIB dwell time, while diameter and periodicity of these pillars is controllable through beam current and step-size respectively, providing an additional degree of freedom for desired functionality. The unique geometry of Gaussian pillars with a smaller tip and extended base enabled efficient light trapping, observed through light reflection and absorption density calculations. Gaussian pillar shaped nanostructures on Si fabricated via developed approach were demonstrated for antireflection and light trapping properties through simulations and experiments exhibiting 10-20% reflectance for a broad wavelength range. A significant absorption enhancement of 50% was observed employing the Gaussian pillar nanostructures over Si. The experimental FIB induced damage characterization revealed formation of amorphous Si nanostructures, while Ga implantation was found below 0.75 weight % due to ion beam processing. Given the tunable nature and nanoscale feature size along with fabrication uniformity, the developed nanofabrication approach is suitable for rapid prototyping applications. In addition, the developed approach is not limited to Si texturing and can be further extended to different materials and application areas such as plasmonics etc. Thanks to the FIB fabrication capabilities and rapid prototyping of Gaussian pillar 3D structures, this work has the potential to encompass different materials to assist future nanoscale light trapping and antireflection applications.

Chapter 4. Direct Fabrication of Subwavelength Nanostructures on Silicon for Multicolor Generation

Color filtering via interaction of visible light with nanostructured surfaces offers high resolution printing of structural colors. A novel approach for color filtering in reflection mode via direct fabrication of subwavelength nanostructures on high-index, low-loss, and inexpensive silicon (Si) substrate is developed. Nanostructures having a unique geometry of tapered holes have been fabricated exploiting the Gaussian nature of a gallium source focused ion beam (FIB). The fabrication process is rapid and single-step i.e. without any pre or post-processing or mask preparation in contrast to previously reported nanostructures for color filtering. These nanostructures are tunable via FIB parameters and a wide color palette has been created. Finite-difference time-domain (FDTD) calculations reveal that the unique tapered nanohole geometry facilitates enhanced color purity via selective absorption of a narrow band of incident light wavelengths and makes it possible to obtain a wide variety of colors suitable for realistic color printing applications. The proposed approach is demonstrated for color printing applications via fabrication of butterflies and letters on Si.

4.1 Introduction

Interaction of visible light with subwavelength nanostructures leads to generation of unique structural colors [111]. These colors arise from resonant scattering of light from subwavelength structures, and are tunable via structure geometry, period etc. Structural colors, originated via light-matter interactions, offer high spatial resolution, beating fundamental resolution limit of light field microscopy. Such structural colors can be printed at a resolution of ~100,000 dots per inch (DPI) [112]. The structural colors produced from resonant behavior of light from nanostructures can be used for optical security [113], polarimetry [114], spectral imaging [115] applications etc.

Structural colors have been widely investigated in metallic nanostructures based on surface plasmon resonances and a variety of plasmonic metasurfaces have been realized including nanohole, nanodisk, nanowire shape etc. [111]–[116]. Gold, silver, and aluminium are most widely used metals for plasmonic color generation [111]. Plasmonic nanostructures, however, suffer significant optical losses and ohmic heating arising due to interband and intraband transitions [117], which results in loss of color purity. In addition, use of noble metals is uneconomical for industrial and large-scale applications. Aluminium, although economical, shows broad resonances in the visible spectrum, hence inefficient to yield sharp colors. Given the issues associated with structural colors based on plasmonics, all-dielectric metasurfaces employing high index material provide promising alternatives. High index nanostructures based on Mie resonances have been efficiently used for antireflection coating and light management in photovoltaics [83]. High index metasurfaces also show resonant behaviour arising from the oscillations of bound electrons. The displacement currents from these oscillating electrons are free from ohmic damping, allowing reduced optical losses and heating [118]. Further, high index dielectric metasurfaces excite Mie-type magnetic and electric resonances. This offers a stronger optical response and nonlinear effects, in contrast to localized field enhancement supported by the electric resonance [119]. Nanostructuring of high index materials offer an enhanced light matter interaction and thus opens an opportunity to manipulate the light in the visible spectrum. Silicon (Si), a widely adopted material in electronics, with a high index value and low loss in visible spectrum is considered to be the most suitable material for structural color printing. Its low cost and compatibility with existing complementary metal oxide semiconductor (CMOS) techniques further makes it an ideal choice.

A wide range of high index color filters in Si have been demonstrated by polarization sensitive designs of nanowires (NW), nanodisks (ND), nanoparticles (NP), and nanoholes (NH) through light scattering from individual NW/ND/NP/NH [120]–[126]. These designs have been shown to exhibit a wavelength selective coupling of visible light with its guiding modes and rendering a specific color. The suppression of light diffraction and strong coupling with localized surface states has also been shown for limited viewing angle independence for structural color generation. A recent work investigated Si nanodisks, exhibiting gradual intensity modulation suitable for nanoscale printing against abrupt intensity modulations offered via their plasmonic counterparts (Al, Ag) [127]. Arrays of

NW/ND/NP/NHs have been fabricated by lithographic patterning of previously deposited Si thin film. Laser has also been used for fabrication of Si nanoparticles with optical response in visible range [128] and post processing of Ge disks fabricated via electron beam lithography (EBL) [129] similar to Al plasmonic disks [116] for colored metasurfaces. Such printing demonstrations arising from femto/nanosecond laser induced melting and morphology induced changes, require careful design, control and have been mostly centered on reshaping previously fabricated nanostructures via EBL. Dielectric color filters down to pixel size ~1 μm holds current state of art and have been demonstrated compatible for backside-illuminated CMOS image sensor (CIS) technology [130]. However, the spatial resolution can be further improved with scaling of pixel size and simpler fabrication approach needs to be developed. It must be noted here that electron beam lithography (EBL) has primarily been used for pattern generation and nanostructure fabrication along with dry/wet etching techniques, which involves multiple steps and complexities in terms of mask-fabrication etc. Significant efforts have been made for redesign of color filters, still most of the demonstrated filters are based on a 2D geometry (ND/NW/NP/NH), which can be further improved for optical performance if a 3D geometry is designed. A high-quality resonance with narrow bandwidth with improved design will lead to extended color purity. Further, most dielectric/hybrid metamaterials exhibiting color filtering require deposition/growth of high index thin films and sample preparation, limiting the printing and commercial/industrial fabrication.

In this work, a direct, mask-less approach for fabrication of color filters using focused ion beam (FIB) is proposed and demonstrated. These color filters are fabricated on high index, low-loss and inexpensive Si. The fabricated color filters are observable easily with bright field optical microscopy. A systematic approach is presented utilizing Gaussian profile of the incoming focused ion beam to fabricate periodically spaced tapered nanohole array. The fabricated color filters exhibit high quality resonance over the visible spectrum with a narrow bandwidth due to unique tapered nanohole geometry, leading to enhanced color purity. The broad range of color generation was verified experimentally and investigated numerically using finite-difference time-domain (FDTD) calculations.

4.2 Experiments and Simulations

The nanostructures were fabricated on 5mm×5mm pre-cut chip from 4-inch Si wafer (Ted Pella Inc., Product 16008). The nanofabrication was carried out using focused ion beam system with a gallium source (dual beam FEI Quanta 3D). The beam current of 1 nA at an acceleration voltage of 30 kV was set for all fabrication experiments. The nanoholes were milled by dwelling a beam at given positions for times ranging from 25-250 milli-seconds (ms). A unique tapered geometry of hole is obtained owing to Gaussian nature of the incident ion beam. The spacing between the holes was controlled using beam overlap function. Multi-pass FIB scans were made to minimize redeposition during ion milling and to ensure cleaner cuts into Si maintaining the fabrication accuracy.

Bright field microscopy was performed on Nikon Eclipse Light Microscope. A white light was used to illuminate the nanostructures using a 20X objective lens. Further, spectral reflectance characteristics were obtained using micro spectrometer (J&M Micro UV-Vis). A halogen lamp coupled with an optical fiber was used to illuminate the sample using 50X objective lens along with numerical aperture (NA) of 0.65. Protected silver mirror (Thorlabs Inc., product PF07-03-P01) was used to normalize the reflectance from Si samples. Optical constants of Si were characterized using spectroscopic ellipsometry (J.A Woollam M-2000DI). AFM measurements were performed on Scanasyst-Air, Bruker instrument with a cantilever of nominal spring constant of 0.4 N/m and nominal frequency of 70 kHz for imaging.

The optical performance of the proposed structures is calculated numerically. A commercial-grade simulator based on the finite-difference time-domain method was used to perform the calculations. Simulation region is defined over a single hole due to symmetry and periodicity of the structures to reduce the computation time and memory. The periodic boundary conditions (PBC) were applied the x and y-direction to account for the periodicity and perfectly matched layer (PML) along the z-direction to confine the simulation domain. The optical constants for silicon were set according to Edwards [131]. A plane wave, visible spectrum (400-700 nm) illumination was used to excite the structure.

To find out the reflectance behavior from tapered nanohole geometry, a frequency-domain power monitor was placed behind the source to measure the total reflectance.

4.3 Results and Discussion

4.3.1 Focused Ion Beam Direct Fabrication of Silicon Nanostructures

Resonant modes in Si can be excited if structure size is smaller than incident light wavelength. This results in localized enhancement of electric fields and light scattering. In the current work, subwavelength nanostructures are milled on Si using a single-step FIB operation. The fabrication approach is simple, involving a single-step as compared to existing lithographic fabrication techniques for color filters fabrication. Gallium FIB is scanned over Si while maintaining a large negative overlap between subsequent scanning pixels. Figure 4.1 (a) shows scanning schematic of FIB for fabrication of color filters via tuning of FIB overlap through step-size and dwell time during scanning. For positive or small negative overlaps, the pixels adjacent to the pixel being scanned are also milled

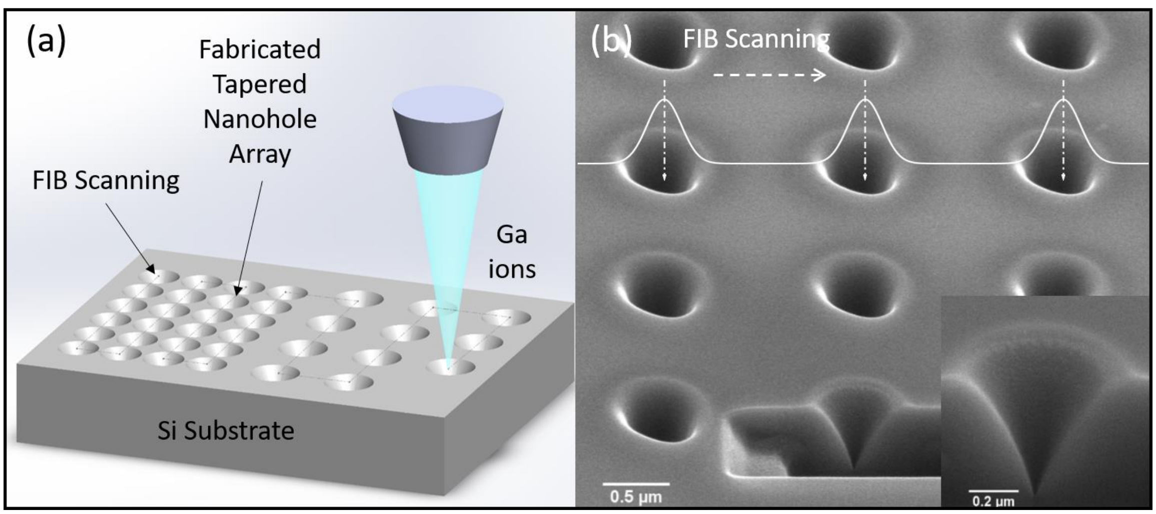

Figure 4.1: Direct fabrication of Si nanostructures: A tightly focused beam of Ga ions is scanned over Si with a gap tuning between the subsequent scanning pixels as shown in (a). (b) Schematic and SEM image showing FIB scanning by Ga ions in a Gaussian profile and fabrication of periodic array of nanoholes on Si, with inset including the cross-sectional SEM image revealing unique tapered hole geometry

partially due to Gaussian profile of incoming Ga ions as the beam diameter is larger than the individual pixel size. In addition, the non-Gaussian wing of the incoming ion beam hitting the sample surface at large angles sputters the surface faster and is major issue in FIB, limiting how closely the desires features can be fabricated [132]. However, a large negative overlap ensures the separation between fabricated nanoholes and is used for controlling the period. It must be noted here that the sputtering issue associated with non-Gaussian wings of ion-beam will become prominent if the period is further decreased further, and eventually it will lead to uniform milling instead of nanohole resonators fabrication. The nanoholes fabricated are observed to have tapered walls due to the Gaussian profile of incident Ga ions. This has been illustrated in Figure 4.1 (b), where scanning electron microscopic (SEM) image of the fabricated tapered nanoholes is shown via FIB scanning. The inset in Figure 4.1 (b) shows a cross-section of a typical nanohole revealing a tapered geometry of nanoholes.

The fabricated periodic array of subwavelength nanoholes allow light manipulation over visible spectrum and leads to generation of unique structural colors. This forms a basis for

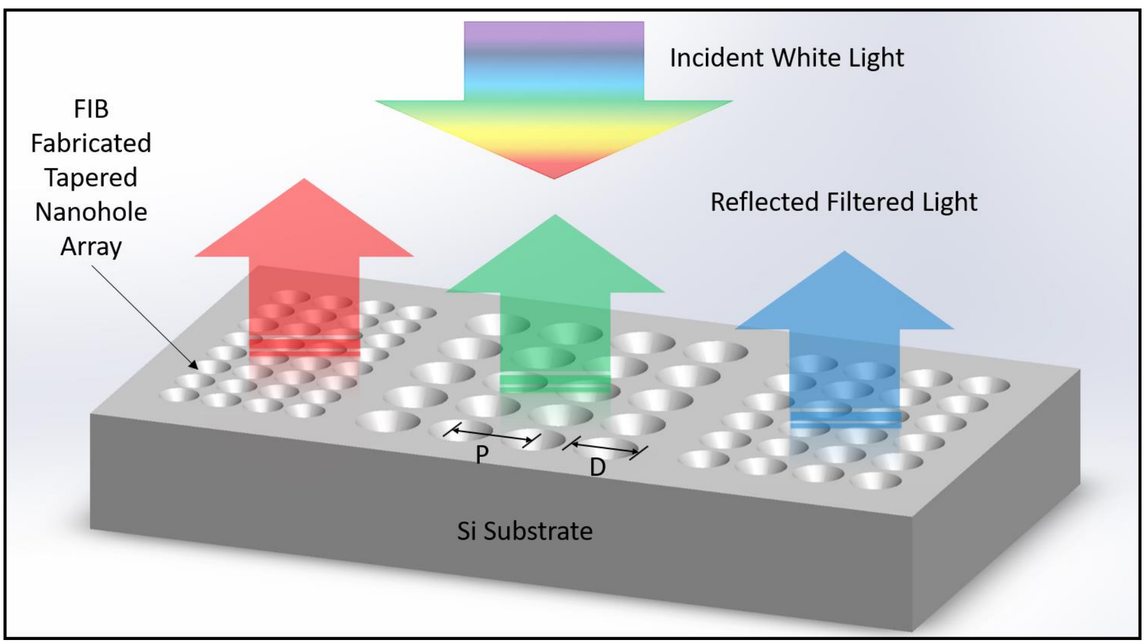

Figure 4.2: Configuration schematic of color filtering via periodic array of nanoholes on Si substrate with a diameter ‘*D*’ and period ‘*P*’ under normal illumination of white light

the single-step fabrication approach of color filters by FIB. The developed approach is fast due to single-step involved compared to multi-step lithography based approaches [120]–[130] and thermal dewetting methods based on FIB templating reported previously [133]. The diameter '*D*' and the period '*P*' of subwavelength nanoholes are controlled via FIB parameters for light manipulation over the visible spectrum and tuning of the structural color generated. Figure 4.2 shows a configuration of color filtering of incident white light via periodic array of fabricated nanoholes in Si substrate. White light is incident normally over the periodic nanohole array and the filtered light is reflected.

4.3.2 Optical Characterization of Nanostructures

4.3.2.1 Bright Field Optical Microscopy

The periodic arrays of nanohole resonators on Si with varying diameter '*D*' (275-500 nm in a step-size of 25 nm) and periodicities '*P*' (525-900 nm in a step-size of 25 nm) have further been fabricated for color filtering and systematic study of color generation phenomenon via light matter interactions. The nanoholes are arranged in a square lattice in each array. The period of fabricated nanohole resonator array is adjusted through beam overlap function, while nanohole diameter is associated with the dwell time being used during FIB milling. Using a bright field optical microscope with a white light illumination, each pattern can be seen reflecting a unique color as shown through a wide color palette in Figure 4.3. Each palette in Figure 4.3 is an optical image of the individual color filter. This demonstrates the capability of simple fabrication methodology to produce tapered holes for the color filtering application. In addition, the fabricated color filters are robust and quite durable, suitable for color printing applications. The palettes show the reflected colors observed in optical microscope as a function of nanohole diameter and period. The effect of these two parameters on the color generation phenomenon is best understood through the reflected colors as follows: for a given period (*P*), increasing hole diameter (*D*) results in large size resonators and the reflected color transitions from short to long wavelengths (i.e. from blue to red), for example from *D*=275 nm to 500 nm in 1st column at *P*=525 nm. This is due to the larger milling depth and sputtering associated with increasing beam

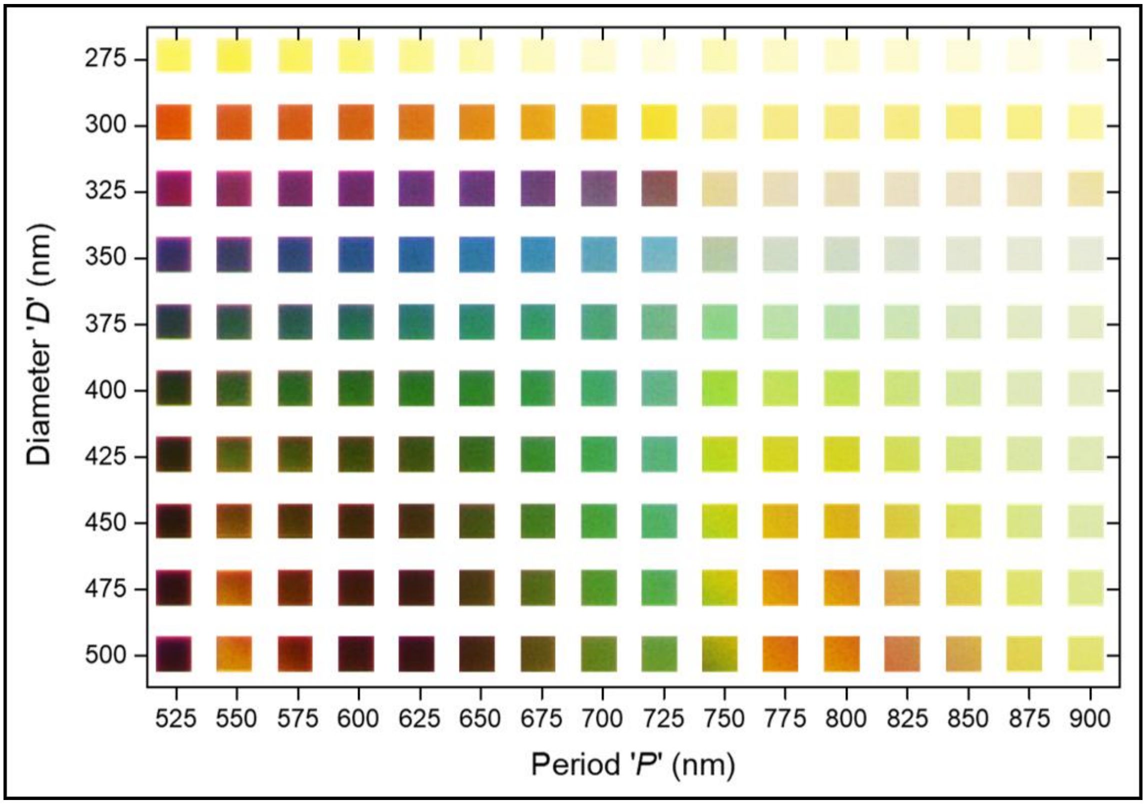

Figure 4.3: A wide color palette obtained via resonator arrays of varying nanohole diameter *D* (275-500 nm in a step-size of 25 nm) and periodicities *P* (525-900 nm in a step-size of 25 nm): bright field (reflectance) optical microscopic images of fabricated color filters

diameter, giving rise to a larger resonator. At a fixed diameter, decreasing the resonator period leads to small size resonator and reflected colors transition towards the shorter wavelength i.e. blue. For large period, the reflected colors begin to taint due to the nanohole resonators supporting multiple resonant modes [133]. This is discussed in more details in next section on spectroscopic reflectance characteristics. The dependence of *P* and *D* of nanohole resonators on color generation arises owing to the coupling of resonance fields. From the fabricated color palette, the three primary filters- Red, Green, and Blue (RGB) correspond to nanohole resonators, *D*=500, 400, 350 nm respectively for a fixed period, *P*=575 nm. This is in accordance with the observed redshift of the reflected colors with the increasing diameters at a fixed period.

4.3.2.2 Spectroscopic Reflectance Characteristics

To understand the color filtering and resonance behaviour through fabricated nanohole array, the structures are further subjected to spectroscopic reflectance analysis. The spectral behaviour of fabricated patterns is as shown in Figure 4.4. Experimentally measured reflectance values are compared for a nanohole resonator diameter D=400 nm and period varying from P=575 nm to 725 nm in the plot of Figure 4.4 (a). Colors can be generated by either an additive or subtractive approach via selective reflection or absorption of light wavelengths respectively through the subwavelength nanostructures. The developed color filters are based on subtractive approach, where the colors are produced by selective wavelength absorption similar to Si-Al hybrid nanodisk reported in the literature [134]. Two distinct spectral dips (minima) are observed in each reflectance spectrum, which show a linear dependence over the visible spectrum on the period for a given nanohole diameter. The reflectance dips for fabricated color filters corresponds to resonance wavelengths. The reflectance spectrum exhibit maxima at either side of these reflectance minima, which determine the reflected color observed in optical microscope through these color filters. The spectral dips in the visible reflectance spectrum is observed to shift slightly towards the longer wavelengths i.e. red. This is in accordance with the observation made in color palettes of Figure 4.3 and due to the reason that as the period is decreased, the coupling effect among neighbouring nanohole resonators is reduced as the nanoholes are separated away from each other.

The resonance dips visible in the reflectance spectrum can be modulated over the entire visible spectrum corresponding to the generation of a specific color, making it possible to obtain a variety of colors, as seen in Figure 4.3. The fact that, the double resonances, corresponding to two distinct spectral dips, which are observed in reflectance spectrum at different P for a given D, makes it possible to fabricate a particular color and obtain a wide color gamut, which is otherwise not possible in the case of broad and single resonances obtained through conventional resonators. The period dependent reflectance spectrum, provides additional benefit offering superior color tunability over Si nanowires, where reflection dip is almost period-independent [122]. This may be due to the much smaller

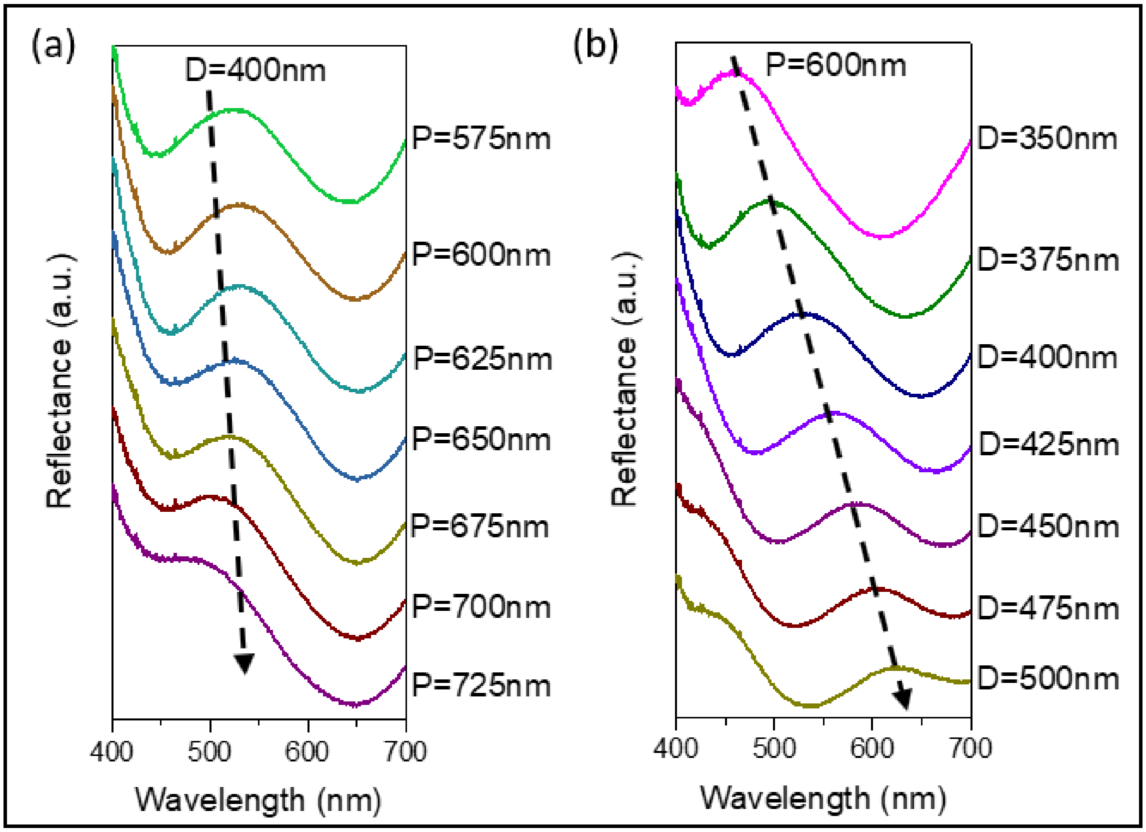

Figure 4.4: (a) Reflectance spectrum of fabricated color filters for fixed nanohole diameter of 400 nm and variation of hole period from 575-725 nm, (b) Reflectance spectrum for a fixed period of 600 nm and hole diameter ranging from 350-500 nm

period employed here, which can allow near-field coupling among adjacent nanohole resonators in contrast to Si nanowires [122]. This behaviour is studied in more details through simulations in the next section of this paper. Reflectance comparison is also shown for a nanohole resonator period P=600 nm for nanohole diameter ranging from 350 nm to 500 nm in Figure 4.4 (b). Two distinct spectral dips, like Figure 4.4 (a), are observed for variation of resonator diameter at a given period. As seen from the reflectance spectrum of Figure 4.4 (b), the larger diameter of the nanohole resonator array results in red-shift of dip positions in the reflectance spectrum. The shift in reflectance spectrum as observed with nanohole resonator diameter is more in visible spectrum as compared to its period.

CIE 1931 Color Space: In order to assess the performance of fabricated color filters in a quantifiable manner, the chromaticity coordinates have been calculated. The CIE

(Commission Internationale de l'Eclairage) 1931 color space [135] defines the color perception in human color vision quantitatively, from the distribution of wavelengths in the visible spectrum. The CIE chromaticity diagram is used for visualization of color gamut.

The X, Y, Z chromaticity factors are calculated using the color matching functions $x(\lambda)$, $y(\lambda)$, $z(\lambda)$ by integrating the spectral reflectance response of color filters in the visible regime according to,

$$X = \int_{400}^{700} R(\lambda)x(\lambda)\, d\lambda; Y = \int_{400}^{700} R(\lambda)y(\lambda)\, d\lambda;\ Z = \int_{400}^{700} R(\lambda)z(\lambda)\, d\lambda \qquad (4.1)$$

where, $R(\lambda)$ is the measured reflectance spectrum. The color matching functions are chromatic response of an observer and shown in Figure 4.5 corresponding to red, green, and blue colors.

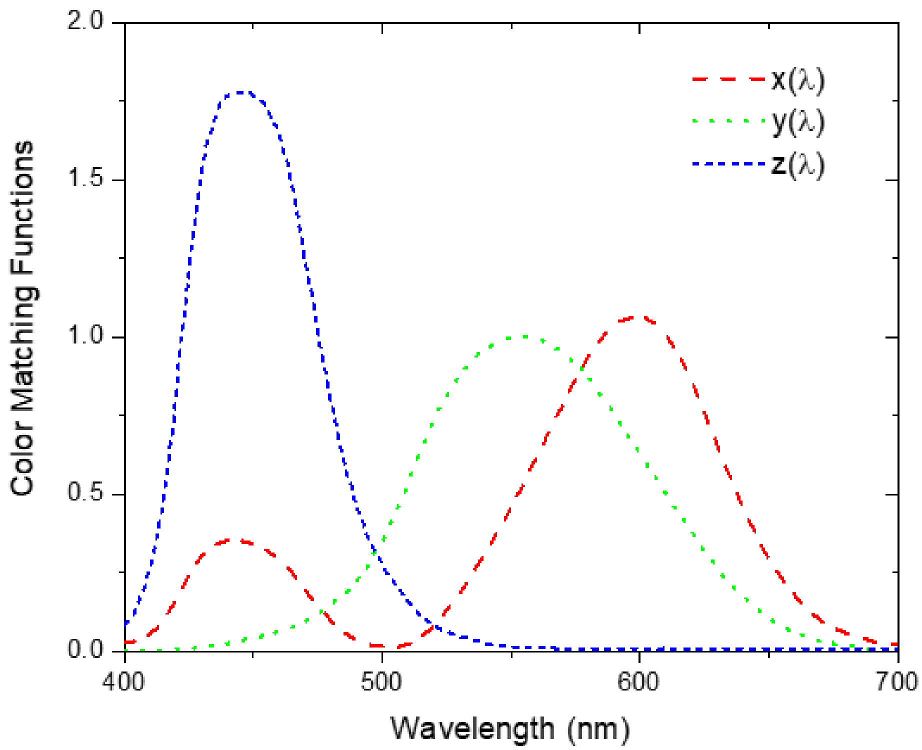

Figure 4.5: Color matching functions x(λ), y(λ), z(λ) used for calculations of CIE 1931 chromaticity coordinates corresponding to Red, Green, and Blue colors respectively

The reduced parameters x, y i.e. coordinates on CIE 1931 color space are then calculated according to,

$$x = \frac{X}{X+Y+Z};\ y = \frac{Y}{X+Y+Z} \tag{4.2}$$

The calculated CIE coordinates of selected color filters in Figure 4.4 are shown in Figure 4.6 on CIE 1931 color space. The chromaticity coordinates are shown for nanohole resonator *D*=400 nm, P=575-725 nm and *P*=600 nm, *D*=350-500 nm. Figure 4.6 (b), (d) show zooms of indicated central region on color space in Figure 4.6 (a), (c) respectively.

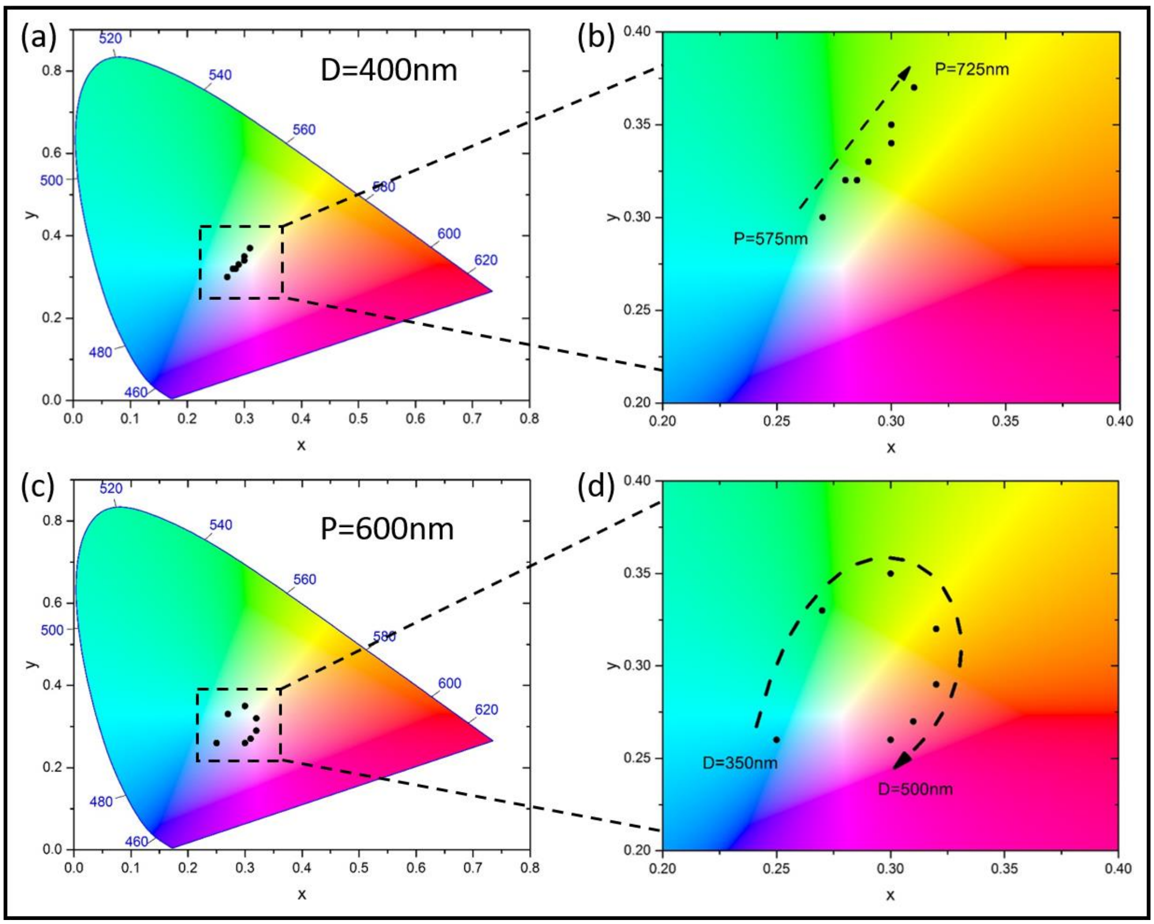

Figure 4.6: Chromaticity coordinates on the CIE 1931 diagram color filters for (a) Fixed nanohole diameter of 400 nm and variation of hole period from 575-725 nm, (c) Fixed period of 600 nm and hole diameter ranging from 350-500 nm with (b), (d) including the magnified views of (a), (c) respectively

Chromaticity coordinates of selected color filters on CIE color space demonstrate the wide color palette availability. The chromaticity coordinates encircling around the white-point indicate the availability of full color palette with the developed fabrication approach and color filter design. Comparing the effect of the resonator period and the diameter on the color space, it can be seen that the effect of diameter over the color performance is more prominent due to the 'spiraling-in' of plotted CIE coordinates toward the white point and increased radial distance from the white point observed. For instance, the purity of color filters is highest for the nanohole resonators with the largest period due to the increased radial distance from white point i.e. nanohole resonator with period *P*=725 nm is less white compared to resonator with *P*=700 nm at *D*=400 nm. The radial distance from the white point is higher for increasing period (except at low values of period i.e. *P*=575 nm) due to the more material available yielding high reflectance for a given diameter in the reflection configuration.

4.3.2.3 Optical Simulations and analysis

Optical performance of the tapered hole nanostructures is further investigated using full wave finite-difference time-domain (FDTD) simulations. Figure 4.7 shows simulation results of nanohole resonators with *D*=300 nm and *P*=500 nm including the reflectance spectrum and the electric field distributions. The geometry used in the simulations for nanohole resonator along with reflectance spectrum is included in Figure 4.7 (a). The optical characteristics of tapered holes are also compared against perfect cylindrical nanohole geometry. It must be emphasized here that additional processing steps are required to arrive at perfect cylindrical geometries using FIB fabrication. Figure 4.7 (a) shows tapered nanoholes offer a better color purity against the cylindrical hole array with the same period and diameter. This is due to narrow band absorption of the incident light wavelengths near the resonance with the tapered holes. In contrast, the reflectance spectrum for cylindrical holes reveal a wider reflectance dip, suggesting color generation via absorption of a wide band of light wavelengths. Thus, the narrow dip in reflectance spectrum through the developed color filters refer to high quality resonance offered via nanohole geometry and leads to enhanced color purity. This narrow dip can be modulated over the entire visible spectrum via adjustment of nanhole parameters- diameter and period, which makes the approach suitable for fabrication of color filters with an extended gamut.

The narrow dip in calculated reflectance spectrum suggests a stronger mode confinement

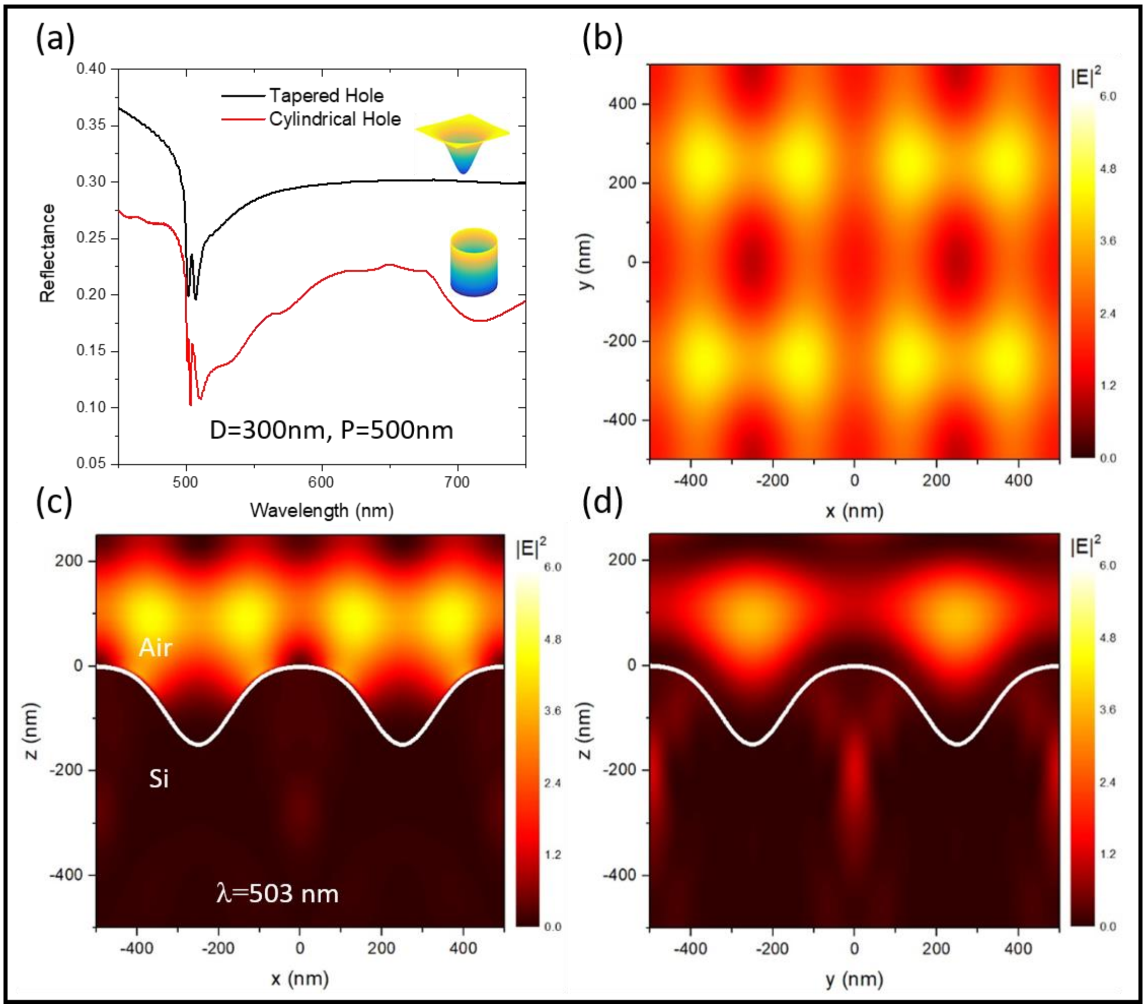

Figure 4.7: (a) FDTD simulation of reflectance through tapered nanohole array and comparison against cylindrical hole demonstrating narrow bandwidth of absorption wavelengths for enhanced color purity, the geometry used for simulations is shown in the inset. The electric field intensity ($|E|^2$) distribution of mode resonance for 2×2 array of nanoholes corresponding to nanohole array with D=300 nm and P=500 nm color filter at λ=503 nm and is shown with side view at a cross-section through nanohole (b) Top (*xy*) view at *z*=100 nm, (c) *xz* at *y*=250 nm, and (d) *yz* at x=250 nm

and offers enhanced color purity. To further investigate the resonance and light absorption phenomenon, the electric field intensity distribution for 2×2 array of nanoholes corresponding to reflectance spectrum are plotted in Figure 4.7 (b). For all the FDTD calculations, the periodic boundary conditions (PBC) were applied along the *x* and *y*-direction to account for the periodicity and perfectly matched layer (PML) along the *z*-direction to confine the simulation domain. The electric field intensity distribution is plotted at the resonant wavelength (λ=503 nm), where a dip in reflectance spectrum is observed. The distribution plot in Figure 4.7 (b) of *xy* plane at *z*=100 nm shows a large proportion of the electric field intensity over the nanohole geometry. The electric field intensity hotspots are maximum above and below the nanohole geometry, as viewed in *xz* plane through nanohole cross section at *y*=250 nm in Figure 4.7 (c), and *yz* plane at *x*=250 nm in Figure 4.7 (d) suggesting a strong confinement of the incident light. The confinement of electric fields inside and around the nanoholes in Si suppresses the reflection of light. The suppression of light wavelengths through Si nanoholes corresponds to the dip in the reflectance spectrum. Thus, the colors are observed in the bright field microscopy because of wavelength selective absorption or suppression of light wavelengths through the Si nanostructures. It can also be noted that the electric field intensity distribution hotspots are largest near the nanohole geometry, which allows each nanohole resonator to act as an individual pixel for the color generation.

The effect of varying nanohole resonator periodicities is also studied numerically. Figure 4.8 (a) shows simulated reflectance spectrum of a nanohole resonator with *D*=400 nm and period from *P*=575 nm to *P*=725 nm. Two dips are observed in reflectance spectrum, suggesting that multiple resonance modes are supported through the nanohole resonators and light is propagated along the neighbouring nanoholes. It results in absorption of light, corresponding to the dips in reflectance spectrum. This explains the color generation mechanism and suggests that the colors are being observed due to partial absorption of particular light wavelengths by the fabricated nanohole array. It can be noted that increasing periodicity of the nanohole resonator at a given diameter yields shifting of the spectrum dips towards the longer wavelengths i.e. red, similar to the experimental spectrum observed in Figure 4.4 (a).

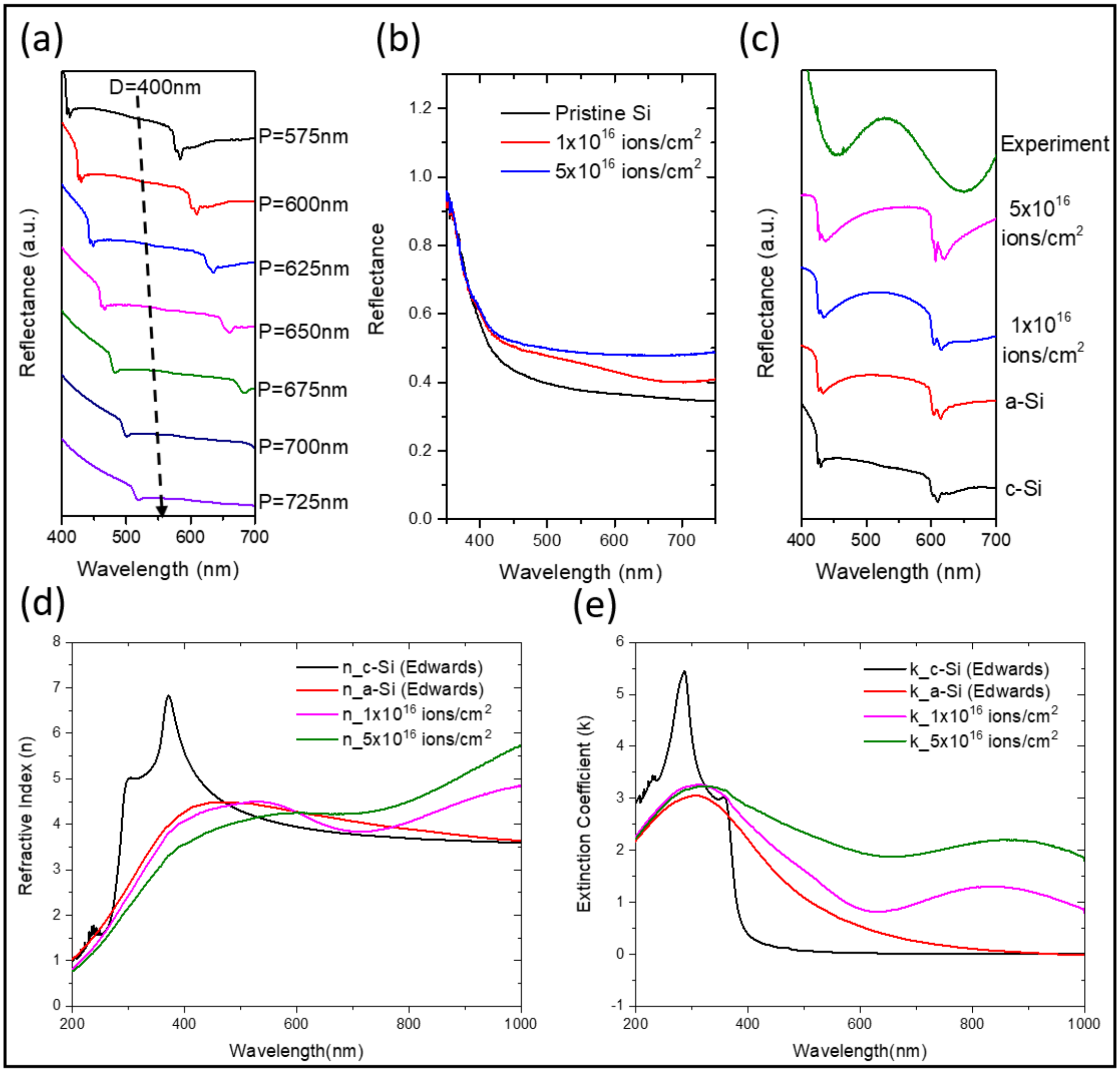

Figure 4.8: (a) Simulated reflectance spectrum for various periodicities *P* for a tapered Si resonator of diameter *D*=400 nm. (b) Reflectance measurements from ion implanted Si with doses of 1×10^{16} and 5×10^{16} ions/cm^2 and comparison against pristine Si (c) Simulations showing effect of Si amorphization on color filter: comparison of calculated reflectance spectrum for Si resonator of diameter *D*=400 nm and period *P*=600 nm against the experiment, the optical constants are set according to values from Edwards (for c-Si and a-Si) and experimental measurements for ion dose of 1×10^{16} and 5×10^{16} ions/cm^2. Experimentally measured Si optical constants- refractive index (d) and extinction coefficient (e) for ion doses of 1×10^{16} and 5×10^{16} ions/cm^2 and comparison against Si optical constants: c-Si, a-Si (60 nm film, from Edwards [131])

4.3.2.4 *Influence of FIB Induced Damage on Optical Behavior*

It is observed that the numerical results exhibit sharper resonant wavelength dips than the dips observed in the experimental reflectance spectrum. The difference between measured and simulated reflectance spectra of tapered nanohole geometries can be attributed primarily to fabrication and measurement errors. In addition, an ion beam-based material removal via sputtering action inherently damages the material, primarily due to Ga ion implantation and ion induced amorphization of Si. Such damage leads to change in properties of the processed material in the affected zones, especially the change in optical characteristics is of prime concern for this study. A controlled dose of ions by FIB was bombarded over Si to study the effect of ion induced damage to Si and its effect on the optical properties. The reflectance behaviour from ion implanted Si with controlled doses is as shown in Figure 4.8 (b). The reflectance spectrum from the ion implanted Si is obtained over the visible spectrum and compared against the reflectance behaviour from pristine c-Si. The results indicate the enhancement in reflectance with higher ion implantation dose. This behaviour can be attributed to the ion induced damage to Si, including ion implantation of gallium ions and the transition from crystalline (c-Si) to amorphous Si (a-Si) [102], [136].

To assess the optical constants and study the effect of ion induced damage on color filters, spectroscopic ellipsometry measurements are performed on ion implanted Si with doses of 1×10^{16} and 5×10^{16} ions/cm^2 over a rectangular area ($200\times200\mu m^2$). Figure 4.8 (d) and (e) show the comparison of measured optical constants (refractive index 'n' and extinction coefficient 'k') of ion implanted Si at doses of 1×10^{16} and 5×10^{16} ions/cm^2 against optical constants of c-Si and a-Si (60 nm film) from Edwards [131]. The results indicate decrease in measured values of refractive indices at shorter wavelengths and increase at longer wavelengths due to the formation of a-Si layers over c-Si. In addition, the refractive indices can be seen shifting towards higher values with increased ion dose, which may have been arising from the formation of a thicker a-Si layer over c-Si at higher doses. To study the effects of ion induced damage in Si over color filters behaviour, reflectance simulations have been performed with optical constants set according to measured values at two different ion doses and compared against reflectance spectrum with optical constants of c-Si and a-Si set according to Edwards [131]. Figure 4.8 (c) shows simulated reflectance spectrum of a color filter corresponding to D=400 nm and P=600 nm with different optical constants. These simulations reveal the effect of Si amorphization and cause of discrepancy in the simulations and experimentally observed dips in reflectance spectrum. The spectral dips in the reflectance spectrum are observed to be wider with FIB induced amorphization of Si. The extent of the ion induced damage and the corresponding changes in the optical properties of the affected region is difficult to quantify, however, the inclusion of the a-Si properties in the simulations indicate that the resonant peaks are getting wider than the dips observed with c-Si. The experimental spectrum in Figure 4.8 (c) shows much wider dips indicating larger variation in the properties of affected region than the one assumed in the simulations. The exact quantification of the change in properties is beyond the scope of the current work although an attempt has been made in that direction. This explains the variation of sharp spectral dips obtained in reflectance spectrum through FDTD simulations in contrast to the dips observed in experimentally measured reflectance spectrum. To notice the effect of Si amorphization on color filtering performance, the chromaticity coordinates corresponding to reflectance spectrums in Figure 4.8 (c) are calculated, which show that the amorphization of Si yields improved radial distance of chromaticity coordinates from white point on color space with ion beam induced Si amorphization. Thus, the presence of a-Si layer over c-Si due to ion beam processing characteristics lead to widening of reflectance dips in the visible spectrum of fabricated filters because of the improved optical constants of Si.

4.3.3 Physical Characterization of Nanostructures

The fabricated nanohole array have been further characterized physically with SEM and atomic force microscopic (AFM) imaging as shown in Figure 4.9 (a). The cross-sectional SEM images reveal the unique geometry of tapered nanohole resonator array used for coloring. The nanohole resonators are seen to increase in depth with diameter, as expected, due to increase in extra depth being milled away as a function of increased dwell time used for fabrication of larger diameter nanohole resonators. The aspect ratio of the holes is found

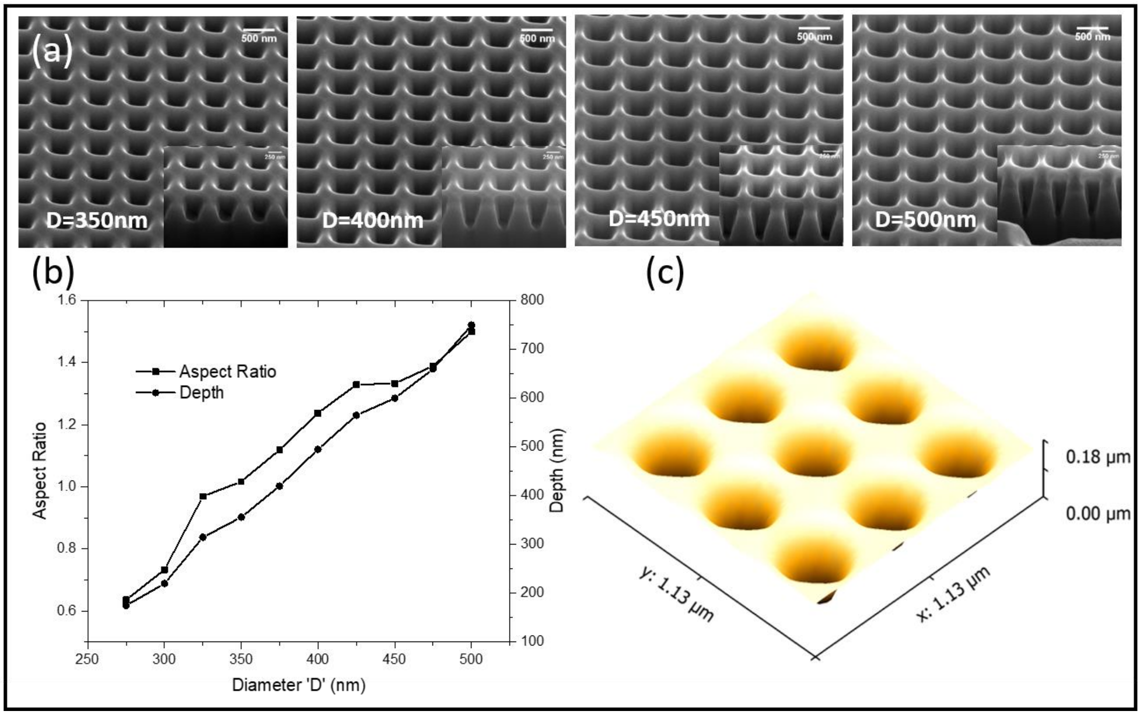

Figure 4.9: (a) SEM images of fabricated color filter arrays with diameter D= 350, 400, 450, and 500 nm with scale bar of 500 nm, inset in each image include SEM image (scale bar 250 nm) of FIB cu cross-section. (b) Aspect ratio, depth as a function of nanohole diameter. (c) Representative AFM image of 3×3 array of nanoholes

to vary between 0.6 and 1.5, suggesting low aspect ratio nanostructures fabricated with FIB. The nanohole resonator depth determined from cross-sectional SEM images and aspect ratio are plotted as a function of nanohole diameter in Figure 4.9 (b), both of which show an upward trend with increasing diameter. The physical characterization reveals the excellent fabrication control, with which nanohole array can written for coloring with FIB. This is further illustrated in Figure 4.9 (c) showing a representative AFM image of a 3×3 array of Si nanoholes with D= 350 nm. The structural characterization also accounts for the difference found in the outcome of FDTD calculations and experimental measurements.

4.3.4 Color printing Applications

The color printing applications through period and diameter tuning of fabricated holes are further demonstrated. Butterflies are a great example of structural color filtering found in nature through the morphological features in their wings [137]. Butterfly patterns are fabricated on Si as shown in Figure 4.10. It includes normal incidence SEM image of fabricated butterfly along with the corresponding bright field optical microscopic image. The wings of butterfly are patterned with tapered nanoholes as its building blocks, shown through magnified SEM image of butterfly in Figure 4.10 (b) and butterfly wing in Figure 4.10 (c). The period and diameter of fabricated holes are varied to obtain a variety of colors from the butterfly wings. Figure 4.10 (d) shows multicolor generation through the wings of fabricated butterflies captured via bright field microscopy imaging in an optical microscope. A Kangaroo, comprised of FIB fabricated nanoholes (shown via magnified

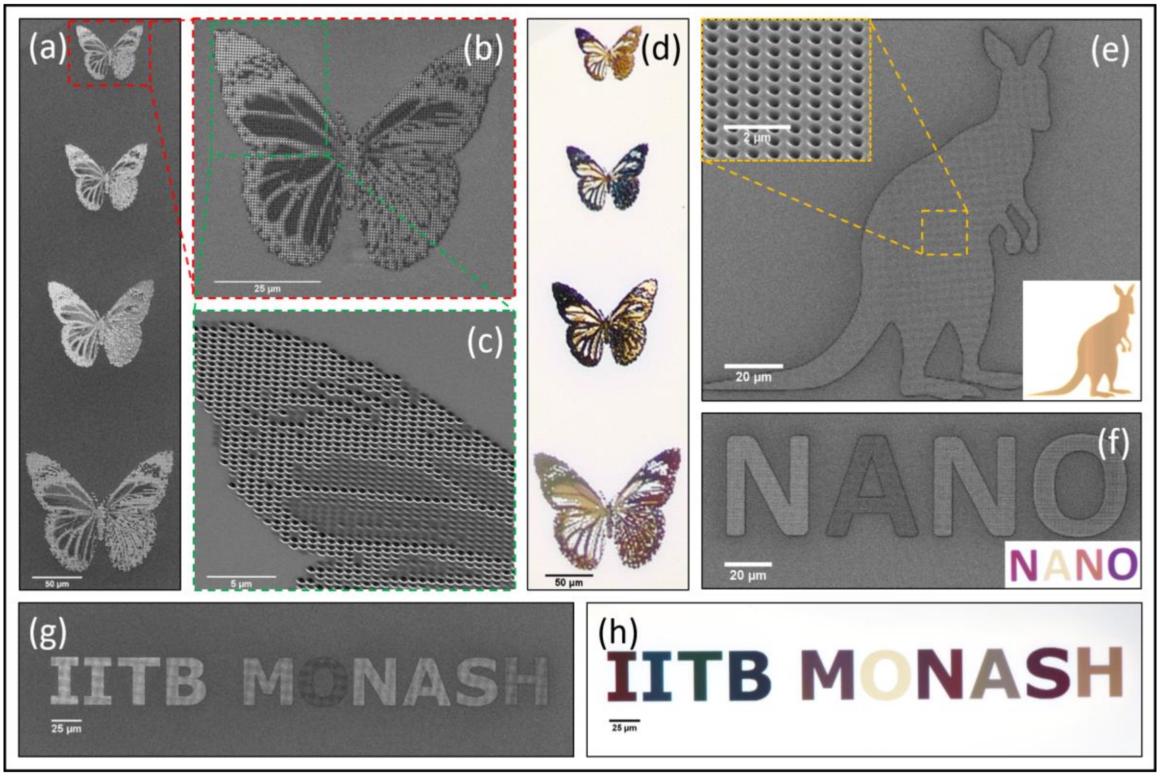

Figure 4.10: Demonstration of color filtering application: Butterfly patterns fabricated on Si as shown in (a)-(c) SEM images and (d) Optical image showing multicolor generation through fabricated butterfly wings. (e) SEM image of a Kangaroo and corresponding optical microscopic image, (f)-(h) Multicolor letters printing through fabrication of alphabets on Si, with (f), (g) Normal incidence SEM images, and (h) Corresponding bright field optical microscopic images

SEM image in top left inset) including corresponding optical microscopic image in bottom right inset, fabricated on Si is shown in Figure 4.10 through SEM image. For another demonstration, alphabets are printed on Si and as shown in Figure 4.10 (f)-(h) including normal incidence SEM image of the fabricated letters on Si and corresponding bright field microscopic image under normal illumination of light. The optical microscopic image in Figure 4.10 (h) show different colors arising from each letter due to selective wavelength absorption and resonant scattering of light depending on nanohole period and diameter. The results indicate the potential of proposed fabrication method to pattern tapered nanohole arrays for color printing applications at micro-scale. The proposed method offers flexibility in terms of use of different FIB apertures, which in turn controls ion beam current for milling. In the experiments, an ion beam current of 1 nA was employed. For example, a period of approximately 500 nm, corresponds to 50,000 dots per inch (DPI), which can be further improved via smaller hole diameter milled using smaller FIB aperture i.e. smaller ion beam current. The resolution of 100,000 DPI roughly amounts to a pixel size of 250 nm, which is achievable given the high resolution of FIB. With the developed technique, the color printing is possible beyond the diffraction limit of an optical microscope and colors at a resolution of ~100,000 DPI can be generated by selecting a lower pixel size and beam current. The developed fabrication approach can be further scaled up in combination with nano-imprint lithography for high throughput and low-cost printing applications.

4.4 Summary

A single-step direct, mask-less novel approach for fabrication of structural color filters by FIB was demonstrated. The proposed color filters are based on an array of unique tapered nanohole geometry. The tapered geometry is attained by utilizing Gaussian nature of focused ion beam. The color filters were fabricated on high index and low-loss Si, without requiring any sample preparation or deposition of thin films in contrast to previously reported color filters. Optical properties of fabricated color filters were studied and explained with experimental and simulation calculations on reflectance. FIB induced damage in Si is assessed with spectroscopic ellipsometry was found to be the reason behind the widening of reflectance dips observed experimentally against the sharp dips observed through optical simulations. The fabricated nanohole geometry can be tuned adjusting FIB process parameters and thus, the colors generated from nanoholes can be tuned across visible spectrum. The demonstrated fabrication approach facilitated enhanced color purity via wavelength selective absorption over a narrow wavelength window and is useful for producing variety of colors. A wide color palette was fabricated, and color generation was experimentally verified through the observation of fabricated color filters on CIE 1931 color space. The larger diameter nanoholes resulted in red-shift of dip position in reflectance spectrum, while the decreasing period resulted in blue-shift of the spectral dip. The results are promising, and color printing applications were demonstrated via fabrication of real-world structures like butterfly wings and alphabets on larger scale. The use of FIB for coloring, in addition to its existing versatile applications range in material science, is an important step forward towards the integration of FIB with structural color filtering applications. The rapid and versatile nature of developed fabrication technique along with the robustness of fabricated color filters will facilitate wide applications ranging from high resolution color printing applications to optical security features.

Chapter 5. Weaving Nanostructures with Site-Specific Ion Irradiation Induced Bidirectional Bending

Site-specific ion-irradiation is a promising tool fostering strain-engineering of freestanding nanostructures to realize 3D configurations towards various functionalities. In this study, a novel-approach for fabricating freestanding silicon 3D nanostructures by precisely controlling chemical-etching using low-dose ion implantation patterns is developed first. The fabricated nanostructures are then deformed by varying the local-irradiation of kiloelectronvolt gallium ions. It has been demonstrated that by tuning the ion-dose, energy, bidirectional bending and various configurations can be realized for new functional 3D nanostructures. Computational results show the spatial-distribution of implanted-ions, dislocated-atoms, have potentially contributed to the local development of stresses. High-resolution electron microscopy investigations confirm the formation of distinguishable ion-irradiated/un-irradiated regions, while the smoothened morphology of the irradiated-surface suggested the bending is also coupled with sputtering at higher ion-doses. The nanostructure bending effects associated with local ion-irradiations in contrast to global ion-irradiations are presented, with the detailed mechanisms elucidated. Finally, weaving of 3D nanostructures is demonstrated through strain engineering for new artefacts including ultra-long fully-bent nanowires, nano-hook and nano-mesh. Aligned growth of bacterial-cells has been observed on the ultra-long Si-nanowires, and a mesh-based "bacterial-trap" for site-specific capture of bacterial-cells is demonstrated, emphasizing versatile nature of the approach.

5.1 Introduction

Energetic ion induced irradiations and implantation are used extensively for doping and inducing functionalities in the nanostructures for desired applications [138], [139]. Nanostructures exhibit unusual transformations under ion induced irradiations, due to the nanostructure dimensions comparable to collision cascade in contrast to their bulk counterparts [138], providing extended functionality in the nanotechnology domain [140], [141]. The mesoscopic properties of these nanostructures under ion irradiations, in addition to the quantum size effects, are governed by the surface effects due to their high surface-to-volume ratio. The interplay among the size, shape, and composition of nanostructures, in addition to the ion species used, governs the physical and chemical characteristics. Mechanical properties such as tensile and compressive stresses can be developed in the lattice atoms under ion irradiations, which induces plastic deformation of nanostructures [142], [143].

The ion-induced plastic deformation is considered as a combined effect of ion implantation, defect formation, vacancy and interstitial generation; and ion irradiations have been demonstrated for tailoring of carbon nanotubes [57], cantilevers [144], semiconductor nanowires (NWs) [145], plasmonic nanostructures [146], 3D and thin film origami nanostructures [59], [147] etc. The irradiation and implantation of ions, depending on the balance between the damage formation and annihilation due to thermal spike, recombination rates [148], can produce stresses of the order of several GPa [149]. Through controlled dose from the ion beam, NWs can be aligned in different orientations towards the beam at enough ion doses. In addition, surface charging effects during ion irradiations result in electrostatic forces, which induce the bending in the direction opposite to the incident ion beam [150]. Ion-induced amorphization and recrystallization is also considered to play an important role during plastic deformation, and bending was demonstrated to occur in the regions which were fully amorphized [151]. Other phenomena are known to occur during ion irradiation, such as void induced stress generation, dynamic annealing of ion-induced defects [152], the formation of interstitial clusters beyond the collision cascade [153] and atomic mass transport [154]. These effects and plastic deformation rely heavily on the ion beam parameters such as energy, ion mass, ion dose, etc., and target properties such as geometry, composition, crystallinity, temperature etc. Nanostructures also exhibit improved sputtering and dynamic annealing of defects in contrast to their bulk counterparts. Thus, the ion induced irradiation and manipulation of nanostructures become important to investigate the underlying mechanisms and cultivating anticipated functionalities.

A novel method for fabrication of functional 3D nanostructures through (1) wet etching of ion implanted silicon (Si) for freestanding nanostructures and (2) ion induced *in-situ* 3D deformation of the nanostructure is developed. To investigate the fundamental mechanisms, focused ion beam (FIB) equipped with a liquid gallium source was employed for *in-situ* bending of the Si nanowires (NWs), which have been fabricated through the proposed combined implantation/wet etching approach. Observation of bidirectional bending of these NWs: i.e. initially bending away and bending towards the ion beam at increased ion dose during successive time intervals, inspires controlled weaving and strain engineering of nanostructures for the realization of advanced 3D nanostructures for desired functionalities. The underlying physics and site-specific ion-induced bending mechanism of Si NWs are investigated through both experimental and computational studies, to provide new insights for controlling nanostructures *in-situ*.

5.2 Experiments and Simulations

5.2.1 FIB Implantation Experiments

Single crystalline (<100>), p-doped Si 10 mm × 5 mm pre-cut chips from 4-inch Si wafer (Ted Pella Inc., Product 16008) were used in this work for FIB implantation and etching experiments. The Si chips were cleaned with conventional cleaning (Isopropyl alcohol and Acetone) to make sure the cleanliness and remove the contaminants if any. The implantation was carried out using FIB with a gallium (Ga) ion source on a FIB/SEM system (FEI Quanta 3D system, Thermo Fisher, USA). The samples were placed at a eucentric height and Ga ion implantation was done at normal incidence. For fabrication of NWs, patterns with an optimized ion dose (2×10^{16} ions/cm^2), and a beam current 10 pA with a beam overlap of 50% were used. To fabricate the suspended NW, two rectangles contacting the NWs were implanted with a sufficiently high ion-beam dose to ensure these areas (contact pads) do not get etched. This way, the NWs are found to be comparatively straight against the NWs fabricated on a single contact pad, which bend due to the unavailability of any support at the other end. For suspended nanostructures, specifically designed grayscale bitmap patterns were used for ion implantation. All the implantation experiments were carried out at an acceleration voltage of 30 kV.

5.2.2 Anisotropic Wet Etching

Etching of Si was carried out with 1.5 mol/L potassium hydroxide (KOH) solution. The KOH solution was prepared by dissolving commercially available KOH pallets (Sigma Aldrich Product Number 221473) in deionized (DI) water. The ion implanted substrates were left in the prepared KOH etchant solution for 3 hrs at room temperature for etching to take place. The etching time was determined from multiple experiments to allow enough etching to obtain fully suspended nanowires/structures. The etching was stopped by removing the substrates from the container and rinsing with DI water twice. The substrates were then placed in an ultrasonic bath in DI water for 1 min prior to drying in an oven at 50°C for 1 min. The use of an N_2 gun for drying the substrate was avoided to suppress any possibility of bending/fracture of nanowires.

5.2.3 *In-situ* Ion Induced Bending

Suspended Si NWs prepared through the implantation followed by wet etching were used for *in-situ* bending experiments in the dual beam FEI Quanta 3D system. The suspended NWs on two contact pads were first cut by ion beam of 1.5 pA current, to produce freestanding NWs for bending experiments. The NW cutting was carried out using a single pixel width line and beam overlap of 50%. No observable bending occurred with the optimized cutting conditions. Site-specific ion-induced bending was employed irradiating a rectangular pattern of dimensions $0.5 \times 0.5\ \mu m^2$ perpendicular to NW length i.e. FIB incidence angle was kept at 90 degrees, unless specified. The rectangular patterns were chosen to be sufficiently larger than NW to avoid any misalignment of ion-beam. Ion dose was varied by controlling the exposure time or several passes, with a constant dwell time of 1 µs, current 1.5 pA, and beam overlap of 50%. Three acceleration voltages high-30 kV, medium-16 kV, and low-2 kV were employed for the bending experiments.

5.2.4 Monte Carlo Simulations

Ion-material interactions, including Ga implantation, atomic displacements, point defects (vacancies and interstitials) formation, are simulated to study the ion-induced bending phenomenon. Monte Carlo (MC) simulations were performed with software package Stopping and Range of Ions in Matter (SRIM) [155] based on binary collision approximations. Monolayer with typical values, threshold displacement energy 15 eV and density 2.32 g/cm^3, was employed for a 100 nm thick Si target. MC calculations are performed at high-30 kV, medium-16 kV, and low-2 kV acceleration voltages to illustrate the bending phenomenon.

5.2.5 TEM Imaging and Characterization

Si NW samples for Transmission Electron Microscopy (TEM) were prepared using FIB lift-out technique using a Kleindiek micromanipulator (Model MM3A-EM) and platinum gas injection system (Pt GIS) equipped with the FIB/SEM system. The NWs fabricated over Si substrate were first welded to the micromanipulator tip with Pt, and the other end of the NW was then cut with FIB, to lift-out the NW from the substrate. The NWs were subsequently transferred and welded to copper lift-out TEM grids (Ted Pella, product 460-204). Exposure to ion beam during imaging was kept to a minimum to avoid unintentional damage and bending of the NWs during transfer. The NW, after transferring to TEM grid, was exposed to FIB at two locations to get bent NW for nanostructural characterizations. TEM imaging of the samples was carried out on a FEG-S/TEM (CM20 FEG-S/TEM, Thermo Fisher, USA) operating at 200 kV.

5.2.6 Cell Sample Preparation and Trapping

The cell samples were first sub-cultured from commercial strain ATCC 13883 and 35218 on agar plates as detailed in previous studies [156], [157]. If fixation is required, the cells were fixed with 2.5% glutaraldehyde in phosphate-buffered saline (PBS) for 1 hr. The cell samples were then rinsed three times with distilled water and stored in 4° C refrigerator. Prior to experiments, the cells in suspension were pipetted to glass slides and confirmed by light microscope. For cell trapping experiment, a droplet of bacterial cells was then pipetted in 45 degrees to the Si wafer surface with the fabricated traps, and the liquid was removed immediately by blotting with filter paper (Waterman blotting paper).

5.3 Results and Discussion

Ion implantation with an ion beam can be used for 3D freeform micro/nanofabrication in conjunction with wet chemical etching. A two-step nanofabrication method utilizing combination of ion implantation and KOH wet etching is shown schematically in Figure 5.1 for fabrication of micro/nanostructures. In the first step, Ga ions in a FIB have been used for ion implantation in Si with a nanometer resolution. The precise nature of ion beam scanning in a FIB enable complex pattern writing for fabrication of various nanostructures. The ion implanted Si is immersed in KOH solution for wet etching in the second step, which enable bulk removal of un-implanted Si. The bulk structuration of Si substrate, based on the implantation design and area, allows fabrication of various functional and 3D micro/nanostructures such as suspended nanostructures, pyramids, nano-trumpets etc. on Si substrate. In this work, a 3D freeform nanofabrication technique for various functional micro/nanostructures is developed by controlling ion implantation through FIB.

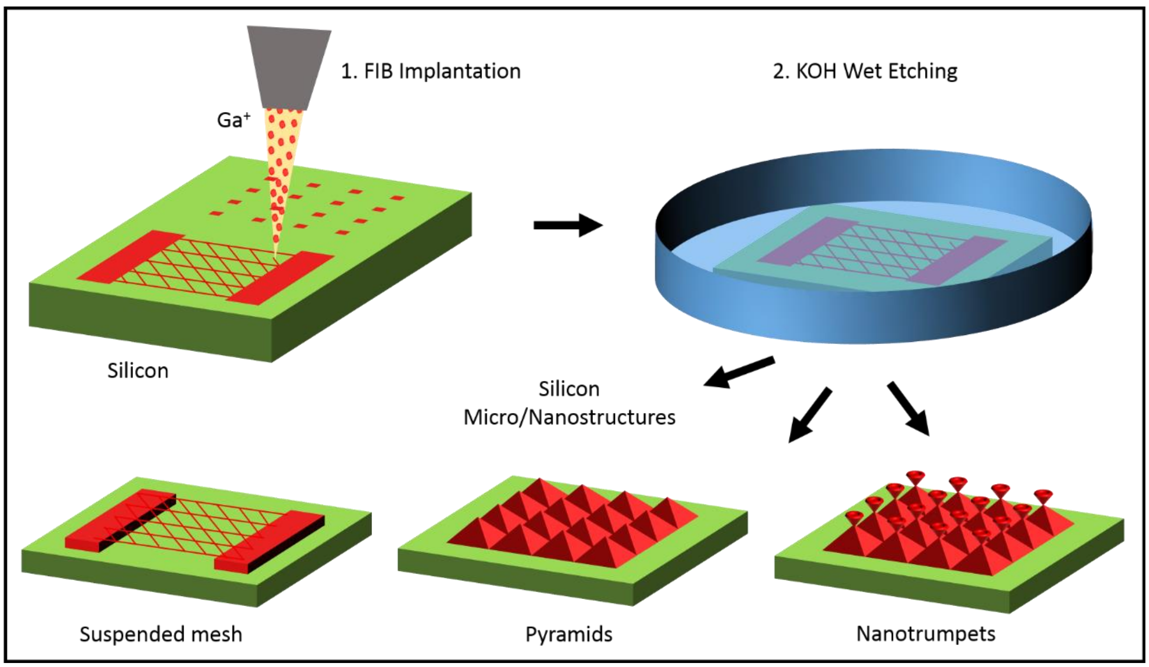

Figure 5.1: Fabrication schematic of 3D freeform micro/nanostructures with ion beam through bulk structuration of Si: Implantation in Si through a Ga focused ion beam and masks writing with a nanometer resolution. Subsequent anisotropic wet etching in KOH solution and fabrication of Si nanostructures via selective removal of un-implanted region

5.3.1 Dose Dependence

The Ga ions undergo electronic and nuclear stopping through collisions with electrons and Si nuclei before coming to rest. Due to these collisions, few Si atoms are ejected from their lattice positions as primary knock on atoms, if the energy transferred through Ga ions is more than displacement energy of Si (~15 eV [158]), and create a Frenkel pair. These primary knock on atoms leave the vacancies at their original lattice position, can further interact with lattice atoms and produce a cascade of atomic displacements, before forming an interstitial atom. Thus, a single Ga ion develops a complete collision cascade, forming point defects (vacancies and interstitials) and Ga implantation in the crystal lattice. The amorphization of Si under ion irradiation occurs when the free energy of the damaged crystalline phase gets higher than the amorphous phase [148]. Ion irradiation induced amorphization occurs near the collision cascade, where most of the ions are implanted. Prolonged exposure of Si to ion irradiations increases the thickness of the generated amorphous layer to a certain extent, which is however, limited by further sputtering of surface atoms by incident ion beam. Si shows anisotropic etching behavior against alkaline etchants [159]. The etching rate of <111> plane is smaller due to the difference in binding energy and availability of only one dangling bond per Si atom, in contrast to other crystallographic directions, which have more dangling bonds; and a smaller number of bonds breaking is required for etching to take place. Si, when doped with a sufficiently high concentration (~10^{19} ions/cm^3) [160] of p-type dopants, can act as a mask against chemical etchants [161]. Ga ion implantation, which is a p-type dopant in crystalline Si (c-Si), leads to the ion implantation and formation of amorphous Si (a-Si), inducing the corrosion resistance against alkaline solutions, such as KOH [160]–[163] etc. The surface chemistry of Si in alkaline KOH solution has been investigated through secondary ion mass spectroscopy (SIMS) and X-ray photoelectron spectroscopy (XPS), and the formation of a thin layer of gallium oxide (GaO_x <1 nm) at the surface was ascribed to the lower etch rate of implanted Si [164].

To investigate the critical ion dose required for the etch stop effect of Ga implanted Si, annular regions with varying ion dose of 1×10^{12} - 5×10^{16} ions/cm^2 and ion beam current of

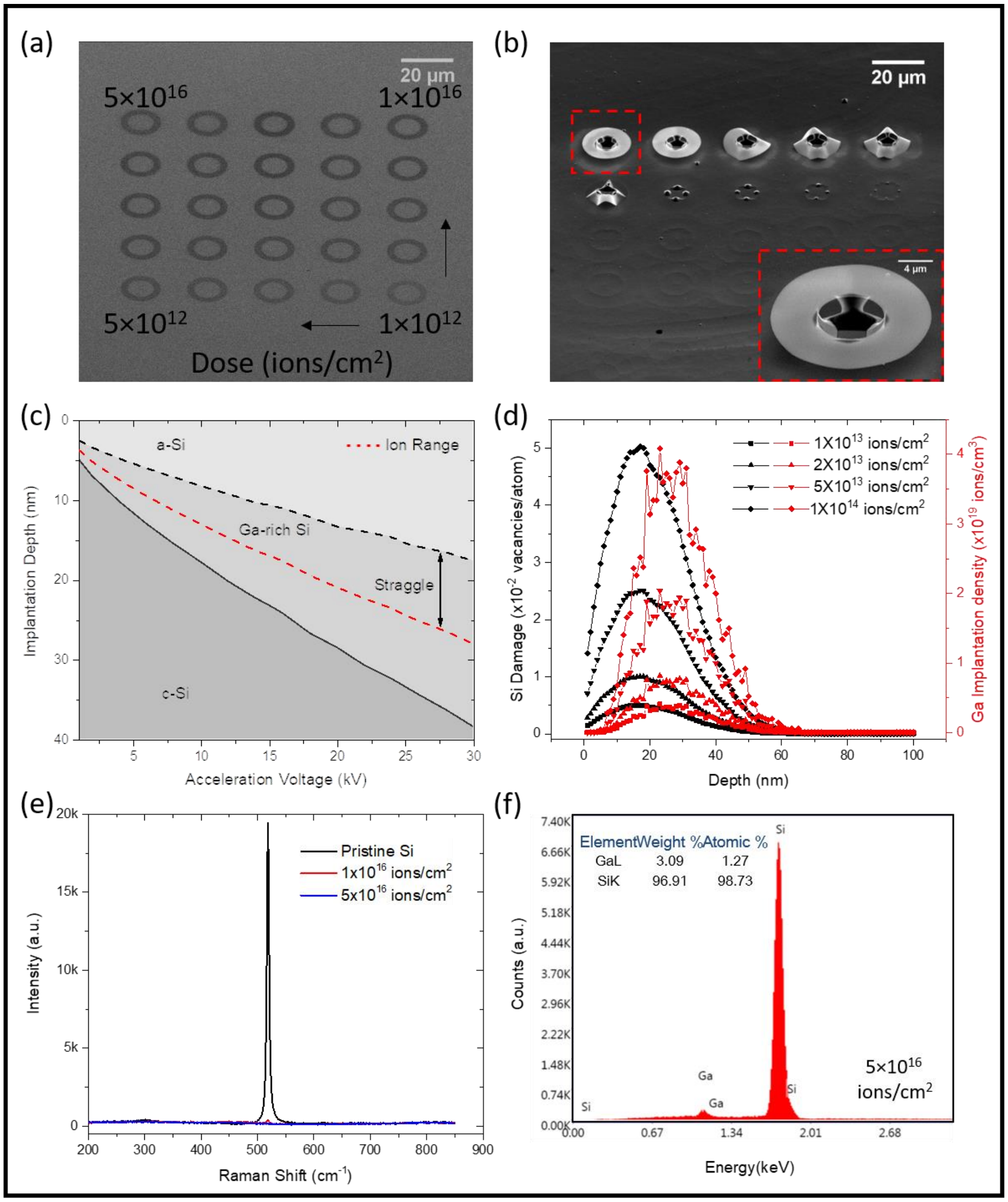

Figure 5.2: Gallium implantation in Si: SEM image of (a) A 5×5 array of annular ring FIB implantation in Si at ion doses of 1×10^{12}-5×10^{16} ions/cm^2, (b) After wet etching, inset shows the magnified SEM image of the annular ring implanted with 5×10^{16} ions/cm^2. Simulation results: (c) Effect of acceleration voltage on implantation depth, (d) Calculated Si damage profiles and Gallium ion distribution for ion doses of 1×10^{13}, 2×10^{13}, 5×10^{13}, and 1×10^{14} ions/cm^2 at 30 kV; (e) Raman spectroscopy, and (f) Energy dispersive spectroscopy (EDS) of ion implanted Si

10 pA were implanted in Si as shown through SEM image in Figure 5.2 (a), where a 5×5 array of annular regions implanted in Si are included. The annular regions with ion dose above 1×10^{13} ions/cm^2 were exhibited to have etching resistance against alkaline KOH solution, however, only the annular regions with ion dose above 4×10^{16} ions/cm^2 were exhibited to achieve completely freestanding Si regions. This is evident from the SEM image of the annular rings after wet etching shown in Figure 5.2 (b), the inset of which shows the magnified SEM image of the annular ring implanted with 5×10^{16} ions/cm^2 having a freestanding Si which has been under-etched. The SRIM simulated implantation depth of Ga ions at 30 kV in Si yields a mean value of 27 nm with one standard deviation of 10 nm as straggle. The effect of acceleration voltage on implantation depth in Si is shown in Figure 5.2 (c). The straggle length of implantation is used for approximation of a-Si and Ga implantation rich layer [165], and the simulations at 30 kV show formation of ~17 nm a-Si to the top due to the implantation damage and next 20 nm as Ga rich amorphous Si. To observe the effect of ion dose on Si damage and Ga implantation density, calculated Si damage profiles and Gallium ion distribution for ion doses of 1×10^{13}-1×10^{14} ions/cm^2 at 30 kV are shown in Figure 5.2 (d). From Figure 5.2 (d), it is observed that ion dose ~2×10^{13} ions/cm^2 yields a sufficiently high Ga implantation density (~10^{19} ions/cm^3) [160] required for the masking effect, which is closer to the dose value (~1×10^{13} ions/cm^2) observed from the dose optimization results in Figure 5.2 (b). It is, however, important to note that only the ion dose above 4×10^{16} ions/cm^2 can result in freestanding Si regions after wet etching for prolonged duration (3 hours at room temperature). To further consolidate the formation of a-Si and characterization of ion induced damage, Raman spectroscopy, and energy dispersive spectroscopy (EDS) of ion implanted Si are presented in Figure 5.2 (e), (f) respectively. The Raman spectroscopy results at ion doses of ~1×10^{16} ions/cm^2 show transition of c-Si to a-Si, evitable from the absence of Raman peak at 521 cm^{-1}. The EDS results identify the Ga implantation in Si (~3 weight %) at ion dose of 5×10^{16} ions/cm^2. Having gained an insight of the process and dose optimization, the Ga implantation is further utilized for fabrication of suspended and freeform Si micro/nanostructures.

5.3.2 Fabrication of Suspended Micro/Nanostructures

Fabrication of suspended Si nanostructures was facilitated by FIB assisted implantation and wet chemical bulk structuration. Improved etching resistance of FIB induced amorphous Si (a-Si) in contrast to crystalline Si (c-Si) is employed as a mask and the Si nanostructures are fabricated in a top-down manner. Figure 5.3 (a) displays the SEM image of FIB line implantation profile over two parallel rectangles with a comparatively higher implantation dose. The rectangles implanted with a higher ion dose work as contact pads to expedite the fabrication of suspended NWs on a Si substrate. The inset in Figure 5.3 (a) also includes a high magnification SEM image of FIB line implantation profile. The wet etching of FIB implanted Si substrate with KOH solution leads to the development of Si NWs, which are suspended over two parallel rectangles as shown through SEM image in Figure 5.3 (b). A representative SEM image of fabricated Si NWs with a typical diameter/width of 100 nm through bulk structuration of Si is shown in the inset of Figure 5.3 (b). The technique can be employed for realization of ultra-high aspect ratio suspended NWs. Si NWs down to ~31 nm were realized with 1.5 pA beam current as shown in through the SEM image in Figure 5.3 (c). An array of NWs was fabricated with increasing line dose of 1×10^{10}-25×10^{10} ions/cm and ion beam currents of 1.5 pA and 10 pA to investigate the effects of ion dose and current on NW width. Figure 5.3 (d) shows the evolution of NW width plotted against line dose at 1.5 pA and 10 pA. The fabricated NWs are shown to exhibit increasing width with ion implanted line dose, in addition to the increasing beam current. This provides the dimensional control of fabricated NWs and desired NW width down to ~31 nm can be realized by appropriate choice of the fabrication parameters. These Si NWs, realized through combination of ion implantation and chemical etching, can be further extended to realize various suspended mesh structures for potential filtering and trapping applications [12]. Figure 5.3 (e) and (f) show SEM images of suspended rectangular and circular mesh respectively as a demonstration. Such suspended mesh structures realized through the developed fabrication approach are tunable and can be designed for desired pore opening and selective trapping of micron sized particles, bacteria etc.

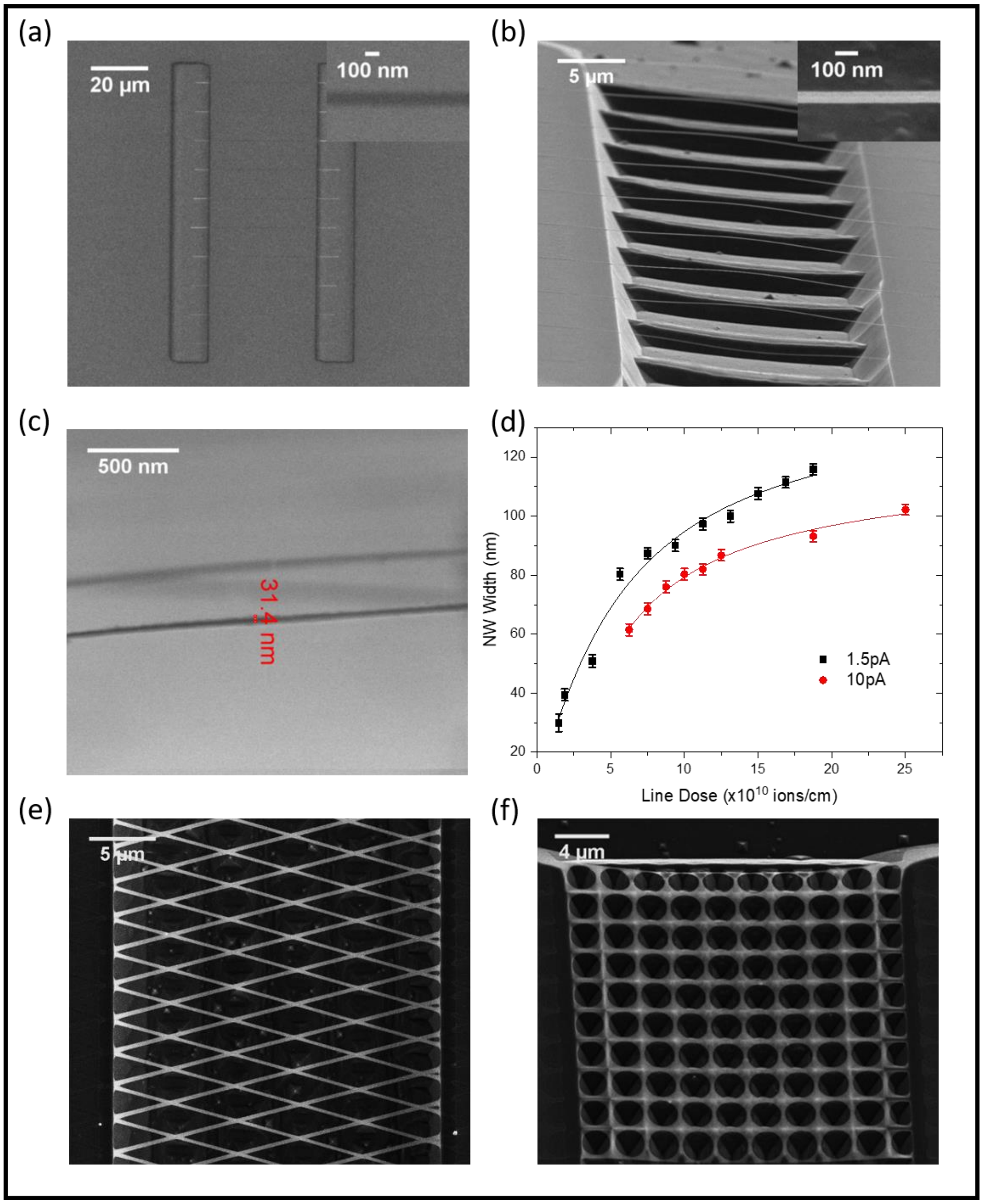

Figure 5.3: Fabrication of suspended Si NWs: SEM image showing (a) FIB implanted line over two contact pads, inset includes a high magnification SEM image showing the typical line implantation; (b) Fabricated high aspect ratio (~625) suspended Si nanowires with length ~25 µm, inset shows a high magnification SEM image of the NW, (c) A high magnification SEM image of a Si NW, with width down to ~31 nm, (d) Evolution of NW width against implantation line dose at 1.5, 10 pA beam current; SEM images of fabricated suspended Si: (e) Rectangular, (f) Circular mesh

5.3.3 Fabrication of Freeform 3D Micro/Nanostructures

The developed nanofabrication approach can be employed further for fabrication of exotic 3D freeform and suspended nanostructures for desired functionalities and potential

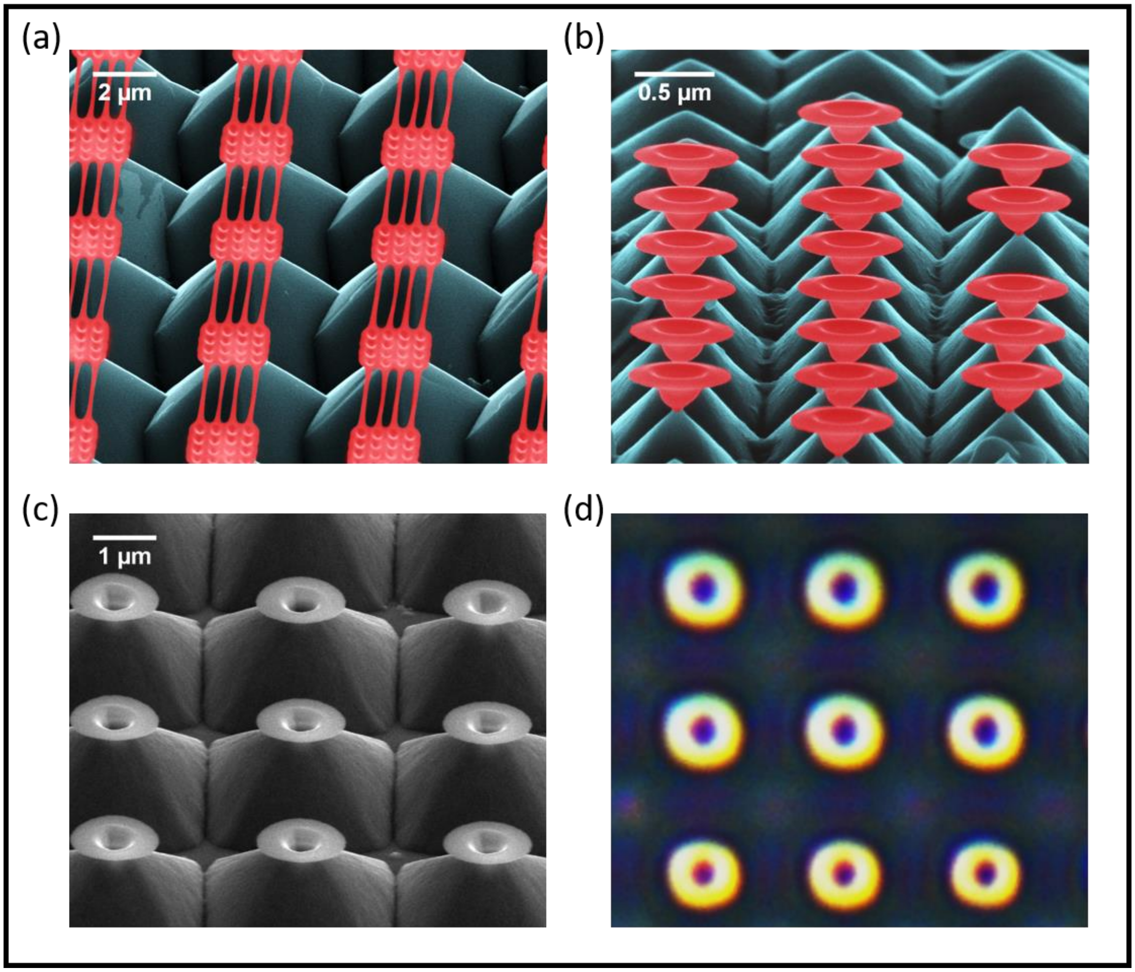

Figure 5.4: Freeform 3D nanostructures: (a) SEM image (false colored) of nano-trumpet array connected through NWs, (b) Freeform fabrication of nano-trumpet geometry over the pyramids, (c) SEM image of engineered nano-trumpets for multicolor generation, (d) Bright field optical microscopic image demonstrating generation of yellow color through the nano-trumpets

applications. Figure 5.4 shows few fabricated freeform 3D Si nanostructures utilizing ion implantation and wet etching of Si. A false color SEM image of an array of Si nano-trumpets connected through Si NWs is shown in Figure 5.4 (a), which are suspended over pyramid array. Figure 5.4 (b) shows freeform fabrication of nano-trumpet geometry over the pyramid array through false colored SEM image. The nano-trumpets are realized through dot implantation, milling and a replica of incoming ion beam profile. Such nano-trumpets, if etched for prolonged duration due to Si under-etching. Such exotic freeform nanoscale structures can be designed for desired functionality and have a potential for various applications in diverse field of nanotechnology. The fabricated nanostructures can be engineered for multicolor generation through control of ion implantation and etching parameters. SEM image in Figure 5.4 (c) shows engineered nano-trumpets for multicolor generation. Figure 5.4 (d) shows bright field optical microscopic image demonstrating the generation of yellow color through nano-trumpets. The freeform geometry of nano-trumpets enables wavelength selective absorption of incident visible light, and colors are generated through reflection of particular wavelengths of light.

5.3.4 Controlled Manipulation of Nanostructures

The fabricated suspended Si NWs demonstrate high fidelity and the technique can be employed for realization of ultra-long aspect ratio suspended NWs for controlled manipulation of nanostructures offering a variety of 3D configurations, extending the FIB nanofabrication capabilities. Si NWs fabricated with FIB implantation and wet chemical etching are utilized for *in-situ* FIB induced bending experiments. Si NWs suspended on two contact pads are cut with FIB to allow the realization of NWs freestanding at one end and clamped to the contact pad at their base to study the bending phenomenon.

Figure 5.5 shows a false-colored composite image of Si NW obtained through a series of representative SEM images acquired at successive time-intervals during 30 kV Ga ion-beam irradiations with increasing dose. The ion beam is incident along the vertical direction as indicated through an arrow in Figure 5.5 and the irradiated sites are away from the NW free end. Initially, the NW starts to bend in the downward direction, i.e. in the direction away from the beam incidence. With the ion dose increased beyond a certain threshold, the NW starts bending in the upward direction. Finally, the NW aligns itself in the vertical direction, i.e. along the direction of beam incidence. The geometry of the bent NW does not change after the ion beam irradiation is stopped, suggesting the NW underwent plastic deformation in the irradiated region. The bidirectional nature of the bending, induced through ion beam dose, provides an additional degree of freedom and can

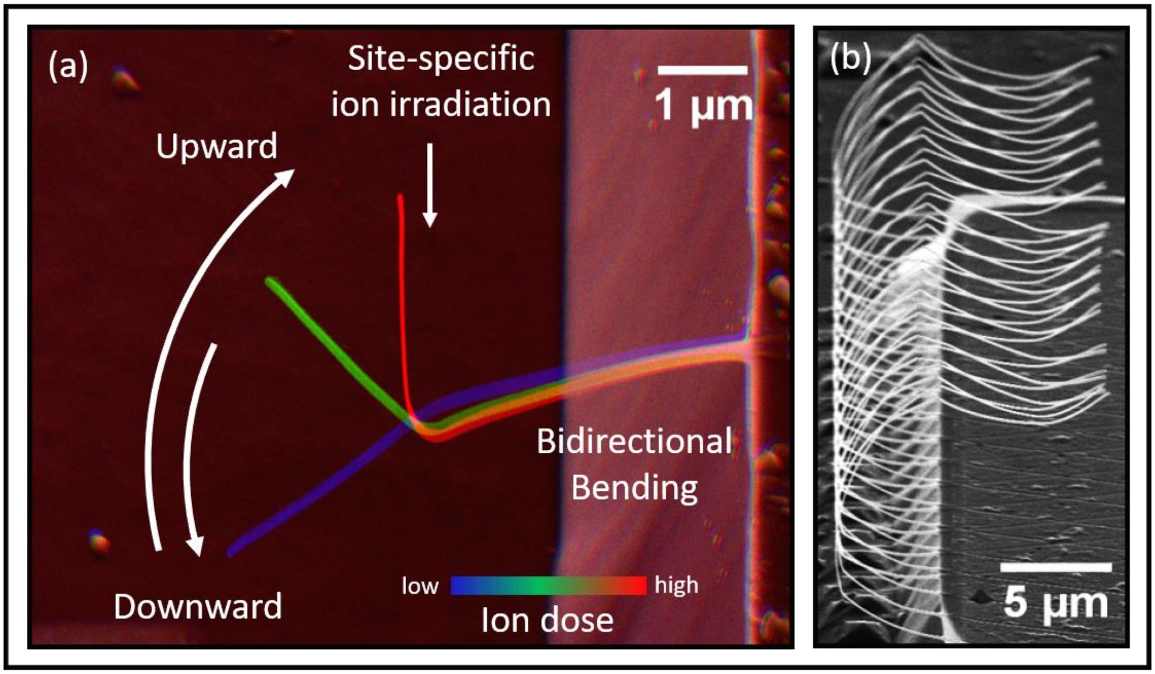

Figure 5.5: Ion-induced site-specific bidirectional bending: (a) A composite SEM image showing the evolution of Si NW with increasing ion dose obtained through a series of representative SEM images acquired at successive time-intervals during Ga ion irradiations in a FIB. Initially, the NW bends in the downward direction and eventually aligns towards the incoming Ga ions, (b) SEM image of a typical 3D mesh structure obtained via nanostructure weaving through ion-induced bidirectional bending

be employed for controlled manipulation of nanostructures offering a variety of 3D configurations, extending the nanofabrication capabilities of ion beams. A typical 3D Si mesh structure obtained via nanostructure weaving through ion-induced bidirectional bending is depicted in Figure 5.5 (b) SEM image. The bending experienced by the nanostructures during *in-situ* FIB irradiations must be a consequence of the stresses originating from the volume change due to implanted ions, and defect clusters in the Si lattice from a physical point of view. The development of such stresses in the lattice can generate a net bending moment, which will, in turn, lead to bending of the nanostructures. The location of these developed stresses with respect to the NW neutral axis, in principle,

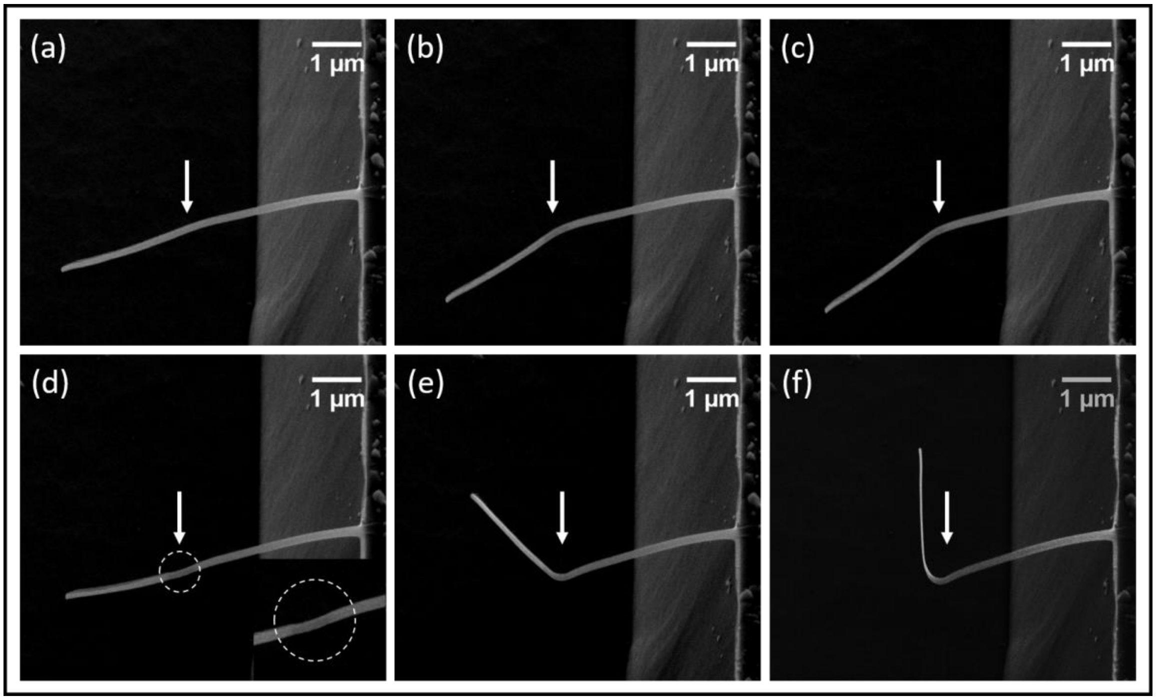

Figure 5.6: A series of representative SEM images acquired at successive time-intervals at 30 kV and ion dose of (a) 3.4×10^{14}, (b) 5.2×10^{14}, (c) 6.9×10^{14}, (d) 1.7×10^{15}, (e) 2.8×10^{15}, and (f) 3.1×10^{15} ions/cm^2

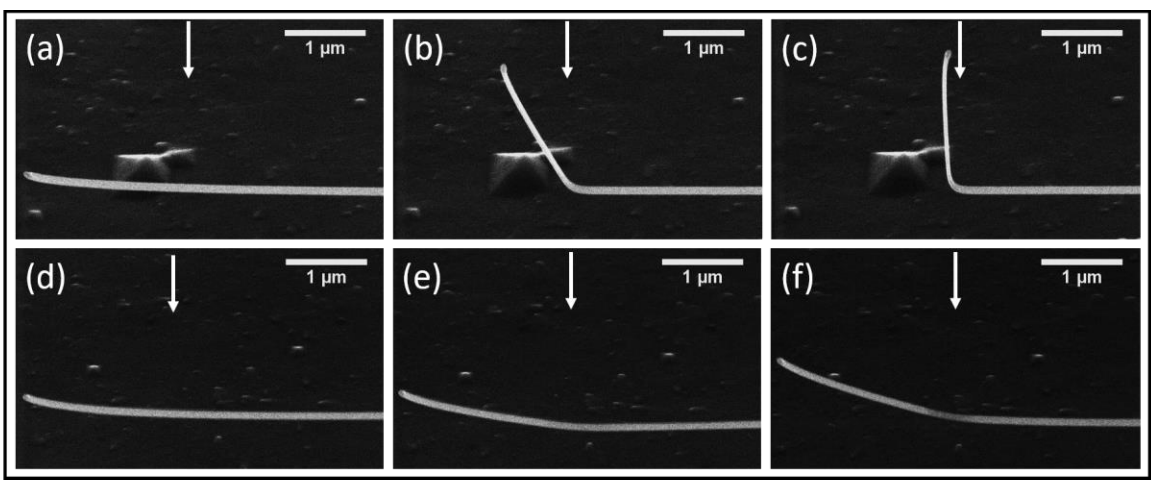

Figure 5.7: A series of representative SEM images acquired at successive time-intervals during experiments at 16 kV and ion dose of (a) 1.1×10^{14}, (b) 7.8×10^{15}, (c) 2.0×10^{16} ions/cm^2; low 2 kV and ion dose of (d) 1.1×10^{14}, (e) 3.1×10^{16}, (f) 1.8×10^{17} ions/cm^2

should govern the nanostructure bending direction. To systematically investigate the effect of ion dose and energies on the bending behaviour of Si nanostructures, Si NWs with a typical diameter of 100-110 nm were employed, which is consistent with the ion implantation range determined in computational studies presented in the next section. Figure 5.6 shows a series of representative SEM images acquired at successive time-intervals during ion beam irradiations and with increasing ion beam doses at 30 kV. To further examine the *in-situ* FIB induced bending of Si NWs, ion implantation at medium (16 kV) and low (2 kV) acceleration voltage respectively were carried out. Figure 5.7 shows a series of representative SEM images during ion irradiations at successive time intervals and with increasing ion dose at 16 kV and 2 kV. A quantitative analysis of SEM images acquired at successive time-intervals corresponding to each ion beam exposure provides insight and clarification of the bending phenomenon experienced by the nanowire. A schematic diagram showing the incident Ga ions on Si NW and the NW bending angle is included in Figure 5.8 (a). The NW bending angle is plotted as a function of the incident FIB dose (ions/cm^2) in Figure 5.8 (b). Negative slope in the plot refers to downward bending, i.e. bending away from ion beam direction, while positive slope indicates the bending in upward direction towards incident ion beam. Significant bending of Si NWs at ion dose as low as 10^{14} ions/cm^2 is observed. The maximum bending angle in the downward direction is approximately 34 degrees, after which a reversal of bending direction is observed. With an increased ion dose, the NW aligns itself in the direction parallel to the incident ion beam, i.e. becomes approximately 90 degrees with respect to its initial orientation in the given configuration.

The bending angle as a function of ion beam dose is plotted in Figure 5.8 (c) and (d) at 16 kV and 2 kV respectively. It can be clearly observed that the formerly straight NW bends towards the incoming ion beam and eventually align itself along the beam incidence direction at high ion beam dose. The bending exhibited at 16 kV is in an upward direction only, which is in contrast with the bidirectional bending of the NWs at 30 kV. For low acceleration voltage of 2 kV, the NW experiences the similar upward bending, however, the NWs undergoes bending up to a maximum angle of 15° only. The bending rate (i.e. the slope of the bending angle curve plotted with respect to the ion dose) is also affected by the acceleration voltage and the NWs are seen to undergo a slower bending rate at the lower acceleration voltages.

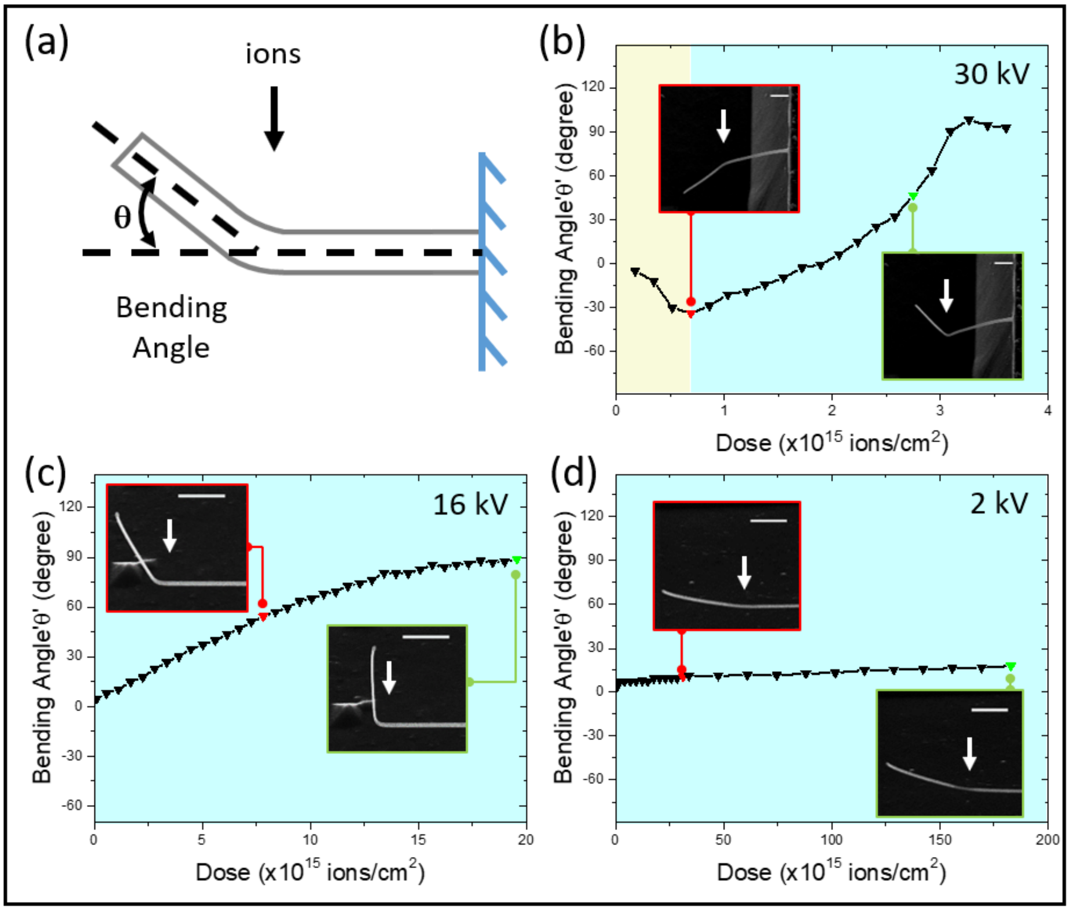

Figure 5.8: Ion induced bending: (a) Schematic diagram showing incident ions on Si NW and bending angle. Bending angle as a function of ion dose at (b) 30 kV, two distinct color regions mark downward and upward bending, (c) 16 kV, (d) 2 kV, the insets show SEM images of bent NW (scale bar 1 µm)

The NWs, in the current study, were irradiated with an ion-beam incident at 90 degrees to the length of the NWs, to avoid any exposure to Si substrate. It should be noted that the NW bending demonstrated in the current work is unlikely due to substrate charging phenomenon as reported earlier [150]. In addition, the NWs employed in the current experiments are freestanding and away from the Si substrate, which further lowers any possibility of substrate charging. The electrostatic charges induced between the ion-beam and the NW (if assumed to be charged due to the previous beam scan), would be negligible due to a significantly small current (1.5 pA) and ions used for bending. This implies that the bending behaviour observed in our case is not determined by electrostatic forces between the ion beam and the NW.

The findings of bidirectional bending are in contrast to the previous studies on carbon cantilevers [144], nanoporous gold (Au) cantilevers [166], [167], Si NWs [168], where the bending towards incident ion beam was observed irrespective of ion beam energies/target thickness. In addition, the bending exhibited at lower ion energies, observed in the current work, is also in contrast to the bending observations at high ion energies. Thus, there must be additional effects, which lead to the alternate bending behaviour exhibited through the NWs at 30 kV in contrast to the upward bending at 16 kV and needs to be investigated. Moreover, the ion hammering effect for origin of stresses, similar to the heavy ion irradiations in amorphous materials [142], [169], cannot be responsible for NW bending due to the positive thermal coefficient of Si. Similar to the calculations on germanium (Ge) NWs [170], Si would require a negative thermal coefficient of expansion. In addition, an anomalous plastic deformation of Si NWs observed under low energy Ar ions [171] based on viscoelastic model for swift heavy ion irradiations, to explain the plastic flow of

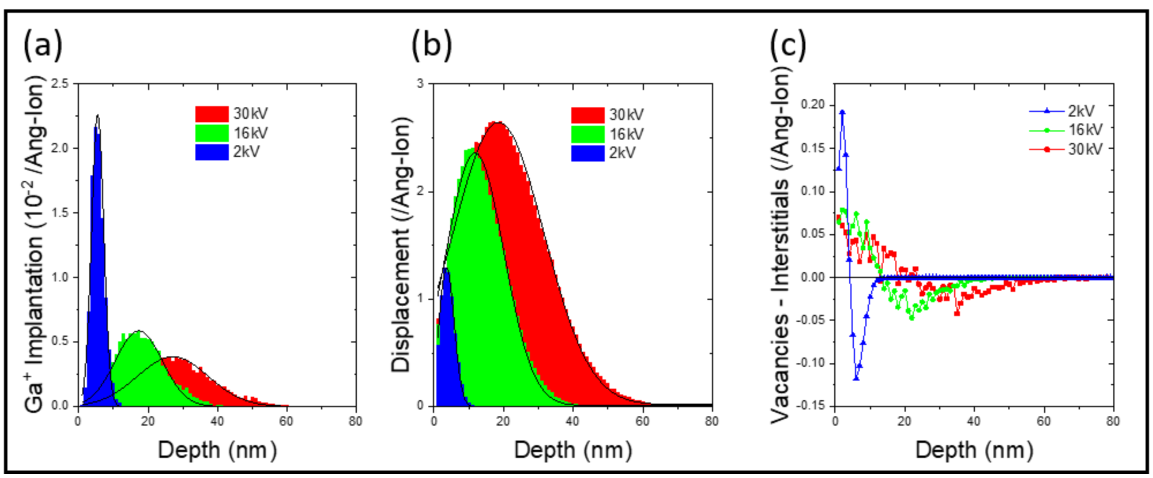

Figure 5.9: (a) Ga ion implantation, (b) Atomic displacement distributions/Angstrom-Ion, (c) The difference between vacancies and interstitials/Angstrom-Ion caused by Ga ions in Si substrate at low (2 kV), medium (16 kV), and high (30 kV) acceleration voltages

amorphous solids on the basis of a thermal spike region of cylindrical shape formed along the ion beam path, is rather contentious, and the model based on electronic energy loss cannot be generalized to low energy irradiations.

To investigate the underlying physics and the mechanisms involved in the ion induced bidirectional bending, the interaction of energetic Ga ions with Si NWs is evaluated through Monte Carlo (MC) simulations. For the low kV beam energies, the implantation and the defect formation are limited to the few tens of nanometres, while increasing the beam energy results in the deeper implantation along the target thickness. The collision cascade is largest for 30 kV and approximately spans 60-65 nm across the target depth, while 16 kV and 2 kV Ga ions are found to create a collision cascade within ~40 nm and ~15 nm of the NW thickness respectively. These values are based on the consideration of amorphous Si target in the MC calculations. Figure 5.9 (a), (b) exhibits the Ga ions distribution and atomic displacements/Angstrom-ion (a sum of vacancies and replacement collisions) in Si caused by Ga ions respectively and calculated using the MC simulations. Approximately 742, 420, and 65 vacancies and interstitial pairs are created at 30 kV, 16 kV, and 2 kV respectively per implanted Ga ion. The vacancy defects in collision cascade can be ripened into voids, and the concurrent densification due to interstitial knock-ons [172]. The distribution of a cascade along the target depth, due to low and high ion energies, can be used to locate the domains of vacancies or interstitials concentrations. The excess of vacancies is found towards the ion-irradiated surface while the interstitials dominates the un-irradiated surface (Figure 5.9 (c)). The volume expansion due to the incorporation of interstitials in the lattice corresponds to the generation of compressive stresses [145], and such lattice strains extend far beyond the collision cascade [173]. The excess of vacancies, on the other hand, corresponds to the generation of tensile stresses associated with a contraction of volume. The generation of such stresses is believed to be the primary reason for ion irradiation induced bending [82], [143]–[145], [174]. The volume expansion or swelling around the interstitial is more than the volume contraction around vacancies [175], thus, the formation and location of interstitial clusters plays a major role for ion induced bending [176]. The formation of such interstitial clusters grows with a prolonged ion exposure followed by sputtering of Si at higher ion doses, and reconstruction. The observation of interstitials in the form of dislocation networks through X-ray diffraction imaging of ion irradiated Au nanocrystal support the dominance of interstitials at high ion doses [173]. However, at low ion doses, the microstructure is dominated by of vacancies. It must be noted that the sputtering rates of nanostructures are higher due to their large surface-to-volume ratio [171], when compared with sputtering of their bulk counterparts. At very low ion doses, it is hardly possible to remove surface atoms from Si NWs with Ga ions due to limited sputtering yield of Si.

In addition to the creation of interstitials/vacancies, the collision cascade due to ion irradiations, accompanied by a thermal spike region, develops an atomic mass transport in the region well beyond the implantation range. Such mass transport has been reported for Si nanopore formation with FIB [177]. In fact, the direction of atomic mass transport via plastic deformation based on the incident ion energy was understood to be the primary factor for controlling the deflection of Al cantilevers through molecular dynamics (MD) simulations [154]. Similar observations were made for ion induced bending of Al cantilevers [153], suggesting the bending due to the transport of interstitial clusters far above the irradiated region. An extended dislocation network observed through X-ray diffraction measurements in ion implanted Au nanocrystals further confirms the generation of lattice strains far beyond the ion-damaged layer [173]. Such dislocation clusters, extending well beyond the ion implantation range are most likely expected to be of interstitial type [178]. Similar formation of dislocation loops in ion irradiated Al have also been observed through TEM imaging [179]. The accumulation of interstitial clusters leads to volume expansion in the region beyond the ion implantation range, causing ion induced bending of Al, Au cantilevers [153], [167]. Low energy ion dosage induces penetration of ions only near the ion-irradiated top region, thereby contributing to the mass transport to the ion-irradiated top region and resulting in upward deflection towards incident ions. High energies ion dosage, on the other hand, induces ion penetration near to the bottom of the ion-irradiated surface (depending on the thickness), and thus providing the mass transport towards bottom surface, resulting in downward deflection away from the incident ion beam. The compressive stresses are built up in the NW at the ion-irradiated region due to the sputtering of Si atoms from top layers and redistribution of the disturbed atoms in the collision cascade, because of further exposure to ions. The formation of such compressive stresses in the NW surface towards the incident ion beam, generates a net bending moment in the upward direction. The NWs, thus, reverses its motion and bends towards the incident ion beam until a new equilibrium state is obtained.

In the current work, the NWs bending away from the incident ions up to a threshold ion dose of ~7×10^{14} ions/cm^2 at high energy (Figure 5.8 (a)) are reported. This is due to the volume expansion towards un-irradiated side (bottom) of the NW. However, in the earlier works on GaAs [145], ZnO [174], Ge NWs [180], the bending of nanostructures away from the incident ions was attributed to the volume expansion in the irradiated side of NWs at shallower depths (low energy irradiation). The alignment towards incident ions was observed during high energy irradiations causing volume expansion towards un-irradiated side [145], [174], [180]. Such anomaly is also observed at low energy irradiations in the current work, where the shallower irradiations induced volume expansion towards the irradiated side (NW top) develop upward bending of the Si NWs.

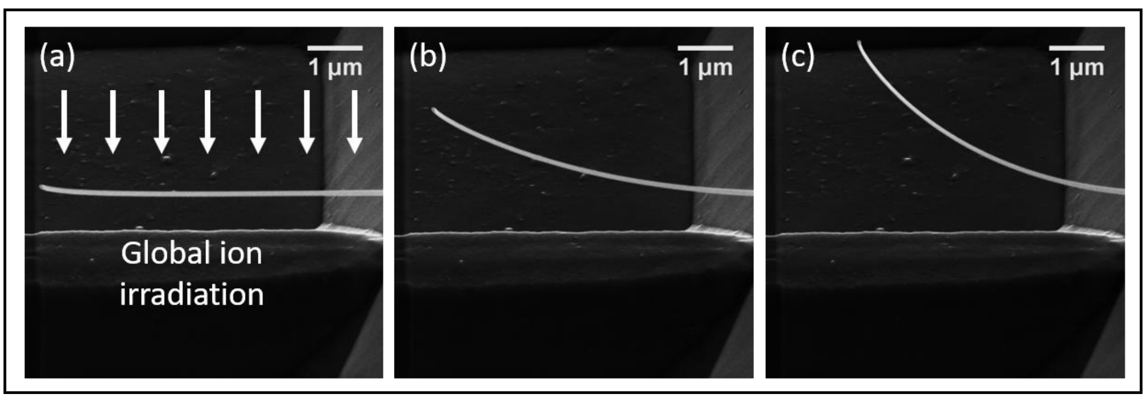

Figure 5.10: Global ion irradiation: (a)-(c) A series of representative SEM images acquired at successive time-intervals during global ion-beam irradiations showing upward bending at 30 kV in contrast to bidirectional bending through site-specific/local ion irradiation at 30 kV

Ion irradiation experiments were further carried out at 30 kV on a Si NW along its entire length (global ion irradiation) like the broad/plasma ion irradiations of the NWs/cantilevers reported earlier [145], [174], [180]. The bending results are in contrast with the site-specific/local ion irradiations used in this work (Figure 5.8). The globally irradiated Si NW, still leading to the volume expansion at 30 kV towards un-irradiated side, was now found to bend upwards/towards incident ions. No bidirectional bending was observed. This is similar to the earlier reported bending of the NWs towards ion beam if the volume expansion is towards the un-irradiated side of the NWs [145], [174], [180]. In fact, local irradiations with a shallow penetrations, limited to the irradiation side, of Si NWs [168], carbon cantilevers [144] cause the nanostructure to bend towards the incident ions. This highlights the strong influence of a choice of irradiation scheme, whether site-specific/local or global, on the bending behaviour of NWs, in addition to the other factors like collision cascade, associated volume changes, mass transport, sputtering etc.

These findings, suggesting the importance of sites being irradiated, i.e. localized or global, are crucial, and provide additional control for weaving of nanostructures in addition to the ion beam parameters. Such bending effects can potentially arise from the density difference

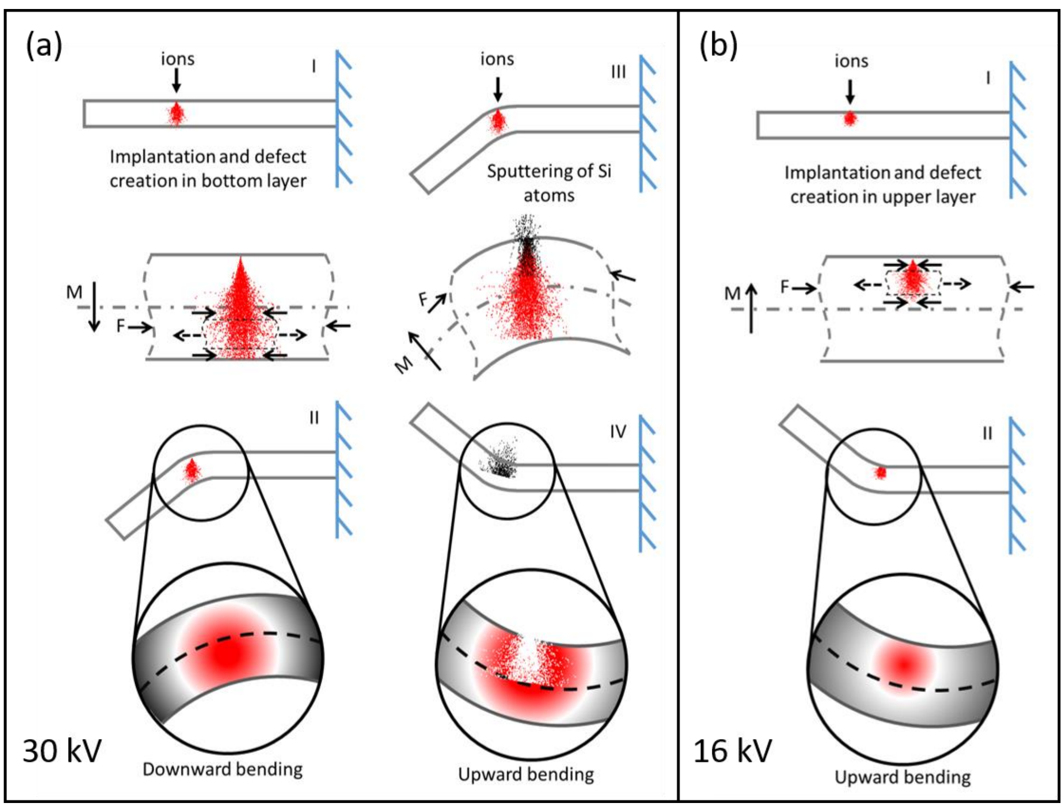

Figure 5.11: Schematic illustration of the proposed bending mechanisms: (a) Bi-directional bending at 30 kV, and (b) Upward bending at 16 kV

between the damaged and un-damaged regions [176]. For local irradiations, the volume expansion in the irradiated domain is surrounded by the un-damaged region leading to such density difference and can be a probable cause for the observed bending effects of localized ion irradiations. The volume expansion develops reactive forces in the un-damaged region. Such forces lead to the generation of a bending moment on the NWs, the direction of which depends on the relative location of volume expansion region.

In light of the above discussion, the bending mechanism is presented schematically in Figure 5.11 (a), (b) for ion induced NW bending at high and low ion energies respectively. The volume expansion, caused at high ion energies towards the NW un-irradiated side, surrounded by the un-damaged region, develops a force towards the region of volume expansion. The development of such force towards the NW un-irradiated side leads to the generation of a downward bending moment, as shown through the schematics in Figure 5.11 (a): I-II, and the NW undergoes a downward bending. The phenomena of sputtering and surface reconstruction starts dominating at higher energies with a continued exposure to ion beam i.e. at high dose (Figure 5.11 (a): III- IV). The removal of atoms at high energies (30 kV), leads to the reversal of the bending moment and the NW bend in reverse direction. At this stage, the NW bending behaviour is dominated by the sputtering of irradiated region, and a faster bending towards incident ion beam is observed (also evident from a steep slope of the bending curve during the upwards bending as seen from Figure 5.8 (a)). For low ion energies, on the other hand, the collision cascade and interstitial including the implanted ions occur towards the ion-irradiated side of the NW (Figure 5.11 (b): I-II). This develops a volume expansion in the NW ion-irradiated top region, and NW undergoes upward bending at low energies and continues aligning itself towards the ion beam direction at successive ion irradiations.

5.3.5 Nanostructural Characterizations

To further consolidate the bending mechanism, nanostructural investigations based on TEM were carried out on Si NWs to study the ion-induced deformations. The TEM images of a fabricated Si NW with diameter ∼110 nm is shown in Figure 5.12 (a), (b). The contrast in the high-magnification TEM image as shown in figure 3 (b), and the associated electron

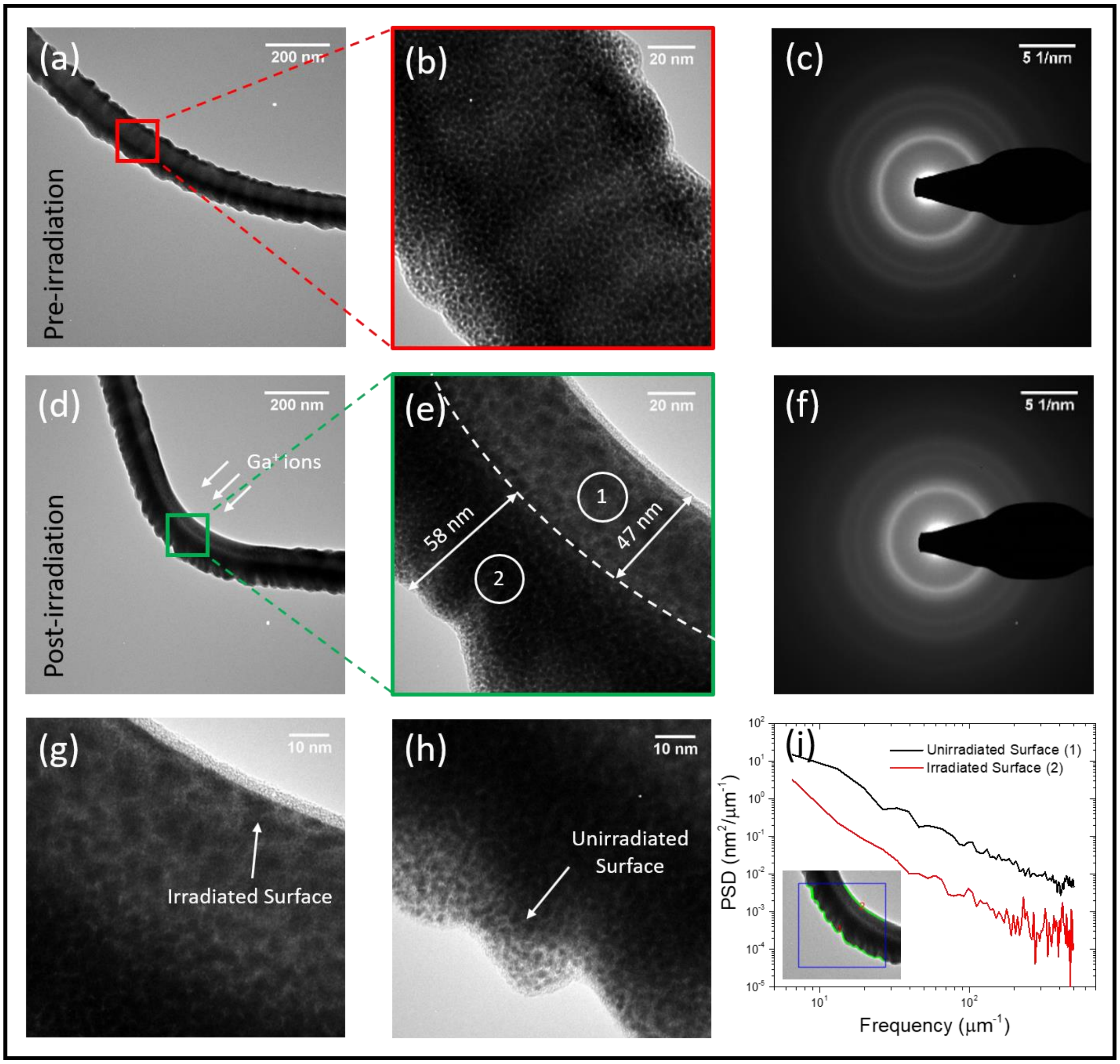

Figure 5.12: Nanostructural characterization of Ga ions irradiated Si nanowires (NW), TEM image showing (a) Fabricated, un-irradiated Si NW, (b) A magnified TEM image of the NW, (c) Diffraction pattern from the NW, (d) Si NW after *in-situ* ion induced bending, (e) Magnified TEM image of bent NW, (f) Diffraction pattern from ion-irradiated NW. (g), (h) Magnified TEM image of ion-irradiated and un-irradiated surface respectively, (i) Power spectral density function against the spatial frequency of the surface roughness for un-irradiated and irradiated surface

diffraction pattern as shown in Figure 5.12 (c), both indicate the near-amorphous nature of fabricated NWs. The near-amorphous transformation of Si NW is believed to be due to ion beam implantation during the fabrication process to obtain the suspended Si NWs. The Si NW was bent with FIB irradiations at an acceleration voltage of 30 kV, and the corresponding TEM characterization results are included in Figure 5.12 (d)-(h). The NW, even after bending, is found to maintain the near-amorphous state as evident from the electron diffraction pattern in Figure 5.12 (f). A high-magnification TEM image of the bent NW is included in Figure 5.12 (e). Upon prolonged exposure (high dose) to Ga ion irradiation, the NW exhibits two clearly distinguishable regions: sparse, ion-irradiated top region (Region (1)) and un-irradiated, bottom region (Region (2)). The sparse ion-irradiated region (Region (1)) in Figure 5.12 (e), (g) contrasts with the un-irradiated region in Figure 5.12 (b), (h) visibly evident from the image contrast. The NW irradiated surface, as evident from the high magnification TEM image in Figure 5.12 (e), (g) exhibiting a smoothened irradiated surface, indicates the ion beam sputtering effects associated during the bending process at high ion doses. The irradiated NW surface, in contrast to the un-irradiated surface, appears to have reduced surface roughness. The power spectral density (PSD) calculations are carried out for analysing and comparing the surface roughness of irradiated and un-irradiated NW surface as shown in Figure 5.12 (i), with a TEM image in the inset showing the outline of compared surfaces. The un-irradiated NW surface has both low frequency and high-frequency roughness towards the higher side as compared to ion-irradiated NW surface. The improvement in surface roughness of ion-irradiated NW surface is an indication of ion-induced smoothening process. Thus, the nanostructural characterization of the bent NW at higher doses confirms that the bending behaviour is dominated by sputtering of the NW atoms at the irradiated surface, and the NW bends towards the incident ion beam.

5.3.6 Weaving 3D Nanostructures

In-situ FIB induced bidirectional bending demonstrated here can be employed for controlled manipulation and weaving of freestanding nanostructures into complex 3-dimensional nanostructures for desired functionality. The main limitation for the realization of such 3-dimensional nanostructures, however, is the fabrication of

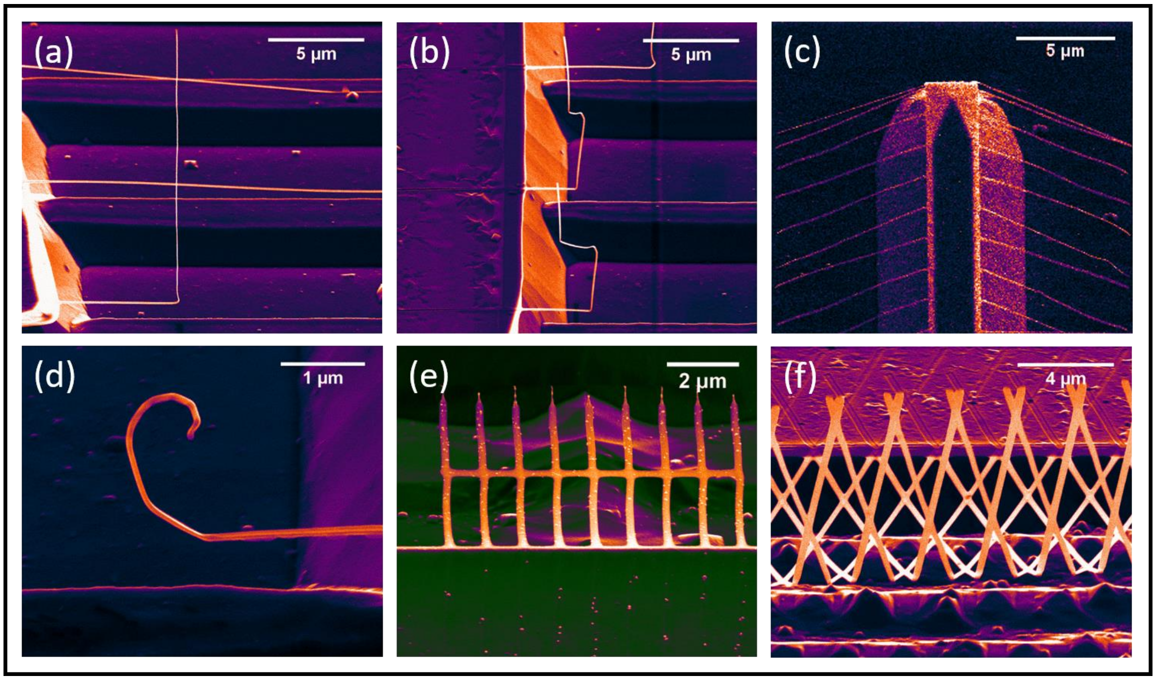

Figure 5.13: Controlled weaving and nanostructure manipulation. SEM image (false-colored) of (a) An ultra-long fully bent NW with normal incident ion beam irradiation on the NW, (b) NWs bent in two alternative directions with three subsequent FIB irradiations in the direction normal to NW, (c) An array of NWs bent in downward direction, (d) A hook-shaped 3D nanostructure fabricated through FIB irradiations repeated multiple times along the NW, (e), (f) 3D folded nanostructures in the form of a mesh

freestanding nanostructures. The residual stresses developed during thin film deposition and fabrication of such freestanding nanostructures can lead to unwanted and uncontrolled deformations. The fabrication of suspended nanostructures through the combination of FIB implantation and bulk structuration via wet etching of Si in this work overcome such issues. Controlled manipulation and weaving of fabricated suspended nanostructures were further carried out with FIB *in-situ* to realize 3D nanostructures, extending the existing capabilities of FIB [181], [182]. Figure 5.13 shows SEM images of 3D nanostructures obtained via controlled weaving and nanostructure manipulation. The effects of sputtering during controlled manipulation and weaving of nanostructures needs to be pointed out. As discussed earlier, the continued exposure to ion beam leads to the sputtering of the nanostructures and reversal of bending at high ion energies. For the controlled manipulation and weaving of nanostructures towards ion beam at 30 kV, the thinning of bending cross-section was observed, which arises from the sputtering of Si with an ion beam dose $\sim 7\times10^{14}$ ions/cm^2 at 30 kV. The sputtering effects associated with ion induced bending during nanomanipulation could be a limiting aspect for geometry sensitive applications. Such sputtering effects, however, can be avoided employing low ion doses with high/low ion energies to induce downward, upward bending respectively.

An ultra-long vertical NW (length 33 µm and high aspect ratio of 300) was obtained via ion beam induced upward bending of a Si NW freestanding at one end and attached to Si post at another end. The ultra-long fully bent NW is shown in Figure 5.13 (a), which has been bent at 90 degrees. Such high aspect ratio NWs can be utilized for multifunctional applications in photonics or material sciences. A pair of the NWs bent in two alternative perpendicular directions is shown in Figure 5.13 (b), where ion beam was irradiated at three locations along the NW length and in the directions perpendicular to the previous scan. The NWs bent in two alternative perpendicular directions were obtained through ion beam irradiation along the NW length at multiple locations. Ion beam was incident perpendicular in subsequent location to the direction in the previous location along the NW length to realize the NWs bent in two perpendicular directions. An array of suspended NWs bent in a downward direction, i.e. in the direction opposite to incident ion beam, is shown in Figure 5.13 (c). Such *in-situ* bidirectional manipulations demonstrate the ease with which the nanostructures can be designed for desired functionality.

A hook-shaped nanostructure, fabricated through multiple FIB irradiations along the NW length, is shown in Figure 5.13 (d). The hook-shaped nanostructure was fabricated via continuous and controlled bending on a Si NW along its length. The NW was irradiated with Ga ions through a line pattern scan, which was moved along the NW length after each irradiation, resulting in continuous bending of NW and formation of a hook shape. This strategy can be further employed for fabrication of exotic 3-dimensional coil nanostructures through continuous and controlled manipulations along the NW length. The controlled weaving of freely suspended Si mesh nanostructures was further employed through *in-situ* ion irradiations of Si nanostructures to realize folded 3D nanostructure. The ion beam was scanned over pre-defined line pattern on Si mesh to bend it. Figure 5.13 (e), (f) include the SEM image of a 3D nanostructure in the form of a mesh, demonstrating the process capability. The analysis of ion induced bending at different processing parameters can be used to ascertain the deterministic nature of the bending process as needed for 3D freeform fabrication. Figure 5.8 (a)-(c) provide an accurate estimate of processing parameters for realizing the controlled bending of nanostructures. For example, referring to Figure 5.8 (a), for a nanostructure close to 100 nm in diameter to bend 30 degrees in the downwards direction, ion dose of ~5×10^{14} ions/cm^2 at 30 kV should be used. Similarly, for a nanostructure with a bend angle of 30 degrees in the upward direction, an ion dose of ~2.5×10^{15} ions/cm^2 at 30 kV or ~4×10^{15} ions/cm^2 at 16 kV should be used. Thus, the availability of these processing parameters as a reference can be used for deterministic bending of nanostructures for controlled manipulation, as has also been shown through the examples in Figure 5.13. This suggests that complex nanostructures can be engineered *in-situ* through ion-induced bending. Thus, the developed approach is effective for fabrication of thin film 3D nanostructured for desired functionalities and will enable the development of future novel nanoscale devices.

5.3.7 Single Cell Applications

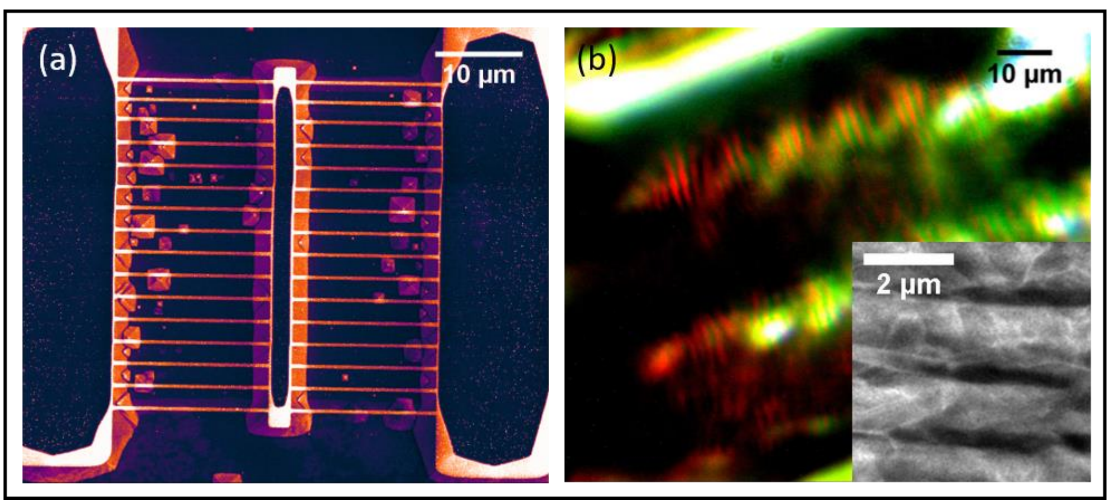

Figure 5.14: (a) SEM image of suspended NWs for live cell imaging, (b) Corresponding optical microscopic image showing the bacteria loaded nanowires with inset including the SEM image of cell showing aligned growth on the NWs

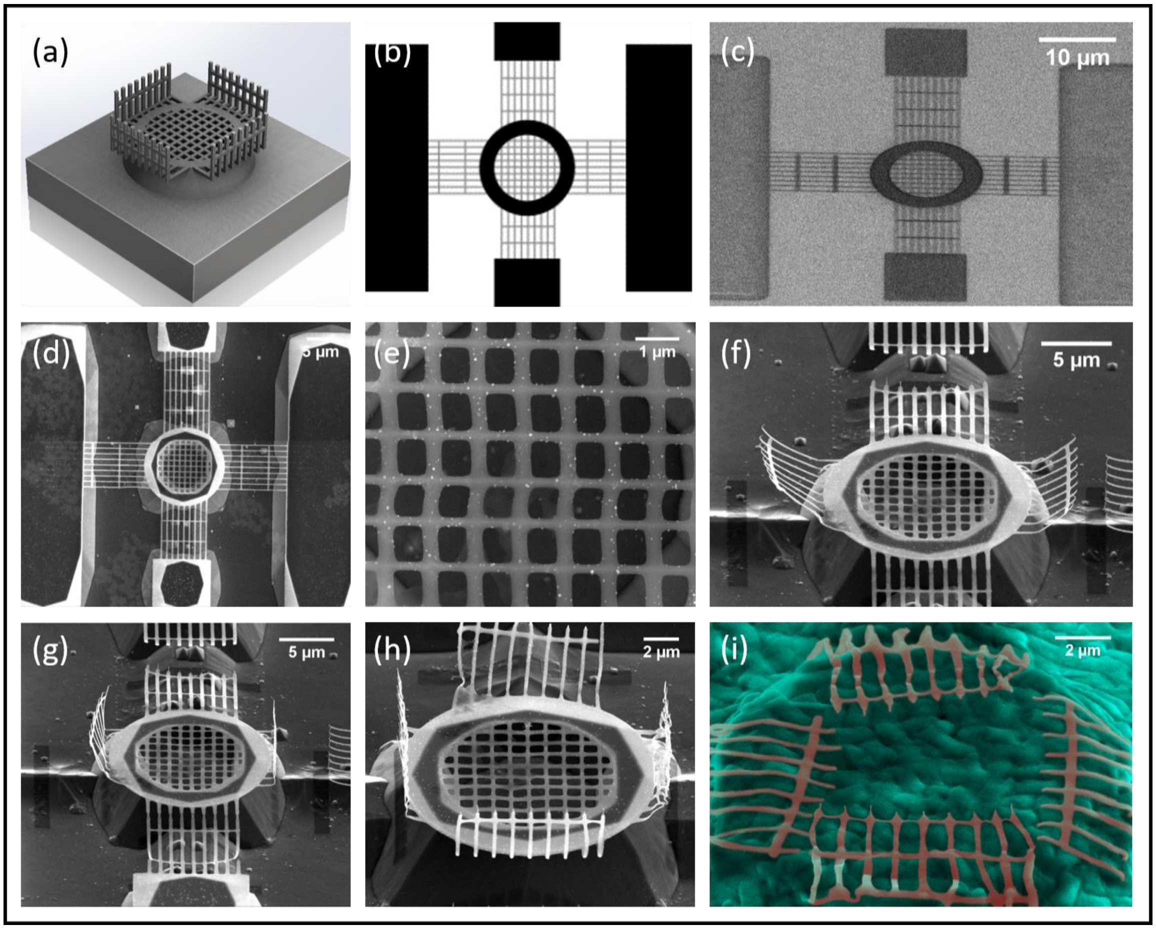

Figure 5.15: (a) Conceptual design of a "bacterial mesh trap", fabrication of bacteria lobster trap: (b) Schematic for ion implantation design (bitmap image), (c) SEM image showing implanted region, (d), (e) SEM images of fabricated mesh structure, (f), (g) Subsequent FIB cutting and *in-situ* folding (h) The "bacterial mesh trap" fabricated via bending of suspended Si mesh, (i) SEM image (false-colored) of the prototype "bacterial mesh trap" after capturing the bacteria cells

The developed approach provides an excellent route for novel single cell applications such as the interactions between bacteria and the Si nanostructures. Bacteria are social organisms, displaying distinct group behaviours, which are often required in large numbers to conduct mechanistic studies for probing the molecular processes for antibiotic resistance etc.[183]. Live cell imaging application of fabricated suspended nanostructures (NWs) is illustrated in Figure 5.14 (b), where an optical image is shown demonstrating the stained live bacterial cells showing aligned patterns. The corresponding array of Si NWs used for live cell imaging is shown through SEM image in Figure 5.14 (a). The SEM image of bacteria loaded nanowires included in the inset of Figure 5.14 (b) shows the aligned growth similar to the self- assembly and adhesion of bacteria cell over vertical NWs [184], [185].

The proposed approach in the study provides a simpler yet more flexible alternative towards the study and understanding of cell adhesion with 3D nanostructures. A new "bacterial mesh trap" is designed through the developed nanofabrication and the *in-situ* FIB manipulation approach for capturing the bacteria cells. Figure 5.15 (a) shows the schematic diagram of the designed bacteria trap. For fabrication of suspended nanostructures in the form of a mesh, a bitmap design (Figure 5.15 (b)) was used for ion implantation with optimized ion dose similar to the Si NW experiment. The SEM image of implanted Si is shown in Figure 5.15 (c). The implanted Si was then etched chemically, and fabricated suspended nanostructure is shown through SEM image in Figure 5.15 (d), (e). Further, the suspended mesh nanostructure is cut and subsequently bent via ion irradiations as shown through SEM images in Figure 5.15 (f)-(g). The fabricated "bacterial mesh trap" is demonstrated to be effective for capturing of bacteria cells in solution as shown in Figure 5.15 (i). The mesh size (∼1 μm) ensured the bacteria capturing within the trap, while permeable to nutrients and waste products through the mesh. The vertical mesh sides further wrapped the bacteria as enclosing walls, facilitating three-dimensional organization, which has been infeasible previously.

5.4 Summary

In this work, novel fabrication of Si 3D nanostructures is demonstrated through a combination of ion implantation and wet etching of Si followed by keV ion induced *in-situ* controlled manipulation. The achievements include (1) suspended Si NWs fabricated through the combination of FIB implantation followed by top-down bulk structuration via anisotropic wet etching of Si. (2) One notable finding is the *bidirectional* bending at higher (~30 kV) ion energies. The Si NWs were found to bend away from incident ion beam initially possibly due to penetration of the incident Ga ions and the resulted formation of defects. The NWs eventually align in the direction of the incoming ion beam due to the removal of atoms from Si lattice possibly from sputtering effects. Unlike irradiation at 30 kV, the NWs only exhibited bending towards incident ions at lower ion energies (including 2 kV and 16 kV). It was further observed that the bending rate of Si NW is dependent on ion energies and found to be decreasing with lowering ion energies. An important consideration of local vs global ion irradiation correlating the bending effects associated with local ion irradiations in contrast to global ion irradiation is presented. (3) The bidirectional nature of ion-induced bending provides an additional degree of freedom, and the proposed method can be utilized for deterministic 3D nanofabrication and manipulation of nanostructures for desired functionalities, such as ultra-long NWs, folded nanomesh, live cell imaging, and “bacterial mesh trap” This work will be inspiring for 3D nanofabrication of unique geometries, and open new avenues in the diverse field of ion beams and applications beyond material science for realization of future nanoscale devices.

Chapter 6. Controlled Manipulation and Multiscale Modelling of Suspended Silicon Nanostructures under Site-specific Ion Irradiation

In this work, controlled bi-directional deformation of suspended nanostructures by site-specific ion irradiation is presented. Multi-scale modelling of the bi-directional deformation of nanostructures by site-specific ion irradiation is presented, incorporating molecular dynamics (MD) simulations together with finite element analysis (FEA), to substantiate the bending mechanism. Strain-engineering of the freestanding nanostructure is employed for controlled deformation through site-specific kiloelectronvolt ion irradiation experimentally using a focused ion beam (FIB). The detailed bending mechanism of suspended silicon (Si) nanostructures through ion induced irradiations is presented. MD simulations are presented to understand the ion solid interactions, defects formation in the silicon nanowire. The atomic-scale simulations reveal that the ion irradiation induced bidirectional bending occurs through the development of localized tensile-compressive stresses in the lattice due to defect formation associated with atomic displacements. With an increasing ion dose, the evolution of localized tensile to compressive stress is observed, developing the alternate bending directions calculated through finite element analysis. The findings of multiscale modelling are in excellent agreement with the bi-directional nature of bending observed through the experiments. The developed in-situ approach for bi-directional controlled manipulation of nanostructures in this work, can be used for nanofabrication of numerous novel 3D configurations and provide a route towards functional nanostructures and devices.

6.1 Introduction

Nanofabrication of 3D configurations holds the key for a myriad of applications, inducing various functionalities [59], [186]–[188]. Focused ion beam (FIB) is a valuable tool in nanotechnology domain with applications ranging from the fabrication of nanostructures for applications such as photonics [189]–[191], plasmonics [146], etc. to material characterization [192], [193], cellular level imaging in biology [194]. Gallium (Ga) ions in a dual-beam microscope can be used for ion irradiation induced bending of nanostructure *in-situ*, which can be used for controlled manipulation of nanostructures in different orientations. Nanostructures undergo unusual transformations, such as improved sputtering and dynamic defect annealing under ion irradiations, in contrast to bulk materials due to the nanostructure dimensions comparable to the collision cascade [138]. Ion irradiation of nanostructures is a promising tool, which can produce stresses of the order of several GPa [149]. Ion induced bending arises due to generation of tensile/compressive stresses and is an effect of defect formation (vacancies and interstitials) due to collision cascade induced by ion implantation. Phenomenon, such as ion induced amorphization [11], void induced stress generation, dynamic annealing of ion-induced defects [152], formation of interstitial clusters beyond the collision cascade [153], atomic mass transport [154], surface charging effects [150] etc. have also been reported for ion induced bending mechanism. In addition, the size, shape, and composition of nanostructures, ion mass, dose, energy also govern the bending mechanism substantially. Ion induced bending enables strain-engineering and manipulation of nanostructures, and a wide variety of configuration/materials such as carbon nanotubes [57], cantilevers [144], semiconductor nanowires (NWs): Si [168], Ge [180], GaAs [145], ZnO [174], self-assembled peptide nanotubes [195] etc. have been reported. Ion induced bending, thus, can be utilized towards the realization of various 3D configurations [187], [188] and inducing functionalities which are otherwise not possible, for example, plasmonic metamaterials [146], 3D and thin film origami nanostructures [59], [147] etc. Thus, the detailed understanding and investigation of ion induced bending of nanostructures becomes important towards realization of functional nanostructures with the desired configuration.

This work presents localized ion irradiation induced controlled manipulation of suspended silicon nanowires in a dual beam FIB-SEM microscope. Further, multiscale modelling of the ion induced bending through MD simulations and finite element analysis is presented for investigation of ion induced bending mechanism. The goal of this study is to understand the details of ion irradiation induced deformation and deterministic bending of nanostructures. The computational studies provide new insights into atomic scale origin of the bidirectional bending for controlled manipulation of nanostructures to cultivate anticipated functionalities.

6.2 Experimental Details

6.2.1 Fabrication of Suspended Si Nanowires

10 mm × 5 mm pre-cut, single crystalline (<100>), p-doped Si chips (Ted Pella Inc., Product 16008) were used for the NW fabrication. Suspended Si NWs were fabricated through a combined approach of ion implantation followed by wet chemical etching of Si [187]. A dual beam FIB/SEM instrument equipped with a gallium (Ga) ion source (FEI Quanta 3D system, Thermo Fisher, USA) was used for implantation experiments at an acceleration voltage of 30 kV, with an optimized ion dose (2×10^{16} ions/cm^2), beam current 10 pA, and beam overlap of 50%. 1.5 mol/L potassium hydroxide (KOH) solution was used for wet chemical etching of Si. Commercially available KOH pallets (Sigma Aldrich Product Number 221473) were dissolved in deionized (DI) water to prepare the KOH solution. Chemical etching of ion implanted Si was carried out for 3 hrs at room temperature, allowing enough etching to obtain suspended nanowires.

6.2.2 Bending Experiments

The fabricated Si NWs were employed for ion irradiation experiments in the dual beam FIB/SEM instrument. The suspended NWs were cut with 1.5 pA current, to realize the NWs freely suspended at one end. A rectangular pattern (0.5×0.5 µm^2) was irradiated site-specifically with increasing ion dose for ion induced bending at an acceleration voltage of 30 kV and beam current 1.5 pA.

6.3 Results and Discussion

6.3.1 Site-Specific Ion Irradiation Induced Bidirectional Bending

Suspended Si NWs, with a typical diameter of ~100 nm, fabricated through ion implantation followed by wet chemical etching are irradiated *in-situ* with Ga ions at 30 kV (Figure 6.1 (a)). Ion irradiation of nanostructures leads to the development of collision cascade and formation of point defects in the lattice. Site-specific ion irradiation of suspended Si NWs exhibits bidirectional bending behavior, and formerly straight NWs

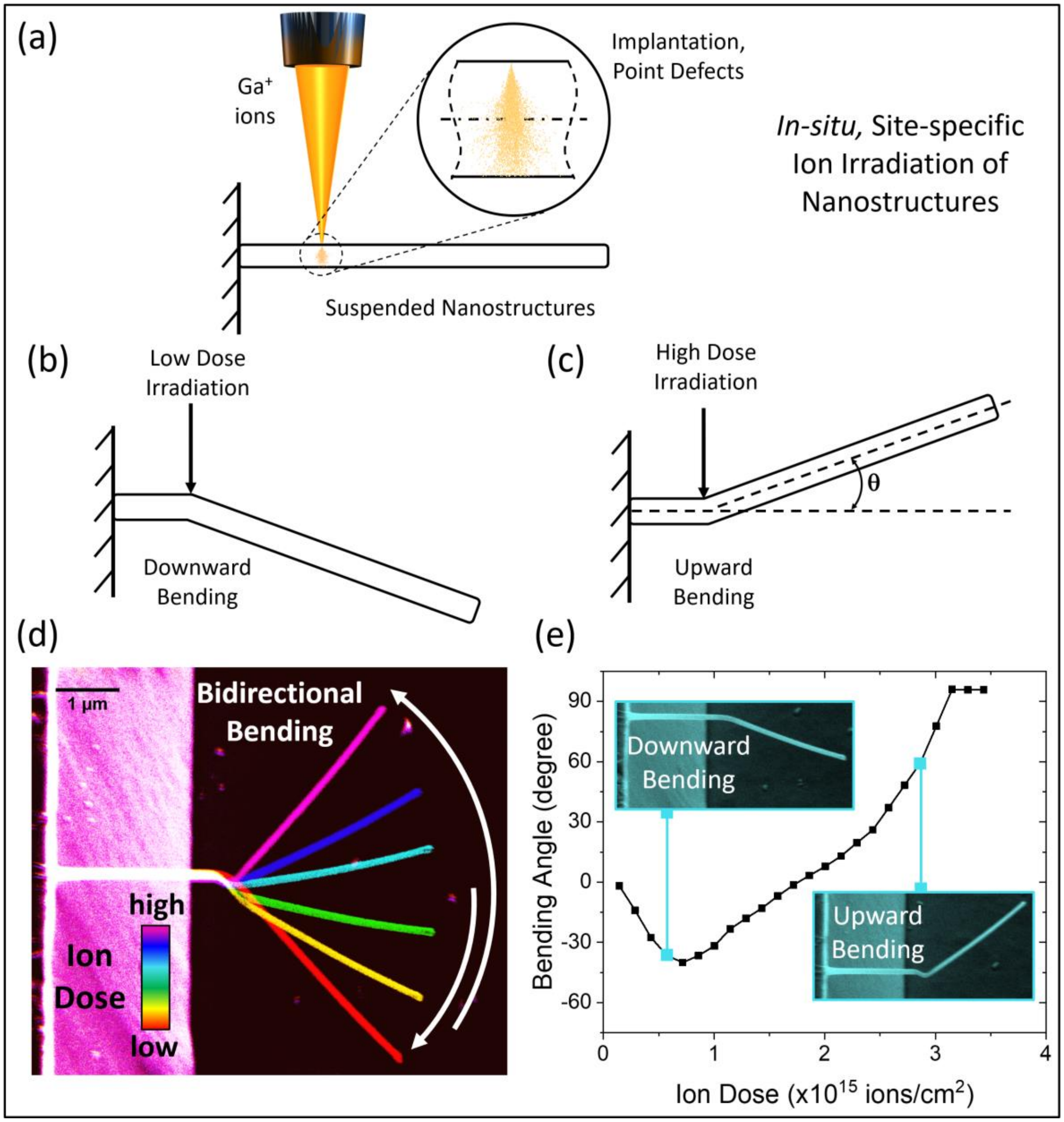

Figure 6.1: Ion irradiation induced bidirectional bending of nanostructures: (a) Schematic showing Ga ion irradiation of suspended nanostructures and ion implantation, point defects formation leading to (b) Downward (low dose) and (c) Upward (high dose) bending of nanostructures (d) Composite SEM image (false color) of Si NW bending away and subsequent bending towards incident ion beam with increasing ion dose (the color bar show ion dose and corresponding NW bending), (e) NW bending angle as a function of ion dose, insets show SEM images of the Si NW bent away and towards incident ion beam

undergoes first bending away (downward) and subsequently bending towards (upward) incident ion beam (Figure 6.1 (b), (c)). The NW, under *in-situ* ion irradiations, show permanent bending, indicating plastic deformation of the NW. A false colored, composite SEM image, exhibiting a typical Si NW undergoing bidirectional bending through ion irradiations, acquired at successive time intervals is shown in Figure 6.1 (d). The bending angle, obtained through the quantitative analysis of SEM images, plotted as a function of incident ion dose is shown in Figure 6.1 (e). From the plot, it can be observed that the Si NWs undergo bending with ion dose as low as 10^{14} ions/cm^2. The NW exhibit a bending rate of ~4.45×10^{-14} degree/ions/cm^2 through the ion irradiation experiments at 30 kV. It can also be observed that the NW bends away from the incident ion beam and undergoes a maximum bending angle of ~40 degree at ~7×10^{14} ions/cm^2. With further exposure to incident ions, the NW reverses its bending direction and is found to bend and eventually aligned towards the incident ion beam. The insets in Figure 6.1 (e) also shows the SEM images of the Si NW bent in two configurations, i.e. bending away and bending towards the incident ion beam at low and high ion doses respectively.

The bidirectional bending behavior exhibited by suspended Si NWs through site-specific, *in-situ* ion irradiation provides an additional degree of freedom, in addition to the ion beam parameters, for controlled manipulation and weaving of nanostructures bidirectionally. The bending effects, associated with ion irradiation of Si NWs, originate from the development of tensile and compressive stresses in the Si lattice [142], [143], which can be of the order of several GPa [149]. Such stresses in the lattice originate due to volume change associated with the formation of point defects (vacancies and interstitials) during the collision cascade following the ion implantation due to ion irradiations. The vacancies, formed due to the migration of the lattice atoms and primary knock-ons, can be ripened into voids. The interstitials, on the other hand, due to the incorporation of displaced constituent atoms or implanted ions in the lattice, can result in the densification [174]. Monte Carlo (MC) simulations of Ga ion irradiation with Stopping and Range of Ions in Matter (SRIM) [155], based on the binary collision approximation, suggest the formation of collision cascade spanning 60-65 nm in Si at 30 kV. The MC simulations, however, provide a basic understanding of ion implantation and collision cascade formation due to ion irradiation.

The energy required to create a defect is also dependent on the crystal orientation, the crystal orientation, however, is neglected in MC simulations. In addition, the MC simulations do not include the effects of damage build-up in the lattice and are limited in terms of thermal damage/annealing effects. Thus, atomic scale understanding of ion-material interaction is important and a detailed analysis of microstructural damage is required to further consolidate the bending mechanism. Molecular dynamics simulations are performed to estimate the evolution of ion induced defects and investigate the bending mechanism.

6.3.2 Molecular Dynamics Simulations

MD simulations are performed for in-depth understanding of ion induced bidirectional bending phenomenon. Figure 6.2 depicts the Si diamond lattice and geometry employed in the MD simulations. The simulation domain consists of fixed region, thermal region, sputter region, along with Ga ions. A hybrid potential combining Modified Stillinger-Weber (SW) potential [196] for Si-Si interactions, and Ziegler–Biersack–Littmark (ZBL) [197] potential for Ga-Si interactions was employed in the MD simulations. The total energy in SW potential is given as [198],

$$\begin{aligned} \mathrm{E} &= \sum_{i<j} \Phi_2(i,j) + \sum_{\substack{i\neq j \\ j<k}} \Phi_3(i,j,k) \\ &= \sum_{i<j} \epsilon\phi_2(r_{ij}) + \sum_{\substack{i\neq j \\ j<k}} \epsilon\phi_3(r_{ij}, r_{jk}, \theta_{ijk}) \end{aligned} \tag{6.1}$$

which is a combination of two- and three-body interaction. The two- and three-body interaction functions of the SW potential are given as,

$$\phi_2(r_{ij}) = \mathrm{A}\left[B\left(\frac{\sigma}{r_{ij}}\right)^p - \left(\frac{\sigma}{r_{ij}}\right)^q\right]\exp\left(\frac{1}{r_{ij}/\sigma - a}\right) \tag{6.2}$$

$$\phi_3(r_{ij}, r_{jk}, \theta_{ijk}) = \lambda\left(\cos\theta_{ijk} + \frac{1}{3}\right)^2 \exp\left(\frac{\gamma}{r_{ij}/\sigma - a}\right)\exp\left(\frac{\gamma}{r_{ik}/\sigma - a}\right)$$

where, σ, ϵ are distance, energy scaling parameters respectively, to get the lattice constant and cohesive energy of Si. The parameters A, B, p, q, λ, and γ allow the tuning of two-three-body interactions as a function of interatomic angles and distances. The modified SW potential improves the threshold displacement energy (TDE), and properties of the amorphous phase, which are critical for cascade simulations. The values of these parameters for modified SW potential are listed in Table 6.1.

Table 6.1: Parameters for modified SW potential [196]

ϵ (eV)	σ (Å)	a	λ	γ	A	B	p	q
1.04190	2.128117	1.80	31.0	1.10	19.0	0.65	3.5	0.5

The ZBL potential is a screened electrostatic potential and involves nucleon-nucleon interactions to model high energy collisions, and has been used previously for Ga-Si interactions [199], [200]. The ZBL potential is given by [197],

$$V_{ij}^{ZBL} = \frac{1}{4\pi\epsilon_0}\frac{Z_1 Z_2 e^2}{r_{ij}}\Phi\left(\frac{r_{ij}}{a}\right) \tag{6.3}$$

where,

$$\emptyset\,(x) = 0.1818e^{-3.2x} + 0.5099e^{-0.9423x} + 0.2808e^{-0.4029x} + 0.02817e^{-0.2016x}$$

$$a = \frac{0.8554a_0}{Z_1^{0.23} + Z_2^{0.23}} \qquad and \qquad \frac{r_{ij}}{a} = x$$

a_0 = 0.539 Å (Bohr radius), $\epsilon_0 = 8.85 \times 10^{-12}$ F/m (vacuum permittivity) and $\Phi(x)$ is the screening function. The simulations were performed on a cluster facility with Xeon-Gold 6150 CPU on 4 nodes and 64 cores. The MD simulations require short time-steps (of the order of fs) for numerical stability and have limitations in terms of time-scales. This poses

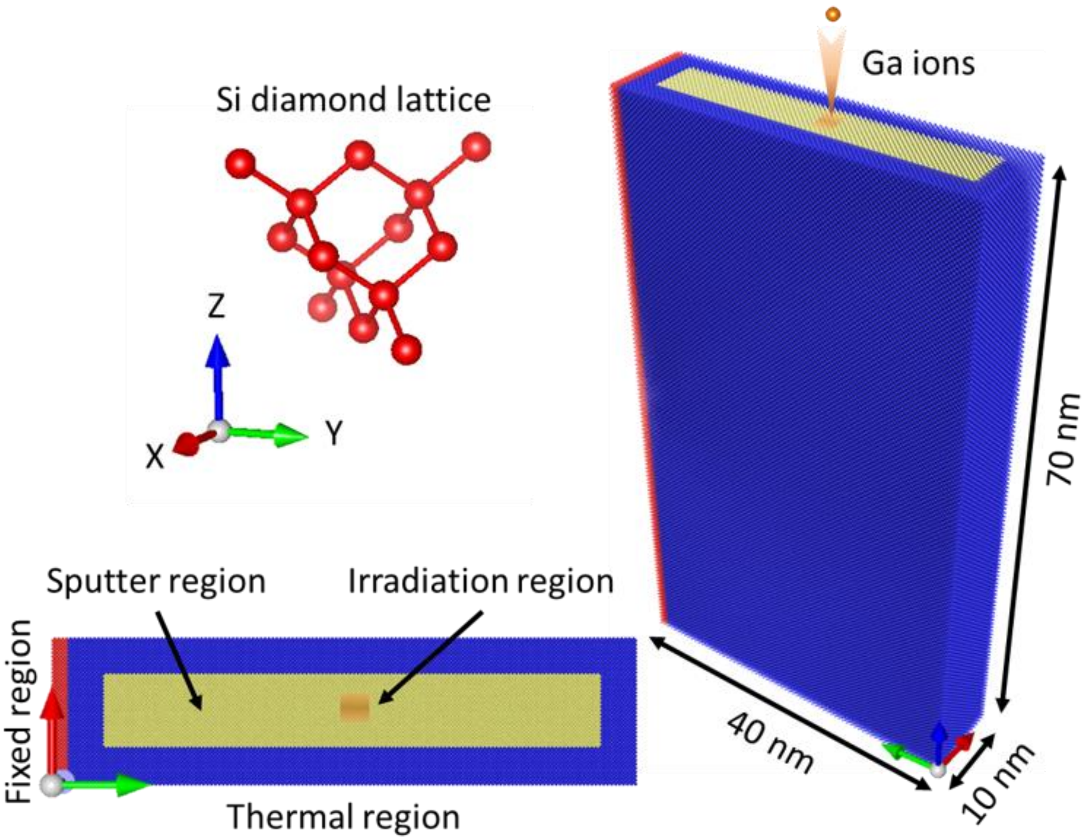

Figure 6.2: MD Simulation of ion irradiation of nanostructures: Si diamond lattice with corresponding coordinate axes and MD simulation set-up, top view and 3D view showing simulation regions and incident Ga ions

challenges for large computations with the available computational resources, especially for the large geometry employed in this work, where the simulation region is defined as 40 nm×10 nm×70 nm containing approximately 1.4 million atoms. Non-periodic finite boundary conditions were employed and a 1 nm thin region of simulation region in *x*-direction was fixed in space to mimic the experimental configuration of the Si NWs employed in this study. The atoms shown in red (fixed region) are immobile through the duration of the simulation. The simulations were performed in a microcanonical (NVE) ensemble, and a variable time-step (1−0.001 fs) was employed on the go to ensure that the atomic displacements in any time-step do not exceed 0.02 Å. An initial time was given for thermal equilibrium until the sputter region atoms come to the room temperature (300 K).

A total of 200 Ga ions were fired randomly on the simulation sputter region at a distance 2 nm above from the surface in an area of 2 nm×2 nm at an incidence angle of 88 degrees (to avoid ion channeling effects, if any), after the thermal equilibrium was maintained. Ga ions were fired corresponding to the ion beam dose of $2.5\times10^{13} - 8.75\times10^{14}$ ions/cm^2, like the ion dose range where the bending reversal in the experiments at 30 kV was observed. The simulations were performed using large scale atomic/molecular massively parallel simulator (LAMMPS) [201], and the results are visualized using the open visualization tool (Ovito) [202]. A thermal spike regime occurs during each incident ions in cascade MD simulations, which requires energy dissipation to maintain the room temperature. This was achieved using a thermostat region of 2.5 nm thickness maintained at 300 K. The atoms in blue shows thermal region employed to dissipate the thermal energy produced after each ion collision via transfer of its kinetic energy. The atoms in yellow are sputter region and used for ion irradiation and production of collision cascade. The Ga ions were fired one at a time, with a velocity corresponding to ion beam energy of 30 kV, and sufficient relaxation time (~25 ps) was provided between each incident ion to allow the thermostat region to dissipate the heat generated and sputter region to come back at room temperature. Figure 6.3 (a) shows temperature profile of the sputter region during ion irradiations. It can be observed that the ion irradiation leads to a sudden increase in the temperature, followed by a gradual decrease during relaxation period. Each incident ion, due to its interaction with lattice atoms and transfer of kinetic energy, develops a thermal spike. The relaxation time after each incident ion ensures that the room temperature is maintained. A typical profile of temperature spike from room temperature and subsequent cooling due to relaxation time is shown in Figure 6.3 (b). It is worth mentioning here that the inclusion of a relaxation period (~25 ps) in the MD simulations for thermal energy dissipation, leads to a high current value (~6.4 nA). The relaxation time used in this work is comparable to the previously used values for MD simulation studies for ion irradiation of materials [154], [203], [204]. Such high value of current employed in the MD simulations, however, is three order of magnitude higher than the current used in experiments (1.5 pA) and poses a limitation in the MD simulations. To employ a small current of 1.5 pA, a high relaxation time (~10^5 ps) would be required and is infeasible for currently available computation

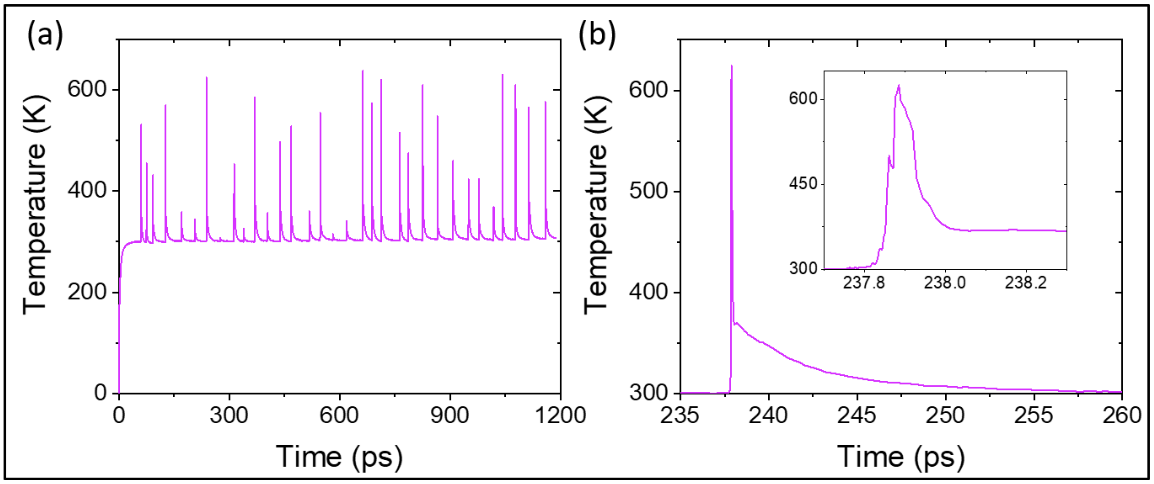

Figure 6.3: (a) Temperature evolution of simulation sputter region, with (b) Showing a typical thermal spike profile corresponding to an incident ion and subsequent cooling

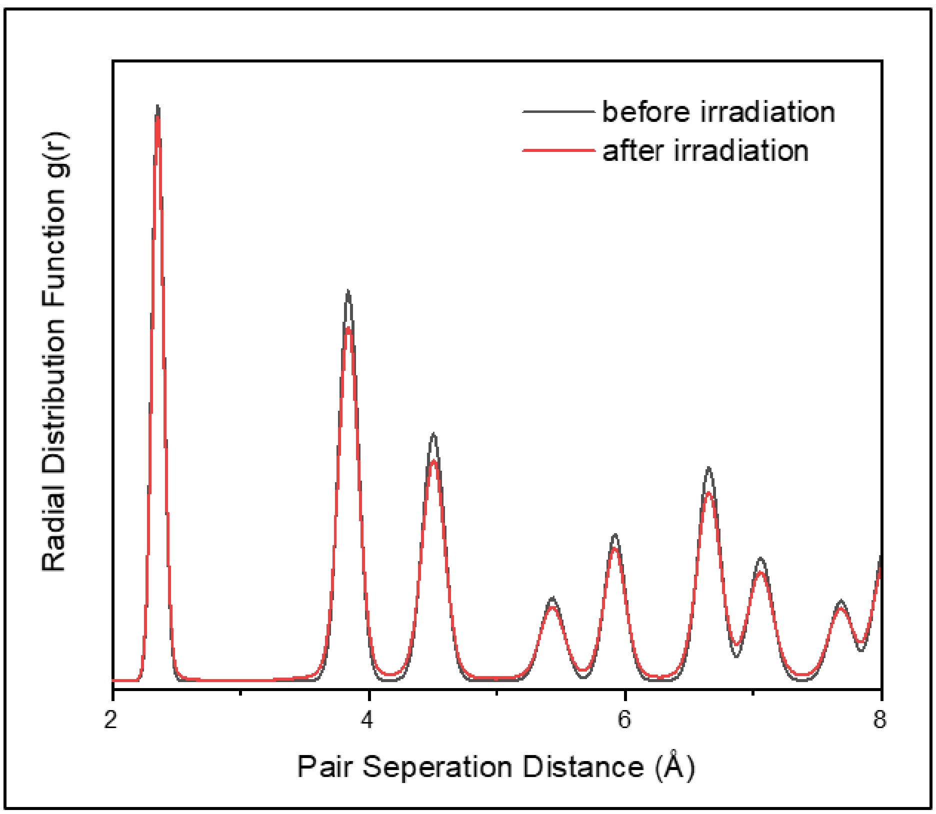

Figure 6.4: Radial distribution function of sputter region before and after ion irradiation

facilities. Thus, in order to arrive at meaningful results with the available computational resources, reasonable values (~25 ps, providing thermal equilibrium) of relaxation time are used in the MD simulations.

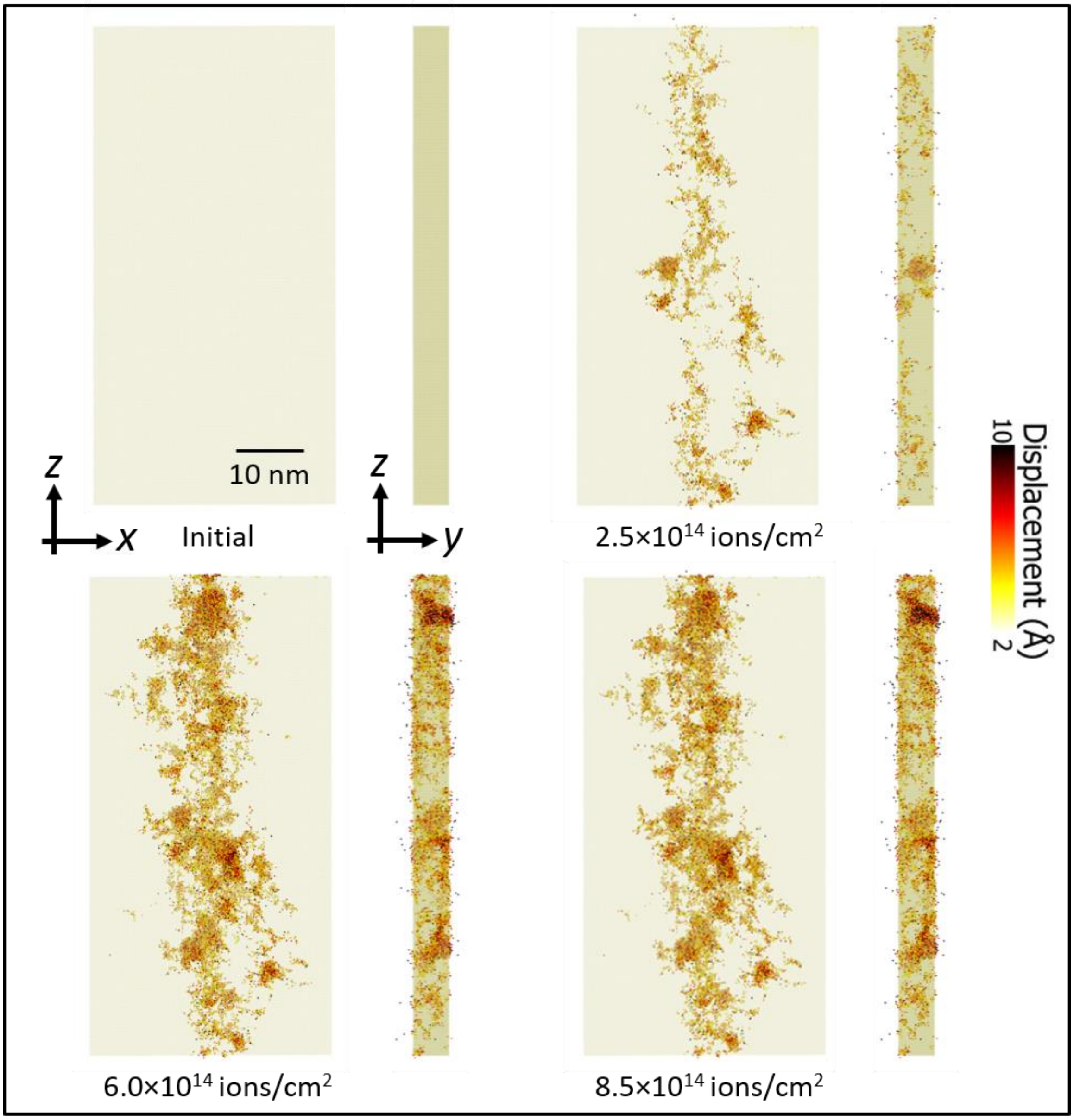

Figure 6.5: Initial lattice configuration and atomic displacements showing development of collision cascade at increasing ion doses of 2.5×10^{14}, 6.0×10^{14}, 8.5×10^{14} ions/cm^2 in *xz* plane at *y*=20 nm and *yz* plane at *x*=5 nm

To characterize the ion induced damage of Si lattice, the radial distribution function (RDF) *g(r)* is further calculated. Figure 6.4 shows the calculated RDF before and after ion irradiation. The discrete peaks observed in the RDF are characteristics of a crystalline structure, and it can be observed in that the peak intensities are lowered for ion irradiated Si. This indicates the formation of amorphous regions of Si by ion irradiations. The evolution of ion irradiation induced damage in Si lattice with increasing ion dose is shown in Figure 6.5. The Si atoms leaving the simulation box were considered sputtered and removed from the simulations for further calculations. The Si atoms were found to leave only from the irradiated region (sputter region) due to ion induced sputtering action, and do not leave from any other side that is not irradiated. All the results are shown after thermal equilibrium. The temperature spikes during ion irradiation introduce a significant damage in the lattice. The inclusion of relaxation time after each irradiation, however, ensures that the thermal energy is completely dissipated. The initial configuration of Si lattice and atomic displacements showing development of collision cascade and ion induced damage are represented in Figure 6.5 at increasing ion doses of 2.5×10^{14}, 6.0×10^{14}, 8.5×10^{14} ions/cm^2 in *xz* and *yz* plane. The evolution and development of growing defects clusters can be observed with increasing ion dose, and it is found that Si atoms undergo atomic displacements as large as 10 Å inside the lattice. It can also be noticed here that the defects clusters are found to spread across the entire Si depth in the simulations. Such spread of atomic displacements and damage formation in Si lattice through MD simulations provide higher penetration depth compared to the MC simulations. This can be attributed to the crystal orientation and channelling effects [199], which are neglected in the MC simulations.

To further understand the effect of ion irradiation induced damage on bending, the stresses generated in the Si lattice due to ion irradiations are calculated. The evolution of the generated stresses due to ion irradiations, in principle, should govern the nanostructure bending. Although, a macroscopic quantity, stresses can be computed through microscopic forces, configurations; and atomistic simulations have been used previously for continuum stress calculations [205], [206]. In particular, MD simulations have also been employed to study atomic scale effects and instability in thin film lamella during FIB milling for TEM sample preparation [207], and FIB milling of strained Si [199]. MD simulations can provide useful insights for ion induced bending through the consideration of stress variation within the nanoscale objects. The atomic stresses can be further averaged over a defined volume to arrive at meaningful average stresses. There are multiple approaches to calculate the stresses in atomistic simulations; a simpler and most widely adopted approach based on virial theorem [208], [209] is used for the calculation of localized stresses generated in the lattice due to ion irradiations. A six component symmetric virial stress tensor for i^{th} atom is given by the following equation [206]:

$$\sigma_{ij} = -\left(m v_i v_j + \frac{1}{2} \sum_{n=1}^{N_p} {}^{n}r_i F_j \right) \tag{6.3}$$

where, m is mass and v_i is velocity of the atom. The first term in the above equation represents the contribution from kinetic energy. F_j are force components of pair-wise interactions and summation is within the cut-off distance of atom's neighbors, with ${}^{n}r_i$ being the displacement components of neighbor atoms relative to i^{th} atom, further details can be found in the reference [206]. The calculated virial stress for each atom can be used for estimation of continuum mechanical stress. The virial stresses are an average of the atomic stress (computed using the atomic volume) over a larger volume that is used. The atomic volumes were evaluated employing the Voronoi tessellation of the atoms in the simulation box using the open source Voro++ package [210]. The stresses generated in the simulation region due to ion irradiations, calculated using the virial theorem are shown in Figure 6.6. The stress distributions in xz plane at y=20 nm, and yz plane at x=5 nm are shown, including the magnified views of irradiated regions. The initial stress distribution in Si is shown in Figure 6.6 (a), while Figure 6.6 (b)-(d) represent stress distribution in Si due to ion irradiation at ion doses of 2.5×10^{14}, 6.0×10^{14}, and 8.5×10^{14} ions/cm^2 respectively. These stress distributions from MD simulation can be used for ion irradiation induced bending of nanostructures.

The ion irradiation of nanostructures leads to the development of localized stresses in the lattice, which in turn governs the bending of the nanostructures. At low ion doses

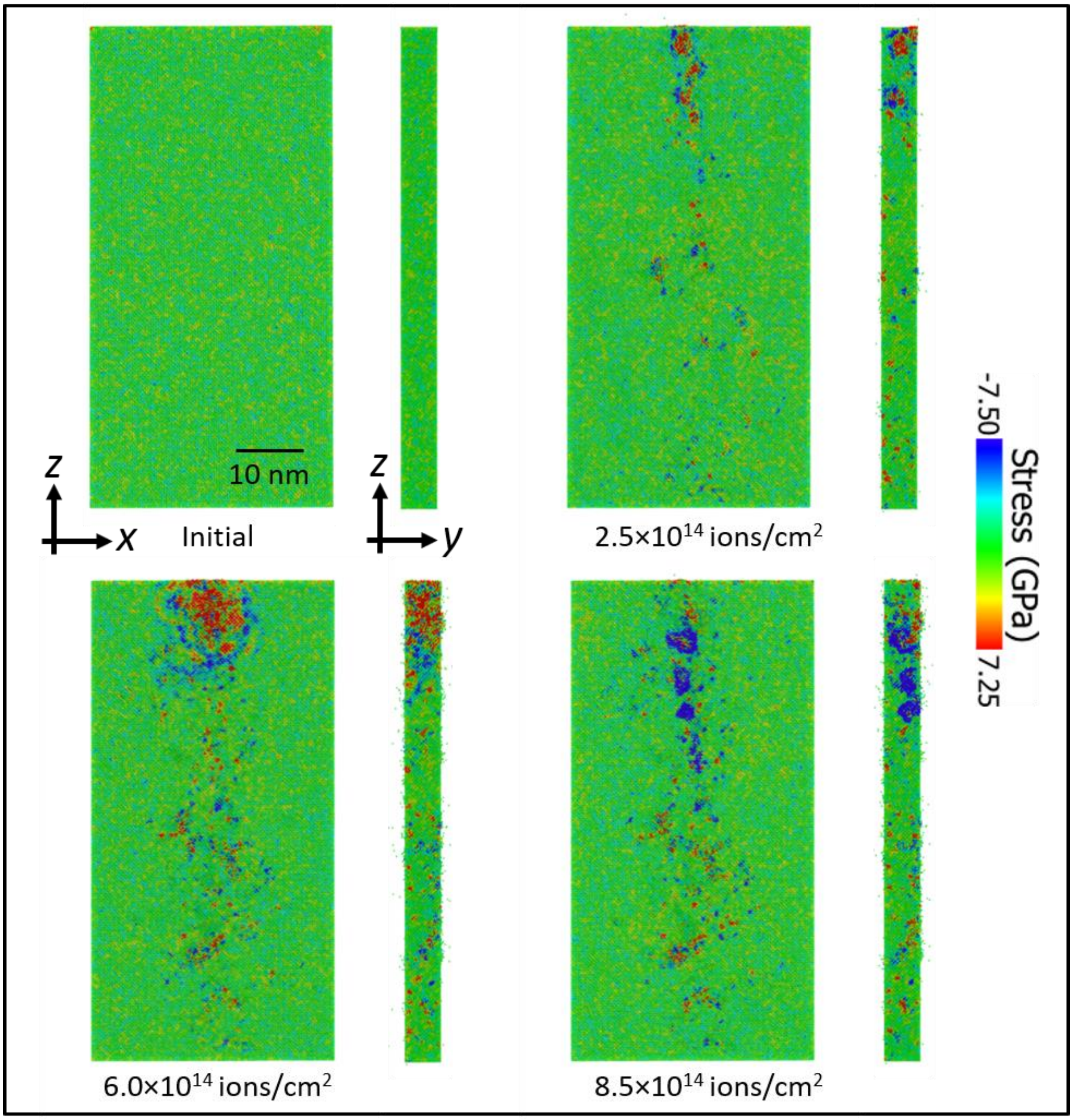

Figure 6.6: Ion irradiation induced stress generation: Initial stress distribution and evolution of localized tensile to compressive stresses towards irradiated region at increasing ion doses of 2.5×10^{14}, 6.0×10^{14}, and 8.5×10^{14} ions/cm^2 in *xz* plane at *y*=20 nm, and *yz* plane at *x*=5 nm

(~2.5×10^{14}-6.0×10^{14} ions/cm^2, Figure 6.6 (b)-(c)), the tensile stresses are observed to develop towards ion irradiated region. With further increase of ion dose, the reversal of stresses is observed, and compressive stresses are developed at high ion doses (~8.5×10^{14}

ions/cm^2, Figure 6.6 (b)). Such reversal of developed stresses in the simulations is close to the experimental ion dose (~7×10^{14} ions/cm^2), where the bending reversal was observed. The stress generation and nanostructure bending process with increasing ion dose can be characterized by two stages,

Low dose ion irradiation: In the first stage of bending at low dose ion irradiations, localized tensile stresses are generated in Si (Figure 6.6 (b)-(c)). At low doses, the target is still crystalline and small volume of the target is damaged. First few atoms irradiating the target creates vacancies towards the surface and interstitials formation in the target as the Si atoms are displaced. The generation of the surface vacancies at low ion doses, causing the surface reconstruction, develops the localized tensile stresses.

***High dose ion irradiation**:* In the second stage of bending with increasing ion dose, localized compressive stresses are generated (Figure 6.6 (d)). At increasing ion doses, the target is amorphized and irradiation surface is damaged heavily with ion implantation and formation of interstitial clusters along the target depth. The formation of interstitial clusters and surface reorganization at high ion doses generates the localized compressive stresses.

The tensile-compressive evolution of stresses in the lattice with increased ion doses is in accordance with the Ar irradiation of Si reported in the literature [211]. The generation and evolution of such localized tensile to compressive stresses in the lattice due to ion irradiations is the driving mechanism for ion induced bidirectional bending of nanostructures. The realization of localized stresses with ion dose provide an opportunity to estimate the continuum bending through transfer of stresses to finite element simulations. To illustrate the effect of such localized stress generation and evaluate the bending phenomenon, the Si NWs are further subjected to the calculated stresses and bending is observed through the finite element analysis.

6.3.3 Finite Element Analysis

Linear elastic deflection simulation using finite element analysis is performed to study the deflection of Si cantilever assuming continuum solid material. The material is considered as homogeneous and elastic. It should be noted that in angstrom scale material may lack continuum property, however deflection nature driven by the lattice stress generation will be the same. The height of the cantilever is taken as 70 nm, young's modulus E = 188 GPa, and poison ratio μ = 0.4 for Si [212]. For a cantilever beam, with (L^3/I) constant, the deflection remains same. Here, L is length of cantilever and I is moment of inertia of the

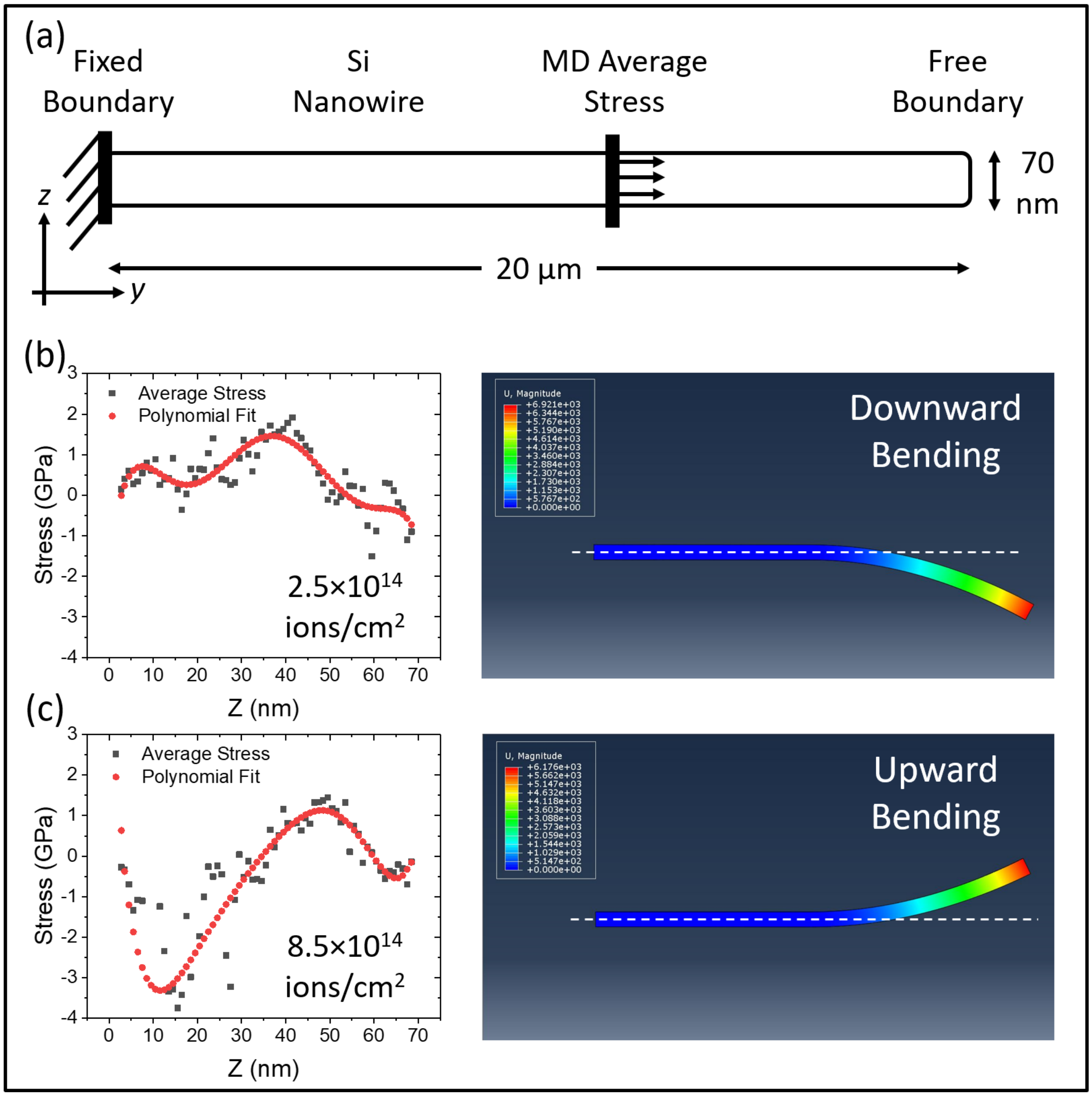

Figure 6.7: Finite element analysis of ion irradiation induced bidirectional bending of nanostructures: (a) Schematic diagram showing simulation set-up and boundary conditions. Average stress distribution along z-axis and development of downward, upward bending of Si NW at increasing ion doses of (b) 2.5×10^{14}, (c) 8.5×10^{14} ions/cm^2

cross-section, which offers resistance for the deflection. So accordingly, length and width of the cantilever can be set to maintain the constant value of *(L^3/I)*. This beam is assumed as stress free i.e. there is no residual stress of any kind prior to the interaction of ions. The encastre boundary condition, to fix the linear and rotational motion, is applied at fixed end of the beam. This ensures all six degrees of freedom of the beam are restricted at fixed end. The variation of average stress distribution along z-direction is estimated from MD simulations. Atom coordinates and corresponding stress tensor are extracted from MD simulations and used for calculation of average stress distribution. The Si target geometry is sliced along z-axis and for all the Si atoms belonging to a slice, hydraulic stress is calculated to get average stress values along the z-direction. The calculated average stress is applied along z-axis in FEA simulations. The simulation set-up and boundary conditions in FEA simulation are shown schematically in Figure 6.7 (a). Simulations are performed using Abaqus/CAE 6.14-2. The element type is taken as cubic (4 nodes per side) e.g. beam. This is the simplest element type for beam, and computationally efficient to precisely quantify the deflection of a simple cantilever.

Finite element simulations were done for ion dose of 2.5×10^{13} – 8.75×10^{14} ions/cm^2 and the cantilever deflection in the y-direction is analyzed. Figure 6.7 (b), (c) shows the average stresses and deflection of the cantilever at successive time intervals with increasing ion doses. The average stress values, calculated from the MD simulations along z-direction, are shown with a polynomial fit, exhibiting the variation of stresses. It can be observed that at low ion dose cantilever shows downward deflection, however at high ion doses, the cantilever deflection changes from downward to upward, exhibiting bidirectional bending. At low ion dose (Figure 6.7 (b)), stress is observed to be tensile towards irradiated region, and the stresses vary from tensile to compressive towards un-irradiated region. Such stress variation results in downward bending of the NW, evident from the finite element simulation result in Figure 6.7 (b). With increasing ion dose (Figure 6.7 (c)), on the other hand, compressive stresses are generated towards irradiated region, and the stresses vary from compressive to tensile towards un-irradiated region. Such stress development results in reversal of bending direction and upward bending of the NW is observed, evident from the FEA simulation result in Figure 6.7 (c). The main contribution for controlling of upward bending angle from the simulation results is the formation of interstitial clusters along the target depth with increasing ion dose. The bending rate, as calculated from the FEA simulations, is ~6.25×10^{-14} degree/ions/cm^2, and the NW is found to undergo bending at a faster rate in contrast to the experiments (~4.45×10^{-14} degree/ions/cm^2). Such difference in the bending rate in the simulations and experiments, may have been arising from the time scale difference in the experiments and MD simulations and cannot be avoided due to the MD time scale limitations and computational resources. However, it is worth mentioning that the overall trend and the observation of bending reversal with increased ion dose in the simulations, is in accordance with the experiments and confirm the ion induced bidirectional bending of nanostructures. The FEA simulations carried out using the different thickness of Si cantilever (70-1000 nm), suggested the decrease in the bending angle/rate with increasing thickness, and the cantilever exhibited almost negligible bending at 1000 nm. Thus, the multiscale modelling results provide bending prediction on a wide scale range and suggesting the constraint on suspended Si nanostructure thickness to be below 1000 nm for ion induced bending at 30 kV. Further, the developed multiscale model can be extended to other materials, thin films (such as Si_3N_4, Au, Ge, Al etc.) or ions (He, Xe, Ar, Ne etc.) via incorporating the interaction potential of ions with different materials in MD simulations for atomic scale origin of stresses, and material properties in FEA simulations for bending direction. In summary, the developed approach for controlled bidirectional manipulation of nanostructures and multiscale modelling for atomic scale origin of the two-regime bending provide insight for 3D nanofabrication towards realization of novel nanostructures with anticipated functionalities, and unique applications such as sub 100 nm sample preparations for atom probe tomography (APT), transmission electron microscopy (TEM) etc. in microscopy and microanalysis.

6.4 Summary

In conclusion, this work presented ion irradiation induced bidirectional bending of nanostructures and detailed investigation of bending mechanism through a multiscale modelling approach. The presented multiscale modelling approach: MD simulations for atomic scale ion solid interactions combined with finite element analysis for estimating continuum bending directions pave the way towards understanding of bi-directional nature of bending exhibited through the nanostructures with controlled ion dose. The MD simulations results revealed the development of localized stresses due to ion irradiation induced defects and atomic displacements. The developed stresses evolve from tensile to compressive with increasing ion dose, which leads to the alternate bending directions as evident from finite element analysis. The computational results provided a detailed understanding of the ion induced bidirectional bending process and atomic-scale origin of localized stresses for controlled manipulation of nanostructures.

Chapter 7. Conclusion and Outlook

7.1 Conclusion

In this work, focused ion beam fabrication of novel 2D/3D nanoscale structures is presented. Following is a brief summary of the work,

- Gaussian pillar shaped nanostructures are developed on Si for antireflection and light trapping properties. The unique geometry of Gaussian pillars with a smaller tip and extended base enabled efficient light trapping, observed through experiments, light reflection and absorption density calculations. Given the tunable nature and nanoscale feature size along with fabrication uniformity, the developed nanofabrication approach is suitable for rapid prototyping applications.
- A novel approach for color filtering in reflection mode via direct fabrication of subwavelength nanostructures on high-index, low-loss, and inexpensive Si substrate was developed. Nanostructures having a unique geometry of tapered holes were fabricated exploiting the Gaussian nature of a gallium source focused ion beam. The proposed approach was demonstrated for color printing applications.
- A novel approach of fabricating freestanding 3D Si nanostructures by combining ion beam implantation with bulk structuration via wet etching was developed. The application of the proposed approach was further demonstrated for fabrication of various suspended and 3D nanostructures such as nanomesh etc. including freestanding Si nanostructures over pyramid array, which were exhibited for unique optical properties. The developed approach for fabrication of various suspended and 3D structures exhibit process capability and will be useful for fabrication of Si micro/nano-mechanical resonators, sensors and semiconductor devices.
- *In-situ* ion induced bending were further carried out for developing designed complex 3D nanostructures. The bidirectional nature of ion induced bending provides an additional degree of freedom, and the proposed method can be utilized for 3D nanofabrication and manipulation of nanostructures for desired functionalities. This work will be of utter importance for 3D nanofabrication with

promising nanoscale-controlled manipulation, strain engineering of nanostructures and will open new avenues in the diverse field of ion beams and applications beyond material science for realization of future nanoscale devices.

- A multiscale modeling approach is further developed for detailed understanding of the ion irradiation induced bending of nanostructures. MD simulations for atomic scale ion solid interactions provided ion irradiation induced defects and atomic scale origin of localized stresses in Si lattice. The developed localized stresses are found to evolve from tensile to compressive with increasing ion dose. The finite element analysis for estimating continuum bending directions, through the application of developed localized stresses, revealed the bi-directional nature of bending exhibited through the nanostructures, in accordance with the experiments.

7.2 Directions for Future Research

High resolution imaging techniques, such as transmission electron microscopy (TEM) and atom probe tomography (APT), are powerful tools for both materials and biological science. The success of imaging, however, rely heavily on sample preparation methods posing several challenges. Samples prepared for TEM need to be electron transparent (50-100 nm). FIB has been a popular choice for site-specific TEM sample from bulk specimens and in-situ lift-out using a micromanipulator [213], [214]. This method, however, is time consuming and requires significant efforts and operator skills despite some recent efforts on process automation.

Controlled manipulation of nanostructures developed in the current work can be employed and extended further for a novel sample preparation method capitalizing *in-situ* ion induced controlled bending for TEM applications. Gallium FIB in a dual beam FEI Quanta 3D system used for fabrication of suspended Si nanowires (NWs), which were subsequently manipulated controllably through ion irradiation induced bending to "*stand-out*" until becoming vertical to the sample surface. The "*stand-out*" method is shown step-by-step

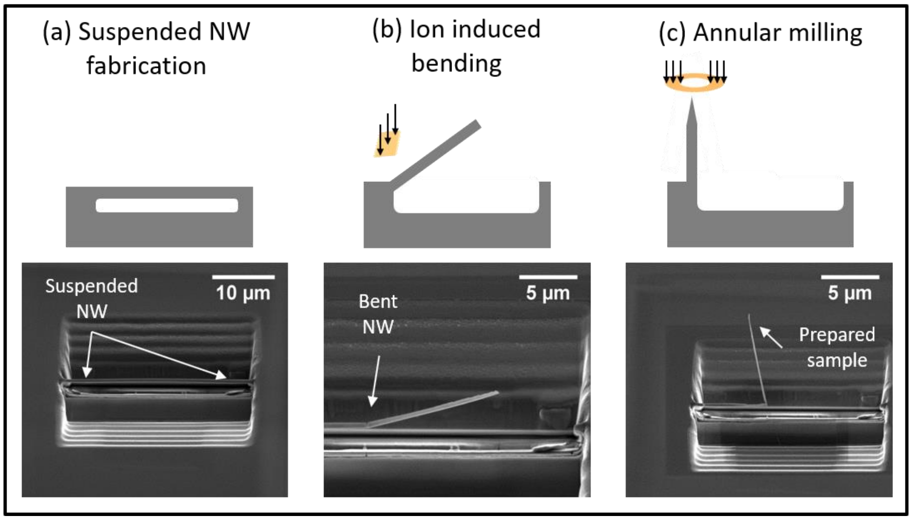

Figure 7.1: Step-by-step illustration of Stand-out sample preparation method for TEM/APT in a dual beam FIB-SEM microscope: Schematic diagrams and SEM images showing (a) Fabrication of suspended nanowire (NW), (b) Ion induced bending for vertical alignment, (c) Annular milling for final polishing

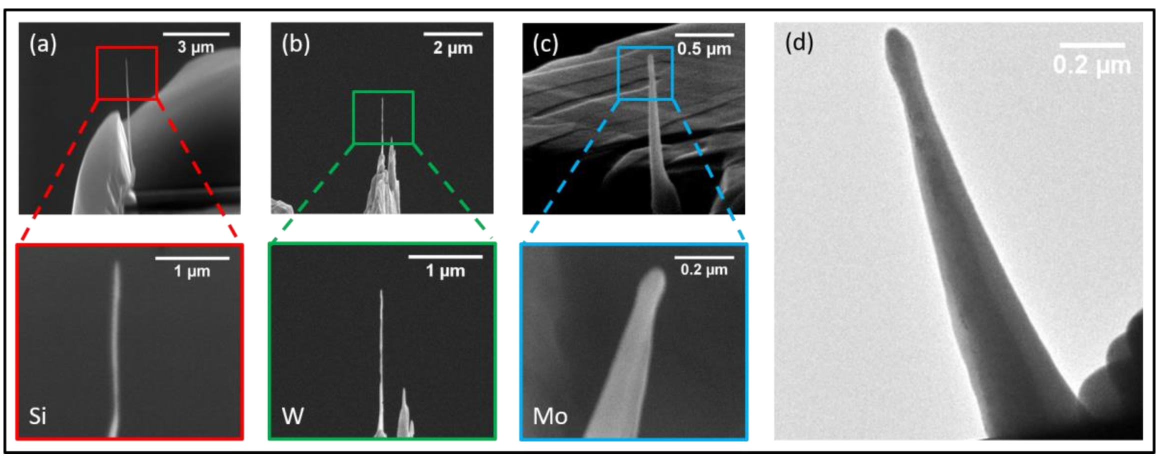

Figure 7.2: SEM images of samples prepared on different materials using stand-out method in a dual beam FIB-SEM microscope: sub 100 nm sample of (a) Si, (b) W, (c) Mo, (d) TEM image of a Mo sample prepared by the "stand-out" approach.

through schematics and scanning electron microscopic (SEM) images (Figure 7.1). Trapezoidal trenches on the planar surface are milled to obtain a thin specimen wall, which is further used to obtain the suspended NW (100-200 nm) employing FIB under-milling

(Figure 7.1 (a)). This suspended NW is cut at one end to enable the bending through controlled dose ion irradiation at the other end (Figure 7.1 (b)). The NW gradually aligns towards incident ion beam with increasing ion dose. The implanted-ions, generation of point defects, and dislocated lattice atoms contributes to the local development of stresses and plastic deformation. Further, annular milling is employed to thin the NW to enable the electron transparency required for TEM imaging (Figure 7.1 (c)).

The proposed methodology is suitable for a variety of materials and demonstrated through TEM sample preparation for different materials such as Silicon (Si), Tungsten (W), Molybdenum (Mo) in Figure 7.2 (a)-(c). A TEM image of a prepared Mo sample is presented (Figure 7.2 (d)). Additionally, the developed *stand-out* method has the potential for atom probe tomography (APT) sample preparation in the form of a sharp needle with an end radius 50-100 nm without requiring the lift-out (Figure 7.2). Thus providing a unique route for correlative imaging with TEM and APT yielding structural and chemical composition not possible previously. In summary, "*stand-out"*, a novel sample preparation method encompassing different materials through *in-situ* ion induced bending in a dual beam FIB-SEM microscope provides a novel approach with a huge potential for TEM/APT applications even in a cryogenic environment. The studies presented in this work will lay foundation for potential applications in multidisciplinary fields with future implications of FIB beyond material science, especially with the rise of plasma FIB.

References

[1] J. Melngailis, “Focused ion beam technology and applications,” *J Vac Sci Technol B*, vol. 5, no. 2, pp. 469–495, 1987.

[2] S. Reyntjens and R. Puers, “A review of focused ion beam applications in microsystem technology,” *J. Micromechanics Microengineering*, vol. 11, no. 4, pp. 287–300, 2001.

[3] C. Lehrer, L. Frey, S. Petersen, and H. Ryssel, “Limitations of focused ion beam nanomachining,” *J. Vac. Sci. Technol. B Microelectron. Nanometer Struct.*, vol. 19, no. 6, p. 2533, 2001.

[4] C. S. Kim, S. H. Ahn, and D. Y. Jang, “Review: Developments in micro/nanoscale fabrication by focused ion beams,” *Vacuum*, vol. 86, no. 8, pp. 1014–1035, 2012.

[5] R. Mote and L. Xiaomin, “Focused Ion Beam (FIB) Nanofinishing for Ultra-Thin TEM Sample Preparation,” in *Nanofinishing Science and Technology*, 0 vols., CRC Press, 2017, pp. 155–176.

[6] W. Li *et al.*, “A Review of Recent Applications of Ion Beam Techniques on Nanomaterial Surface Modification: Design of Nanostructures and Energy Harvesting,” *Small*, vol. 15, no. 31, p. 1901820, 2019.

[7] J. Fu and S. Joshi, “Optimization Based Geometric Modeling of Nano/Micro Scale Ion Milling of Organic Materials for Multidimensional Bioimaging,” *J. Nanotechnol. Eng. Med.*, vol. 1, no. 3, pp. 031003–031003, Aug. 2010.

[8] A. Al-Abboodi, J. Fu, P. M. Doran, and P. P. Y. Chan, “Three-dimensional nanocharacterization of porous hydrogel with ion and electron beams,” *Biotechnol. Bioeng.*, vol. 110, no. 1, pp. 318–326, Jan. 2013.

[9] V. R. Adineh, B. Liu, R. Rajan, W. Yan, and J. Fu, “Multidimensional characterisation of biomechanical structures by combining Atomic Force Microscopy and Focused Ion Beam: A study of the rat whisker,” *Acta Biomater.*, vol. 21, pp. 132–141, Jul. 2015.

[10] F. De Angelis *et al.*, “3D Hollow Nanostructures as Building Blocks for Multifunctional Plasmonics,” *Nano Lett.*, vol. 13, no. 8, pp. 3553–3558, Aug. 2013.

[11] M. F. Abdullah *et al.*, “Research and development efforts on texturization to reduce the optical losses at front surface of silicon solar cell,” *Renew. Sustain. Energy Rev.*, vol. 66, pp. 380–398, Dec. 2016.

[12] J. Zhu *et al.*, “Optical Absorption Enhancement in Amorphous Silicon Nanowire and Nanocone Arrays,” *Nano Lett.*, vol. 9, no. 1, pp. 279–282, Jan. 2009.

[13] X. Xiong, S.-C. Jiang, Y.-H. Hu, R.-W. Peng, and M. Wang, “Structured Metal Film as a Perfect Absorber,” *Adv. Mater.*, vol. 25, no. 29, pp. 3994–4000, 2013.

[14] U. T. Sanli *et al.*, “3D Nanoprinted Plastic Kinoform X-Ray Optics,” *Adv. Mater.*, vol. 30, no. 36, p. 1802503, 2018.

[15] J.-R. Fan, J. Zhu, W.-G. Wu, and Y. Huang, “Plasmonic Metasurfaces Based on Nanopin-Cavity Resonator for Quantitative Colorimetric Ricin Sensing,” *Small*, vol. 13, no. 1, p. 1601710, 2017.

[16] G.-T. Yun *et al.*, “Springtail-inspired superomniphobic surface with extreme pressure resistance,” *Sci. Adv.*, vol. 4, no. 8, p. eaat4978, Aug. 2018.

[17] V. Narasimhan *et al.*, “Multifunctional biophotonic nanostructures inspired by the longtail glasswing butterfly for medical devices,” *Nat. Nanotechnol.*, vol. 13, no. 6, pp. 512–519, Jun. 2018.

[18] A. Elbourne *et al.*, “Multi-directional electrodeposited gold nanospikes for antibacterial surface applications,” *Nanoscale Adv.*, vol. 1, no. 1, pp. 203–212, Jan. 2019.

[19] V.-C. Su, C. H. Chu, G. Sun, and D. P. Tsai, “Advances in optical metasurfaces: fabrication and applications [Invited],” *Opt. Express*, vol. 26, no. 10, pp. 13148–13182, May 2018.

[20] Q. Wang and W. Zhou, “Direct fabrication of cone array microstructure on monocrystalline silicon surface by femtosecond laser texturing,” *Opt. Mater.*, vol. 72, pp. 508–512, Oct. 2017.

[21] A. Modrić-Šahbazović *et al.*, “Silicon nanostructuring by Ag ions implantation through nanosphere lithography mask,” *Opt. Mater.*, vol. 88, pp. 508–515, Feb. 2019.

[22] M. F. Abdullah *et al.*, “Research and development efforts on texturization to reduce the optical losses at front surface of silicon solar cell,” *Renew. Sustain. Energy Rev.*, vol. 66, pp. 380–398, Dec. 2016.

[23] A. A. Tseng, “Recent Developments in Nanofabrication Using Focused Ion Beams,” *Small*, vol. 1, no. 10, pp. 924–939, Oct. 2005.

[24] X. Jiang, S. Hu, Z. Li, J. Lv, and G. Si, “Fabrication and characterization of plasmonic nanorods with high aspect ratios,” *Opt. Mater.*, vol. 58, pp. 323–326, Aug. 2016.

[25] H. Högström, S. Valizadeh, and C. G. Ribbing, “Optical excitation of surface phonon polaritons in silicon carbide by a hole array fabricated by a focused ion beam,” *Opt. Mater.*, vol. 30, no. 2, pp. 328–333, Oct. 2007.

[26] M. J. Vasile, Z. Niu, R. Nassar, W. Zhang, and S. Liu, “Focused ion beam milling: Depth control for three-dimensional microfabrication,” *J. Vac. Sci. Technol. B Microelectron. Nanometer Struct.*, vol. 15, no. 6, p. 2350, 1997.

[27] Y. Fu and N. K. A. Bryan, “Fabrication of three-dimensional microstructures by two-dimensional slice by slice approaching via focused ion beam milling,” *J. Vac. Sci. Technol. B Microelectron. Nanometer Struct.*, vol. 22, no. 4, p. 1672, 2004.

[28] C. S. Kim, J. Park, W. S. Chu, D. Y. Jang, S. D. Kim, and S. H. Ahn, “Fabrication of silicon micro-mould for polymer replication using focused ion beam,” *Microelectron. Eng.*, vol. 86, no. 4–6, pp. 556–560, 2009.

[29] R. Qin, J. Fu, Z. Yin, and C. Zheng, “Large-scale process optimization for focused ion beam 3-D nanofabrication,” *Int. J. Adv. Manuf. Technol.*, vol. 64, no. 1–4, pp. 587–600, Aug. 2012.

[30] H. X. Qian, W. Zhou, J. Miao, L. E. N. Lim, and X. R. Zeng, “Fabrication of Si microstructures using focused ion beam implantation and reactive ion etching,” *J. Micromechanics Microengineering*, vol. 18, no. 3, p. 035003, 2008.

[31] I. Utke, P. Hoffmann, and J. Melngailis, “Gas-assisted focused electron beam and ion beam processing and fabrication,” *J. Vac. Sci. Technol. B*, vol. 26, no. 4, pp. 1197–1276, Jul. 2008.

[32] A. Sabouri, C. J. Anthony, J. Bowen, V. Vishnyakov, and P. D. Prewett, "The effects of dwell time on focused ion beam machining of silicon," *Microelectron. Eng.*, vol. 121, pp. 24–26, Jun. 2014.

[33] C. Lehrer, L. Frey, S. Petersen, and H. Ryssel, "Limitations of focused ion beam nanomachining," *J. Vac. Sci. Technol. B Microelectron. Nanometer Struct.*, vol. 19, no. 6, p. 2533, 2001.

[34] S. Alaie *et al.*, "Thermal conductivity and nanocrystalline structure of platinum deposited by focused ion beam," *Nanotechnology*, vol. 26, no. 8, p. 085704, 2015.

[35] J. F. Ziegler and J. P. Biersack, "The Stopping and Range of Ions in Matter," in *Treatise on Heavy-Ion Science*, D. A. Bromley, Ed. Springer US, 1985, pp. 93–129.

[36] Y. Q. Fu, N. K. A. Bryan, O. N. Shing, and N. P. Hung, "Influence of the Redeposition effect for Focused Ion Beam 3D Micromachining in Silicon," *Int. J. Adv. Manuf. Technol.*, vol. 16, no. 12, pp. 877–880, 2000.

[37] J. Orloff, "High-resolution focused ion beams," *Rev. Sci. Instrum.*, vol. 64, no. 5, pp. 1105–1130, May 1993.

[38] D. P. Adams and M. J. Vasile, "Accurate focused ion beam sculpting of silicon using a variable pixel dwell time approach," *J. Vac. Sci. Technol. B*, vol. 24, no. 2, pp. 836–844, Mar. 2006.

[39] G. A. Glass, J. F. Dias, A. D. Dymnikov, and B. Rout, "900 keV gold ion sputter etching of silicon and metals," *Nucl. Instrum. Methods Phys. Res. Sect. B Beam Interact. Mater. At.*, vol. 266, no. 14, pp. 3330–3331, Jul. 2008.

[40] N. Yao, *Focused Ion Beam Systems: Basics and Applications*. Cambridge University Press, 2007.

[41] T. L. Burnett *et al.*, "Large volume serial section tomography by Xe Plasma FIB dual beam microscopy," *Ultramicroscopy*, vol. 161, pp. 119–129, Feb. 2016.

[42] N. Chekurov, K. Grigoras, A. Peltonen, S. Franssila, and I. Tittonen, "The fabrication of silicon nanostructures by local gallium implantation and cryogenic deep reactive ion etching.," *Nanotechnology*, vol. 20, no. 6, p. 065307, 2009.

[43] N. Chekurov, K. Grigoras, L. Sainiemi, A. Peltonen, I. Tittonen, and S. Franssila, "Dry fabrication of microdevices by the combination of focused ion beam and

cryogenic deep reactive ion etching," *J. Micromechanics Microengineering*, vol. 20, no. 8, p. 085009, 2010.

[44] B. Schmidt, S. Oswald, and L. Bischoff, "Etch Rate Retardation of Ga+ Ion Beam Irradiated Silicon," *J. Electrochem. Soc.*, vol. 152, no. 11, p. G875, 2005.

[45] S. Matsui, "Lithographic approach for 100 nm fabrication by focused ion beam," *J. Vac. Sci. Technol. B Microelectron. Nanometer Struct.*, vol. 4, no. 4, p. 845, 1986.

[46] M. Erdmanis and I. Tittonen, "Focused ion beam high resolution grayscale lithography for silicon-based nanostructures," *Appl. Phys. Lett.*, vol. 104, no. 7, pp. 1–6, 2014.

[47] S. Reyntjens and R. Puers, "Focused ion beam induced deposition: fabrication of three-dimensional microstructures and Young's modulus of the deposited material," *J. Micromechanics Microengineering*, vol. 10, no. 2, pp. 181–188, 2000.

[48] S. Matsui, "Three-Dimensional Nanostructure Fabrication by Focused Ion Beam Chemical Vapor Deposition," *Springer Handb. Nanotechnol.*, pp. 211–229, 2010.

[49] M. Esposito *et al.*, "Nanoscale 3D Chiral Plasmonic Helices with Circular Dichroism at Visible Frequencies," *ACS Photonics*, vol. 2, no. 1, pp. 105–114, Jan. 2015.

[50] R. J. Young, J. R. A. Cleaver, and H. Ahmed, "Gas-assisted focused ion beam etching for microfabrication and inspection," *Microelectron. Eng.*, vol. 11, no. 1, pp. 409–412, Apr. 1990.

[51] J. Munoz-Garcia, L. Vazquez, R. Cuerno, J. A. Sanchez-Garcia, M. Castro, and R. Gago, "Self-Organized Surface Nanopatterning by Ion Beam Sputtering," in *Toward Functional Nanomaterials*, Z. M. Wang, Ed. Springer US, 2009, pp. 323–398.

[52] W. J. MoberlyChan, "Dual-beam focused ion beam/electron microscopy processing and metrology of redeposition during ion–surface 3D interactions, from micromachining to self-organized picostructures," *J. Phys. Condens. Matter*, vol. 21, no. 22, p. 224013, Jun. 2009.

[53] W. J. MoberlyChan and R. Schalek, "Ion Beam Induced Surface Modulations from Nano to Pico: Optimizing Deposition During Erosion and Erosion During Deposition," *MRS Proc.*, vol. 1059, pp. 1059–KK01-07, 2007.

[54] J. E. E. Baglin, “Ion beam nanoscale fabrication and lithography—A review,” *Appl. Surf. Sci.*, vol. 258, no. 9, pp. 4103–4111, Feb. 2012.

[55] B. Ziberi, F. Frost, Th. Höche, and B. Rauschenbach, “Ripple pattern formation on silicon surfaces by low-energy ion-beam erosion: Experiment and theory,” *Phys. Rev. B*, vol. 72, no. 23, p. 235310, Dec. 2005.

[56] Y. Zhang and G. Ran, “Self-assembly of well-ordered and highly uniform nanoripples induced by focused ion beam,” *Phys. E Low-Dimens. Syst. Nanostructures*, vol. 41, no. 10, pp. 1848–1852, Oct. 2009.

[57] Park B. C., Jung K. Y., Song W. Y., O B.-h., and Ahn S. J., “Bending of a Carbon Nanotube in Vacuum Using a Focused Ion Beam,” *Adv. Mater.*, vol. 18, no. 1, pp. 95–98, Nov. 2005.

[58] C. Borschel *et al.*, “Permanent bending and alignment of ZnO nanowires,” *Nanotechnology*, vol. 22, no. 18, p. 185307, 2011.

[59] Z. Liu, H. Du, J. Li, L. Lu, Z.-Y. Li, and N. X. Fang, “Nano-kirigami with giant optical chirality,” *Sci. Adv.*, vol. 4, no. 7, p. eaat4436, Jul. 2018.

[60] S. Lancaster *et al.*, “Focused ion beam implantation for the nucleation of self-catalyzed III-V nanowires,” *Microelectron. Eng.*, vol. 177, pp. 93–97, Jun. 2017.

[61] A. B. Mosberg, S. Myklebost, D. Ren, H. Weman, B. O. Fimland, and A. T. J. van Helvoort, “Evaluating focused ion beam patterning for position-controlled nanowire growth using computer vision,” *J. Phys. Conf. Ser.*, vol. 902, p. 012020, Sep. 2017.

[62] M. T. Langridge, D. C. Cox, R. P. Webb, and V. Stolojan, “The fabrication of aspherical microlenses using focused ion-beam techniques,” *Micron*, vol. 57, pp. 56–66, 2013.

[63] J. Lv *et al.*, “Maskless fabrication of slanted annular aperture arrays,” *Nanotechnology*, vol. 28, no. 22, p. 225302, 2017.

[64] M. V. Gorkunov, O. Y. Rogov, A. V. Kondratov, V. V. Artemov, R. V. Gainutdinov, and A. A. Ezhov, “Chiral visible light metasurface patterned in monocrystalline silicon by focused ion beam,” *Sci. Rep.*, vol. 8, no. 1, p. 11623, Aug. 2018.

[65] S. Gorelick and A. de Marco, “Refractive micro-lenses and micro-axicons in single-crystal lithium niobate,” *Opt. Express*, vol. 26, no. 24, pp. 32324–32331, Nov. 2018.

[66] X. Huang, C. Lou, and H. Zhang, "Experimentally demonstrating plasmonic lattice mode in periodic Ag nanoparticle arrays on quartz trapezoidal pillars," *J. Phys. Appl. Phys.*, vol. 51, no. 46, p. 465101, 2018.

[67] J. Melngailis, "Focused ion beam technology and applications," *J. Vac. Sci. Technol. B Microelectron. Nanometer Struct.*, vol. 5, no. 2, p. 469, 1987.

[68] H. Kuwano, "Dry development of resists exposed to low-energy focused gallium ion beam," *J. Appl. Phys.*, vol. 55, no. 4, p. 1149, 1984.

[69] M. Erdmanis and I. Tittonen, "Focused ion beam high resolution grayscale lithography for silicon-based nanostructures," *Appl. Phys. Lett.*, vol. 104, no. 7, pp. 1–6, 2014.

[70] M. S. Alias *et al.*, "Enhanced Etching, Surface Damage Recovery, and Submicron Patterning of Hybrid Perovskites using a Chemically Gas-Assisted Focused-Ion Beam for Subwavelength Grating Photonic Applications," *J. Phys. Chem. Lett.*, vol. 7, no. 1, pp. 137–142, Jan. 2016.

[71] S. Matsui, T. Kaito, J. Fujita, M. Komuro, K. Kanda, and Y. Haruyama, "Three-dimensional nanostructure fabrication by focused-ion-beam chemical vapor deposition," *J. Vac. Sci. Technol. B Microelectron. Nanometer Struct.*, vol. 18, no. 6, p. 3181, 2000.

[72] J. Fujita, M. Ishida, T. Ichihashi, Y. Ochiai, T. Kaito, and S. Matsui, "Growth of three-dimensional nano-structures using FIB-CVD and its mechanical properties," *Nucl. Instrum. Methods Phys. Res. Sect. B-Beam Interact. Mater. At.*, vol. 206, pp. 472–477, 2003.

[73] T. Hoshino *et al.*, "Development of three-dimensional pattern-generating system for focused-ion-beam chemical-vapor deposition," *J. Vac. Sci. Technol. B*, vol. 21, no. 6, pp. 2732–2736, Nov. 2003.

[74] G. Lalev, S. Dimov, J. Kettle, F. van Delft, and R. Minev, "Data preparation for focused ion beam machining of complex three-dimensional structures," *Proc. Inst. Mech. Eng. Part B J. Eng. Manuf.*, vol. 222, no. 1, pp. 67–76, Jan. 2008.

[75] M. Esposito, V. Tasco, F. Todisco, A. Benedetti, D. Sanvitto, and A. Passaseo, "Three Dimensional Chiral Metamaterial Nanospirals in the Visible Range by

Vertically Compensated Focused Ion Beam Induced-Deposition," *Adv. Opt. Mater.*, vol. 2, no. 2, pp. 154–161, Feb. 2014.

[76] M. J. Burch *et al.*, "3D Nanostructures Grown via Focused Helium Ion Beam Induced Deposition," *Microsc. Microanal.*, vol. 24, no. S1, pp. 332–333, Aug. 2018.

[77] J. Dai, H. Chang, E. Maeda, S. Warisawa, and R. Kometani, "Approaching the resolution limit of W-C nano-gaps using focused ion beam chemical vapour deposition," *Appl. Surf. Sci.*, vol. 427, pp. 422–427, Jan. 2018.

[78] R. Córdoba, A. Ibarra, D. Mailly, and J. M. De Teresa, "Vertical Growth of Superconducting Crystalline Hollow Nanowires by He+ Focused Ion Beam Induced Deposition," *Nano Lett.*, vol. 18, no. 2, pp. 1379–1386, Feb. 2018.

[79] W. Zhou, A. Cuenat, and M. J. Aziz, "Formation of self-organized nanostructures on Ge during focused ion beam sputtering," in *Conference Series-Institute of Physics*, 2003, vol. 180, pp. 625–628.

[80] X. Xu, J. Wu, X. Wang, H. Li, Z. Zhou, and Z. M. Wang, "Site-controlled fabrication of Ga nanodroplets by focused ion beam," *Appl. Phys. Lett.*, vol. 104, no. 13, p. 133104, Mar. 2014.

[81] X. Xu *et al.*, "Ion-Beam-Directed Self-Ordering of Ga Nanodroplets on GaAs Surfaces," *Nanoscale Res. Lett.*, vol. 11, no. 1, p. 38, Jan. 2016.

[82] W. J. Arora, S. Sijbrandij, L. Stern, J. Notte, H. I. Smith, and G. Barbastathis, "Membrane folding by helium ion implantation for three-dimensional device fabrication," *J. Vac. Sci. Technol. B Microelectron. Nanometer Struct. Process. Meas. Phenom.*, vol. 25, no. 6, pp. 2184–2187, Nov. 2007.

[83] M. L. Brongersma, Y. Cui, and S. Fan, "Light management for photovoltaics using high-index nanostructures," *Nat. Mater.*, vol. 13, no. 5, pp. 451–460, May 2014.

[84] M. Burresi, F. Pratesi, F. Riboli, and D. S. Wiersma, "Complex Photonic Structures for Light Harvesting," *Adv. Opt. Mater.*, vol. 3, no. 6, pp. 722–743, Jun. 2015.

[85] P. Balling *et al.*, "Improving the efficiency of solar cells by upconverting sunlight using field enhancement from optimized nano structures," *Opt. Mater.*, vol. 83, pp. 279–289, Sep. 2018.

[86] Q. Li *et al.*, “Absorption enhancement in nanostructured silicon fabricated by self-assembled nanosphere lithography,” *Opt. Mater.*, vol. 70, pp. 165–170, Aug. 2017.

[87] A. Peter Amalathas and M. M. Alkaisi, “Efficient light trapping nanopyramid structures for solar cells patterned using UV nanoimprint lithography,” *Mater. Sci. Semicond. Process.*, vol. 57, pp. 54–58, Jan. 2017.

[88] Y. Hou *et al.*, “Photoelectrocatalysis and electrocatalysis on silicon electrodes decorated with cubane-like clusters,” *J. Photonics Energy*, vol. 2, no. 1, pp. 26001–26016, 2012.

[89] I. M. Peters, H. Hauser, N. Tucher, and B. Bläsi, “Optical Modeling of Honeycomb Textures for Multicrystalline Silicon Solar Cells,” *IEEE Journal of Photovoltaics*, vol. 6, no. 6. pp. 1480–1487, 2016.

[90] J. Wang, Z. Li, N. Singh, and S. Lee, “Highly-ordered vertical Si nanowire/nanowall decorated solar cells,” *Opt. Express*, vol. 19, no. 23, pp. 23078–23084, 2011.

[91] P. Aurang, R. Turan, and H. E. Unalan, “Nanowire decorated, ultra-thin, single crystalline silicon for photovoltaic devices,” *Nanotechnology*, vol. 28, no. 40, p. 405205, 2017.

[92] K. X. Wang, Z. Yu, V. Liu, Y. Cui, and S. Fan, “Absorption Enhancement in Ultrathin Crystalline Silicon Solar Cells with Antireflection and Light-Trapping Nanocone Gratings,” *Nano Lett.*, vol. 12, no. 3, pp. 1616–1619, Mar. 2012.

[93] B. Wang and P. W. Leu, “Enhanced absorption in silicon nanocone arrays for photovoltaics,” *Nanotechnology*, vol. 23, no. 19, p. 194003, May 2012.

[94] Y. Li, P. Gao, Q. Chen, J. Yang, J. Li, and D. He, “Nanostructured semiconductor solar absorbers with near 100% absorption and related light management picture,” *J. Phys. Appl. Phys.*, vol. 49, no. 21, p. 215104, 2016.

[95] M. Hussein, M. F. O. Hameed, N. F. F. Areed, A. Yahia, and S. S. A. Obayya, “Funnel-shaped silicon nanowire for highly efficient light trapping,” *Opt. Lett.*, vol. 41, no. 5, pp. 1010–1013, Mar. 2016.

[96] X. Chen *et al.*, “Wedge-shaped semiconductor nanowall arrays with excellent light management,” *Opt. Lett.*, vol. 42, no. 19, pp. 3928–3931, Oct. 2017.

[97] Y.-S. Park and J. S. Lee, “Correlating Light Absorption with Various Nanostructure Geometries in Vertically Aligned Si Nanowire Arrays,” *ACS Photonics*, Sep. 2017.

[98] S. Zhong, W. Wang, M. Tan, Y. Zhuang, and W. Shen, “Realization of Quasi-Omnidirectional Solar Cells with Superior Electrical Performance by All-Solution-Processed Si Nanopyramids,” *Adv. Sci.*, p. 1700200, Jul. 2017.

[99] J. Proust, A.-L. Fehrembach, F. Bedu, I. Ozerov, and N. Bonod, “Optimized 2D array of thin silicon pillars for efficient antireflective coatings in the visible spectrum,” *Sci. Rep.*, vol. 6, p. 24947, Apr. 2016.

[100] E. D. Palik, *Handbook of optical constants of solids*. Academic Press, 1998.

[101] L. R. Harriott, “Beam-size measurements in focused ion beam systems,” *J. Vac. Sci. Technol. A*, vol. 8, no. 2, pp. 899–901, Mar. 1990.

[102] A. A. Tseng, “Recent developments in micromilling using focused ion beam technology,” *J. Micromechanics Microengineering*, vol. 14, no. 4, p. R15, 2004.

[103] A. Kalburge, A. Konkar, T. R. Ramachandran, P. Chen, and A. Madhukar, “Focused ion beam assisted chemically etched mesas on GaAs(001) and the nature of subsequent molecular beam epitaxial growth,” *J. Appl. Phys.*, vol. 82, no. 2, p. 859, Jun. 1998.

[104] Y. Yamamura, Y. Itikawa, and N. Itoh, “Angular dependence of sputtering yields of monatomic solids,” Jun. 1983.

[105] W.-K. Rhim and K. Ohsaka, “Thermophysical properties measurement of molten silicon by high-temperature electrostatic levitator: density, volume expansion, specific heat capacity, emissivity, surface tension and viscosity,” *J. Cryst. Growth*, vol. 208, no. 1, pp. 313–321, 2000.

[106] W. J. Yang, Z. Q. Ma, X. Tang, C. B. Feng, W. G. Zhao, and P. P. Shi, “Internal quantum efficiency for solar cells,” *Sol. Energy*, vol. 82, no. 2, pp. 106–110, Feb. 2008.

[107] P. Spinelli *et al.*, “Plasmonic light trapping in thin-film Si solar cells,” *J. Opt.*, vol. 14, no. 2, p. 024002, 2012.

[108] G. P. S. Balasubramanian and R. Hull, "Mechanisms of Focused Ion Beam Implantation Damage and Recovery in Si," *J. Electron. Mater.*, vol. 45, no. 6, pp. 3236–3243, Jun. 2016.

[109] Y. J. Xiao, F. Z. Fang, Z. W. Xu, W. Wu, and X. C. Shen, "The study of Ga+ FIB implanting crystal silicon and subsequent annealing," *Nucl. Instrum. Methods Phys. Res. Sect. B Beam Interact. Mater. At.*, vol. 307, pp. 253–256, Jul. 2013.

[110] M. Taguchi *et al.*, "24.7 % Record Efficiency HIT Solar Cell on Thin Silicon Wafer," *IEEE J. Photovolt.*, vol. 4, no. 1, pp. 96–99, Jan. 2014.

[111] A. Kristensen *et al.*, "Plasmonic colour generation," *Nat. Rev. Mater.*, vol. 2, no. 1, p. natrevmats201688, Nov. 2016.

[112] K. Kumar, H. Duan, R. S. Hegde, S. C. W. Koh, J. N. Wei, and J. K. W. Yang, "Printing colour at the optical diffraction limit," *Nat. Nanotechnol.*, vol. 7, no. 9, pp. 557–561, Sep. 2012.

[113] Lochbihler Hans, "Polarizing and angle-sensitive color filter in transmittance for security feature applications," *Adv. Opt. Technol.*, vol. 4, no. 1, p. 71, 2015.

[114] T. Ellenbogen, K. Seo, and K. B. Crozier, "Chromatic Plasmonic Polarizers for Active Visible Color Filtering and Polarimetry," *Nano Lett.*, vol. 12, no. 2, pp. 1026–1031, Feb. 2012.

[115] T. Xu, Y.-K. Wu, X. Luo, and L. J. Guo, "Plasmonic nanoresonators for high-resolution colour filtering and spectral imaging," *Nat. Commun.*, vol. 1, p. ncomms1058, Aug. 2010.

[116] X. Zhu, C. Vannahme, E. Højlund-Nielsen, N. A. Mortensen, and A. Kristensen, "Plasmonic colour laser printing," *Nat. Nanotechnol.*, vol. 11, no. 4, pp. 325–329, Apr. 2016.

[117] J. B. Khurgin, "How to deal with the loss in plasmonics and metamaterials," *Nat. Nanotechnol.*, vol. 10, no. 1, pp. 2–6, Jan. 2015.

[118] D. G. Baranov *et al.*, "All-dielectric nanophotonics: the quest for better materials and fabrication techniques," *Optica*, vol. 4, no. 7, pp. 814–825, Jul. 2017.

[119] M. R. Shcherbakov *et al.*, "Enhanced Third-Harmonic Generation in Silicon Nanoparticles Driven by Magnetic Response," *Nano Lett.*, vol. 14, no. 11, pp. 6488–6492, Nov. 2014.

[120] E.-H. Cho *et al.*, "Two-dimensional photonic crystal color filter development," *Opt. Express*, vol. 17, no. 10, pp. 8621–8629, May 2009.

[121] L. Cao, P. Fan, E. S. Barnard, A. M. Brown, and M. L. Brongersma, "Tuning the Color of Silicon Nanostructures," *Nano Lett.*, vol. 10, no. 7, pp. 2649–2654, Jul. 2010.

[122] K. Seo *et al.*, "Multicolored vertical silicon nanowires," *Nano Lett.*, vol. 11, no. 4, pp. 1851–1856, Apr. 2011.

[123] S.-C. Yang, K. Richter, and W.-J. Fischer, "Multicolor generation using silicon nanodisk absorber," *Appl. Phys. Lett.*, vol. 106, no. 8, p. 081112, Feb. 2015.

[124] E. Højlund-Nielsen, J. Weirich, J. Nørregaard, J. Garnaes, N. Asger Mortensen, and A. Kristensen, "Angle-independent structural colors of silicon," *J. Nanophotonics*, vol. 8, no. 1, pp. 083988–083988, 2014.

[125] J. Proust, F. Bedu, B. Gallas, I. Ozerov, and N. Bonod, "All-Dielectric Colored Metasurfaces with Silicon Mie Resonators," *ACS Nano*, vol. 10, no. 8, pp. 7761–7767, Aug. 2016.

[126] B. Yang, W. Liu, Z. Li, H. Cheng, S. Chen, and J. Tian, "Polarization-Sensitive Structural Colors with Hue-and-Saturation Tuning Based on All-Dielectric Nanopixels," *Adv. Opt. Mater.*, vol. 6, no. 4, p. 1701009, Feb. 2018.

[127] V. Flauraud, M. Reyes, R. Paniagua-Domínguez, A. I. Kuznetsov, and J. Brugger, "Silicon Nanostructures for Bright Field Full Color Prints," *ACS Photonics*, vol. 4, no. 8, pp. 1913–1919, Aug. 2017.

[128] U. Zywietz, A. B. Evlyukhin, C. Reinhardt, and B. N. Chichkov, "Laser printing of silicon nanoparticles with resonant optical electric and magnetic responses," *Nat. Commun.*, vol. 5, p. ncomms4402, Mar. 2014.

[129] X. Zhu, W. Yan, U. Levy, N. A. Mortensen, and A. Kristensen, "Resonant laser printing of structural colors on high-index dielectric metasurfaces," *Sci. Adv.*, vol. 3, no. 5, p. e1602487, May 2017.

[130] Y. Horie *et al.*, “Visible Wavelength Color Filters Using Dielectric Subwavelength Gratings for Backside-Illuminated CMOS Image Sensor Technologies,” *Nano Lett.*, vol. 17, no. 5, pp. 3159–3164, May 2017.

[131] D. F. Edwards, “Silicon (Si)*,” in *Handbook of Optical Constants of Solids*, E. D. Palik, Ed. Burlington: Academic Press, 1997, pp. 547–569.

[132] G. Seniutinas *et al.*, “Tipping solutions: emerging 3D nano-fabrication/ -imaging technologies,” *Nanophotonics*, vol. 6, no. 5, pp. 923–941, 2017.

[133] T. Wood *et al.*, “All-Dielectric Color Filters Using SiGe-Based Mie Resonator Arrays,” *ACS Photonics*, vol. 4, no. 4, pp. 873–883, Apr. 2017.

[134] W. Yue, S. Gao, S.-S. Lee, E.-S. Kim, and D.-Y. Choi, “Subtractive Color Filters Based on a Silicon-Aluminum Hybrid-Nanodisk Metasurface Enabling Enhanced Color Purity,” *Sci. Rep.*, vol. 6, p. srep29756, Jul. 2016.

[135] T. Smith and J. Guild, “The C.I.E. colorimetric standards and their use,” *Trans. Opt. Soc.*, vol. 33, no. 3, pp. 73–134, Jan. 1931.

[136] R. Mote and L. Xiaomin, “Focused Ion Beam (FIB) Nanofinishing for Ultra-Thin TEM Sample Preparation,” in *Nanofinishing Science and Technology*, CRC Press, 2017, pp. 155–176.

[137] H. Ghiradella, “Light and color on the wing: structural colors in butterflies and moths,” *Appl. Opt.*, vol. 30, no. 24, pp. 3492–3500, Aug. 1991.

[138] A. Johannes, H. Holland-Moritz, and C. Ronning, “Ion beam irradiation of nanostructures: sputtering, dopant incorporation, and dynamic annealing,” *Semicond. Sci. Technol.*, vol. 30, no. 3, p. 033001, 2015.

[139] W. Huang *et al.*, “Ion Beam Defect Engineering on ReS2/Si Photocathode with Significantly Enhanced Hydrogen Evolution Reaction,” *Adv. Mater. Interfaces*, vol. 6, no. 3, p. 1801663, 2019.

[140] S. Saremi *et al.*, “Electronic Transport and Ferroelectric Switching in Ion-Bombarded, Defect-Engineered BiFeO3 Thin Films,” *Adv. Mater. Interfaces*, vol. 5, no. 3, p. 1700991, Feb. 2018.

[141] F. Cao *et al.*, “An Ultrasensitive and Ultraselective Hydrogen Sensor Based on Defect-Dominated Electron Scattering in Pt Nanowire Arrays,” *Adv. Mater. Interfaces*, vol. 6, no. 1, p. 1801304, Jan. 2019.

[142] S. Klaumünzer, C. Li, S. Löffler, M. Rammensee, G. Schumacher, and H. C. Neitzert, “Ion-Beam-Induced plastic deformation: A universal behavior of amorphous solids,” *Radiat. Eff. Defects Solids*, vol. 108, no. 1, pp. 131–135, May 1989.

[143] T. Yoshida, A. Baba, and T. Asano, “Fabrication of Micro Field Emitter Tip Using Ion-Beam Irradiation-Induced Self-Standing of Thin Films,” *Jpn. J. Appl. Phys.*, vol. 44, no. 7S, p. 5744, Jul. 2005.

[144] S. K. Tripathi, N. Shukla, S. Dhamodaran, and V. N. Kulkarni, “Controlled manipulation of carbon nanopillars and cantilevers by focused ion beam,” *Nanotechnology*, vol. 19, no. 20, p. 205302, 2008.

[145] C. Borschel *et al.*, “Alignment of Semiconductor Nanowires Using Ion Beams,” *Small*, vol. 5, no. 22, pp. 2576–2580, Nov. 2009.

[146] A. Cui *et al.*, “Directly patterned substrate-free plasmonic ‘nanograter’ structures with unusual Fano resonances,” *Light Sci. Appl.*, vol. 4, no. 7, p. e308, Jul. 2015.

[147] Chalapat Khattiya, Chekurov Nikolai, Jiang Hua, Li Jian, Parviz Babak, and Paraoanu G. S., “Self-Organized Origami Structures via Ion-Induced Plastic Strain,” *Adv. Mater.*, vol. 25, no. 1, pp. 91–95, Oct. 2012.

[148] L. Pelaz, L. A. Marqués, and J. Barbolla, “Ion-beam-induced amorphization and recrystallization in silicon,” *J. Appl. Phys.*, vol. 96, no. 11, pp. 5947–5976, Nov. 2004.

[149] Y. Ishii, C. S. Madi, M. J. Aziz, and E. Chason, “Stress evolution in Si during low-energy ion bombardment,” *J. Mater. Res.*, vol. 29, no. 24, pp. 2942–2948, Dec. 2014.

[150] A. Cui *et al.*, “Ion-beam-induced bending of freestanding amorphous nanowires: The importance of the substrate material and charging,” *Appl. Phys. Lett.*, vol. 102, no. 21, p. 213112, May 2013.

[151] E. F. Pecora, A. Irrera, S. Boninelli, L. Romano, C. Spinella, and F. Priolo, "Nanoscale amorphization, bending and recrystallization in silicon nanowires," *Appl. Phys. A*, vol. 102, no. 1, pp. 13–19, Jan. 2011.

[152] N. S. Rajput, Z. Tong, and X. Luo, "Investigation of ion induced bending mechanism for nanostructures," *Mater. Res. Express*, vol. 2, no. 1, p. 015002, 2015.

[153] D. R. Gomes, A. A. Turkin, D. I. Vainchtein, and J. Th. M. De Hosson, "On the fabrication of micro- and nano-sized objects: the role of interstitial clusters," *J. Mater. Sci.*, vol. 53, no. 10, pp. 7822–7833, May 2018.

[154] C.-L. Wu, F.-C. Li, C.-W. Pao, and D. J. Srolovitz, "Folding Sheets with Ion Beams," *Nano Lett.*, vol. 17, no. 1, pp. 249–254, Jan. 2017.

[155] J. F. Ziegler, M. D. Ziegler, and J. P. Biersack, "SRIM – The stopping and range of ions in matter (2010)," *Nucl. Instrum. Methods Phys. Res. Sect. B Beam Interact. Mater. At.*, vol. 268, no. 11–12, pp. 1818–1823, Jun. 2010.

[156] B. Liu *et al.*, "In situ probing the interior of single bacterial cells at nanometer scale," *Nanotechnology*, vol. 25, no. 41, p. 415101, 2014.

[157] J. Li *et al.*, "Controlled graphene encapsulation: a nanoscale shield for characterising single bacterial cells in liquid," *Nanotechnology*, vol. 29, no. 36, p. 365705, 2018.

[158] J. W. Corbett and G. D. Watkins, "Production of Divacancies and Vacancies by Electron Irradiation of Silicon," *Phys. Rev.*, vol. 138, no. 2A, pp. A555–A560, Apr. 1965.

[159] K. E. Petersen, "Silicon as a mechanical material," *Proc. IEEE*, vol. 70, no. 5, pp. 420–457, May 1982.

[160] B. Schmidt, L. Bischoff, and J. Teichert, "Writing FIB implantation and subsequent anisotropic wet chemical etching for fabrication of 3D structures in silicon," *Sens. Actuators Phys.*, vol. 61, no. 1, pp. 369–373, Jun. 1997.

[161] I. L. Berry and A. L. Caviglia, "High resolution patterning of silicon by selective gallium doping," *J. Vac. Sci. Technol. B Microelectron. Process. Phenom.*, vol. 1, no. 4, pp. 1059–1061, Oct. 1983.

[162] A. J. Steckl, H. C. Mogul, and S. Mogren, “Localized fabrication of Si nanostructures by focused ion beam implantation,” *Appl. Phys. Lett.*, vol. 60, no. 15, pp. 1833–1835, Apr. 1992.

[163] H. Fuhrmann, M. Döbeli, R. Kötz, R. Mühle, and B. Schnyder, “Thin oxides on passivated silicon irradiated by focused ion beams,” *J. Vac. Sci. Technol. B Microelectron. Nanometer Struct. Process. Meas. Phenom.*, vol. 17, no. 6, pp. 3068–3071, Nov. 1999.

[164] B. Schmidt, S. Oswald, and L. Bischoff, “Etch Rate Retardation of Ga + -Ion Beam-Irradiated Silicon,” *J. Electrochem. Soc.*, vol. 152, no. 11, pp. G875–G879, Nov. 2005.

[165] M. D. Henry, M. J. Shearn, B. Chhim, and A. Scherer, “Ga + beam lithography for nanoscale silicon reactive ion etching,” *Nanotechnology*, vol. 21, no. 24, p. 245303, 2010.

[166] S. Punzhin, E. Detsi, A. Kuzmin, and J. T. M. D. Hosson, “Deformation of nanoporous nanopillars by ion beam-induced bending,” *J. Mater. Sci.*, vol. 49, no. 16, pp. 5598–5605, Aug. 2014.

[167] D. R. Gomes, A. A. Turkin, D. I. Vainchtein, and J. Th. M. De Hosson, “On the mechanism of ion-induced bending of nanostructures,” *Appl. Surf. Sci.*, vol. 446, pp. 151–159, Jul. 2018.

[168] K. Jun, J. Joo, and J. M. Jacobson, “Focused ion beam-assisted bending of silicon nanowires for complex three dimensional structures,” *J. Vac. Sci. Technol. B Microelectron. Nanometer Struct. Process. Meas. Phenom.*, vol. 27, no. 6, pp. 3043–3047, Nov. 2009.

[169] A. Hedler, S. L. Klaumünzer, and W. Wesch, “Amorphous silicon exhibits a glass transition,” *Nat. Mater.*, vol. 3, no. 11, pp. 804–809, Nov. 2004.

[170] L. Romano, N. G. Rudawski, M. R. Holzworth, K. S. Jones, S. G. Choi, and S. T. Picraux, “Nanoscale manipulation of Ge nanowires by ion irradiation,” *J. Appl. Phys.*, vol. 106, no. 11, p. 114316, Dec. 2009.

[171] A. Johannes, S. Noack, W. Wesch, M. Glaser, A. Lugstein, and C. Ronning, "Anomalous Plastic Deformation and Sputtering of Ion Irradiated Silicon Nanowires," *Nano Lett.*, vol. 15, no. 6, pp. 3800–3807, Jun. 2015.

[172] J. S. Williams, M. J. Conway, B. C. Williams, and J. Wong-Leung, "Direct observation of voids in the vacancy excess region of ion bombarded silicon," *Appl. Phys. Lett.*, vol. 78, no. 19, pp. 2867–2869, May 2001.

[173] F. Hofmann *et al.*, "3D lattice distortions and defect structures in ion-implanted nano-crystals," *Sci. Rep.*, vol. 7, p. 45993, Apr. 2017.

[174] C. Borschel *et al.*, "Permanent bending and alignment of ZnO nanowires," *Nanotechnology*, vol. 22, no. 18, p. 185307, 2011.

[175] M. Tang, L. Colombo, J. Zhu, and T. Diaz de la Rubia, "Intrinsic point defects in crystalline silicon: Tight-binding molecular dynamics studiesof self-diffusion, interstitial-vacancy recombination, and formation volumes," *Phys. Rev. B*, vol. 55, no. 21, pp. 14279–14289, Jun. 1997.

[176] O. Camara *et al.*, "Shape Modification of Germanium Nanowires during Ion Irradiation and Subsequent Solid-Phase Epitaxial Growth," *Adv. Mater. Interfaces*, vol. 5, no. 13, p. 1800276, 2018.

[177] K. Das, J. B. Freund, and H. T. Johnson, "Mechanisms of material removal and mass transport in focused ion beam nanopore formation," *J. Appl. Phys.*, vol. 117, no. 8, p. 085304, Feb. 2015.

[178] H. Idrissi *et al.*, "Point Defect Clusters and Dislocations in FIB Irradiated Nanocrystalline Aluminum Films: An Electron Tomography and Aberration-Corrected High-Resolution ADF-STEM Study," *Microsc. Microanal.*, vol. 17, no. 6, pp. 983–990, Dec. 2011.

[179] S. Lee, J. Jeong, Y. Kim, S. M. Han, D. Kiener, and S. H. Oh, "FIB-induced dislocations in Al submicron pillars: Annihilation by thermal annealing and effects on deformation behavior," *Acta Mater.*, vol. 110, pp. 283–294, May 2016.

[180] I. Hanif *et al.*, "Ion-beam-induced bending of semiconductor nanowires," *Nanotechnology*, vol. 29, no. 33, p. 335701, 2018.

[181] V. Garg, R. G. Mote, and J. Fu, “Coloring with Focused Ion Beam Fabricated Nanostructures,” *Microsc. Microanal.*, vol. 24, no. S1, pp. 856–857, Aug. 2018.

[182] P. Gu, W. Zhang, and G. Zhang, “Plasmonic Nanogaps: From Fabrications to Optical Applications,” *Adv. Mater. Interfaces*, vol. 5, no. 19, p. 1800648, 2018.

[183] J. L. Connell, A. K. Wessel, M. R. Parsek, A. D. Ellington, M. Whiteley, and J. B. Shear, “Probing Prokaryotic Social Behaviors with Bacterial ‘Lobster Traps,’” *mBio*, vol. 1, no. 4, pp. e00202-10, Oct. 2010.

[184] K. K. Sakimoto, C. Liu, J. Lim, and P. Yang, “Salt-Induced Self-Assembly of Bacteria on Nanowire Arrays,” *Nano Lett.*, vol. 14, no. 9, pp. 5471–5476, Sep. 2014.

[185] P. K. Sahoo *et al.*, “Nanowire Arrays as Cell Force Sensors To Investigate Adhesin-Enhanced Holdfast of Single Cell Bacteria and Biofilm Stability,” *Nano Lett.*, vol. 16, no. 7, pp. 4656–4664, Jul. 2016.

[186] A. Cui *et al.*, “Directly patterned substrate-free plasmonic ‘nanograter’ structures with unusual Fano resonances,” *Light Sci. Appl.*, vol. 4, no. 7, p. e308, Jul. 2015.

[187] V. Garg *et al.*, “Weaving nanostructures with site-specific ion induced bidirectional bending,” *Nanoscale Adv.*, vol. 1, no. 8, pp. 3067–3077, Aug. 2019.

[188] V. Garg *et al.*, “Ion Induced Bidirectional Bending for Controlled Manipulation at Nanoscale,” *Microsc. Microanal.*, vol. 25, no. S2, pp. 852–853, Aug. 2019.

[189] V. Garg, R. G. Mote, and J. Fu, “Focused Ion Beam Direct Fabrication of Subwavelength Nanostructures on Silicon for Multicolor Generation,” *Adv. Mater. Technol.*, vol. 3, no. 8, p. 1800100, Aug. 2018.

[190] V. Garg, R. G. Mote, and J. Fu, “Rapid prototyping of highly ordered subwavelength silicon nanostructures with enhanced light trapping,” *Opt. Mater.*, vol. 94, pp. 75–85, Aug. 2019.

[191] B. Kamaliya, R. G. Mote, M. Aslam, and J. Fu, “Enhanced light trapping by focused ion beam (FIB) induced self-organized nanoripples on germanium (100) surface,” *APL Mater.*, vol. 6, no. 3, p. 036106, Mar. 2018.

[192] C. A. Volkert and A. M. Minor, “Focused Ion Beam Microscopy and Micromachining,” *MRS Bull.*, vol. 32, no. 5, pp. 389–399, May 2007.

[193] V. Garg, S. Zhang, R. G. Mote, Y. Chen, L. Cao, and J. Fu, "'Stand-Out': A Novel Approach for Preparing Sub-100 nm Samples Through in situ Ion Induced Bending," *Microsc. Microanal.*, vol. 25, no. S2, pp. 898–899, Aug. 2019.

[194] K. Narayan and S. Subramaniam, "Focused ion beams in biology," *Nat. Methods*, vol. 12, no. 11, pp. 1021–1031, Nov. 2015.

[195] N. Gour and S. Verma, "Bending of peptide nanotubes by focused electron and ion beams," *Soft Matter*, vol. 5, no. 9, pp. 1789–1791, Apr. 2009.

[196] L. Pizzagalli *et al.*, "A new parametrization of the Stillinger–Weber potential for an improved description of defects and plasticity of silicon," *J. Phys. Condens. Matter*, vol. 25, no. 5, p. 055801, 2013.

[197] J. F. Ziegler and J. P. Biersack, "The Stopping and Range of Ions in Matter," in *Treatise on Heavy-Ion Science: Volume 6: Astrophysics, Chemistry, and Condensed Matter*, D. A. Bromley, Ed. Boston, MA: Springer US, 1985, pp. 93–129.

[198] F. H. Stillinger and T. A. Weber, "Computer simulation of local order in condensed phases of silicon," *Phys. Rev. B*, vol. 31, no. 8, pp. 5262–5271, Apr. 1985.

[199] J. Guénolé, A. Prakash, and E. Bitzek, "Atomistic simulations of focused ion beam machining of strained silicon," *Appl. Surf. Sci.*, vol. 416, pp. 86–95, Sep. 2017.

[200] A. M. Korsunsky *et al.*, "Quantifying eigenstrain distributions induced by focused ion beam damage in silicon," *Mater. Lett.*, vol. 185, pp. 47–49, Dec. 2016.

[201] S. Plimpton, "Fast Parallel Algorithms for Short-Range Molecular Dynamics," *J. Comput. Phys.*, vol. 117, no. 1, pp. 1–19, Mar. 1995.

[202] A. Stukowski, "Visualization and analysis of atomistic simulation data with OVITO–the Open Visualization Tool," *Model. Simul. Mater. Sci. Eng.*, vol. 18, no. 1, p. 015012, 2010.

[203] A. K. Revelly *et al.*, "High-purity Zirconium under Niobium ion implantation: possibility of a dynamic precipitation?," *Philos. Mag.*, vol. 95, no. 33, pp. 3727–3744, Nov. 2015.

[204] A. K. Revelly *et al.*, "Orientation sensitivity of focused ion beam damage in pure zirconium: direct experimental observations and molecular dynamics simulations," *Philos. Mag.*, vol. 94, no. 14, pp. 1601–1621, May 2014.

[205] J. A. Zimmerman, E. B. WebbIII, J. J. Hoyt, R. E. Jones, P. A. Klein, and D. J. Bammann, “Calculation of stress in atomistic simulation,” *Model. Simul. Mater. Sci. Eng.*, vol. 12, no. 4, pp. S319–S332, Jun. 2004.

[206] A. P. Thompson, S. J. Plimpton, and W. Mattson, “General formulation of pressure and stress tensor for arbitrary many-body interaction potentials under periodic boundary conditions,” *J. Chem. Phys.*, vol. 131, no. 15, p. 154107, Oct. 2009.

[207] E. Holmström, J. Kotakoski, L. Lechner, U. Kaiser, and K. Nordlund, “Atomic-scale effects behind structural instabilities in Si lamellae during ion beam thinning,” *AIP Adv.*, vol. 2, no. 1, p. 012186, Mar. 2012.

[208] H. Eyring and T. Ree, “A Generalized Theory of Plasticity Involving the Virial Theorem,” *Proc. Natl. Acad. Sci.*, vol. 41, no. 3, pp. 118–122, Mar. 1955.

[209] D. H. Tsai, “The virial theorem and stress calculation in molecular dynamics,” *J. Chem. Phys.*, vol. 70, no. 3, pp. 1375–1382, Feb. 1979.

[210] C. H. Rycroft, “VORO++: A three-dimensional Voronoi cell library in C++,” *Chaos Interdiscip. J. Nonlinear Sci.*, vol. 19, no. 4, p. 041111, Oct. 2009.

[211] N. Kalyanasundaram, M. C. Moore, J. B. Freund, and H. T. Johnson, “Stress evolution due to medium-energy ion bombardment of silicon,” *Acta Mater.*, vol. 54, no. 2, pp. 483–491, 2006.

[212] M. A. Hopcroft, W. D. Nix, and T. W. Kenny, “What is the Young’s Modulus of Silicon?,” *J. Microelectromechanical Syst.*, vol. 19, no. 2, pp. 229–238, Apr. 2010.

[213] L. A. Giannuzzi and F. A. Stevie, “A review of focused ion beam milling techniques for TEM specimen preparation,” *Micron*, vol. 30, no. 3, pp. 197–204, Jun. 1999.

[214] D. W. Saxey, J. M. Cairney, D. McGrouther, T. Honma, and S. P. Ringer, “Atom probe specimen fabrication methods using a dual FIB/SEM,” *Ultramicroscopy*, vol. 107, no. 9, pp. 756–760, Sep. 2007.

[215] T. Diaz de la Rubia and G. H. Gilmer, “Structural Transformations and Defect Production in Ion Implanted Silicon: A Molecular Dynamics Simulation Study,” *Phys. Rev. Lett.*, vol. 74, no. 13, pp. 2507–2510, Mar. 1995.

Appendix A

Rapid Prototyping of Subwavelength Nanostructures: Experimental Details

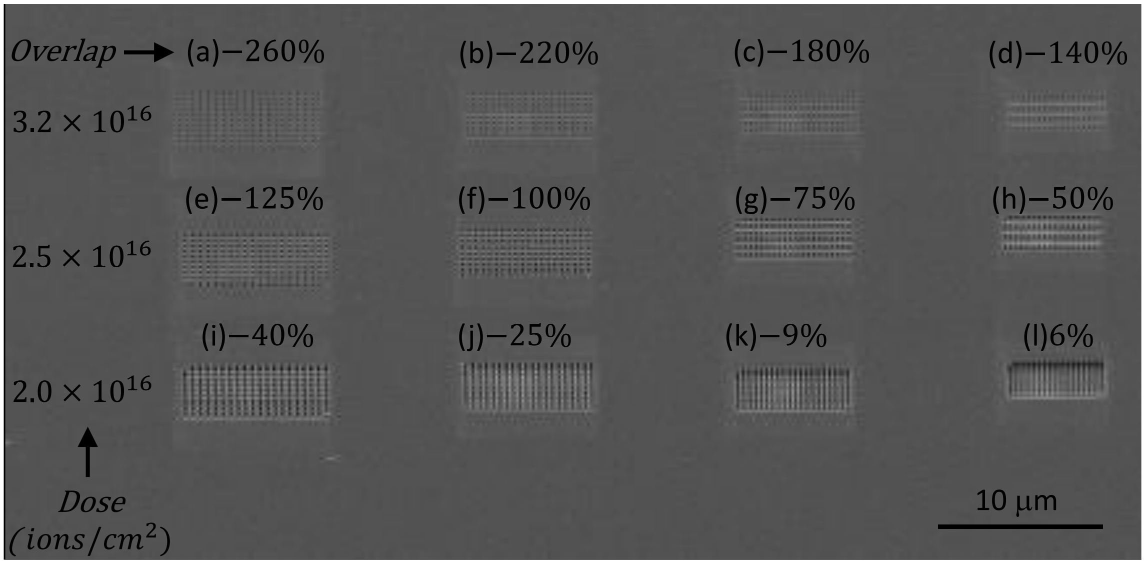

Figure A.1: Experiment details: Variation of ion dose (2×10^{16}-3.2×10^{16} ions/cm^2), overlap (-260%-6%) and fabricated structures

Figure A.1 shows the experiment details for rapid prototyping of subwavelength nanostructures on Si through direct FIB milling. Ion dose and beam overlap are adjusted for fabrication of Gaussian pillar like nanostructures on Si. The beam currents of 50, 100 and 200 pA at a constant dwell time of 50 millisecond (ms) were used in the experiments, with the variation of the beam overlap ranging from -260 % to 6 %. A SEM image is shown in Figure A.1, where variation of ion dose (2×10^{16}-3.2×10^{16} ions/cm^2) and overlap (-260%-6%) is shown for nanostructure fabrication. Acceleration voltage was kept at 30 kV for all experiments. The milling area consisted of total 200 pixels (20×10 array) and took 100 seconds to mill each region demonstrating the rapid formation of the nanostructures. The fabricated nanostructures are shown in Figure A.2, where SEM images are included in the sequence as shown in Figure A.1. The results indicate the change of fabrication geometry from nano-hole to nano-pillar with increasing beam overlap.

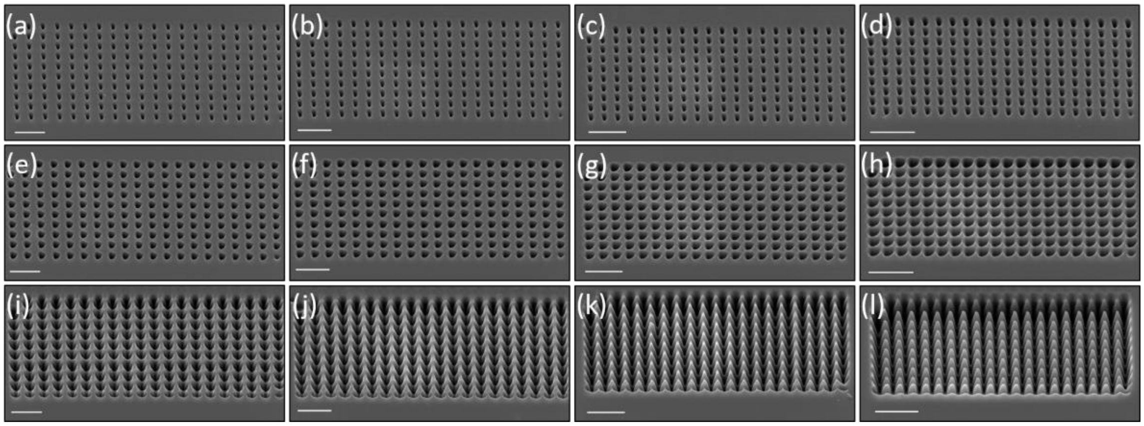

Figure A.2: SEM images of fabricated subwavelength nanostructures: the images are shown according to the sequence shown in experimental figure S1 with dose and overlap variation. Scale bar 1 µm

Light Incidence Direction Calculations

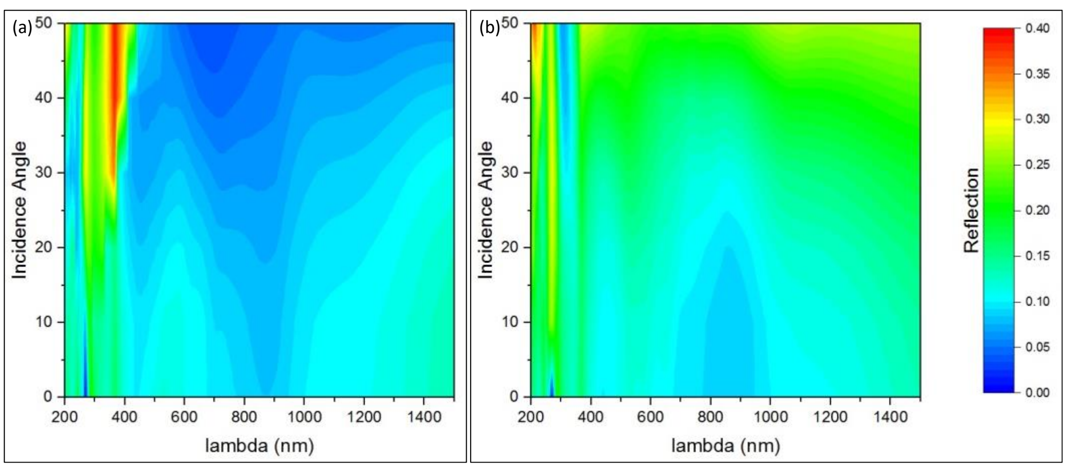

Figure A.3: Contour plots of calculated total reflection: variation of incidence angle at a fixed height, base and period of 500, 250 and 250 nm respectively (a) TE polarization (b) TM polarization

The effect of varying light incidence direction on Gaussian pillar geometry is investigated. Figure A.3 shows the contour plot of reflection spectra of proposed Gaussian pillar for TE and TM polarized light at different incidence angles (0-50). Broadband fixed angle source technique (BFAST) was used to avoid the change of actual injection angles for broadband simulation. This technique is used to avoid the requirement of sweep over the centre wavelength of the source to obtain accurate results and requires only a single simulation for entire wavelength range. The simulations were run for designed Gaussian pillar with a fixed height, base, and period of 500, 250, and 250 nm respectively and incidence angle was varied from normal incidence to 50 degrees. This technique applies to periodic structures illuminated with a broadband source and allows simulations at angled illumination. The reflection was found out to be mostly invariant and less than 10% in the range of 0-30 degree, while it further reduces to almost 0% for incidence angles 30-50 degree for TE polarization of light. This suggests that proposed Gaussian pillars offer significant reduction in reflection and remain invariant with respect to change in incidence angle of light. For TM polarization also the reflection was found out to be in the range of 10-15% over entire broadband with respect to incidence angle. A slight increase of approximately 5% over 40-degree incidence angle for the proposed geometry resulted in minute effect for overall reflection calculation over entire wavelength range.

Appendix B

Direct Fabrication of Tapered Nanostructures: Experimental Details

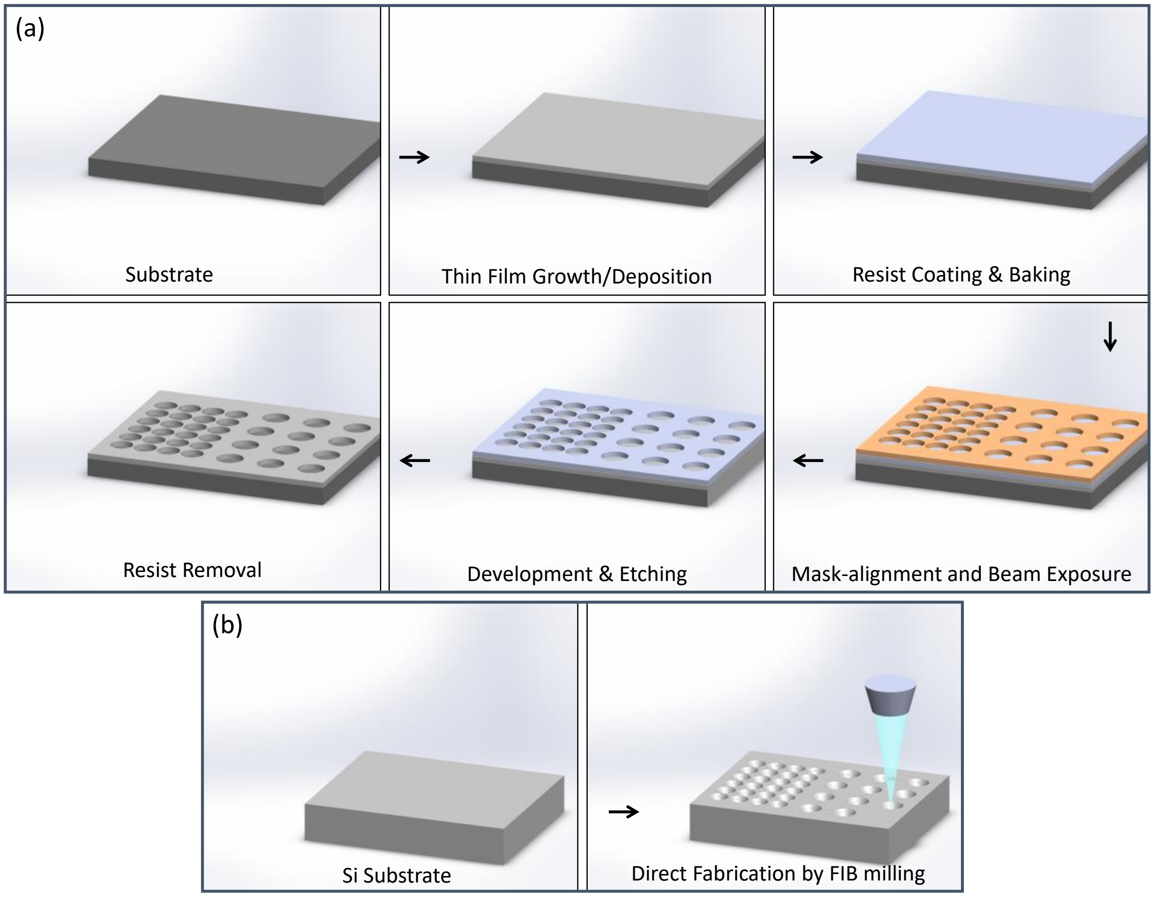

Figure B.1: (a) Multi-step lithography, involving deposition of thin films on a substrate, resist coating and baking, mask fabrication and alignment, exposure to e-beam, development and dry/wet etching, resist removal; while (b) Shows single step direct fabrication of tapered hole nanostructures on Si substrate by FIB milling and tuning of diameter and period for multicolor generation

A comparison of existing lithography-based approach to developed FIB milling based direct approach for fabrication of subwavelength nanostructures for multicolor generation is shown in Figure B.1. Gallium focused ion beam has been tuned for the fabrication of tapered hole nanostructures on Si. The nanostructures have been fabricated directly via incoming Gaussian profile of FIB. Ga FIB is generally used with a positive overlap for uniform milling. Here, FIB with a negative overlap is used for fabrication of nanoholes corresponding to each pixel scanned. Figure B.2 shows scanning schematic of 2×2 array of nanoholes via scanning of pixels by FIB with a large negative overlap. The beam is dwelled at desired pixel locations,

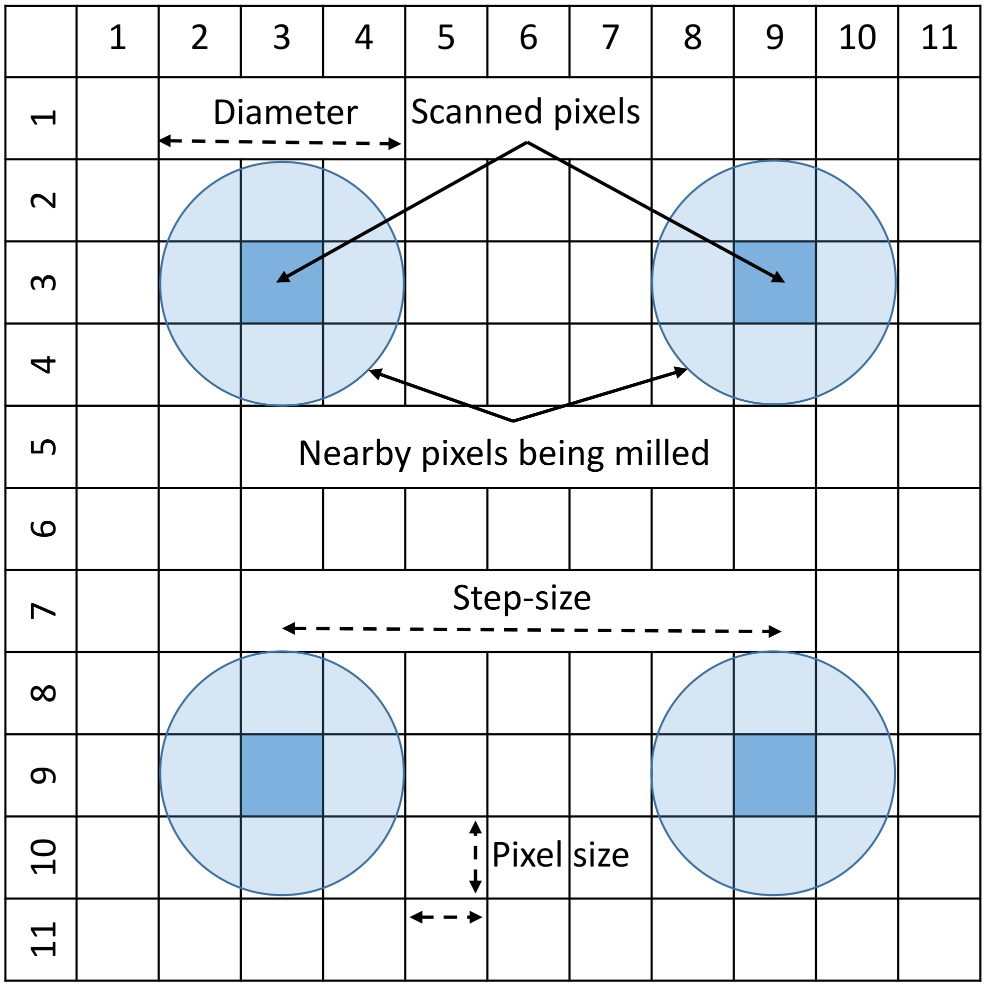

Figure B.2: Fabrication of subwavelength nanostructures by FIB for multicolor generation: pixels are scanned by FIB keeping a large negative overlap between consecutive scanning pixels. Nearby pixels adjacent to scanned pixels are milled due to Gaussian geometry of incoming Ga FIB, which leads to the development of a uniquely tapered nanohole geometry

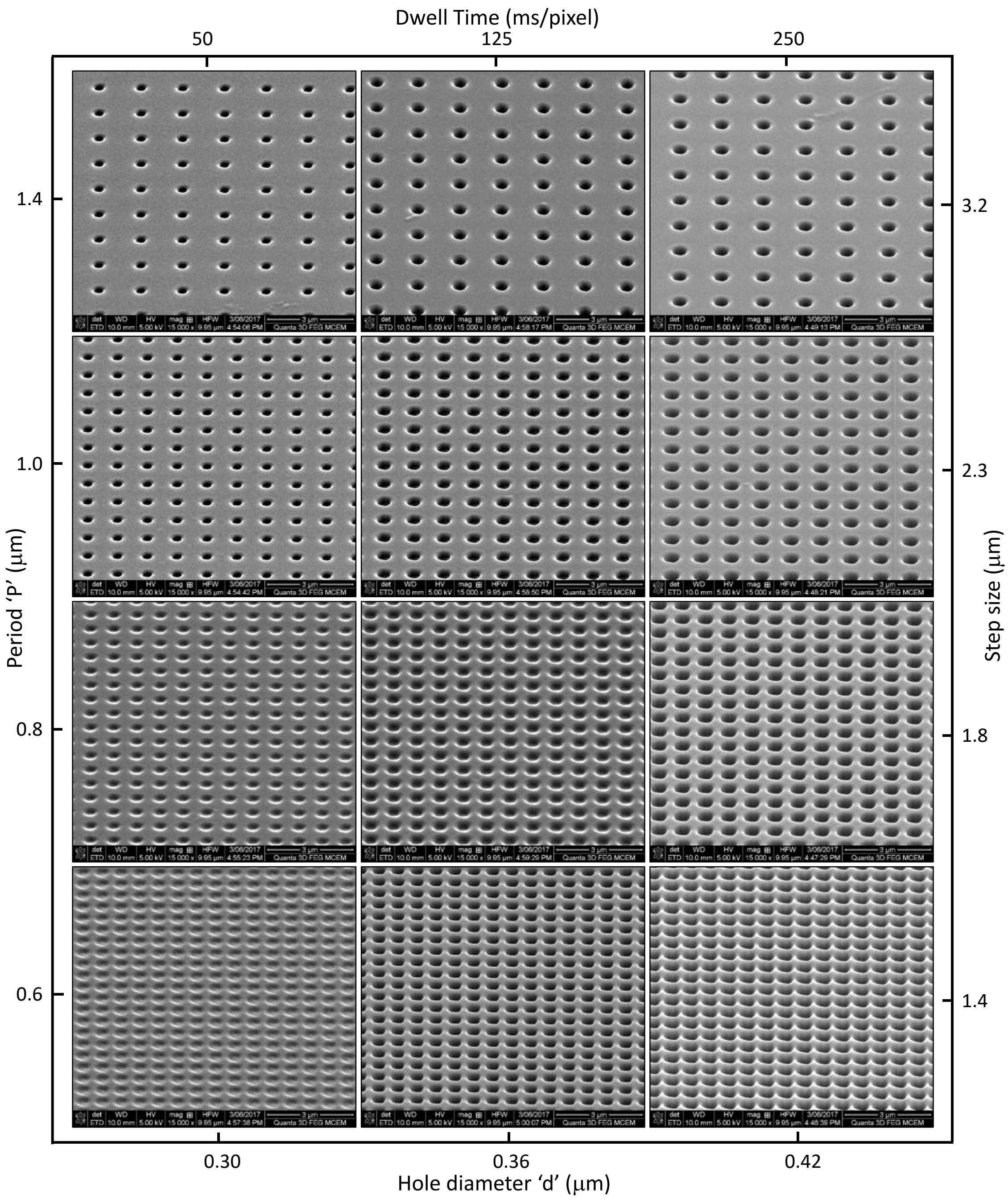

Figure B.3**:** Experimental details for fabrication and tuning of periodic tapered nanohole array: Tilted incidence SEM images of fabricated color filters on Si (scale bar 3 µm). On X-axis dwell time for fabrication is shown leading to change in diameter and depth of fabricated tapered hole nanostructures. On Y-axis period variation is shown which is being controlled by step size during FIB fabrication which leads to the milling of nearby pixels in addition to the pixel being centered due to beam diameter being larger than the pixel size and Gaussian profile of FIB. The pixel size in FIB milling is tuned via magnification change. The step size during FIB milling is used for controlling the period of fabricated nanohole array, while the diameter is controlled by the dwell time during pixel scanning. Figure B.3 shows tilted SEM view of a 4×3 array of fabricated periodic Si nanostructures. The dwell time per pixel and step-size are shown on X and Y-axis in order to tune the diameter and the period of fabricated hole nanostructures respectively.

Color Printing

The fabrication of butterflies for color printing demonstrations was carried out employing the user defined stream files. A grayscale bitmap pattern of butterfly was first created (Figure B.4 (a)). This bitmap pattern was used to define the scanning profile and dwell time distribution at each pixel during FIB milling (Figure B.4 (b)). This was achieved through conversion of the bitmap file to stream file (Figure B.4 (c)), which contains the information on the number of passes, total number of scanning pixels, pixel locations (x, y), and dwell time at each pixel.

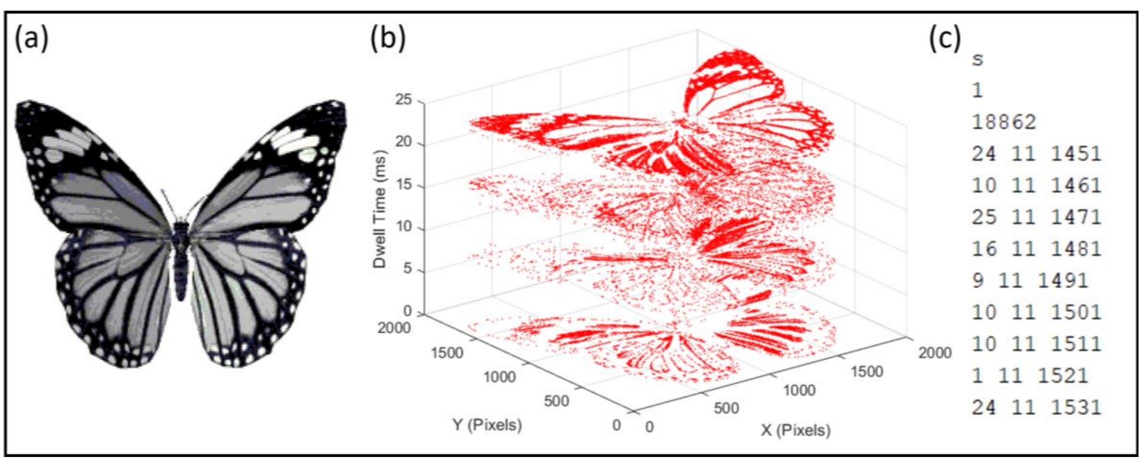

Figure B.4: (a) Grayscale bitmap image, (b) Scanning profile and dwell time distribution, and (c) A typical stream file example used for the fabrication of butterflies

The periodicity of fabricated tapered nanoholes is controlled via beam overlap during FIB milling and can be adjusted either via control of FIB magnification during the experiment or adjacent pixel locations in the stream file. The diameter of the fabricated nanoholes on the other hand can be controlled through the control of dwell time or current. The control of diameter and periodicity of fabricated nanohole resonator arrays can be used for generation of a large variety of colors (Figure 4.3). The realization of a variety of colors

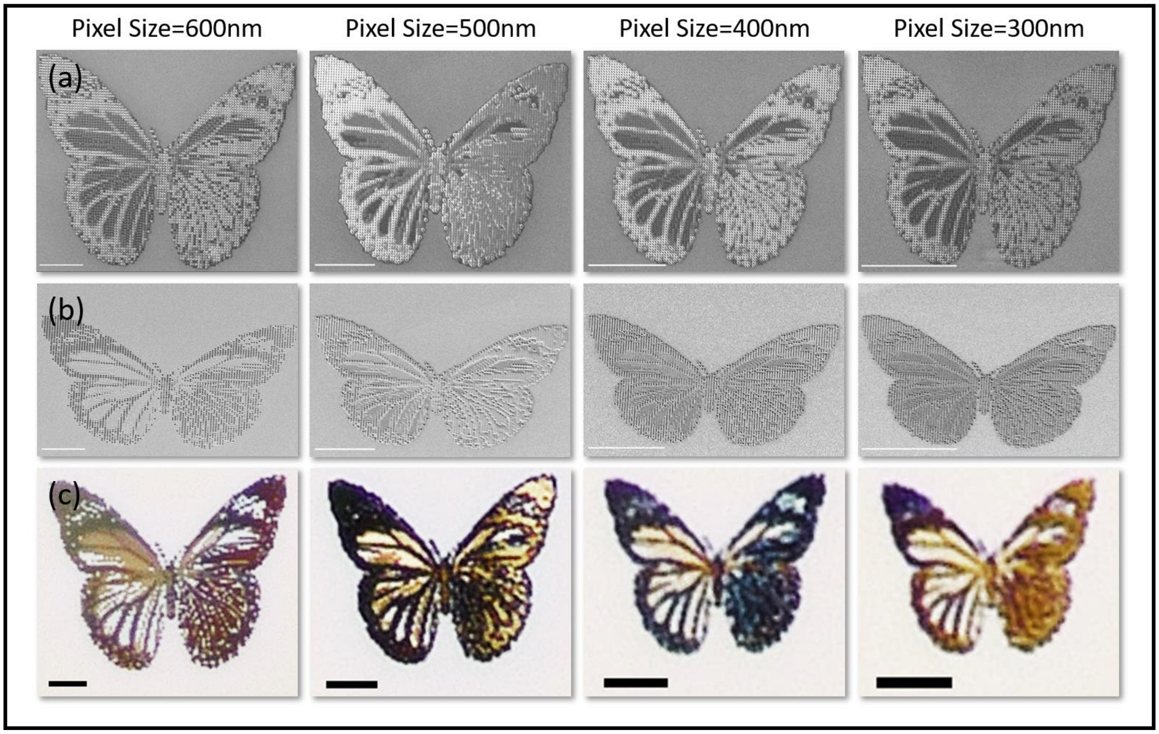

Figure B.5: (a) SEM normal view, (b) Tilted view, and (c) Corresponding optical images of fabricated butterflies with varying pixel size and showing multicolor generation (scale bar 25 μm)

with the developed fabrication technique allows realization of color printing applications through precise control of generated color through diameter and period. Figure B.5 shows the fabricated butterflies for color printing demonstrations through SEM images, corresponding bright field optical microscopic images with different pixel sizes and leading to the development of multicolor generation through color filtering. It can be seen that the butterfly wings can be designed successfully for reflection of a particular color based on

Figure B.6: Designed color printing through direct fabrication of nanostructures: (a) SEM image of letters comprising of nanohole resonator arrays with controlled diameter and period, (b) Corresponding bright field optical microscopic image

the design parameters. In addition, the control of pixel size allows control of color printing resolution (DPI, dots per inch), enabling the developed fabrication method suitable for rapid prototyping of nanostructures for desired color printing. An example of controlled and desired color printing is shown in Figure B.6, where a SEM image and corresponding optical microscopic image of fabricated letters is shown. Each letter was designed for a particular color and with reference to the color palette, design parameters from Figure 4.3. From the optical microscopic image in Figure B.6 (b), it can be seen that each individual letter reflects a particular color. For example, the letter ‘S’ was designed for blue color, and fabricated with design parameters D=350 nm, P=600 nm. Thus, with the developed nanostructures fabrication approach for multicolor generation provide excellent control and the method can be used for specific color generation based on the design and color printing applications.

Appendix C

Fabrication of Pyramid Microstructures

The combination of ion implantation and wet etching can be used for fabrication of 3D pyramid microstructures. Figure C.1 shows fabrication and characterization of pyramid microstructures. A SEM image of a periodic array of fabricated microstructures is included in Figure C.1 (a), while the top view is shown in Figure C.1 (b). The bitmap pattern used for ion implantation is also included in the inset of Figure C.1 (a), with white and black pixels denoting the beam on and off area respectively. A high magnification SEM image demonstrating the pyramid fabrication geometry is shown in Figure C.1 (c). Such 3D pyramid microstructures can be employed for a variety of applications, such as in the area of photonics. The fabricated pyramid microstructures were further subjected to UV visible light reflection tests and these microstructures were found to exhibit light trapping and antireflection properties. The measured reflectance spectrum of pyramid microstructures over visible spectrum is shown and compared against planar Si surface in Figure C.1 (d), which also includes the simulation results obtained through FDTD calculations. The pyramid microstructures exhibit reflectance values down to 5-10 % over the wavelength range of 500-700 nm in contrast to a high reflectance from planar Si. The experimentally measured reflectance results are found to differ from simulation results towards shorter and longer wavelengths, which may have been arising from the difference in the simulation and actual fabrication geometry and the reflectance normalization used in the experiments. To further investigate the resonance and light reflectance phenomenon, the electric field intensity distribution for pyramid microstructure corresponding to reflectance spectrum are plotted. The electric field intensity ($|E|^2$) distribution of mode resonance for the Si pyramid microstructure corresponding to λ=600 nm is shown in Figure C.1 (e), (f) with *YZ* view at *X*=2.5 µm, and *XZ* view at Y=2.5 µm respectively. The distribution plots show a large proportion of the electric field intensity around the pyramid geometry. The electric field intensity hotspots are maximum above and below the pyramid geometry, as viewed in *XZ* plane through nanohole cross-section at *Y* = 2.5 µm in Figure C.1 (f), suggesting a strong

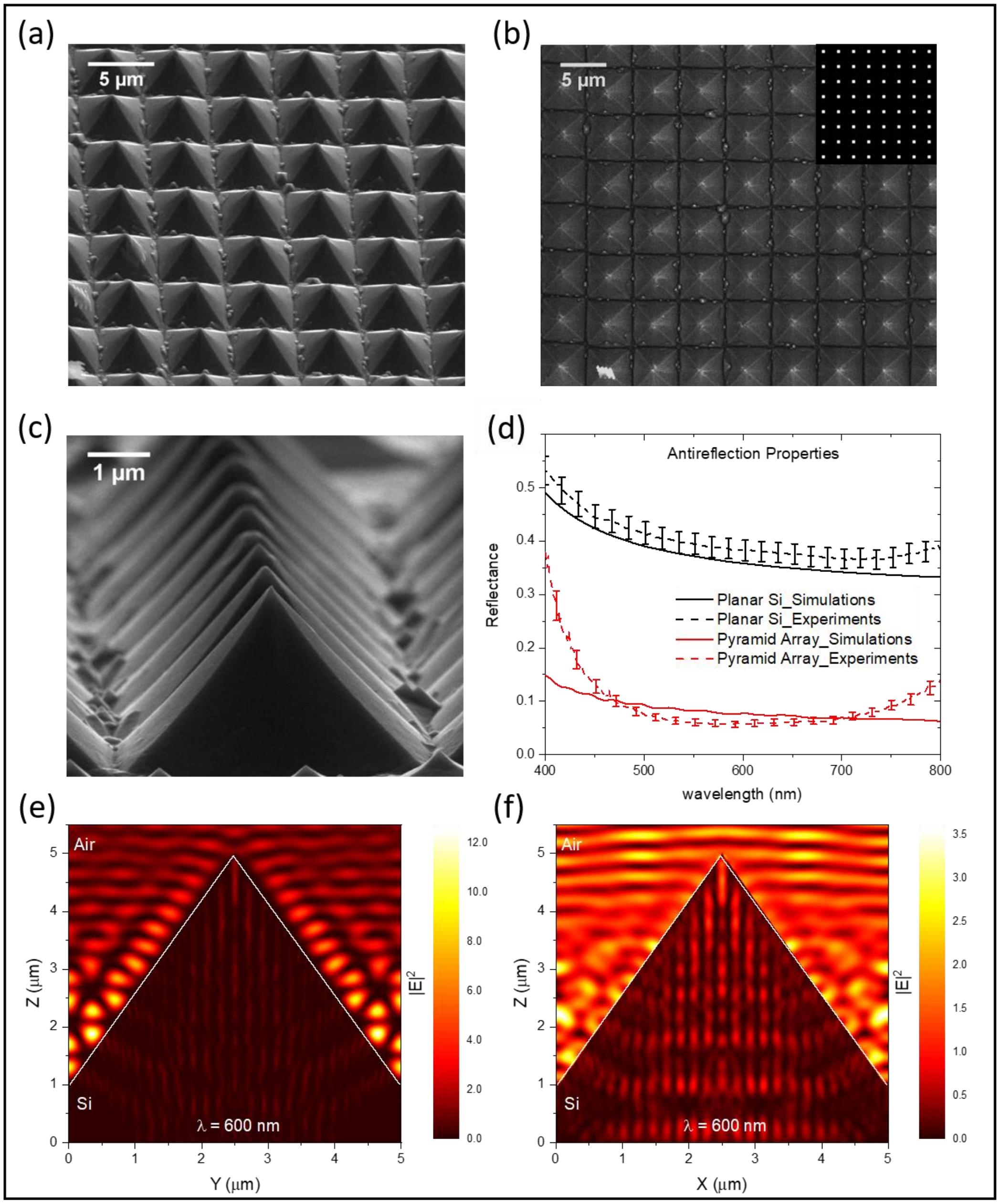

Figure C.1: Fabrication and characterization of pyramid microstructures: (a) SEM image of a periodic array of fabricated pyramid microstructures with inset showing the bitmap pattern used for implantation, with white pixels showing the implantation regions, (b)-(c) SEM images of the fabricated pyramids, (d) Comparison of UV visible reflectance spectrum through fabricated pyramid array against planar Si. Simulated electric field intensity ($|E|^2$) distribution of mode resonance for the Si pyramid corresponding to λ=600 nm shown with (e) *YZ* view at *X*=2.5 μm, and (f) *XZ* view at Y=2.5 μm confinement of the incident light. The confinement of electric fields inside and around the pyramid in Si suppresses the reflection of light and leads to light trapping effects.

Nano-Trumpet Fabrication

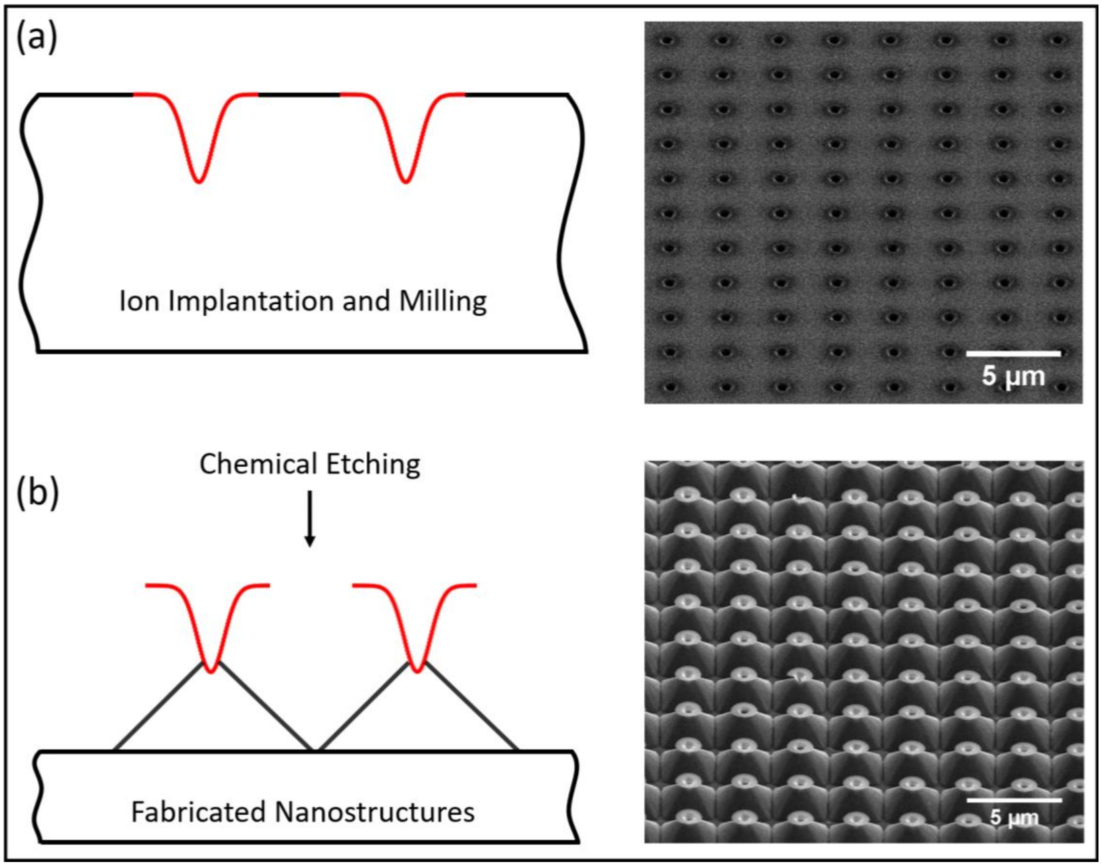

Figure C.2: Schematic diagram and corresponding SEM images showing (a) Ion implantation and milling on Si, (b) Fabricated nano-trumpets after chemical etching

The freeform fabrication of nano-trumpets is carried out through ion implantation and milling during FIB scanning. An ion beam current of 500 pA with ion dose of 25 ms/pixel was used for the implantation. It should be noted here, that such high value of dose per pixel ensures milling of Si in addition to the Ga implantation, which serves as the basis for realization of trumpet shaped geometries after wet chemical etching. The detailed fabrication approach adopted for fabrication of trumpet shaped structures is provided in Figure C.2. The incident Ga ions in the FIB are scanned over the Si substrate with a large negative overlap, such that the implanted/milled spots are spaced periodically. This ensures that there is sufficient undamaged Si left in between the adjacent implanted spots. The schematic diagram and SEM image of ion implantation and milling of Si is shown in Figure C.2 (a). The implanted/milled spot region in Si acts as a mask against the KOH wet etching and does not get etched. The schematic diagram and corresponding SEM image of Si after chemical etching is shown in Figure C.2 (b). It can be noted here that the fabricated trumpets are a replica of incoming ion beam profile. In addition, the trumpets are found to stand over pyramid shaped microstructures, which are arising out of anisotropic etching of Si. Further, it is possible to control the nano-trumpet geometry and periodicity through the control of fabrication parameters. The dwell time per pixel and current can be used for the geometry and beam overlap/step size for periodicities control. Thus, the developed approach allows for the fabrication of freeform nanostructures, which can be engineered towards desired functionality.

Appendix D

Monte Carlo Simulations

The Ga ions undergo electronic and nuclear stopping through collisions with electrons and Si nuclei before coming to rest. Due to these collisions, few Si atoms are ejected from their lattice positions as primary knock on atoms, if the energy transferred through Ga ions is more than displacement energy of Si (∼15 eV) [158], and create a Frenkel pair. These primary knock on atoms leave the vacancies at their original lattice position, can further interact with lattice atoms and produce a cascade of atomic displacements, before forming an interstitial atom. Thus, a single Ga ion develops a complete collision cascade, forming point defects (vacancies and interstitials) and Ga implantation in the crystal lattice. However, if the threshold energy is lower, only local heating occurs, known as thermal spike regime. The thermal spike regime of the cascade can cause significant melting and formation of amorphous pockets in the collision cascade, which contain more displaced atoms than calculated with binary collisions [148], [215]. The trajectories and interaction volume of caused by Ga ions in 80 nm thick Si substrate is calculated with Monte Carlo (MC) simulations performed with software package Stopping and Range of Ions in Matter (SRIM) [155] based on binary collision approximations is shown in Figure D.1 (a) with 30, 16, and 2 kV ion energy.

Further, the formation of vacancies and interstitials distributions in Si due to ion irradiation is calculated. There is a slight difference between the number of vacancies and interstitials formation in the Si target (Figure D.1 (b)-(c)). Vacancy formation in the Si corresponds to volumetric contraction. The volumetric contraction is responsible for generation of tensile stress. In contrast the interstitials distribution of ion leads to volume expansion, which will give rise to compressive stresses in the target [145]. The comparison of difference in vacancies and interstitials at low and high kV reveals the relative location of vacancy/interstitials excess along the target depth as a result of Ga FIB bombardment.

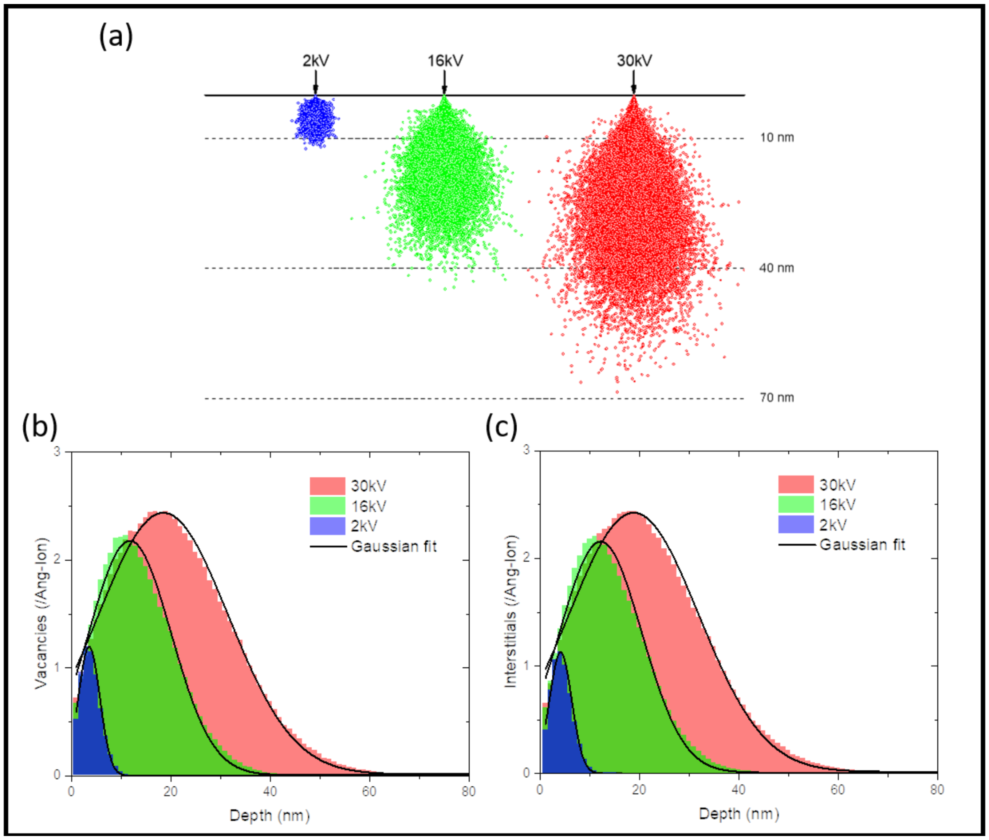

Figure D.1: (a) Interaction volume, (b) Vacancy, and (c) Interstitial distributions in Si irradiated with 30, 16, and 2 kV incident Ga ions in 80 nm thick Si substrate calculated with Monte Carlo SRIM simulations

The total number of atomic displacements/Si damage is calculated by vacancy and replacement collisions as follows:

Displacements=Vacancies + Replacement collisions

The total numbers of vacancies are calculated using SRIM simulations and according to following:

Vacancies=interstitials + atoms exited from Si

The Si recoil atoms calculated from SRIM simulations are the sum of replacement collisions and interstitials, thus the number of interstitials can be calculated as follows:

Interstitials= Si recoils – replacement collisions

Appendix E

Si Nanowires (NWs) TEM Sample Preparation

The Si NWs TEM samples for microstructural characterization were prepared using FIB lift-out. A Kleindiek micromanipulator equipped with FIB/SEM system was used for

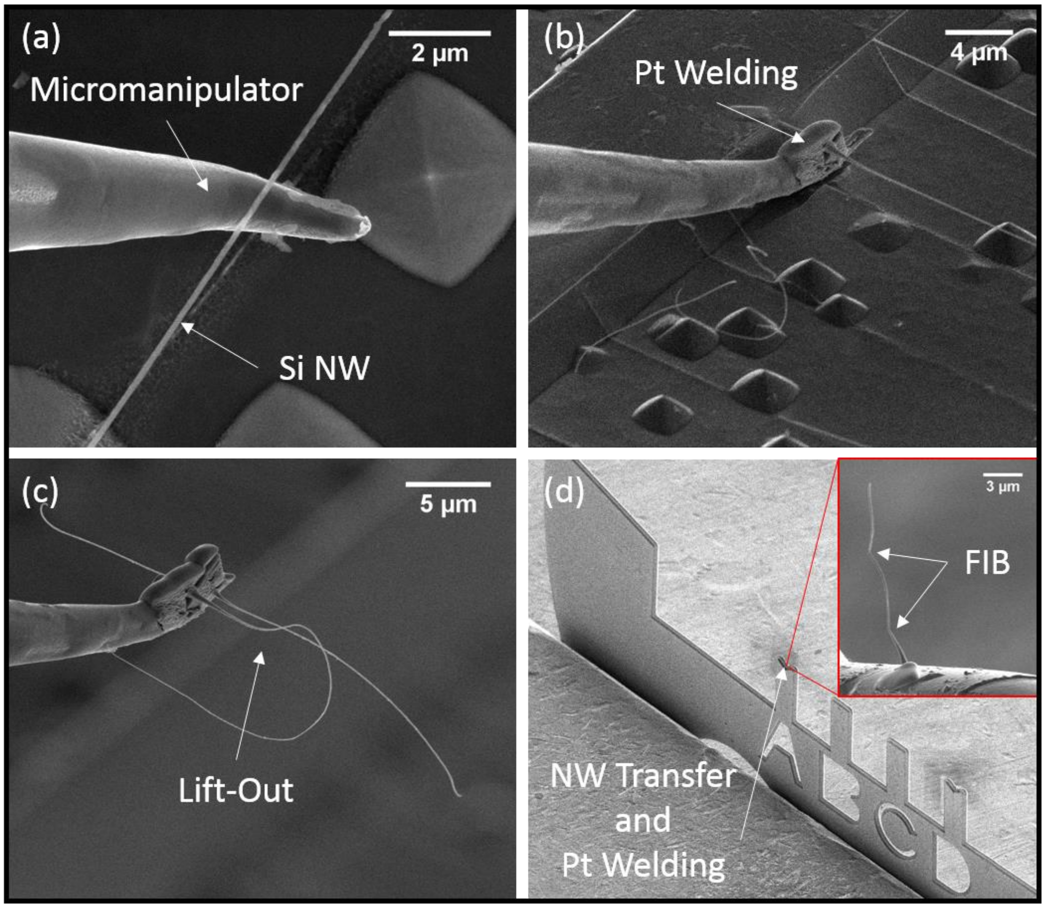

Figure E.1: Si NW TEM sample preparation for microstructural characterization: SEM images showing (a) Kleindiek micromanipulator tip positioned below the NW on Si substrate; (b) Pt welding to fix NW over micromanipulator; (c) Lift-out from the substrate; (d) NW transfer to TEM grid and Pt welding of NW to the grid, inset in (d) shows a transferred NW which is welded with Pt to TEM grid. The transferred NW is further exposed to FIB for ion induced bending characterization over two cross-sections as depicted in inset of (d) transferring the Si NWs from the substrate to the TEM grid, suitable for TEM experiments. Figure E.1 shows the details of TEM sample preparation through SEM images. The micromanipulator tip is first positioned below the NW and welded with Pt deposition through FIB (Figure E.1 (a)-(b)). The NW is subsequently lifted-out and transferred to TEM grids (Figure E.1 (c)-(d)), where it is positioned and welded over the grid securely with Pt deposition.

Controlled Bending of Nanostructures

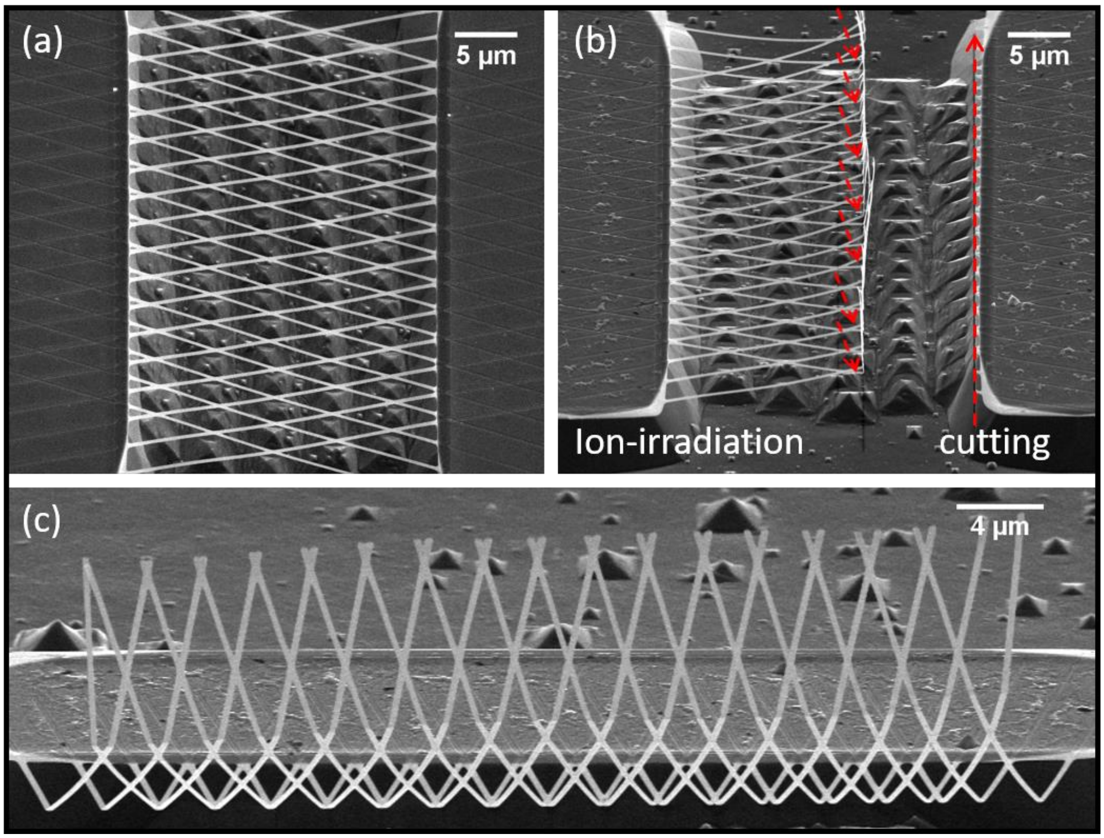

Figure E.2: Weaving nanostructures: controlled manipulation and bending of suspended Si mesh structure. SEM image in (a) shows the fabricated Si mesh structure suspended over two contact pads. The suspended mesh is cut with FIB and subsequently bent via ion irradiations as shown through SEM image in (b). SEM image in (c) shows the fabricated nanostructure after manipulation with FIB

The suspended nanostructures fabricated through wet etching of ion implanted Si were further subjected to ion irradiation to fabricate the 3D nanostructures through controlled bending. Figure E.2 (a) shows SEM image of a suspended mesh structures. The structure was fabricated through chemical etching of ion implanted mask design and is suspended over two contact pads. This structure can be further manipulated or desired configurations through controlled bending. Figure E.2 (b) shows the controlled bending approach through SEM image of the mesh structures. First, a line cut is made with FIB, in order to obtain a freely suspended mesh structure. Further, the mesh structures is bend in the desired configuration with ion irradiation. The bidirectional nature of ion irradiation induced bending provides additional degree of freedom and makes it possible to fabricate a variety of functional nanostructures for desired application. Figure 5.8 provides an accurate estimate of ion dose and energies for controlled bending of nanostructures, which can be utilized for weaving of nanostructures. Figure E.2 (c) shows SEM image of the fabricated nanostructure after manipulation with FIB.

Publications

Journal Articles

- V. Garg, B. Kamaliya, R. Singh, A. Panwar, J. Fu, R. G. Mote, "Controlled Manipulation and Multiscale Modelling of Suspended Si Nanostructures under Site-specific Ion Irradiation," *ACS Applied Materials and Interfaces*, 12, 6581-6589, 2020
- V. Garg, R. G. Mote, T. Chou, A. Liu, A. D. Marco, B. Kamaliya, S. Qiu, and J. Fu, "Weaving Nanostructures with Site-Specific Ion Induced Bidirectional Bending," *Nanoscale Advances*, 1, 2019
- V. Garg, R. G. Mote, and J. Fu, "Rapid Prototyping of Highly Ordered Subwavelength Silicon Nanostructures with Enhanced Light Trapping, *Optical Materials*, 94, 75-85, 2019
- V. Garg, R. G. Mote, and J. Fu, "Focused Ion Beam Direct Fabrication of Subwavelength Nanostructures on Silicon for Multicolor Generation," *Advanced Materials Technologies*, 3, 8, 1800100, 2018

Book Chapter

- V. Garg, R. G. Mote, and J. Fu, "Focused Ion Beam Fabrication: Process Development and Optimization Strategy for Optical Applications," in *Precision Product-Process Design and Optimization*, Springer, Singapore, pp. 189–209, 2018

Conference Proceedings, Presentations

- V. Garg, B. Kamaliya, S. Qiu, T. Chou, A. Liu, A. D. Marco, A. S. Panwar, R. G. Mote, and J. Fu, "Towards Functional Nanostructures with Focused Ion Beam," *26th Australian Conference on Microscopy and Microanalysis (ACMM),* 2020, Canberra, Australia
- V. Garg, S. Zhang, R. G. Mote, Y. Chen, L. Cao, and J. Fu, ""“Stand-Out”: A Novel Approach for Preparing Sub-100 nm Samples Through *In-Situ* Ion Induced

Bending," *Microscopy and Microanalysis*, vol. 25, no. S2, pp. 898–899, 2019, Portland, Oregon, USA

- V. Garg, R. G. Mote, and J. Fu, "Nonnegative Quadratic Programming Optimization of Focused Ion Beam Fabricated 3D Nanostructures for Structural Colors,", *MRS Spring Meeting*, 2019, Phoenix, Arizona, USA
- V. Garg, R. G. Mote, and J. Fu, "High Aspect Ratio Silicon Nanowires and 3D Nanostructures via Selective Focused Ion Beam Implantation and Wet Etching: Fabrication and Characterization," *19th International Microscopy Congress (IMC19)*, 2018, Sydney, Australia
- V. Garg, R. G. Mote, and J. Fu, "Coloring with Focused Ion Beam Fabricated Nanostructures," *Microscopy and Microanalysis*, vol. 24, no. S1, pp. 856–857, 2018, Baltimore, Maryland, USA
- V. Garg, R. G. Mote, and J. Fu, "FIB fabrication of highly ordered vertical Gaussian pillar nanostructures on silicon," *2017 IEEE 17th International Conference on Nanotechnology*, pp. 707–712, 2017, Pittsburgh, USA

Awards, Recognitions

- Tata Consultancy Services (TCS), PhD Research Scholarship, 2015-2020
- NTC Fellowship, 17th IEEE International Conference on Nanotechnology (IEEE NANO 2017)
- Best Micrograph Award, Microscopy and Microanalysis Meeting 2018, Baltimore, Maryland, USA
- Student Scholar Award, Microscopy and Microanalysis Meeting 2018, Baltimore, Maryland, USA
- Best Conference Paper Award, Oskar 2018, IITB Monash Research Academy, Mumbai, India
- Microscopic Gardening: Tiny Blossoms of Silicon, ANFF-VIC Image of the Year 2018, Melbourne, Australia
- Poster Prize 2nd Place, 26th Australian conference on Microscopy and Microanalysis 2020, Canberra, Australia

Acknowledgements

I take this opportunity to thank all the people without whom this thesis would not have been possible. First and foremost, I sincerely thank my supervisors Prof. Rakesh G. Mote and Prof. Jing Fu for their excellent guidance, encouragement, and help towards the project, and beyond. I am grateful for providing the opportunity to work in their research groups. Prof. Mote has always shown a lot of faith and confidence in me, which has helped immensely. Prof. Jing has been a great mentor and his excitement for research has been a driving force. I thank him for extending his support and funding for an extended Monash stay. My both supervisors have been a great critic of my work and have taught how to pay attention to every tiny details. They always encouraged to think beyond, and their enthusiasm has been a driving force for my efforts in research. I am indebted to them.

I thank my doctoral committee members Prof. Pradeep Dixit, Prof. Sankara Sarma Tatiparti, and Prof. Wenyi Yan for their valuable inputs. I thank Prof. Ajay Panwar for his help and fruitful discussions on molecular dynamics simulations. I thank Prof. Ramesh Singh for lab facilities at Machine Tools Lab (MTL). I thank Prof. Alex De Marco, Monash University for the access to Plasma FIB and support for the experiments.

I am grateful to Prof. Suhas Joshi, IIT Bombay for his motivation and recommendation for pursuing the doctoral studies. I also thank Prof. Deepak Marla for being a constant source of motivation.

I thank Dr. Amelia Liu, Monash Centre for Electron Microscopy (MCEM) for FIB training and her excellent support for the instrument. I am thankful to Dr. Peter Miller, Dr. Xiya Fang, Dr. Yu Chen, Dr. Renji Pan, and all MCEM staff for their excellent support. I express my sincere gratitude to Dr. Hemayat Uddin, Dr. John Zhu, Dr. Vahid Adineh for their support on various facilities at Melbourne Centre for Nanofabrication (MCN). I thank Dr. Finlay Shank, School of Chemistry for his help on Raman and UV visible spectroscopy. I thank Dr. Tsengming Chou, Stevens Institute of Technology for his support with TEM characterization. I thank all the project staff, teaching assistants of Centre of Excellence in Nanoelectronics (CEN), Sophisticated Analytical Instrument Facility (SAIF), Centre for

Research in Nanotechnology & Science (CRNTS), and Metallurgical Engineering & Materials Science (MEMS) at IIT Bombay for their support in the experiments.

I have been fortunate to meet some wonderful people over last 4 years. I sincerely thank Bhaveshkumar Kamaliya for his invaluable help and support. I thank my lab mates and friends Laxman Malla, Sagar Agnihotri, Abhishek Mukherjee, Chitresh Bhargava, Tanesh Gamot, Ganesan G., Anandita Singh, Kamlesh Joshi, Rinku Mittal, Meinam Annebusham Singh, Nilanjan Banerjee, Mukesh Tak, Mayur Darak, Yeonuk Kim, Vahid Adineh, Changxi Zheng, Shuo Zhang, and Shi Qiu for their support.

The staff at IITB Monash Research Academy, IIT Bombay, Monash University have been of immense support throughout the course of my stay. I am thankful to Prof. Murali Sastry for the support, and facilties during my tenure. I thank Dr. Kyatanahali Nagabhushana, Mr. Adrian Gertler, Mrs. Kuheli Banerjee, Mrs. Jayasree Narayanan, Mrs. Laya Vijayan, Mrs. Beena Pillai, Mr. Kiran More, Mrs. Nancy Sowho, Mr. Stelios Konstantinidis, Ms. Fiona Pyrczak, and others for helping through the complicated formalities including form submissions, paper-work etc.

I sincerely acknowledge PhD Research Scholarship and financial support from Tata Consultancy Services (TCS) for the project. I extend my thank to financial support received from IITB Monash Research Academy, IIT Bombay, and Monash University.

Last but not the least, I thank my parents and sister for their patience and support during my PhD work. Their love has made this possible. I thank Nisha, for being a constant support and brighten up the cloudy days.

-Vivek Garg